Louisiana State University
LSU Digital Commons

LSU Doctoral Dissertations | Graduate School

12-18-2021

Functional Structure of Biomacromolecules in Plant Biomass Using Solid-State NMR and Dynamic Nuclear Polarization

Alex Kipchirchir Kirui
Louisiana State University and Agricultural and Mechanical College

Follow this and additional works at: https://digitalcommons.lsu.edu/gradschool_dissertations

 Part of the Physical Chemistry Commons

Recommended Citation

Kirui, Alex Kipchirchir, "Functional Structure of Biomacromolecules in Plant Biomass Using Solid-State NMR and Dynamic Nuclear Polarization" (2021). *LSU Doctoral Dissertations*. 5732.
https://digitalcommons.lsu.edu/gradschool_dissertations/5732

This Dissertation is brought to you for free and open access by the Graduate School at LSU Digital Commons. It has been accepted for inclusion in LSU Doctoral Dissertations by an authorized graduate school editor of LSU Digital Commons. For more information, please contactgradetd@lsu.edu.

FUNCTIONAL STRUCTURE OF BIOMACROMOLECULES IN PLANT BIOMASS USING SOLID-STATE NMR AND DYNAMIC NUCLEAR POLARIZATION

A Dissertation

Submitted to the Graduate Faculty of the
Louisiana State University and
Agricultural and Mechanical College
in partial fulfillment of the
requirements for the degree of
Doctor of Philosophy

in

The Department of Chemistry

by
Alex Kipchirchir Kirui
BTech., Technical University of Kenya, 2015
May 2022

To my wife Diana Nyamisa Bosire, thank you for your patience, sacrifice, and being a source of inspiration to me. Thank you for your service in serving in the United States Navy by ensuring the liberties and values of this country are deeply protected.

To our unborn daughter Himari, you are the most wonderful thing that has ever occurred to us. In our lives, you are a great source of joy and happiness.

ACKNOWLEDGEMENTS

I would like to thank my advisor, Professor Tuo Wang. I am extremely grateful for his invaluable advice, continuous support, and patience during my PhD research and in life. His immense knowledge in NMR and plentiful experience have encouraged me in all the time of my academic research and positively changed my attitude towards research. I could not have imagined a better advisor and mentor for my Ph.D study. I am grateful for his strong support and helpful advice both in life and on my professional growth. Thank you for believing in me and inspiring me beyond excellence.

I would like to thank to my thesis committee members: Dr. Megan Macnaughtan, Dr. Louis Haber, and Dr. Sara Thomas-Sharma for serving in my committee and providing valuable feedback towards improving my research and dissertation as well as their constructive and insightful experience.

My PhD journey has been rewarding because of my lab mates in the Tuo Wang's group. I would like to specially thank Dr. Xue Kang for training me in my first year. I would like to extend my gratitude to present and past members of Wang group for their continuous support ad valuable discussions about research and life. They are Dr. Chandra Shekar, Dr. Fabien Deligey, Dr. Nader Ghassemi, Malitha Chathuranga, Arnab Chakraborty, Liyanage (Dev) Fernando, and Wancheng Zhao.

I wish to thank all my scientific collaborators for insightful discussions, and great collaborations. Many thanks to Dr. Fred Mentink-Vigier at the National High Magnetic Field Laboratory for training me in Dynamic Nuclear Polarization (DNP) and his endless efforts in making me a better scientist; Dr. Andrew Lipton at Pacific Northwest National Laboratory; Dr. Alfred French at USDA, New Orleans; Dr. Zhe Ling at Nanjing Forest University; and Dr.

Chaowen Xiao at Sichuan University. Their discussions and passion for research in their respective fields inspire me to be a better scientist.

I will always be grateful to my parents, Joseph and Gladys Kerich. Their words of encouragement and wisdom, prayers, and unending love aided in shaping me into the person I am today. A special thank you to my awesome siblings, Ken, Mercy, Victor, Collins, and Vincent who always know the right thing to say to put a smile on my face even when things get tough.

Finally, to my wonderful wife, Diana, and our unborn daughter Himari Kirui: your love and understanding helped me through the dark times. Without you believing in me, I never would have made it. It is time to celebrate; you earned this degree right along with me. I am truly blessed to have you in my life.

TABLE OF CONTENTS

ABSTRACT

This dissertation summarizes the recent findings on complex biomacromolecules in cell wall of plants and fungi which perform important roles in cell recognition, structural build up, and energy storage. Because of the technical difficulty in characterizing these biomacromolecules, which are often polymorphic and disordered in structure, the functional structure of these biomacromolecules remains elusive. In this dissertation, I present two solid-state nuclear magnetic resonance (ssNMR) and dynamic nuclear polarization (DNP) studies of carbohydrate-rich biosystems: the energy-rich plant biomass and disease-relevant, pathogenic fungi.

First, we have investigated the secondary cell wall of plant biomass which is a carbohydrate-rich biosystem using solid state nuclear magnetic resonance spectroscopy. In the intact stems of energy crops, such as switchgrass and maize, lignin self-aggregates to create hydrophobic nanodomains, which are connected to cellulose microfibrils *via* broad xylan interfaces. Through electrostatic interactions, non-flat xylan conformers bind the intrinsically disordered aromatics of lignin, whereas flat conformers bind the cellulose microfibrils surface. In woods, lignin principally packs with the xylan in a non-flat conformation *via* non-covalent interactions and partially binds the junction of flat-ribbon xylan and cellulose surface as a secondary site. All molecules are homogeneously mixed in softwoods; this unique feature enables water retention even around the hydrophobic aromatics. These findings shed light on into the functional structure of polysaccharides, their interaction with other biomolecules such as lignin and proteins, and the molecular architecture structure of cell walls. Additionally, the statistical analysis and structural elucidation of unlabeled biomacromolecules using DNP is discussed. Indeed, DNP is frequently used to overcome sensitivity limitations and to examine the intermolecular interface interactions.

Second, we studied the fungal cell walls of a major pathogen *Aspergillus fumigatus* and found it to contain a hydrophobic frame of α-1,3-glucan, and chitin, which is encased in a hydrated model of diversely connected glucans and, glycoprotein-rich outer layer. These findings created the first high-resolution model of fungal cell walls using ssNMR, allowing for in-cell, high-resolution drug impact characterization to aid in the development of antifungals that target fungal cell walls.

CHAPTER 1. INTRODUCTION

1.1. Carbohydrate-Rich Cell Wall

1.1.1. Background

The carbohydrate-rich cell wall is a unique and versatile component found in plants, bacteria, fungi, and algae that concurrently provides the cell with sufficient mechanical strength to keep its integrity and morphology under stress and retains remarkable plasticity to expand during cell growth[1,2]. These functions are carried out by polysaccharides, protein and lignin in cell wall whose three-dimensional structure, interactions and packing have not been fully characterized due to the amorphous and insoluble nature of nature of the cell wall.

Plant cell walls are made up of primary and secondary cell walls. These polysaccharides in both primary and secondary cell walls are very essential in plants because they perform key roles such as energy storage, structural building, and cell recognition. Polysaccharides are polymeric carbohydrates made up of long chains of monosaccharide units linked by glycosidic linkages. They range from simple linear structures to complex branched structures. The identity and configuration of the subunits, the position of the glycosidic linkages and their anomeric configuration, the eventual branching pattern on the main chain and substitution by methyl or acetyl groups, and more subtly, variations in the torsional conformations, all play a role in the structural polymorphism of complex carbohydrates.

1.1.2. Plant Cell Wall

1.1.2.1. Primary Cell Wall of Plants

The primary cell wall of plants mainly contains cellulose, hemicellulose and pectins. Cellulose consists of β-(1-4)-glucan chains and exist as microfibrils of ~5 nm in diameter[2-4] in primary cell wall[5]. Hemicellulose has shorter chains compared to cellulose and is highly branched. The

branching of hemicellulose provides a ground for interaction with cellulose. In dicots, for example *Arabidopsis*, the major hemicellulose is xyloglucan (XG), which is made up of a β-1,4-glucose backbone with α-D-xylose (Xyl) replaced substituted at regular intervals. Some of the Xyl is replaced with β-D-galactose (Gal) and α-L-fucose (Fuc). Pectins are anionic polysaccharides rich in α-D-galacturonic acid and they take part in some complex physiological process like plant growth and cell differentiation and therefore determine the integrity and rigidity of plant tissues. In dicots, homogalacturoran (HGA), rhamnogalacturoran (RG) I and RG II constitute the main pectins. RG I is made up of alternating 1,4-α-D-GalA and 1,2-α-L- rhamnose (Rha) units[5,6]. Pectins have a variety of functions, including regulating cell wall porosity, cell signaling, controlling cell adhesion and, and adjusting pH and ionic balance[7].

1.1.2.2. Interactions in Secondary Cell Wall

Secondary cell wall is deposited once the plant stops growing, and is mainly made up of cellulose, hemicellulose (glucomannan and xylan), and aromatic biopolymer lignin. In secondary cell walls, glucomannan and xylan have been found to bind cellulose microfibrils[8], but the mechanism of their interaction is not well known. Being the main hemicellulose in plant secondary cell wall, xylan interaction with cellulose is expected to have great effect on the cell wall characteristics and properties such as wood recalcitrance. This is supported by the fact that *Arabidopsis*, a plant with reduced xylan quantity has weak cell walls and is unable to develop a robust vascular system[9]. Molecular dynamic studies have shown that xylan layers can wrap cellulose microfibrils. Recently, Dupree and colleagues pioneered the study of secondary cell wall using ssNMR to probe the interactions between xylan and cellulose. They revealed that xylan shows polymorphism in secondary cell wall of *Arabidopsis* and interacts with cellulose by adopting two-fold conformation (one 360° twist per two glycosidic bonds)[10]. These studies provide

a fundamental foundation in understanding the molecular architecture of secondary cell wall in its native state. However, lignin which accounts about 20-35% of the dry weight of cell wall has not been fully studied on atomic level. Extraction and dissolution of lignocellulosic material using organic solvents has been relied heavily for solution-NMR characterization and analysis[11-13]. These methods greatly interfere with molecular interactions making it difficult to fully understand cell wall structure.

1.1.3. Fungal Cell Wall

Fungal cell walls contain glucans, glycoproteins, and a small portion of chitin. Fungal glucans contain predominantly linear β-1,3-linkage, and a small portion, about 10% of β-1,6- and β-1,4-linkages. Using ssNMR, we discovered that chitin and α-1,3-glucans form a hard and hydrophobic scaffold that is surrounded by a soft and well-hydrated matrix of -glucans in a recent work on *Aspergillus fumigatus*. Glycoproteins and a small fraction of α-1,3-glucans coat the cell wall surface in a highly dynamic shell[14].

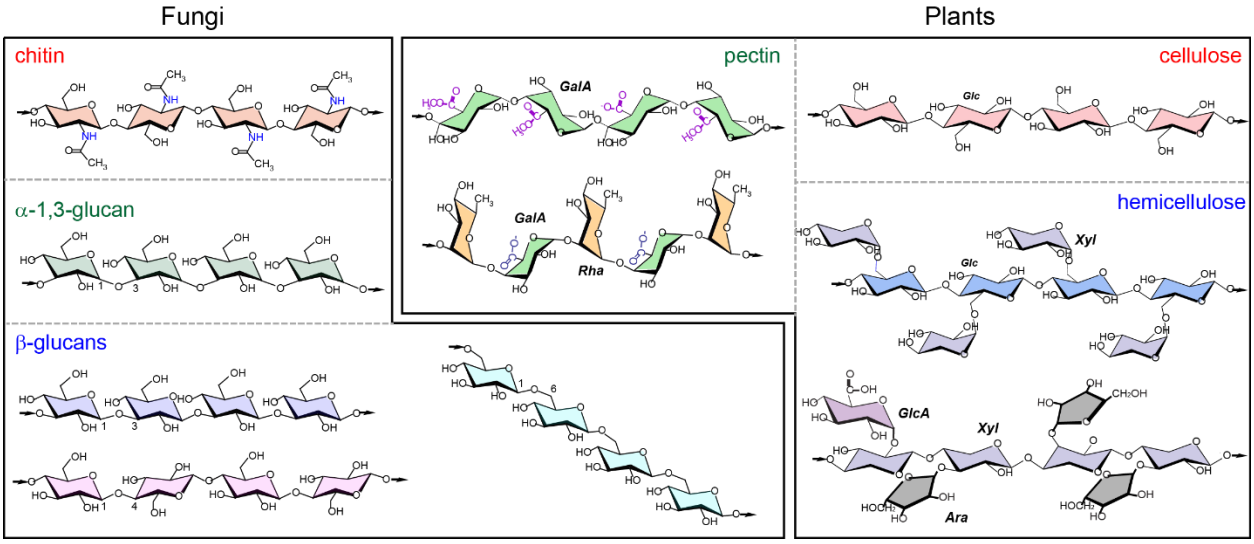

Figure 1.1. Representative sugar structures in plants and fungi.

1.1.4. Proteins

Proteins are also a vital component of the cell wall's structure. Plant cell walls have relatively small amounts of proteins compared to other biomolecules such as cellulose, with the exception of some algae that have cell walls comprised entirely of proteins, hemicellulose and pectins[15]. Primary cell walls contain more proteins than secondary cell walls. The best known structural proteins are extensins or hydroxyproline (Hyp)-rich glycoproteins (HRGPs)[16]. These extensins are rich in lysine (Lys) making the basic proteins, and their basic nature make interact with the acidic pectic blocks in the cell wall[17].

1.1.5. Significance of Cell Wall Study

Although plant cell wall chemical compositions are well known, how they interact and form three-dimensional network to provide rigidity and mechanical have not been fully understood. For decades, cell wall structure and characterization mainly involved sequential chemical extractions of the cell wall components, sugar analysis and microscopy. These methods are limited by highly cross-linked structure of the wall polymers to obtain sufficient resolution. The hydrogen bonding interactions in cellulose pattern have been well studied using X-ray diffraction and ssNMR studies. However, the interactions between cellulose microfibrils and hemicellulose has been a subject of discussion and debate for several decades. Xyloglucan, the main hemicellulose in primary cell wall have been thought to cross link cellulose microfibrils[3,18]. Recent studies have employed multidimensional ssNMR spectroscopy to study the spatial arrangement of macromolecules in ^{13}C-labeled primary cell walls, the fast-growing part, of several plants as well as and the mechanism through which the functional proteins unlock polysaccharide networks to initiate cell expansion during plant growth. In recent years, Hong and colleagues pioneered the study of the plant primary cell wall using high resolution magic angle spinning (MAS) ssNMR spectroscopy. They have revealed that only a small portion of xyloglucan interacts

with cellulose but they observed a strong interaction between cellulose[19] and pectin from the dicot model plant *Arabidopsis*[5,20] they investigated in their studies. They have also shown that cellulose interacts with GAX in *Brachypodium*[21,22] which provides insights to the polysaccharide interactions in grasses.

Due to the lack of high-resolution methods to study the insoluble and disordered polymers in native cell walls, we do not fully understand how complex carbohydrates interact with each other and other biomolecules to form polymer networks with versatile functions[20]. For example, the up-to-date model of secondary plant cell walls, the majority of plant biomass, depicts cellulose microfibrils to be aggregated to form loose bundles that are typically tens of nanometers across (Figure 1.2a).

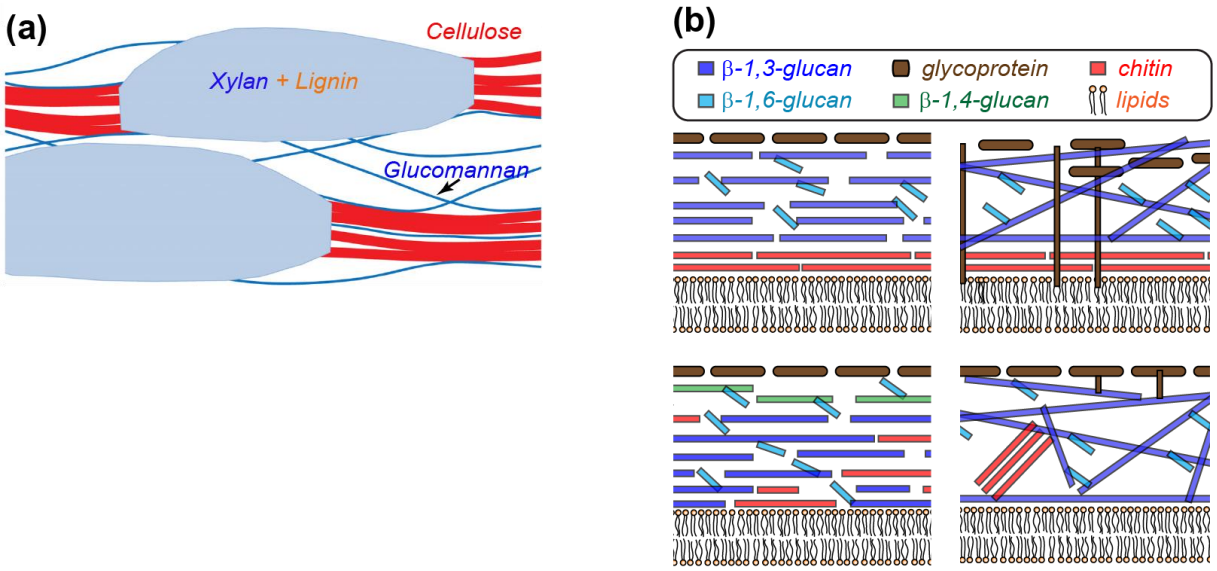

Figure 1.2. Putative models of a) secondary plant cell walls and b) fungal cell walls. Panels (a) and (b) are adapted with permission from reference[3] Copyright 2021 Frontiers and Elsevier respectively

It has been proposed that xylans and lignin are extensively coating the cellulose surface, and glucomannan crosslinks multiple cellulose aggregates[3], but this hypothetical model is still

ambiguous at the molecular level. Another important system is the fungal cell walls, which have attracted tremendous attention in the last decade due to its potential as the target of antifungal compounds. As the plant cell walls, the detailed structural information of fungal cell walls remains debatable, and the prevailing models differ considerably in the spatial distribution of wall polymers (Figure 1.2b)[2]. All models depict chitins to be close to the plasma membranes, and most glycoproteins to be on the surface, but it is unclear whether chitins can penetrate throughout the cell wall, which, by expectation, will provide the cell wall with more homogeneous rigidity. A broader question is if there is a generalized structural module that is commonly adopted by all types of cell walls, and if yes, under what biochemical principles are these polysaccharides placed and interacted to empower cell walls to fulfill its functions?

ssNMR and DNP[23-25] helps us to clarify and substantiate the molecular evidence of lignocellulose structure. The ^{13}C-labeled stems of three energy crops (maize, rice, switch grass) and the model plant *Arabidopsis* were investigated[8]. In chapters 5 and 6, we show that xylan bridges lignin and cellulose microfibrils in a conformation-dependent way. This finding, together with a prior study[10] showing that flat xylan conformers bind cellulose, has revealed the structure-function relationship for xylan as well as the versatility of branching hemicellulose in bridging distinct biomolecules due to its variable conformational shape. These results provide a revised understanding of the architecture of secondary cell wall in plants which will facilitate development of higher digestibility crops biomass conversion into biofuels.

1.2.1. Techniques for Investigating Cell Wall Biomacromolecules Using Solid-State NMR

ssNMR spectroscopy is a non-destructive method which is suited for determining the atomic structure of insoluble, complex biosystems and biopolymers. ssNMR has been utilized to study ^{13}C labeled cell walls of fungal cell walls, bacteria, primary cell walls, and secondary cell

walls of intact plants in native state to probe polysaccharide structure, hydration, molecular interactions, and dynamics to reveal biochemical and structural information that other orthogonal methods such as solution NMR, single crystal X-ray, and biochemical assays are unable to reveal. This section reviews the solid-state NMR techniques used in this thesis to investigate uniformly labeled ^{13}C plant secondary cell walls of plants, and fungi.

1.2. Introduction to Nuclear Magnetic Resonance Spectroscopy

When atomic nuclei are put in an external magnetic field and a specific frequency of electromagnetic radiation is given, a physical phenomenon of resonance known as Nuclear Magnetic Resonance (NMR) happens when transition between the magnetic energy levels occurs. Atomic nuclei have a physical feature called spin, which can be viewed as the rotation of a nucleus on its own axis: the rotation of a charged nucleus generates a magnetic field, giving the nucleus a magnetic moment. In the presence of an external static magnetic field, the nuclear magnetic moment aligns parallel to the external field resulting in a net magnetic moment within the sample. The sample temperature (T), the strength of the external magnetic field (B_0), and gyromagnetic ratio (γ) of the nucleus, all influence the amount of this bulk magnetic moment, also known as net magnetization ($M_\circ$)[26].

$$M_\circ \alpha \ (\gamma \hbar B_\circ)/kT \qquad \textbf{(1.1)}$$

$\hbar$ – Planck's constant
k – Boltzmann constant

The gyromagnetic ratio (γ) is nucleus dependent, and this thesis covers the spin ½ nuclei such as ^{1}H, ^{13}C, ^{15}N as some of the biologically relevant NMR-active nuclei. It is worth noting that ^{1}H has the largest gyromagnetic ratio and it is the most abundant isotope in nature, therefore, it is mostly used for cross-polarization (CP) experiments to enhance sensitivity of lowly abundant isotopes

such as ^{13}C and ^{15}N through polarization transfers. To obtain information on molecular environments of atoms, radiofrequency (*rf*) pulses with varying B1 fields strengths and frequencies close to the Larmor frequency of the nuclei of interest are used to manipulate the bulk magnetization vector.

1.2.1. Static and Magic Angle Spinning Spectroscopy

Nuclear magnetic interactions are anisotropic which means that their energy levels and resonance frequencies, are determined by the direction of the resulting magnetic moment with respect to the static magnetic field. Rapid isotropic motions of molecules in solution result in efficient averaging out of nuclear magnetic interactions' orientational dependence, leaving only the isotropic component discernible. NMR investigations in solid-phase samples, which means that they don't undergo fast isotropic molecular tumbling, produce broad lines with intensity and frequency profiles that depict the molecular orientational patterns in the sample[27]. Under the static state, orientation-dependent dipolar couplings, chemical shift anisotropy (CSA), and quadrupolar couplings all lead to broad "powder patterns". While these broad lines provide important information about the electronic structure and local geometric of the molecules being studied investigated, they are also associated with resolution loss, that prevents studying multiple sites in the sample, as well as severely reduction in sensitivity due to spectral intensity distribution over a large range of frequency. As a result, by spinning the sample rotor at the magic angle (54.74°) with respect to the external magnetic field direction, anisotropic interactions are averaged out. If the spinning frequency is substantially higher than the coupling strength, dipolar interactions will be averaged out to zero under magic angle spinning (MAS). Under moderate MAS frequencies, however, the ^{13}C-^{1}H dipolar coupling is not averaged out. The MAS-achieved narrow spectral line widths provide enough spectral resolution for chemical shift assignment, allowing for the solid-

state analysis of complex biomolecules and biosystems. Similarly, if the MAS frequency is high enough, dipolar interactions will be averaged out to zero. For example, spinning frequencies substantially higher than 22 kHz will be necessary to average out the ^{13}C-^{1}H dipolar coupling strength of 22 kHz (for a C-H bond distance of ~1.1Å). To sharpen ^{13}C peaks and avoid signal loss due to homogenous line widening, ^{13}C-^{1}H dipolar decoupling sequences are required for moderate MAS of 20 kHz.

In practice, depending on the sample under investigation and the information being sought, both total and averaging regimes via MAS are extensively used in solid-phase specimen experiments. When many sites must be identified, MAS NMR observations are frequently performed in a multidimensional format, with isotropic chemical shift dimension supplemented with the indirect dimension, which records anisotropic chemical shifts, isotropic interactions, or multiple-quantum coherences. Specially tailored *rf* pulse techniques are employed to restore anisotropic information in the indirect dimension, where the interference between sample rotation and the rf field, also known as recoupling, causes the perturbation of MAS averaging[27].

1.2.2. Multidimensional Correlation Spectroscopy

Multidimensional correlation NMR spectroscopy is usually required because of chemical shift overlap of biomolecules. Although one dimensional (1D) can provide information relative to chemical shifts and quantification, it cannot be fully used for characterization and analysis due to overlap and ambiguity. In addition, various polarization transfer methods and selective filters are particularly important for characterizing biomacromolecules in the cell wall. Various selection methods using CSA, chemical shift, and T1 or T2 relaxation times are useful for selectively determining magnetization at a specific site with specific dynamic range compared to other sites

in the sample. In this section, I will discuss several multidimensional homonuclear experiments used for structural determination of complex plant cell walls in chapters 3-7.

1.2.3. Homonuclear Correlation Spectroscopy

High resolution two dimensional (2D) homonuclear ^{13}C-^{13}C is particularly useful in determining chemical shifts of lignocellulose and studying their intramolecular and intermolecular interactions. Intramolecular correlations are very useful in resonance assignments while intermolecular correlations provide insight to interactions and arrangement of molecules in space. The intramolecular correlations are defined by the short ^{13}C-^{13}C polarization transfer periods while intermolecular correlation utilizes long mixing time which probe both intra and inter-residue correlations. Different nuclei and techniques also define short- and long-range correlation. The higher the gyromagnetic ratio of a nuclei, the larger the distance-reach of polarization, for example, ^{1}H and ^{19}F that have higher gyromagnetic ratios. Therefore, ^{13}C-^{13}C correlation measurements are only limited to sub-nanometer scale.

Most of the multidimensional experiments comprise of a few fundamental building blocks namely: initial excitation, mixing time for polarization transfer, t1 evolution for indirect dimension, and t2 detection for direct dimension. Initial polarization is routinely created using cross polarization (CP), direct polarization (DP) or through insensitive nuclei enhanced by polarization transfer (INEPT)[28]. Since ^{1}H spins are abundant in biological samples, CP is widely used in biomolecular ssNMR to increase the of the low-γ nuclei such as ^{13}C or ^{15}N. Theoretically, polarization is enhanced by a factor of γ_H/γ_X. which translates to about 4-fold for ^{13}C and 10-fold for ^{15}N NMR. During CP, the ^{1}H spins (source) and sink nuclei like ^{13}C are respectively spin locked in the transverse plane by a synchronized rf radiation on ^{1}H and the observed ^{13}C nucleus satisfying the "Hartmann-Hann condition" ($\omega_{1,H} \pm \omega_{1,C} = n\omega_r$)[26]. The INEPT scheme which is J-

coupling based works strictly for protonated nuclei. INEPT preferentially detects very mobile regimes while CP preferentially detects rigid species. DP is used to detect mobile components but not very mobile as is the case for INEPT.

The structure of plant cell wall in this thesis is studied by a variety of 2D ^{13}C-^{13}C homonuclear and heteronuclear correlation experiments. Spins that are close together in space can transfer polarization via dipolar interactions, whereas spins coupled by chemical bonds can do so via the scalar J-coupling. These experiments serve diverse purposes, have varying distance restrictions, and have varied operational circumstances since they use different mechanisms. Here, I will discuss the three major schemes for homonuclear correlation spectroscopy: proton-driven spin diffusion (PDSD), Incredible Natural Abundance Double Quantum Transfer (INADEQUATE) type, and CHHC experiments.

Proton-driven spin diffusion (PDSD) is a homonuclear correlation experiment where magnetization is transferred from a highly abundant nuclei like ^{1}H to a lowly abundant nucleus like ^{13}C through CP and from here it is transferred to other ^{13}C that are close in space. This ^{13}C-^{13}C polarization transfer is assisted to a great extent by reintroduction of ^{1}H-^{13}C dipolar couplings[29-32]. With relatively slow spinning (<20 kHz), weak ^{13}C-^{13}C dipolar couplings are averaged by MAS. However, due of their interactions with the environment, polarization transfer between carbons is still possible. ^{13}C-^{1}H dipolar couplings are reintroduced by turning off the ^{1}H-^{13}C dipolar decoupling during the mixing period, therefore, broadening the carbon lineshapes and increasing spectral overlap. The spectral overlap between two broadened carbons peaks with a small chemical shift difference, or the overlap between a carbon signal and the spinning sidebands of another peak[33] allows effective polarization transfer among different ^{13}C spins. To minimize

magnetization due to ms timescale ^{13}C T2 relaxation, the magnetization is stored along z-axis. To retain site resolution, ^{1}H-^{13}C decoupling is applied during t1 evolution ad t2 detection periods.

PDSD experiment is commonly used for measuring long-range correlations because the mixing period does not require rf irradiation which heats up the sample. In PDSD, however, short mixing periods of about 100 ms can be employed to establish intra-residue ^{13}C-^{13}C short range correlations. For the studies in this thesis, the optimal mixing time for inter-residue correlations is 1-1.5 s to optimize between maximum distance-reach and the signal loss due to ^{13}C T1 relaxation.

Under low spinning speeds ~10 kHz and low to moderate magnetic fields (<14 kHz), the PDSD experiments are more efficient. At higher MAS frequencies and under higher magnetic fields, the dipolar-broadening effect is reduced, and larger chemical shift differences decrease spectral overlap, reducing the polarization transfer efficiency. Therefore, the dipolar recoupling methods, such as RFDR, CORD, and DARR sequences, can be used to achieve efficient polarization transfer under high magnetic field and fast MAS. However, CORD, and sequences utilize constant rf irradiation for dipolar recoupling, thus, cannot be set for a very long time due to rf heating.

In CHHC experiments[34,35], (Figure 1.3b**), t**he strong ^{1}H-^{1}H dipolar couplings and small chemical shift distribution in protons allow the ^{1}H spin diffusion to be much more efficient than ^{13}C spin diffusion. Compared to PDSD, the CHHC scheme makes use of ^{1}H spin diffusion. The ^{1}H-^{1}H magnetization transfers of 10-15Å are in principle achievable with mixing times of a few milliseconds. However, the efficient ^{1}H spin diffusion in the dense ^{1}H network within a sphere of 10-15Å radius causes the immediate loss of ^{1}H magnetization to the ^{1}H cloud making the sensitivity of any individual transfer very small. In these experiments, three cross-polarization

steps are used to transfer polarization between ^{1}H and ^{13}C, which causes a significant reduction in sensitivity. Additionally, the nature of the sample can affect the efficiency of this experiment.

Another method for ^{13}C-^{13}C homonuclear correlation is the INADEQUATE[36,37] experiment. This experiment utilizes J-couplings for polarization transfer and provides unambiguous through-bond correlations for resonance assignments. During the first τ-180°-τ period, the ^{13}C magnetization evolves under ^{13}C-^{13}C J-coupling to generate anti-phase terms, which are then converted to double quantum (DQ) coherence of $-2I_xS_x - 2I_yS_x$ by the second 90° pulse. The DQ coherence evolves under the sum of the chemical shifts of two directly bound carbons during the t1 evolution and is encoded in the indirect ω1 dimension. The third 90° pulse converts DQ coherence to antiphase single-quantum (SQ) coherence, while the second τ-180°-τ period establishes $I_y + S_y$ in phase single quantum coherence for t2 detection. The resulting spectrum is asymmetric and diagonal-free.

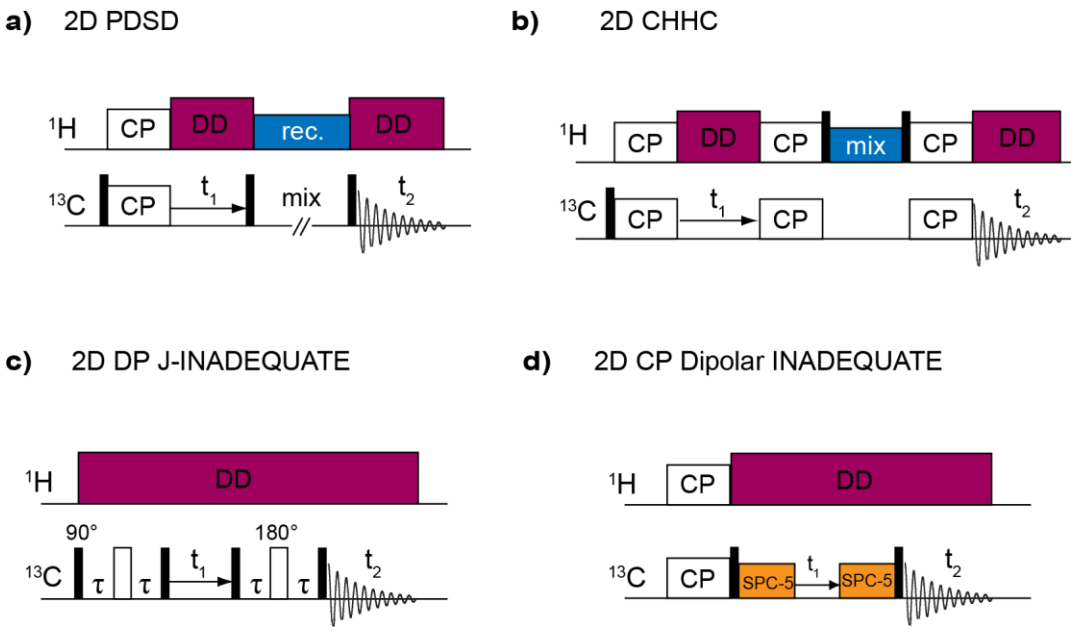

Figure 1.3. Homonuclear correlation experiments. a) ^{13}C-^{13}C spin diffusion experiment ^{13}C-^{1}H dipolar couplings are reintroduced. b) ^{13}C homonuclear correlation experiment that utilizes ^{1}H -^{1}H spin diffusion. c) J-INADEQUATE experiment. d) dipolar-based INADEQUATE experiments.

The DP J-INADEQUATE experiment favors sharp signals from dynamic species since the combination of direct polarization and the long J-evolution period (10-20 ms) preferentially detects the signals of mobile species. The CP-based version of INADEQUATE preferentially detects rigid components. This experiment recouples the homonuclear ^{13}C-^{13}C dipolar coupling to transfer polarization between directly bonded carbon spins and creates DQ coherence via the symmetry-based SPC-5 recoupling sequence. SPC-5 block requires rotor-synchronization of rf field strengths: the ^{13}C field strength is to achieve SPC-5 recoupling, and the ^{1}H-^{13}C decoupling strength should be at least 2.5 times the ^{13}C rf field strength for it to be effective. For 12 kHz MAS with a ^{13}C-^{13}C recoupling field strength of 60 kHz, we should use ^{1}H decoupling of ≥150 kHz, which is not feasible for the conventional NMR probe circuit. Therefore, slow spinning rates and low-field magnets are favorable for this sequence in order to avoid very strong rf pulses.

1.2.4. Molecular Dynamics: Rate and Amplitude

The heteronuclear dipolar couplings and NMR relaxations provide important structural information on the orientation and dynamics of the molecule. Plant cell wall provides a perfect niche for studying dynamics because it is chemically and dynamically heterogenous and these dynamics are important in characterizing the cell wall. Correlating the one-bond ^{13}C-^{1}H dipolar couplings with ^{13}C chemical shifts, the dipolar-chemical-shift DIPSHIFT[38,39], and Lee-Goldberg CP (LG-CP) determine the site-specific information about rigidity of a given chemical species.

In my thesis research, DIPSHIFT was used extensively. The motionally averaged dipolar coupling ($\bar{\delta_D}$) is directly measured. The ratio of the measured dipolar coupling to the rigid-limit value ($\bar{\delta_D}$) is the dipolar order parameter (S_{XH}) of a bond X-H. The angle between the motional axis and the bond of interest, denoted by (S_{XH}), represents the motional amplitude. In this experiment, the ^{13}C-^{1}H dipolar coupling is allowed to evolve for a fraction of a rotor period under

^{1}H-^{1}H homonuclear dipolar decoupling such as MREV[40] or FSLG[41] which prevents ^{1}H spin diffusion and maintains site specificity. Chemical shift evolution is refocused by a 180° pulse, placed after one rotor period, before detection of ^{13}C magnetization. Variable dipolar evolution times are measured and correlated with ^{13}C isotropic chemical shifts to get a ^{13}C-^{1}H dipolar dephasing curve for each ^{13}C site.

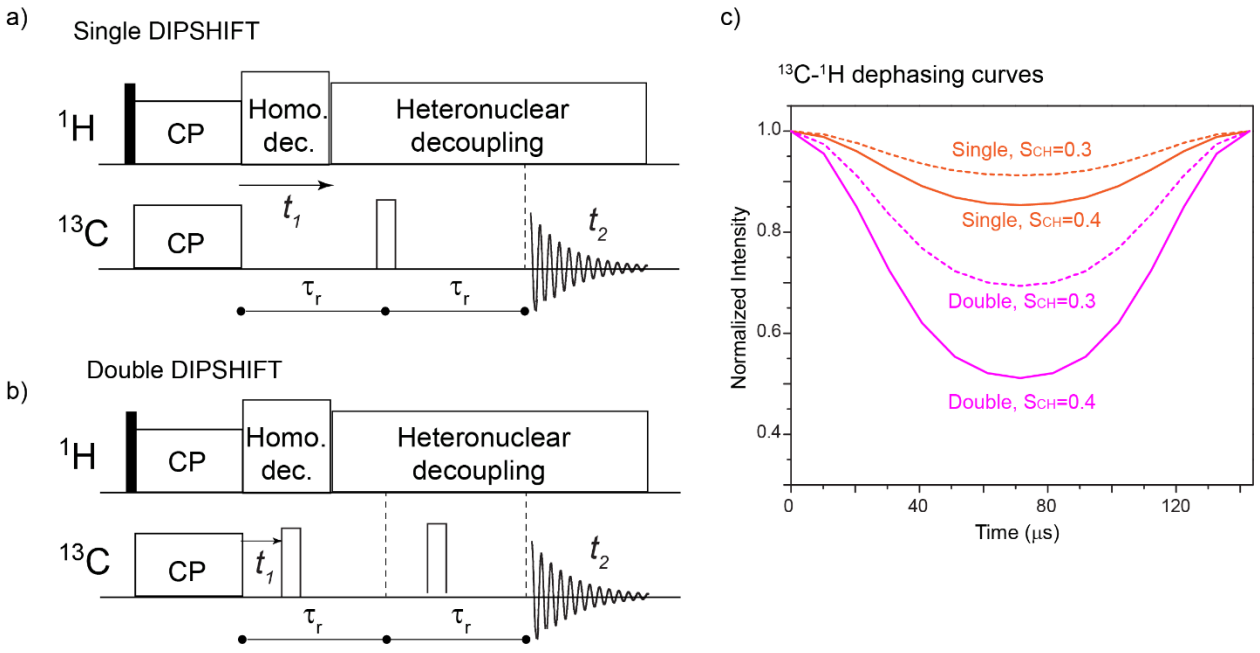

Figure 1.4. ^{13}C-^{1}H DIPSHIFT pulse program and experiments. a) Single version DIPSHIFT pulse sequence. b) Double version DIPSHIFT pulse sequence c) Single- and double- dipolar dephasing curves using FSLG for 1 H homonuclear decoupling. Dephasing is more significant and well-dispersed with small order values of 0.3 or 0.4 for double DIPSHIFT than in the single DIPSHIFT.

The experimental ^{13}C-^{1}H dipolar dephasing curves are fit to obtain the measured ^{13}C-^{1}H dipolar coupling for each ^{13}C chemical shift. Homonuclear decoupling reduces the effective ^{13}C-^{1}H coupling and the measured coupling is divided by a scaling factor to obtain the true motionally-averaged ^{13}C-^{1}H dipolar couplings. The scaling factor is 0.577 for FSLG and 0.47 for MREV-8 schemes. The ratio between the apparent dipolar couplings and the theoretical rigid limit value (δ = 22.7 kHz) is the molecular order parameter S_{CH}

It's worth noting that both chemical shift interaction and ^{13}C-^{1}H are doubled after the first 180° pulse but the isotropic and anisotropic chemical shifts are refocused after the second 180° pulse. Figure 1.4c shows smaller order parameters (<0.5) due to weak dipolar couplings and have better separation by use of double DIPSHIFT experiments. This experiment was used in chapter 4 to compare the motion of highly dynamic polysaccharides in two mutants and wild-type cell wall samples.

1.3. Dynamic Nuclear Polarization

The use of dynamic nuclear polarization (DNP) for signal amplification is one of the most recent significant discoveries in NMR. DNP is based on a concept similar to CP: using the abundant polarization of a receptive spin to boost the polarization of a less abundant one. The polarization of electron spins is transferred to nuclear spins in DNP (most commonly to ^{1}H spins). Only 1.1 % of carbon pairings can yield a 2D ^{13}C-^{13}C correlation because the first ^{13}C nucleus must be neighbored by another ^{13}C nucleus to be measured. The most common method to conduct experiments is using magic angle spinning- dynamic nuclear polarization (MAS-DNP) which utilizes the use of stable biradicals doped into the sample and spinning the sample in NMR spectrometer under cryogenic temperatures (~100 K) while irradiating the sample with microwave.

MAS-DNP benefits from the huge sensitivity enhancement from the unpaired electrons Under identical experimental conditions, the gyromagnetic ratio of the unpaired electron spins results in polarization that is ~660 times larger than ^{1}H and 2660 times greater than ^{13}C. Experimentally, this is achieved by either dissolving or suspending the material in a radical solution, which is then frozen during the experiment. By impregnating a sample with a radical-containing solution, surfaces of materials can be polarized. This places the radical near to the surface, resulting in a high sensitivity.

1.3.1. DNP Characterization of Unlabeled Biomaterials

To date, most of the biomolecular NMR investigations require isotope-labeling for feasible sensitivity but it becomes too costly for biosystems with large size and long lifecycles (trees for example). It also becomes impractical for in-situ investigations of many biomedical materials such as the fungal isolates from patients. The difficulty and expenses associated with isotope labeling have turned into a major barrier. The development of DNP, a technique enhances NMR sensitivity by tens to hundreds of times by transferring the polarization from electrons in radicals to NMR-active nuclei in biomolecules (Figure 1.5 a-c), has enabled the measurement of 2D ^{13}C-^{13}C/^{15}N spectra on unlabeled samples using the very low natural abundance of ^{13}C (1.1%) and ^{15}N (0.4%). This method has been employed with spectral editing methods as well as statistical chemical shift analysis to determine the structure of polysaccharides in whole-cell systems.
To achieve this goal, we need to overcome three technical barriers: the very low sensitivity due to the low natural abundance of isotopes, the limited resolution due to the high structural polymorphism of molecules in intact cells, and the difficulty in correlating NMR chemical shifts with carbohydrate structure. We propose to employ DNP to enhance the NMR sensitivity, and spectral editing techniques that selectively detect a subset of molecules at one time to improve resolution. We have employed this method to investigate the functional structure of cotton with and without mechanical processing (Figure 1.5c-e)[42] and rice mutants with altered degree of acetylation in the hemicellulose arabinoxylan. We are also able to investigate many plant and fungal mutants with the attenuated biosynthesis of cell wall components, which will further reveal the structural function of the related polysaccharides. These samples include mutants with altered cellulose crystallinity, decreased content of lignins, or xylans with different sidechain substitution patterns for plants, and chitin and glucan mutants of fungi.

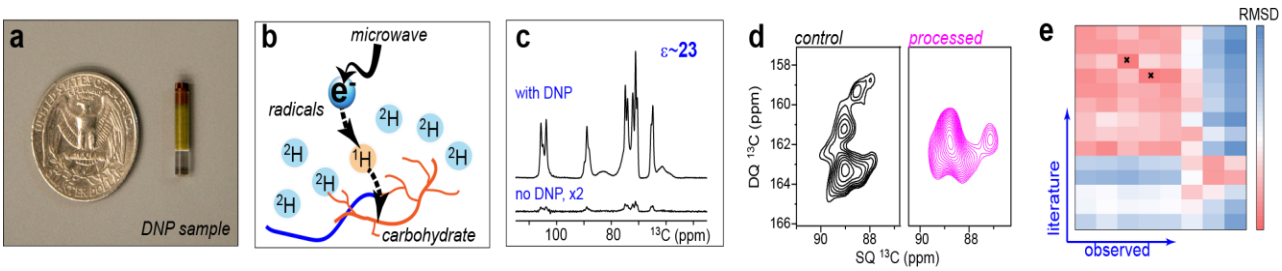

Figure 1.5. DNP methods for characterizing unlabeled biomaterials. a) Representative DNP sample. b) DNP mechanism. c) DNP enhances the NMR sensitivity for 23-fold on cotton. d) Natural-abundance ^{13}C-^{13}C 2D spectra of unlabeled cotton reveal structural changes by mechanical processing. e) Statistical analysis of NMR chemical shifts help identify the comparable structure (black cross).

1.4. Thesis Organization

This thesis is primarily composed of published studies that use solid-state NMR and DNP to better understand the structure, interactions, hydration, and dynamics of plant cell walls and fungi. **Chapter 1** introduces plant cell wall and fungi and the significance of the research work. Additionally, discussion of ssNMR techniques and methods are included in this chapter.

Chapter 2 is a protocol showing how ^{13}C and ^{15}N fungi samples can be produced and how they can be processed for ss NMR experiments and DNP. The plant biomass sample preparation procedure is extensively described. Measurement of 1D and 2D ^{13}C-^{13}C/^{15}N for high resolution structural elucidation is possible with ssNMR with sensitivity boosting DNP. Quantifying the intensity in 1D spectra and the polarization transfer efficiency in 2D correlation spectra, as well as looking at the relaxation durations, can be used to investigate isotope labeling. Isotope labeled samples have faster relaxation times compared to natural abundance samples.

Chapter 3 utilizes the sensitivity-enhancing technique of dynamic nuclear polarization with statistical analysis of chemical shifts reported and in literature to investigate the molecular structure of unlabeled cotton cellulose. The atomic resolution allows us to track the loss of Iα and

Iβ allomorphs as well as the formation of a unique structure during ball-milling, demonstrating the necessity of high crystallite size in sustaining Iα and Iβ model structures. A discrete distribution of well resolved peaks has been observed in the "disordered" regions, indicating partial order.

In Arabidopsis primary cell walls, a pectin methyltransferase regulates polysaccharide dynamics and interactions. In **chapter 4**, we determined the pectin modification in *Arabidopsis* wild-type and mutant cell walls using ^{13}C-labeled cell walls. Microsecond dynamics were improved in the mutants due to polymer disorder, but motional amplitudes were constrained due to tighter pectin-cellulose interactions, as measured by relaxation and dipolar order parameters. These findings shed light on the polymer structure and packing in these two pectin mutants, allowing researchers to better understand how pectin influences cell wall design, cell wall dynamics, and plant growth at the nanoscale.

In **chapter 5**, we investigated the secondary cell wall of plant biomass using *Zea mays* which is a carbohydrate-rich biosystem using ssNMR. Using isotopically enriched whole-cell samples, we determined the conformation, packing, hydration, and motion of polysaccharides and associated biomolecules. DNP is required for overcoming the sensitivity limitation for probing the polymer interface. We found out that lignin preferentially binds to the non-flat region of xylan, which is linked to the flat-ribbon xylan domains that are coating the even surface of cellulose microfibrils.

The cell wall of *Aspergillus fumigatus*, a major fungal pathogen, is examined in **chapter 6**. The sub-nanometer packing, ns-μs motion, and hydration of biomolecules in intact cell walls of native fungi were measured using a series of 2D ^{13}C-^{13}C/^{15}N studies. The hydrophobic framework of chitin and α-1,3-glucan present in fungal cell walls is surrounded by a hydrated matrix of diversely connected -glucans and capped by a dynamic, outer layer rich in glycoproteins.

CHAPTER 2. PREPARATION OF FUNGAL AND PLANT MATERIALS FOR STRUCTURAL ELUCIDATION USING DYNAMIC NUCLEAR POLARIZATION SOLID-STATE NMR

2.1. Introduction

Carbohydrates play a central role in various biological processes such as energy storage, structural building, and cellular recognition and adhesion. They are enriched in the cell wall, which is a fundamental component in plants, fungi, algae, and bacteria [2,43,44]. The cell wall serves as a central source for the production of biofuel and biomaterials, as well as a promising target for antimicrobial therapies[45-50].

Our understanding of these complex materials has been substantially advanced by decades of efforts that were devoted to the structural characterization using four major biochemical or genetic methods. The first major method relies on sequential treatments using harsh chemicals or enzymes to break down the cell walls into different portions, which is followed by compositional and linkage analysis of sugars in each fraction[51]. This method sheds light on the domain distribution of polymers, but the interpretation may be misleading due to the chemical and physical properties of biomolecules. For example, it is difficult to determine whether the alkali-extractable fraction originates from a single domain of less structured molecules or from spatially separated molecules with comparable solubility. Second, the extracted portions or whole cell walls can also be measured using solution NMR to determine the covalent linkages, also termed as crosslinking, between different molecules[12,52-55]. In this way, the detailed structure of covalent anchors could be probed to a great detail, but limitations may exist due to the low solubility of polysaccharides, the

---

This is adapted from Kirui, A., Dickwella Widanage, M. C., Mentink-Vigier, F., Wang, P., Kang, X., Wang, T. Preparation of Fungal and Plant Materials for Structural Elucidation Using Dynamic Nuclear Polarization Solid-State NMR. *J. Vis. Exp.* (144), e59152, doi:10.3791/59152 (2019).

relatively small number of crosslinking sites, and the ignorance of non-covalent but similarly important effects for stabilizing polysaccharide packing, such as the hydrogen-bonding, van der Waals force, electrostatic interaction and polymer entanglement. Third, the binding affinity could be determined *in vitro* using isolated polysaccharides[56-59], but the purification procedures may substantially alter the structure and properties of these biomolecules. This method also fails to replicate the sophisticated deposition and assembly of macromolecules after biosynthesis. Finally, the phenotype, cell morphology and mechanical properties of genetic mutants with attenuated production of certain cell wall component shed lights on the structural functions of these polysaccharides, but more molecular evidence is needed to bridge these macroscopic observations with the engineered function of protein machineries[60].

Recent advances in the development and application of multidimensional solid-state NMR spectroscopy have introduced a unique opportunity for solving these structural puzzles. 2D/3D Solid-state NMR experiments enable high-resolution investigation of the composition and architecture of carbohydrate-rich materials in the native state without major perturbation. Structural studies have been successfully conducted on both primary and secondary cell walls of plants, the catalytically treated biomass, bacterial biofilm, the pigment ghosts in fungi and, recently by our group, the intact cell walls in a pathogenic fungus *Aspergillus fumigatus*[10,25,61-69]. The development of Dynamic Nuclear Polarization (DNP)[70-77] substantially facilitates the structural elucidation, and its sensitivity enhancement markedly shortens the experimental time on these complex biomaterials. Here we present a protocol for isotope-labeling the fungus *A. fumigatus* and the procedures for preparing fungal and plant samples for solid-state NMR and DNP measurements. Similar labeling procedures should be applicable to other fungi but with altered

medium, and the sample preparation procedures should be generally applicable to other carbohydrate-rich biomaterials.

2.2. Protocol

2.2.1. Growth of ^{13}C, ^{15}N-labeled *Aspergillus fumigatus* Liquid Medium

2.2.1.1. Preparation of unlabeled and ^{13}C, ^{15}N-labeled growth medium

Note: Both Yeast Extract Peptone Dextrose medium (YPD) and the improved minimal medium[78] were used for maintenance of fungal culture. All steps after autoclaving are performed in a laminar flow hood to minimize contamination.

2.2.1.1.1. Preparation of unlabeled liquid medium

Dissolve 6.5 g of YPD powder is dissolved in 100 mL water and then autoclaved for 25 min at 134 °C.

2.2.1.1.2. Preparation of unlabeled solid medium

- Add 1.5 g agar and 6.5 g YPD powder in 100 mL distilled water.

Autoclave the medium for 25 min at 121 °C and then cool down to approximately 50 °C.

- Transfer 13-15 mL of the medium into each pre-sterile plastic Petri dish and cover the dish using a lid immediately.

2.2.1.1.3. Preparation of ^{13}C, ^{15}N-labeled liquid medium

Note: To prepare the growth solution for isotope labeling, a minimal medium containing ^{13}C-glucose and ^{15}N-sodium nitrate and a trace-element solution are prepared separately and then mixed before use.

- Prepare 100 mL solution of the isotope-containing minimal medium as listed online in Table 1. Adjust the pH to 6.6 using NaOH (1 M) or HCl (1M) solution.

Autoclave the minimal medium for 25 min at 134 °C.

- Prepare 100 mL (1000x) trace elements solution, dissolve the salts listed in the online Table 2 in the distilled water. Autoclave the solution for 25 min at 134 °C. Cool down and storethe solution at 4 °C for short-term use. The pH will be about 6.5 and can be checked using a pH meter.

- Add 0.1 mL trace elements solution to 100 mL ^{13}C, ^{15}N-labeled minimal medium before use.

Table 2.1. The composition of the minimal medium

Chemical name	Chemical formula	Concentration (grams per liter)
^{13}C-Glucose	^{13}Glucose	10.0 g
^{15}N- Sodium Nitrate	$^{15}NaNO_3$	6.0 g
Potassium Chloride	KCl	0.52 g
Monopotassium Phosphate	KH_2PO_4	0.815 g
Dipotassium Phosphate	K_2HPO_4	1.045 g
Magnesium Sulfate Heptahydrate	$MgSO_4 \cdot 7H_2O$	0.52 g

Table 2.2. The composition of the trace-element solution (concentrated).

Chemical name	Chemical formula	Concentration (g/L)
Zinc Sulfate Heptahydrate	$ZnSO_4 \cdot 7H_2O$	22 g
Boric acid	H_3BO_3	11 g
Manganous Chloride Tetrahydrate	$MnCl_2 \cdot 4H_2O$	5 g
Ferrous Sulfate Heptahydrate	$FeSO_4 \cdot 7H_2O$	5 g
Cobaltous Chloride Hexahydrate	$CoCl_2 \cdot 6H_2O$	16 g
Cupric Sulfate Pentahydrate	$CuSO_4 \cdot 5H_2O$	16 g
Ammonium Molybdate Tetrahydrate	$(NH_4)_6Mo_7O_{24} \cdot 4H_2O$	11 g
Tetrasodium Ethylenediaminetetraacetate	$Na_4EDTA \cdot 4H_2O$	60 g

Note that for preparing unlabeled fungi, unlabeled glucose and unlabeled sodium nitrate can be used.

2.2.1.2. Growth of the fungal materials

- Transfer a small amount of fungi from the storage onto a YPD plate using an inoculating loop in a laminar flow hood. Keep the culture at 30 °C for 2 days in an incubator.

- Use an inoculating loop to transfer an active growing fungal edge to the ^{13}C,^{15}N-labeling solution in a laminar flow hood. Keep the culture at 30 °C for 3-5 days at 220 rpm in a shaking incubator.

- Centrifuge at 5000 rpm (4000 x g) for 20 minutes. Remove the supernatant and collect the pellet.

- Keep the collected pellet hydrated for NMR studies or long-term storage. Loss of hydration at any point will substantially worsen the spectral resolution. If needed, a small amount (0.1 gram) of the hydrated mycelia can be separated and fully dried in a hood or a lyophilizer to estimate the hydration level and calculate the dry mass percentage. Usually, we can obtain a pellet containing ~0.3 g dry mass after 3 days.

- Mix the remaining material with 20% (v/v) of glycerol and keep in a -80 ^{o}C freezer for long-term storage.

2.2.2. Preparation of *A. fumigatus* for Solid-State NMR and DNP Studies

2.2.2.1. Preparation of *A. fumigatus* for solid-state NMR experiments

- Dialyze the fungal sample in phosphate buffer (pH 7.0) using a dialysis bag with a 3.5 kDa molecular weight cutoff to remove residual small molecules from the growth medium for a total period of 3 days. The buffer is changed twice daily.

- Transfer the sample into a 15 mL tube and centrifuge for 3-4 mins. Remove the supernatant and collect the remaining fungal materials.

- Pack 70-80 mg of the uniformly ^{13}C-labeled and well-hydrated sample paste into a 4-mm ZrO_2 rotor or 30-50 mg to 3.2 mm rotors for solid-state NMR experiments. This is achieved by squeeze the sample gently using a metal rod and use a piece of Kimwipes paper to absorb the excess water. This process is repeated until no more materials can be added.

- Tightly cap the rotor and insert the sample into the spectrometer for solid-state NMR characterization.

Note: The brand-new rotors are suggested to minimize the possibility of rotor crash and sample spill in the NMR spectrometer. If needed, a disposable Kel-F insert with sealing screws can be used to serve as a secondary container inside the rotor.

2.2.2.2. Preparation of *A. fumigatus* samples for DNP experiments

- Prepare 100 µL of DNP solvents[67,79] (also known as the DNP matrix) in an Eppendorf tube for ^{13}C,^{15}N-labeled fungal samples. This DNP matrix contains a mixture of d_8-glycerol/D_2O/H_2O (60/30/10 Vol%).

Note: If unlabeled samples are to be investigated, then prepare the DNP matrix using ^{13}C-depleted d_8-glycerol ($^{12}C_3$, 99.95%; D_8, 98%, Cambridge Isotope Laboratory) and D_2O and H_2O to avoid ^{13}C signal contribution from the solvents.

Add 0.7 mg of AMUPol[80] to form 10 mM radical stock solution. Vortex for 2-3 minutes to ensure that radicals are fully dissolved in the solution.

- Soak 10 mg of dialyzed ^{13}C, ^{15}N-labeled fungal materials into 50 µL of AMUPol solution, and mildly grind the mixture using a pestle and a mortar to ensure penetration of the radicals into the porous network of fungal cell walls.

Note: To reduce the rate of hydration loss, the grinding can also take place in an Eppendorf tube using an Eppendorf micropestle.

- Add another 30 µL of the radical solution to the grinded pellet to ensure well-hydration of the fungal sample.

- Pack the pellet into 3.2-mm sapphire rotor, squeeze mildly and remove the excess DNP solvent. Add a silicone plug to prevent the loss of hydration. Typically, 5-30 mg of sample can be packed to the rotor and the exact amount need to be determined by the sensitivity requirement of the experiments to be conducted.

- Insert and spin up the sample in a DNP spectrometer, test the sensitivity enhancement under microwave irradiation and run the designed experiments to determine cell wall structure.

2.2.2.3. Preparation of plant biomass for NMR and DNP studies

2.2.2.3.1. Preparation of plant materials for solid-state NMR

- Uniformly ^{13}C-labeled plants could be directly purchased from isotope-labeling companies or produced in-house using $^{13}CO_2$ supplies in a growth chamber or ^{13}C-glucose medium as described previously[81,82].

Note: ^{13}C-glucose can only be used in dark growth to avoid the introduction of ^{12}C to the samples.

- Cut the uniformly ^{13}C labeled plant material into small pieces (typically a few mm in dimension) using a laboratory razor blade.

- If the sample was previously dried, add 100 µL water to 30 mg of plant materials in an Eppendorf tube, vortex, equilibrate at room temperature for 1 day. Centrifuge at 4000 x g for 10 mins and remove the excess water using a pipette.

- If the sample was never-dried at any point, the sample can be directly used without further treatment.

- Pack the resulting plant materials into 3.2-mm or 4-mm ZrO2 rotors for solid-state NMR experiments.

2.2.2.3.2. Preparation of plant materials for DNP studies

- Prepare 60 µL stock solution of 10 mM AMUPol radical as described in steps 2.2.2.2.

- Weigh 20 mg of the plant materials that were generated in prior steps (3.1.2).

- Hand grind the plant pieces prepared in 3.1.2 into small particles (~1-2 mm in size) using a mortar and pestle. The final powders should have a homogenous appearance.

- Add 40 µL of the stock solution to the plant material and grind mildly for 5 minutes to ensure homogeneous mixing of the plant material and the radical.

- Add another 20 µL of the stock solution to the plant material after grinding.

- Pack the equilibrated plant sample into a 3.2-mm sapphire rotor for DNP experiments. Insert a silicone plug to avoid the loss of hydration.

2.2.2.4. Standard Solid-State NMR experiments for initial characterization of carbohydrate-rich biomaterials

Note: a brief overview of the NMR experiments is provided in this section. However, structural elucidation typically requires extensive expertise. Therefore, collaborative efforts with NMR spectroscopists is recommended.

- Measure 1D ^{13}C Cross Polarization (CP), ^{13}C Direct Polarization (DP) with 2-s and 35-s recycle delays, and ^{1}H-^{13}C INEPT[83,84] spectra to obtain a general understanding of the dynamical distribution of cell components (Figure 2.1a). The cell walls are typically the relatively rigid portion and should exhibit dominant signals in the CP spectrum.

- Measure a series of standard 2D ^{13}C-^{13}C correlation experiments for resonance assignments of ^{13}C signals. Start with refocused INADEQUATE[85,86] to obtain carbon connectivity, which need to be assisted by a series of through-space experiments such as 1.5-ms RFDR[87] (Figure 2.1b) and 50-ms CORD/DARR[88] experiments.

- Conduct 2D ^{15}N-^{13}C correlation experiments can be measured to facilitate the resonance assignments of proteins and nitrogenated carbohydrates.

Note that the resonance assignment is typically time-consuming. A method is currently being developed in our group to facilitate the resonance assignment of carbohydrate signals for those scientists without prior experience.

- Measure more specialized experiments to determine the spatial proximities (Figure 2.1c, d), hydration and mobilities of complex biomolecules to determine the three-dimensional structure of the carbohydrate-rich materials as systematically described previously

2.3. Representative Results

The isotope labeling substantially enhances the NMR sensitivity and makes it possible for measuring a series of 2D ^{13}C-^{13}C and ^{13}C-^{15}N correlation spectra to analyze the composition, hydration, mobility and packing of polymers, which will be integrated to construct a three-dimensional model of cell wall architecture (Figure 1). If the uniform labeling succeeds, a complete set of 1D ^{13}C and ^{15}N spectra could be collected within an hour and each standard 2D spectrum should take no longer than 24 hours of measurement.

Well-prepared samples usually have both high NMR intensities and sharp lines and compensation to any of these two parameters indicate un-optimized sample preparation. The fungal samples should be prepared in a never-dried manner, and partial dehydration during the packing steps could lead to a notable broadening of the linewidth. If the experimental time is substantially longer than expected for a fully packed NMR sample, the labeling level might be low. If off-diagonal signals are difficult to obtain in the 2D ^{13}C-^{13}C correlation spectrum, statistical labeling might have occurred (Figure 2.1b). The two ^{13}C peaks at 96 and 92 ppm are signature carbon 1 signals of glucose[89], therefore, their strong intensities in the quantitative ^{13}C direct polarization (DP) spectra measured with long recycle delays of 35 s typically indicate the dominance of small molecules due to insufficient dialysis (Figure 2.1a).

2.4. Discussion

Compared with the biochemical methods, solid-state NMR has advantages as a non-destructive but high-resolution technique. NMR is also quantitative in compositional analysis, and unlike most other analytical methods, does not have uncertainties due to limited solubility. It should be noted that, however, the resonance assignment and data analysis can be time-consuming

and usually require systematic training. Our group is currently developing tools and databases to help scientists without prior experience to overcome this barrier.

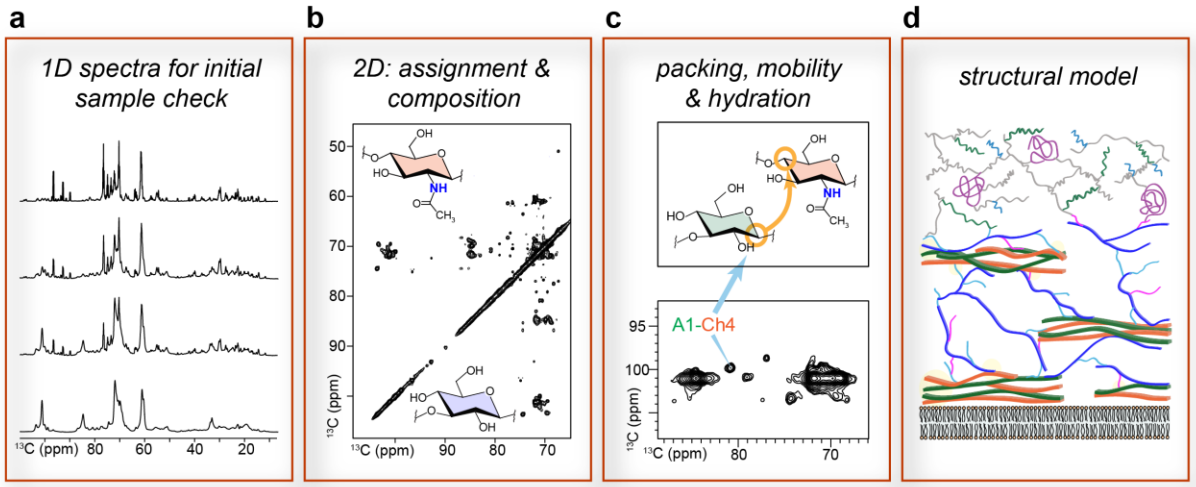

Figure 1. Flow chart for characterizing fungal cell wall structure using solid-state NMR. (a) 1D spectra for initial sample screening. From the top to the bottom are INEPT, ^{13}C DP with 2-s recycle delays, ^{13}C DP with 35-s recycle delays and ^{13}C CP spectra, with decreasing mobility for the detected molecules. (b) 2D ^{13}C-^{13}C correlation spectrum measured using 1.5-ms RFDR recoupling. (c) Representative intermolecular cross peak detected using 15-ms PAR spectrum. (d) Structural model obtained from NMR data.

DNP is often necessary to these challenging whole-cell systems. Typically, a 20-40-fold enhancement of sensitivity could be achieved on an optimized sample on a 600 MHz/395 GHz DNP spectrometer and this value increases with decreasing field, for example, almost doubled on a 400 MHz/263 GHz DNP[25,90,91]. There are several factors that could affect the DNP efficiency. First, the penetration of radicals into the porous network of cell walls is crucial and this process can be substantially facilitated by mild grinding of the biomaterials in the radical-containing DNP matrix. Second, the physical properties, the stiffness for example, of the sample affects the choice of microwave power, the DNP matrix "melts" under 12 W irradiation as evidenced by the sharpening of ^{1}H resonances, which was not a problem for the stiffer plant stems. As a result, a more isotropic pattern of the ^{1}H solvent peak is observed, with substantially lower spinning sidebands and attenuated DNP enhancement. Therefore, weaker power is recommended for softer

materials. Third, the composition of DNP matrix should be optimized. It turns out that d_8-glycerol/D_2O/H_2O is generally the overall best solvents for soft materials while a simpler and cheaper choice of D_2O/H_2O can also be effective in some cases because the presence of sugars also serves as a cryoprotectant to some extent. In contrast, the d_6-DMSO/D_2O/H_2O solution fails in both the plants and fungi, with less than 10-fold of sensitivity enhancement, thus it is not recommended for use unless for special purposes. A matrix-free protocol has recently been demonstrated to be highly effective due to solvent depletion, which creates additional space to accommodate more materials[72,92]. However, the loss of hydration presents a major perturbation to the structure of biomolecules, thus this method might not be suitable for biological systems. If unlabeled cell walls are to be studied, ^{13}C-depleted d_8-glycerol/D_2O/H_2O is the optimal solvent that does not contribute any natural abundance ^{13}C signals nor sacrifices any sensitivity enhancement.

CHAPTER 3. ATOMIC RESOLUTION OF COTTON CELLULOSE ENABLED BY DYNAMIC NUCLEAR POLARIZATION SOLID-STATE NMR

3.1. Introduction

For decades of studies on cellulose structure and crystallinity, solid-state NMR (ssNMR) has been a standard method that relies primarily on the measurement of 1D ^{13}C spectra followed by analysis of peak multiplicity and intensities[93-96]. Due to limited resolution, ambiguity may exist in the spectral deconvolution and resonance assignment of different components. Recent studies on uniformly ^{13}C-labeled plant materials have substantially improved the resolution by measuring two- and three-dimensional (2D/3D) ^{13}C-^{13}C correlation spectra, which have advanced our understanding of the structure of cellulose and its interactions with matrix polymers[10,61,69,97]. The atomic resolution of ssNMR allows us to resolve seven types of cellulose allomorphs in plant primary cell walls and directly measure their spatial location and hydroxymethyl conformation[22,98]. Two types of glucan chains that primarily adopt the *gauche-trans* (*gt*) conformation for the O-6 primary alcohol are found on the cellulose surfaces, while another five types of glucan chains having O-6 in the *trans-gauche tg* conformation form the internal cores of microfibrils. The conformational structures of these cellulose forms in primary plant cell walls are found to differ substantially from the crystallographic structures of Iα and Iβ allomorphs that were determined using purified cellulose microcrystals from tunicate and algae[99-101]. This inconsistency is also retained in the secondary cell walls from the mature stems of grasses and woods[8] indicating that cellulose structures in their native cell walls are far more complicated than in the purified, highly

---

This chapter was previously published as A Kirui, Z Ling, X Kang, MC Dickwella Widanage, F Mentink-Vigier, AD French, T Wang, "Atomic Resolution of Cotton Cellulose Structure Enabled by Dynamic Nuclear Polarization Solid-State NMR, in *Cellulose,* (2019) 26:329-339, copyright 2021 Springer Nature. All rights reserved. https://dx.doi.org/10.1007%2Fs10570-018-2095-6

crystalline state. Therefore, it becomes imperative to establish non-destructive and high-resolution methods to evaluate the consistency and diversity of cellulose structure from a wide range of sources using 2D ssNMR. However, isotope enrichment, a pre-requisite for multidimensional ssNMR, has been a major barrier. Feeding a plant with $^{13}CO_2$ and/or ^{13}C-glucose as the sole carbon source is typically very expensive and becomes impractical for plants with large size and/or long lifecycles. Without isotope-labeling, we can still rely on the very low natural ^{13}C abundance (1%) for 1D experiments, but the probability for observing a cross peak between two carbons in 2D spectra is only 0.01%, making it unrealistic for conventional NMR. This issue can be addressed by the implementation of the cutting-edge technique of Dynamic Nuclear Polarization (DNP), which enhances NMR sensitivity by tens to hundreds of times by transferring polarization from the electrons in radicals to the NMR-active nuclei in biomacromolecules[23,24,74,102]. This method has been applied to study many ^{13}C/^{15}N-labeled carbohydrate-rich systems such as the cell walls in plants, bacteria, and fungi[14,21,25]. More importantly, it enables structural characterization of unlabeled materials using 2D ^{13}C correlation spectroscopy[92,103,104], thus allowing us to rapidly screen cellulose structures in various systems without worrying about isotope-enrichment.

Here we employ DNP ssNMR on a Wiley-milled cotton sample (the control) and a subsequently ball-milled cotton sample to characterize the structural change of cellulose using unlabeled samples. 2D ^{13}C-^{13}C correlation on these unlabeled samples, assisted by statistical analysis of ^{13}C chemical shifts, allows us to obtain unprecedented molecular information on the structural changes of cellulose. First, the control cotton sample has a good match with the Iα and Iβ structures from model cellulose. Second, these Iα and Iβ structures of Wiley-milled cotton cellulose are fully removed by 2 hours ball-milling. Third, the ball-milled cellulose adopts a new

type of chain-arrangement that cannot align with any of the existing structures. Fourth, the disordered domains consist of a collection of discrete conformers instead of a continuous distribution of conformations. Statistical analysis of ^{13}C chemical shifts revealed how these observed sub-forms correlate with literature structures. These data suggest that the crystallographic structures only apply to model cellulose with relatively large crystallite size and revise our understanding of the disordered domains that were otherwise difficult to characterize. These methods are widely applicable to other functional cellulose or lignocellulosic materials.

3.2. Methods

3.2.1. Wiley-Milled and Ball-Milled Cotton Samples

Wal-Mart White Cloud cotton balls were chopped in a Wiley mill (Eberbach E3300 mini cutting mill, Eberbach Corp., Belleville, Michigan) until they passed through a 20-mesh screen. Subsequently, the powdered samples were placed in a locally built ball mill with a motor running at 1750 rpm. The 1 L steel jar was chromium plated and the balls (500 mL) were 0.25 in. (~4 mm) stainless steel. A fan was blown at the mill to minimize heating during the milling for 120 minutes. Samples were processed in an air-conditioned laboratory but without other attention to moisture at this stage.

3.2.2. Matrix-Free Preparation of DNP Samples

The Wiley-milled cotton sample and the 120 min ball-milled material were processed using the matrix-free protocol for DNP experiments[92,105]. Briefly, the stock solution of 10 mM AMUPol radical (Sauvee et al. 2013), the DNP matrix, was prepared using D_2O and a radical concentration of 10 mM. About 60 mg of the cotton sample was immersed in 150 µL of the AMUPol solution. The sample was stored in an Eppendorf tube and dried in a desiccator under vacuum for about ten hours. The excess radicals that did not mix well with cotton formed orange crystals that were

manually removed using a needle. Another 3 μL D_2O were added to ensure the moisturization of these cotton samples, previously reported to be essential for ensuring sensitivity enhancement[92]. Around 50 mg of sample was packed into a thin-wall 3.2 mm zirconium rotor for DNP experiments. No silicone soft plug is used so that more space will be created. These thin-wall rotors allow us to pack 10-20 mg more material than the standard sapphire rotors.

Compared with the conventional methods that typically sacrifices a large volume for solvents, such as d_8-glycerol, D_2O, and H_2O, the matrix-free method maximizes the amount of cotton material that can be packed into an NMR rotor, which increases the absolute sensitivity and accelerates the measurement of 2D ^{13}C-^{13}C correlation spectra at natural abundance. This protocol is appropriate for our cotton samples and other cellulose materials that are largely dried in their native state, but it is not suitable for well-hydrated bio-samples, such as plant seedling or stems.

3.2.3. DNP-NMR Experiments

The DNP experiments were carried out on a 600MHz/395 GHz MAS-DNP spectrometer[106]. The experiments were conducted using a 3.2 mm probe under 8 kHz MAS frequency. The microwave irradiation power was set to ~12 W and the temperature was 104 K with the microwave on and 98-100 K with the microwave off. The DNP buildup time was 7.2 s for the control cotton and 2.5 s for the material processed with 120 min ball-milling, which has better association with paramagnetic radicals due to enhanced disorder or surface area. 2D ^{13}C-^{13}C INADEQUATE spectra[37] were measured using the SPC5 sequence[107] under 8 kHz MAS with 5 ms total recoupling time (2.5 ms each for excitation and reconversion). The recycle delays were set to be 1.3 times of the DNP buildup time: 9.4 s for the control cotton and 3.2 s for the ball-milled sample. The acquisition time was 18 ms and 5-6 ms for the direct and indirect dimensions. A spectral width of 60 ppm (130-190 ppm) was used for the indirect dimension of both spectra.

This spectral width can effectively cover the double-quantum chemical shifts of cellulose and many other polysaccharides in plants, but it should be extended slightly (130-200 ppm) if arabinose exists in the sample. The number of t_1 increment is 110 and 90 for the Wiley-milled and ball-milled samples, respectively. The number of scans was 32 and 64 the Wiley-milled and ball-milled samples, respectively. The experimental time is 9.5 hrs for the control sample and 5 hrs for the ball-milled sample.

3.3. Results and Discussion

3.3.1. DNP Enables structural Characterization of Unlabeled Cotton Cellulose with Atomic Resolution

Multidimensional (2D/3D) solid-state spectroscopy is an indispensable method for characterizing the structure of cellulose, especially for those with substantial structural disorder and polymorphism, or those mixed with other biopolymers such as pectin, hemicellulose, and lignin[3,5]. This method, however, was not applicable to materials without isotope-enrichment due to the challenging sensitivity until the recent development of Dynamic Nuclear Polarization (DNP) technique. Figure 1a shows the 23-fold enhancement of NMR sensitivity achieved for the Wiley-milled cotton sample, which translates to a saving of NMR experimental time by 529-fold. It is remarkable that the spectral resolution is retained at the low temperature (104 K) of DNP experiment, evidenced by the 0.8-0.9 ppm ^{13}C linewidth of resolved peaks, which could be explained by the high structural order of these cellulose materials. The peak multiplicity is also consistent with the Iα and Iβ allomorphs in literature (Kono et al. 2003b). A slightly lower enhancement, 18-fold, is achieved for the ball-milled sample, providing a time-saving of 324 fold for NMR experiments (Figure 3.1b).

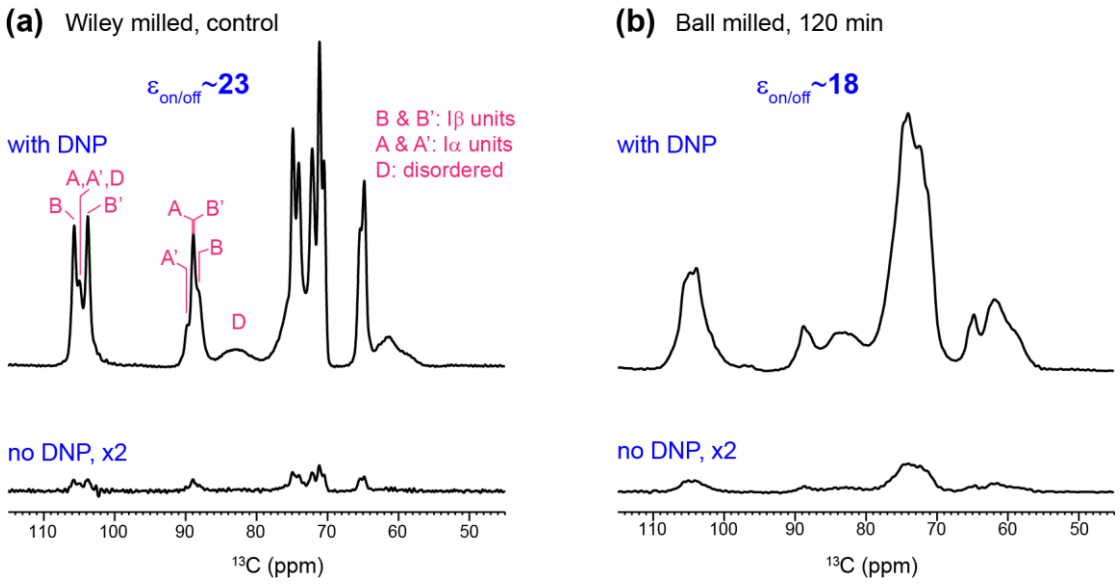

Figure 3.1. Sensitivity enhancement from Dynamic Nuclear Polarization (DNP). The DNP-enhancement spectra measured with microwave irradiation provide sensitivity enhancement of 23 and 18-fold for (a) Wiley-milled cotton and (b) ball-milled samples, respectively. The $\varepsilon_{on/off}$ is the enhancement factor by comparing spectra recorded with microwave on and off. In contrast, the non-DNP spectra have very low intensities even with the same number of scans and measurement time. The representative positions for Iα and Iβ cellulose and their non-equivalent glucose units are labeled in magenta

Compared with room-temperature spectra[108], the intensity of the disordered cellulose (relative to the ordered forms) has reduced for both Wiley-milled and ball-milled samples. This can be attributed to the better association of DNP radicals with the surface disordered cellulose, which causes a more pronounced paramagnetic relaxation enhancement that suppresses the intensity of molecules nearby, within a few nanometers. In contrast, the room-temperature samples do not contain DNP radicals and their spectra are reported in an accompanying paper[108].

The benefit from the good sensitivity is that these 1D experiments can be finished within 5 mins, with only 8 to 32 scans, and the signal-to-noise ratios are 400-700, which is almost "noiseless." With this sensitivity boost, we measured 2D ^{13}C-^{13}C correlation spectra that allow us to resolve many unique molecular environments, for both crystalline and non-crystalline domains.

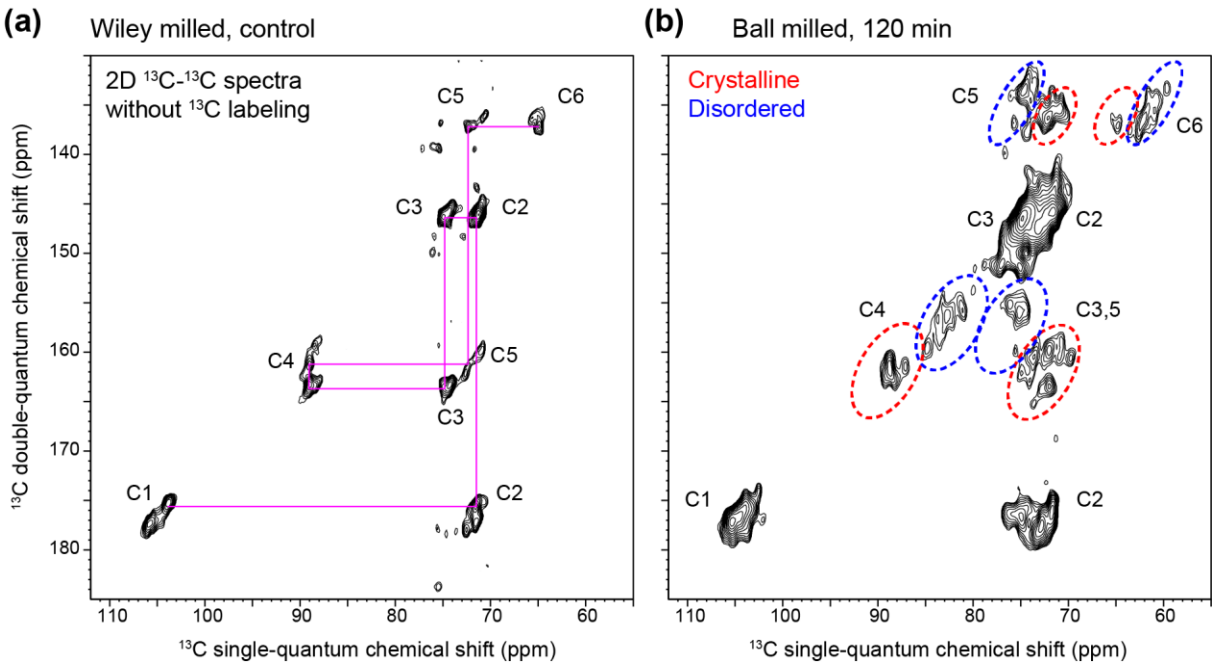

Figure 3.2. DNP enables 2D spectroscopy on unlabeled cellulose. All 2D spectra are measured using the natural abundance (1.1%) of ^{13}C. 2D ^{13}C-^{13}C INADEQUATE spectra have been measured on (a) Wiley-milled cotton and (b) ball-milled sample. The two spectra were plotted so that the crystalline domains of cellulose show comparable contour lines. Representative carbon connectivity is shown in magenta. The representative regions of crystalline and disordered cellulose are highlighted using red and blue dashed-line circles, respectively

The *de novo* assignment is achieved by first identifying the well-resolved C4-C5 and C3-C4 signals, from which the connectivity to other carbons can be found. Peak intensities are tracked to validate the connectivity-based assignment and carbons from the same cellulose form should have comparable intensities. The control cotton sample mainly contains the crystalline cellulose, with negligible signals for non-crystalline domains, and the representative carbon connectivity is shown in Figure 3.2a, without any ambiguity. In contrast, the ball-milled sample shows dominant signals from the disordered cellulose (Fig. 2b). The complete ^{13}C-connectivity and resonance assignments have been identified for all crystalline forms and for two types of disordered cellulose, among the five forms identified (Fig. S1). The ^{13}C-chemical shifts have been documented in Table 1.

Table 3.1. ^{13}C-chemical shifts of cellulose in Wiley-milled and ball-milled cotton samples.

Sample	Type	C1 (ppm)	C2 (ppm)	C3 (ppm)	C4 (ppm)	C5 (ppm)	C6 (ppm)
Wiley-milled cotton	A	105.0	71.1	74.1	89	71.8	64.9
	A'	105.0	71.4	74.9	89.8	72.5	64.9
	B	105.8	71.4	74.9	88.5	70.7	65.5
	B'	103.8	71.5	74.3	89.2	72.4	64.9
Ball-milled	Crystalline, major	104.5	71.7	74	88.8	72	64.9
	Crystalline, minor	104.5	72.5	74.9	87.1	74.1	63.6
	Disordered, type-1	105.1	73	75.6	84.9	75.6	61.1
	Disordered, type-2	105.1	73.1	75.1	82.8	75.1	59.8

3.3.2. The Standard Iα and Iβ Structures are Removed After 120-min Ball-Milling

The 2D spectra of crystalline cellulose in Wiley-milled cotton allow us to resolve the signals of all carbons in four glucose units (Figure 3.3a), The typical signal-to-noise ratio is 10-20 and the full-width at half maximum linewidth (FWHM) is as sharp as 0.9 ppm (Figure 3.3a). The ^{13}C chemical shifts of these glucose residues dovetail well with the Iα and Iβ allomorphs that were previously measured on ^{13}C-labeled samples from *Cladophora* and tunicate (Kono et al. 2003b; Kono and Numata 2006). The four glucose types are better resolved at the C4, C5 and C1 sites rather than the C6 site, suggesting that the C6 hydroxymethyl conformation and the χ' (C4-C5-C6-O6) torsion angle are relatively focused, primarily at the *tg* conformational minima as revealed by the C6 chemical shift at 65 ppm.

The limited resolution of 1D spectra in the many conventional ssNMR studies on cellulose and carbohydrate-rich materials can easily lead to misinterpretations, and here is an example. The C4 region of crystalline cellulose (88-90 ppm) in Wiley-milled and 120-min ball-milled sample shows comparable spectral patterns in 1D spectra except for the substantially reduced intensity (Figure 1), which naturally misleads us to assume that the remaining crystalline cellulose retains the same molecular structure, but with a considerably decreased amount. However, this is wrong. The well-resolved signals of the crystalline C4 unambiguously differ for these two samples (Figure 3.3b). Although both samples show a major signal at 89 ppm for single-quantum (SQ) chemical

shift, which will result in similar 1D patterns in the C4 region, their double-quantum (DQ) chemical shift that sums the SQ chemical shifts of two bonded carbons completely differs, revealing a change in the adjacent carbons, C3 and C5. Therefore, the Iα and Iβ structures are not retained in the heavily ball-milled samples.

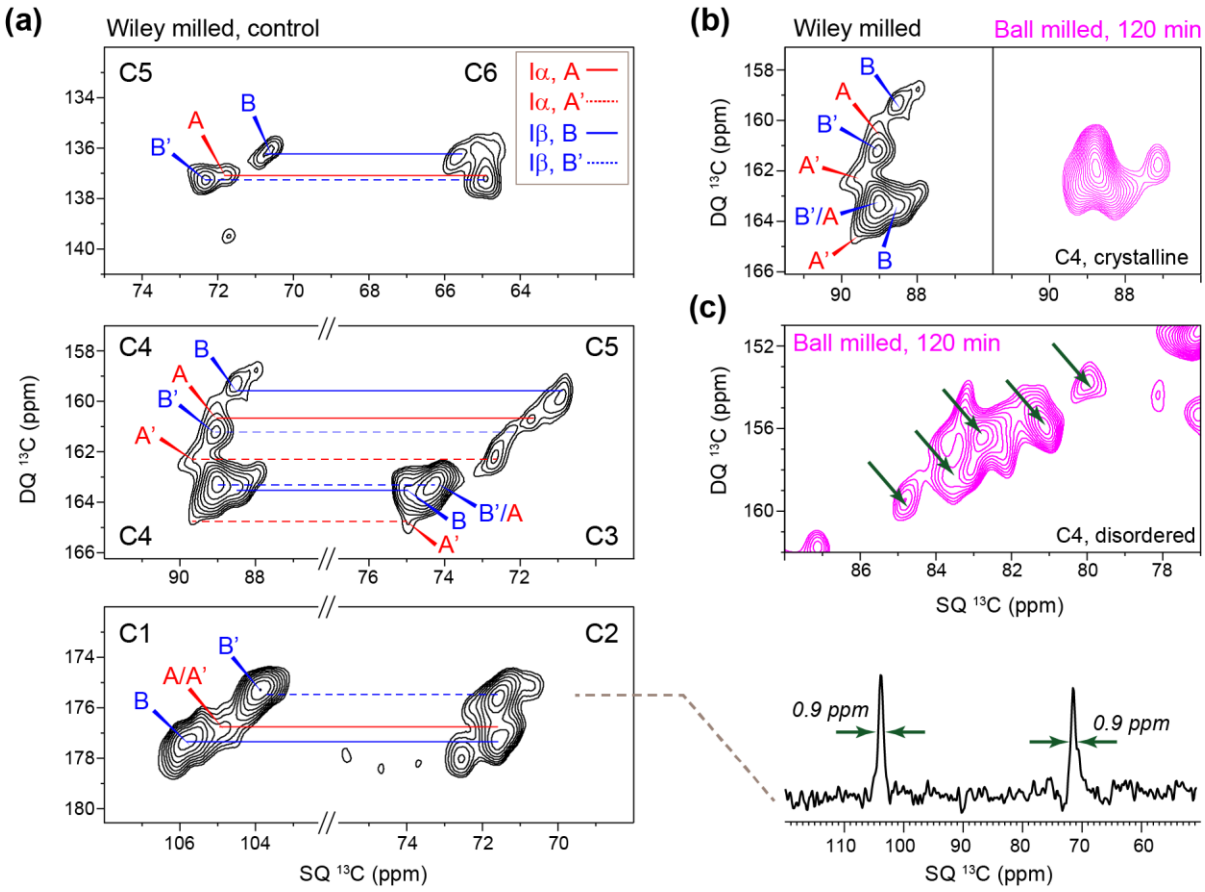

Figure 3.3. High-resolution structural insights of cellulose in unlabeled cotton. (a) Resonance assignments of Iα and Iβ signals in Wiley-milled cotton. Representative ^{13}C cross section shows a typical ^{13}C linewidth is 0.9-1.0 ppm. The double-quantum and single-quantum chemical shifts are abbreviated as DQ and SQ, respectively. (b) The crystalline region of cellulose is altered after 2 h of ball-milling. The spectral features of Iα and Iβ cellulose in the control Wiley-milled sample are fully removed in the ball-milled sample. (c) The C4 region of disordered cellulose in ball-milled sample resolved five sub-forms as indicated using arrows

This substantial change cannot be detected in conventional NMR studies since they only use the well-resolved C4 peaks as the indicators of structure, sometimes with the help of partially resolved C1 and C6 signals, while the C2, C3 and C5 signals are fully ignored. Therefore, any

structural change of these spectroscopically "invisible" carbons will be omitted in the conventional 1D work, as shown above.

What is the cause of the structural inconsistency observed here? We speculate that the Iα and Iβ can only exist in large cellulose aggregates with high crystallinity across a large dimension. After 120 min of ball milling, the remaining material is not bulky enough to support the molecular organization of these model allomorphs. This is supported by the recent observation that Iα and Iβ structures are not present in the native cell walls of plant seedlings, coleoptile, mature stems, woody branches, and bark in a variety of plants, from dicot to monocot and from grasses to trees[8,62,69]. Examples include *Arabidopsis*, *Brachypodium*, maize, switchgrass, rice, spruce, poplar, and *Eucalyptus*, which collectively indicate that the Iα and Iβ model structures cannot be extended to cellulose from many of the natural sources.

The exact size of the crystallites is difficult to measure directly but could be roughly estimated using NMR-derived crystallinity, a parameter reflecting the ratio between internal and surface chains in cellulose[22,109]. The crystallinity of the control sample (68%) derived from room-temperature 1D ^{13}C spectra best fit a simplified model with 81 crystalline chains arranged as a 9 x 9 matrix, with another 40 disordered chains coating the surface. This will result in large lateral dimensions of 6-9 nm, which is enough to support the presence of Iα and Iβ structures. Because there is rising evidence that plants produce fundamental or elementary fibrils with 18 molecules[110-114], the averaged cellulose structure of cotton cellulose should contain at least six or seven such fibrils. Note that the real dimension of these crystallites may be substantially larger than the value estimated above because the signals of disordered chains may have contributions from primary cell walls, whose cellulose is much smaller. Also, other processes may introduce structural disorder, for example, the bundling process of multiple elementary microfibrils. If we adopt a

previous model that include both accessible and inaccessible surfaces (the aggregated surface between multiple elementary fibrils), a lateral dimension of 11-12 chains is estimated[96]. However, we should be aware that large uncertainties may exist due to the ambiguity of these models and our limited understanding of the crystalline and disordered cellulose, as well as their spectral characteristics (Figure 4).

3.3.3. Partial Structural Order Exists in the "Disordered" Domains

Our contemporary views of the disordered domains of cellulose usually involve a less ordered form in the interior of the fibril (para-crystalline cellulose) and multiple components of fibrillar surface. The inaccessible surface induced by fibril aggregation is often assumed as a dominant disordered form (70-90% of the surface chains), which is typically presented as a very broad component (FWHM linewidth of 4-9 ppm) resonating at ~84 ppm in 1D ^{13}C spectra[96,115]. The introduction of this component simplified the spectral deconvolution process, and the broad lineshape used in fitting usually suggest a Gaussian distribution of conformations. The disordered C4 region of the ball-milled sample, however, shows several well-resolved peaks, the linewidth of each one is not much broader than the crystalline forms (Figure 3c). These high-resolution data indicate that conformational disorder happens in a discrete manner instead of a continuous distribution: several energetic minima of cellulose conformation are present even in the heavily ball-milled sample that bears a great degree of disorder. Although the concept of "crystallite surface" was proposed two decades ago[116], our 2D data provides, with high-resolution, a far more direct and striking view of this partial order.

3.3.4. Structural Comparison of Cellulose from Various Sources

It has long been difficult to extract useful structural information out of the NMR observables, for example, chemical shifts, which sometimes are "indirect" for non-NMR scientists.

To begin to understand the ^{13}C chemical shifts for these samples, they can be compared with those for cellulose from other sources. Figure 4 shows "heat maps" of the root-mean-square deviation (RMSD) values for comparisons of the chemical shifts of the corresponding peaks from each source with those of the control and ball-milled samples. A good correlation between two structures will exhibit low RMSD values. The ^{13}C chemical shifts of Iα and Iβ, II and III have been systematically measured by Kono and coworkers using a series of 2D ^{13}C-^{13}C and ^{13}C-^{1}H correlation spectra on uniformly ^{13}C-labeled model cellulose[117-119]. These cellulose materials are typically produced in model algae, bacterial or tunicate for the ease of ^{13}C-labeling, followed by isolation, purification, or chemical treatment. Values for cellulose in native cell walls of dicots and grasses are also included for comparison[69].

The crystalline cellulose in Wiley-milled cotton exhibits poor correlation with surface disordered chains (f and g) in plant cell walls or cellulose II/III structures (Figure 4). Instead, it correlates better with the Iα and Iβ allomorphs and the interior crystalline chains in native cell walls. For the B and B' units in cotton and tunicate, a very low RMSD of 0.2-0.3 ppm is observed, indicating a highly preserved structure of Iβ. For A and A' in cotton, however, reasonably good correlations (0.4-0.6 ppm RMSD) are established with many cellulose subtypes, including the A and A' in *Cladophora*, the B' in tunicate and the a and e types in plant cell walls. Clearly, in cotton, the structural characteristics of Iα allomorph are more ambiguous than those of Iβ. This finding might be relevant to an unresolved question of how these two major allomorphs are mixed on the molecular level.

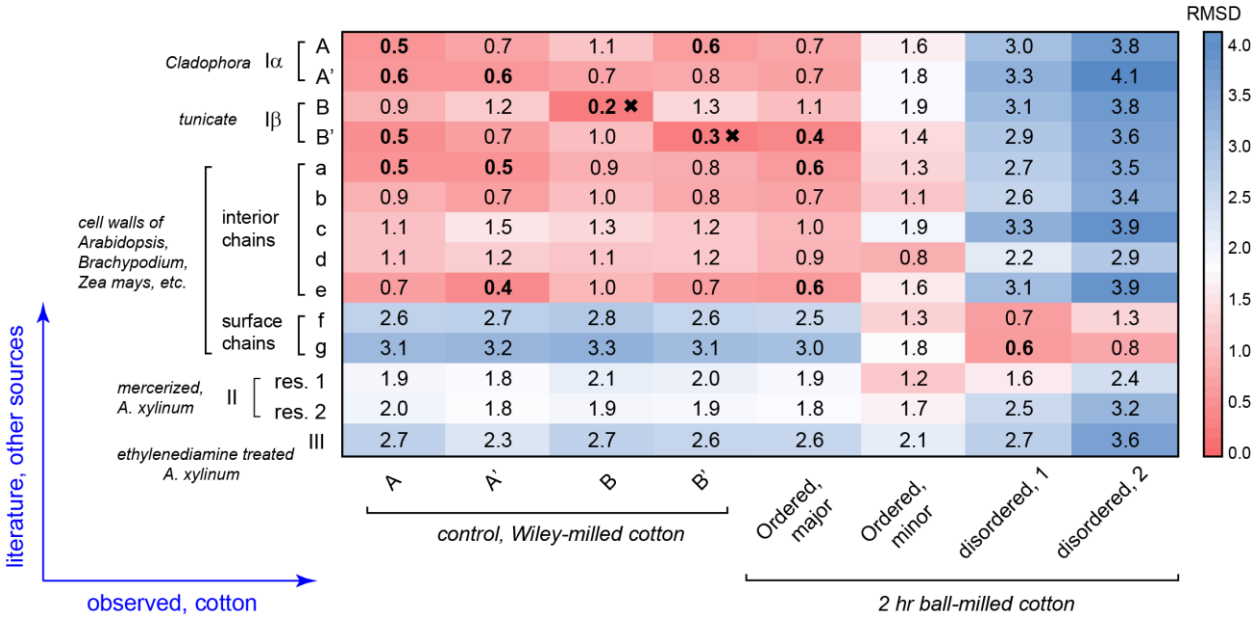

Figure 3.4. ^{13}C chemical shift RMSD map for comparisons between cotton and other cellulose sources. The color scale is shown and the units are ppm. The x-axis contains the observed cellulose forms in Wiley-milled and 2 hr ball-milled cotton. The y-axis contains various cellulose types including Iα, Iβ, II, III and cellulose in native cell walls. The source and treatments are in italic. All good correlations with RMSD of 0.6 ppm or less are highlighted in bold. The crosses indicate very good correlations with RMSD of 0.3 ppm or less.

A more interesting goal here is to identify similarities between the ball-milled cotton and the known cellulose structures. The major signals of crystalline cellulose in the ball-milled sample have high similarity to tunicate Ib B', with a low RMSD of 0.4 ppm. In Iβ, B' and B only form B-B or B'-B' repeating units, each forming a different type of glucan chain arranged in alternating sheets (the center and origin chains): one sheet contains only B units and the adjacent sheet only has B' units[1,99,100,120]. The fact that the remaining crystallites resemble B' rather than B indicate that, after thorough ball-milling, the remaining crystallites adopt a structure that could be viewed as stacked B' sheets. Further computational effort is needed to connect ^{13}C chemical shifts with molecular structure and reveal how this structure is stabilized by inter-sheet C-H O hydrogen bonds[121-123]. In contrast, a minor type of crystalline cellulose in the ball-milled sample does not match Iα or Iβ structures. Instead, similarity is found with the type-d cellulose in plants, which is

a special type responsible for interacting with matrix polysaccharides, and thus, is considered to bear higher disorder. Therefore, this minor form can be treated as an intermediate between crystalline and disordered cellulose. In contrast, the disordered component of ball-milled cellulose clearly shows better correlations with the surface chains (type-f and g) of cellulose microfibrils in plant cell walls than with any of the crystalline structures.

3.4. Conclusions and Future Perspectives

This study shows how atomic-level structural insight can be obtained on unlabeled cellulose samples by integrating DNP ssNMR spectroscopy with chemical shift analysis. The methods presented here can be readily applied to various functional cellulose materials or carbohydrate-rich polymers. This strategy can be substantially facilitated by the implementation of a solid-state NMR database and its auxiliary software that systematically indexes and analyzes the megadata of cellulose and other complex carbohydrates, which are currently being developed by our lab.

The high-resolution and large data analysis presented in this study also provides novel insights into cellulose structure. A large crystallite size is needed to accommodate the Iα and Iβ crystallographic structures, causing their absence in many types of plants. These model allomorphs will be fully abolished by ball-milling, thus our evaluations of the function-structure relationship of cellulose-based materials need to be cautious under many circumstances, especially for those with mechanical processing, chemical treatment, or other structure-perturbing mechanisms. The fact that partial order exists in the “disordered” domains also urges us to revise our thinking of cellulose structure and substantiate it with further molecular evidence from different physical methods.

CHAPTER 4. A PECTIN METHYLTRANSFERASE MODULATES POLYSACCHARIDE DYNAMICS AND INTERACTIONS IN ARABIDOPSIS PRIMARY CELL WALLS: EVIDENCE FROM SOLID-STATE NMR

4.1. Introduction

Cell walls are carbohydrate-rich composites that are constructed outside the plasma membrane. They are common components of cells in plants, bacteria, fungi, and algae. As a natural biomaterial, the cell wall confers mechanical strength and flexibility to simultaneously maintain cellular integrity and facilitate morphological changes [3,4]. The versatile functions of cell walls are enabled by delicate adjustments of biopolymer structures and interactions at the molecular level. Polysaccharides are long, unbranched, or branched chains of monosaccharide units bound together by glycosidic bonds. Structural polymorphism can exist across the identities and anomeric configurations of monosaccharide subunits, patterns of glycosidic linkages and branching, chemical substitution by methyl or acetyl groups, and distributions of torsional conformations [124].

In the primary walls of growing plant cells, three classes of carbohydrate polymers, namely cellulose, hemicelluloses, and pectins, interact to form the bulk of the wall. Cellulose consists of β-(1-4)-glucan chains and exists as microfibrils of coalesced glucan chains that are ~3-5 nm in diameter in primary walls [1]. Hemicelluloses contain shorter chains than cellulose and are often branched. The major hemicellulose in the primary walls of eudicots, for example *Arabidopsis thaliana*, is xyloglucan, which consists of a β-1,4-glucan backbone substituted with α-xylose (Xyl) sidechains [125]. Some of the Xyl are substituted with β-galactose (Gal) and α-fucose (Fuc). Pectins

---

This chapter was previously published in as A Kirui, J Du, W Zhao, W Barnes, X Kang, C. Anderson, C Xiao, T Wang, "A Pectin Methyltransferase Modulates Polysaccharide Dynamics and Interactions in Arabidopsis Primary Cell Walls: Evidence from Solid-State NMR", *Carbohydrate Polymers* 270, 118370 (2021), copyright 2021 Elsevier Ltd. All rights reserved https://doi.org/10.1016/j.carbpol.2021.118370.

are typically anionic due to the presence of deprotonated α-D-galacturonic acid (GalA). Pectins have diverse functions that include regulating wall porosity, influencing cell expansion and differentiation, modulating pH and ionic balance, participating in wall integrity signaling, and controlling cell-cell adhesion [7,126].

Homogalacturonan (HG), rhamnogalacturonan-I (RG-I), and RG-II constitute the major structural domains of pectins [127]. HG is the most abundant pectic domain in that it constitutes 50-70% of all pectic polysaccharides in primary walls, and is composed of unbranched α-1,4-linked GalA residues [128]. The carbon 6 (C6) carboxyl groups of GalA residues in HG are often methyl-esterified upon delivery to the cell wall and become negatively charged after de-methyl-esterification [129]. The degree of HG methyl-esterification can therefore affect the net charge and chemical properties of pectin, and furthermore, the physical properties of cell walls [127,130,131]. RG-I is the second most abundant form of pectin in primary walls and has a backbone of alternating 1,4-α-GalA and 1,2-α-rhamnose (Rha) units with neutral sidechains largely composed of arabinan and galactan [6]. RG-II is a complex molecule composed of at least 12 sugar types and 20 linkages, which are embodied in six types of sidechains along a backbone of homogalacturonan. The adhesive properties of pectic polymers are determined by their degree of methyl-esterification, which is regulated by the pectin methyltransferases (PMTs) that add methyl groups to pectin during synthesis in the Golgi apparatus [132] and the pectin methylesterases (PMEs) that de-methyl-esterify homogalacturonan in the apoplast [133,134].

Mounting evidence suggests that pectins can exist in integrated complexes formed by polysaccharides and proteoglycans. Treatments by glycosyl hydrolases or harsh chemicals, such as strong acids or bases, are required to isolate the pectic carbohydrates RG-II and RG-I due to their linkages to the other wall polymers [135]. For example, RG-I and HG chains can exist as the

side chains of arabinogalactan proteins (AGPs) such as arabinoxylan pectin arabinogalactan protein1 (APAP1) [135,136]. AGPs have been found to complex with pectins and xylan in other studies [137,138], and rhamnose residues on the arabinogalactan side chains of AGPs have also been suggested as potential attachment sites for RG-I [139]. HG, RG-I, and RG-II can be covalently interconnected through their backbones, but it remains unclear whether these HG and RG fragments are grouped in a particular order or not.

Relatively little is known about the structural roles of pectins and their contributions to the interactions between cell wall components. This is because these acidic polysaccharides are easily extracted from cell walls using hot water, ionic solutions, or alkali and do not efficiently bind to cellulose *in vitro* except for some neutral sidechains [58,140]. Recently, the concept that pectins and cellulose exist in different "phases" in native cell walls has been partially reshaped by solid-state NMR (ssNMR) studies that revealed extensive physical contacts between cellulose and pectic polymers, in particular HG and RG-I, in the intact primary cell walls of *Arabidopsis*. This was achieved through a series of structural studies of plant primary cell walls using multidimensional (2D and 3D correlation) magic-angle spinning (MAS) ssNMR spectroscopy [141]. This method is particularly powerful for detecting intermolecular interactions on the sub-nanometer scale [142], which is a gap between the scales of microscopic and diffraction approaches [109,143-145]. These methods have also revealed that cellulose only interacts with xyloglucan at specific spots [19,146]. Instead, at least 25-50% of the surfaces of cellulose microfibrils lie in close contact with pectins [5], via a robust polymer interaction that is independent of the hydration history of the samples [61].

The extent of pectin-cellulose interactions is also correlated with cell wall extensibility [5,61]. This has been demonstrated using two transgenic lines targeting *POLYGALACTURONASE INVOLVED IN EXPANSION1* (*PGX1*), a gene encoding a polygalacturonase that hydrolyzes the

HG backbone [147,148]. These two transgenic lines either promote (in the case of *PGX1*^{AT} overexpression line) or limit (in the case of *pgx1* knockout line) cell expansion, shoot elongation, and adult plant development. The alterations in cell and organ growth can potentially be ascribed to changes in the structural characteristics of HG and its interactions with cellulose [147]. For example, increased polygalacturonase activity in *PGX1*^{AT} plants could contribute to the production of short HG chains with high esterification, potentially weakening the extent of calcium cross-linking and producing self-aggregated clusters of HG that lie apart from cellulose microfibrils. In contrast, reduced polygalacturonase activity in the *pgx1-2* mutant gives rise to longer HG chains with low esterification, and tighter packing with cellulose. These findings imply that it is the pectin backbones rather than side chains that might interact with cellulose to regulate wall extensibility [148], although *in vitro* binding assays show that the neutral arabinan and galactan sidechains bind cellulose to a greater extent than charged pectin backbones [58,140], highlighting differences between *in vitro* and *in vivo* cell wall assembly.

It should be noted that in addition to pectin-cellulose interactions, many additional structural factors are likely to modulate cell wall extensibility and plant growth, with notable examples being HG content and pectin-pectin interactions. For example, a pectin biosynthesis gene galacturonosyltransferase 4 (*GAUT-4*) has pectin biosynthetic activity, and its knockdown decreases the content of HG and RG-II in cell walls. When *GAUT4* is downregulated, HG-Ca^{2+} and RG-II–borate diester cross-linking also decrease, which increases wall porosity. The model derived from these data postulates that the increases in growth and biomass degradability in *GAUT4* knockdown plants are attributable to reductions in pectin-pectin interactions and in the tightness of interactions between wall polymer networks [149].

Several putative methyltransferases and acetyltransferases have been implicated in pectin biosynthesis in *Arabidopsis*. The GalA residues can be acetylated at the O2 or O3 positions in both HG and RG-I. Acetylation is carried out by pectin acetyltransferases, which transfer acetyl groups from donor acetyl-CoA to the GalA residues of HG or RG-I [128]. Although no specific protein has yet been validated as a pectin acetyltransferase *in vivo*, recently, PMR5, a protein involved in plant resistance to fungal pathogens, was determined to transfer acetyl groups to oligogalacturonides (OGAs) *in vitro* [150]. Methyl-esterification of GalA has been proposed to be conducted by the methyltransferase QUASIMODO2 (QUA2) and other related enzymes such as QUASIMODO3, COTTON GOLGI-RELATED2 (CGR2), and GGR3 [151-154], but the precise contribution of each of these enzymes to HG methyl-esterification remains to be determined. Recently, it was shown that QUA2, a Golgi-localized *Arabidopsis* protein with a methyltransferase domain, displays *homogalacturonan methyltransferase* (HG–MT) activity *in vitro* [132]. In *Arabidopsis*, *qua2* mutants have a dwarfed phenotype and contain less extractible HG in alcohol-insoluble residue [153]. Mutant screening studies have identified genes that are required for normal plant development and morphogenesis [155]. A mutant allele of *QUASIMODO2*, called *tumorous shoot development2* (*tsd2*), develops tumor-like tissue which causes uncoordinated shoot development. The *tsd2* mutant displays increased activity of axial meristems, reduced root growth, and reduced cell-cell adhesion [154]. Each allele encodes a premature stop codon in the *QUASIMODO2* gene, and morphological phenotypes are more severe in the *tsd2* sample than in the *qua2* sample[153,154].

Recently, we reported that both *qua2* and *tsd2* mutants exhibit compromised cellular adhesion and plant growth [132]. Moreover, both mutants show significant alternations in the patterning of cortical microtubules and the orientation of cellulose microfibrils deposited in their cell walls. In these mutants, cellulose microfibrils are more heterogeneously oriented [132]. We

hypothesize that the phenotypes and cell wall properties are caused by perturbations in cellulose-pectin interactions precipitated by the deficiency in pectin biosynthesis, but this hypothesis requires support from molecular evidence regarding polymer packing. Here, we employed one- and two-dimensional (1D and 2D) ssNMR methods to examine cell wall structure in uniformly ^{13}C-labeled *Arabidopsis* samples, including wild-type, *qua2*, and *tsd2* seedlings. Pectin structure has been modified in these mutants: compared to the wild-type control, both *qua2* and *tsd2* walls show an increase in the amount of arabinans, together with an increased degree of branching in these pectic sidechains. The mutants also show stronger pectin-cellulose cross peaks in 2D correlation spectra, pinpointing the enhanced intermolecular contacts between these polysaccharides. In addition, cellulose and its associated pectic polysaccharides are both more mobile on the microsecond timescale in the mutants due to enhanced disorder but show reduced motional amplitudes that are restricted by the tight packing of these polymers. These findings have provided valuable data for us to examine the potential contributions of pectin-cellulose interactions to cell wall properties and plant growth phenotypes. The methods applied here are also widely applicable to other biomaterials rich in carbohydrate polymers.

4.2. Materials and Methods

4.2.1. Preparation of ^{13}C-labeled Cell Walls

Arabidopsis (*Arabidopsis thaliana*) ecotype Colombia (Col), *qua2*, and *tsd2* mutants were used in this study. Never-dried primary cell walls were prepared according to a recently developed protocol [148]. Briefly, 100 mg *Arabidopsis* seeds were surface-sterilized in 30% bleach containing 0.1% (w/v) SDS. After washing four times with sterile water, the seeds were grown in a Murashige and Skoog (MS) liquid medium (pH 5.6) with ^{13}C-labeled glucose (Cambridge Isotope Laboratories) as the sole carbon source in dark in a 22°C chamber with a rotation of 100 rpm.

Seedlings were harvested after growing for 14 days, then frozen and ground into fine powder in liquid nitrogen. About 250 mg wall materials were treated with α-amylase (5,000 units per 30 mL; Sigma-Aldrich) in MES buffer (pH 6.8) at 37°C overnight, and treated with Pronase (200 units, 5 mg/20 mL, Sigma-Aldrich) in MES buffer (pH 7.5) to digest proteins at 40°C overnight. The samples were washed with 1.5% (w/v) SDS in water, and starch, cell membranes, and proteins were removed by centrifugation at 4500 *g* for 10 min. Bulk water was removed by centrifugation with 4500 *g* for 30 min; the resulting cell walls remained well-hydrated with 40-50 wt% water content and were kept at 4°C before use. In total, 69 mg of wild-type, 71 mg of *tsd2* mutant and 104 mg of *qua2* mutant material was packed in 4-mm zirconia rotors for solid-state NMR analysis. Therefore, the data collected on each sample represents the averaged composition and structure of many seedlings.

4.2.2. Solid-State NMR Analysis

Solid-state NMR is a powerful tool for analyzing carbohydrate-rich materials [64,156]. All the solid-state NMR experiments were conducted on a 400-MHz Bruker AVANCE spectrometer at 9.4 Tesla using a 4-mm MAS probe. The typical radiofrequency field strength was 62.5 kHz for ^{13}C and 62.5 to 83 kHz for ^{1}H. The ^{13}C chemical shift was externally referenced to the adamantane CH_2 peak at 38.48 ppm on the tetramethylsilane (TMS) scale. Spectra were recorded at 293 K under 10 kHz MAS frequency unless specifically mentioned. All 1D ^{13}C MAS spectra were measured using either direct polarization (DP) or ^{1}H-^{13}C cross polarization (CP) to create the initial ^{13}C magnetization. DP experiments were measured with a long recycle delay of 30 s, which is sufficient for quantitatively detecting all polysaccharides in uniformly ^{13}C-labeled cell wall samples, wherein the longest ^{13}C spin-lattice relaxation times are ~6 s [61,62]. A short recycle delay of 2 s was also employed in the DP experiment to selectively detect dynamic polysaccharides. The

intensity ratios between these two spectra represent the relative mobility of cell wall molecules. CP experiments were measured to select the rigid molecules. For signal averaging, we collected 256 scans for each 1D ^{13}C DP spectrum and 1024 scans for 1D CP spectra.

To assign ^{13}C signals of different polysaccharides, we performed a 2D refocused J-INADEQUATE experiment [37], which correlates the double-quantum (DQ) or sum chemical shifts of two directly bonded ^{13}C spins with the single-quantum (SQ) chemical shifts of each ^{13}C. The experiment was conducted using DP; the use of ^{13}C-^{13}C J coupling and short recycle delays of 1.6 s substantially suppresses the dominant signals from rigid cellulose, which allows us to resolve and assign the ^{13}C chemical shifts of mobile matrix polysaccharides. The spectral widths were 496 ppm and 80 ppm for the direct and indirect dimensions, respectively. The ^{1}H decoupling field strength is 81 kHz for both the J-mixing period and the decoupling. The number of scans is 384-448 for these samples, with a measurement time of 13-14 h for each sample. In addition, 2D ^{13}C-^{13}C correlation spectra were measured with 53-ms CORD mixing [157] for resonance assignment.

To determine intermolecular interactions of wall polysaccharides, we performed 1.5 s long-mixing proton-driven spin diffusion (PDSD) experiments for all three samples to obtain through-space correlation signals. These spectra were measured at 253 K to immobilize both cellulose and pectin, facilitating magnetization transfer. The window width of the indirect dimension was minimized to be 140 ppm. Key cross sections of cellulose and pectin spectra were extracted and compared among the wild-type and mutant samples. For each sample, 320 scans (25 h) were collected in order to obtain enough sensitivity for identifying intermolecular cross peaks.

To investigate the mobility of polysaccharides, we measured the ^{13}C-T_1 that reflects nanosecond motions and the ^{1}H-$T_{1\rho}$ that reflects microsecond motions relaxation times. ^{1}H-$T_{1\rho}$ was measured using a spin-lock field on the ^{1}H channel, with an effective field of 62.5 kHz and a

variable spin-lock time of 0-19 ms. The ^{1}H polarization is then transferred to ^{13}C via a 1 ms Lee–Goldberg (LG) CP for heteronuclear detection. The LG-CP is used to avoid ^{1}H spin diffusion during the 1 ms contact time and ensure site-specificity. During the LG-CP, the ^{13}C field is 62.5 kHz and the ^{1}H effective field is set to 62.5 kHz (transverse field of 51 kHz). A two-pulse phase modulated (TPPM) decoupling sequence of 71 kHz was employed. Standard inversion recovery sequence with ^{13}C DP was used to measure ^{13}C T_1 experiment, with long recycle delays of 30 s to obtain quantitative intensities. Motional amplitudes were probed using a 2D ^{13}C–^{1}H dipolar chemical shift (DIPSHIFT) correlation experiment [39,158] under 7.5 kHz MAS frequency using a recycle delay of 2 s. The experiment was imitated with a CP for magnetization creation. ^{1}H homonuclear decoupling was achieved using the frequency-switched Lee–Goldburg (FSLG) sequence [41] which has a theoretical scaling factor of 0.577 based on measurements of the rigid model peptide formyl-Met-Leu-Phe. The ^{1}H transverse field used for FSLG was 83 kHz, which is projected to 102 kHz of effective field. The ratio between the true coupling and the rigid-limit value of 22.7 kHz gives the dipolar order parameters (S_{CH}). It should be noted that the rigid-limit values for the C-H dipolar coupling in both CH and CH2 groups are the same (22.7 kHz). However, the difference of CH and CH_2 was accounted for during the fitting of these dipolar curves using a custom Python script (available at http://meihonglab.com/hong-lab-software/).

4.3. Results and Discussion

4.3.1. Polysaccharide Structure and Composition are Altered in *qua2* and *tsd2* Mutants

To determine how nanoscale polysaccharide structure and cell wall architecture are modified by mutation of the pectin methyltransferase gene *QUASIMODO2*, we produced uniformly ^{13}C-labeled *Arabidopsis* primary cell walls for solid-state NMR characterization. Uniformly ^{13}C-labeled cell walls were isolated from 14-day-old *Arabidopsis* seedlings that were

grown in the dark using ^{13}C-glucose as the sole carbon source. This method has proven useful for investigating plant cell walls, especially for characterizing the structure and physical packing of cellulose and matrix polymers [22,61]. Carbohydrate composition was quantified using 1D ^{13}C spectra

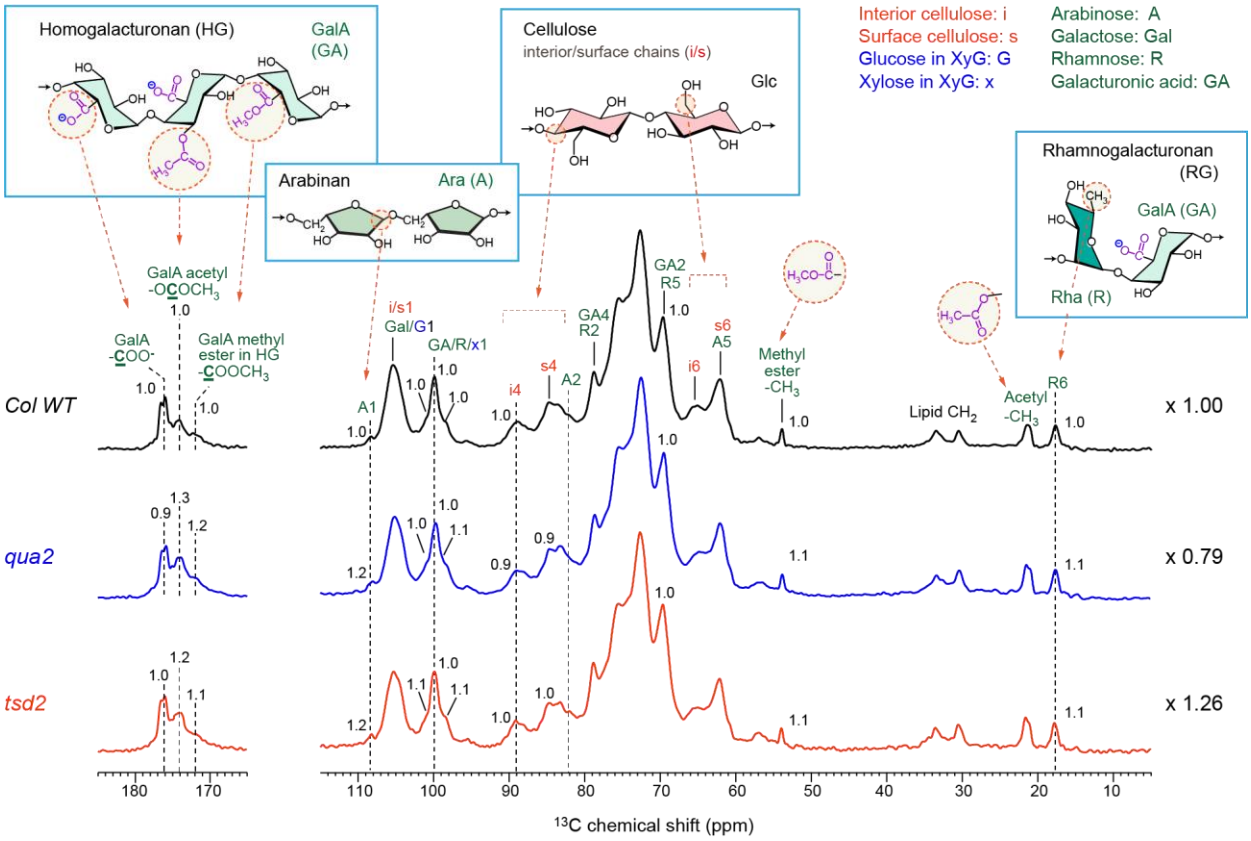

Figure 4.1. Polysaccharide composition revealed by 1D quantitative ^{13}C spectra. 1D ^{13}C spectra of *Arabidopsis* cell walls at 293 K under 10 kHz magic-angle spinning of wild-type (black), *qua2* (blue), and *tsd2* (orange) seedling samples. The representative structure of cellulose and pectin backbones and sidechains are shown, with the key functional motifs or carbon sites connected to their corresponding peaks in the spectra. The assignments include the NMR abbreviations of carbohydrates and the carbon numbers. For example, R6 is short for Rhamnose (Rha) carbon 6. The spectra were plotted after multiplying the *tsd2* spectral intensities by 1.26 and *qua2* spectral intensities by 0.79 to account for sample amount differences. The ratios of the height of peaks among the three samples are indicated by intensity values.

measured with ^{13}C direct polarization (DP) and long recycle delays of 30 s (Figure 4.1). The recycle delays are more than five times longer than the ^{13}C-T_1 relaxation times of polysaccharides

(typically below 6 s for uniformly ^{13}C-labeled cell walls), to ensure re-equilibrium of magnetization between two scans and enable the quantitative detection of all molecules.

Wild-type, *tsd2*, and *qua2* samples exhibited similar quantitative ^{13}C spectra, indicating similar compositions. Minor changes (10-20%) were observed for a few pectin peaks due to changes in abundance or structure (Figure 4.1). When comparing across samples, we normalized the spectra by the integral (area) of the whole spectra, that is, the total amount of carbon in each cell wall sample. In order to account for differences in sample amounts, the *qua2* and *tsd2* mutants were scaled by a factor of 0.79 and 1.26, respectively. These scaling factors were determined by comparing the spectral integral of each mutant to that of the wild-type sample. The differences in peak height across genotypes were relatively minor (0-20%) for all molecules as detected in quantitative DP (Figure 4.1) and for the rigid portion as shown using ^{13}C-^{1}H cross polarization (CP) (Supplementary Figure 4.1). This is the same method used recently to analyze a series of *Arabidopsis* seedlings and inflorescences [81,148]. We did not use deconvolution methods and peak integrals to avoid further uncertainties introduced by fitting procedures. Compared to wild-type cell walls, cellulose content remained comparable in *tsd2* but decreased by ~10% in the *qua2* mutant (Figure 4.1), which is signified by the change of peak height at 89 ppm for interior cellulose C4 (i4). The amount of Rha increased by ~10% in both *tsd2* and *qua2* mutants. In addition, the pectin mutants consistently showed a 20% increase in the intensity of Ara carbon 1 (A1) at 108 ppm, with an error bar of 10-12% as propagated from NMR signal-to-noise ratios (Supplementary Figure 4.2). Because arabinans are neutral sidechains of RG-I and a component of AGPs [159], we interpret this result as indicating that the number of arabinan side chains in RG-I and/or the amount of arabinan in AGPs have increased notably in these two mutants. For better comparison, overlays of spectra collected on the wild-type and mutant samples are shown in Supplementary Figure 4.3.

It should be noted that spectral overlap can lead to uncertainty for some peaks; therefore, only relatively resolved peaks were used for compositional comparison as a standard way of analysis used in previous studies [81,148]. The signal-to-noise ratios of most peaks are between 20 and 100; therefore, all intensity ratios labeled in Figure 4.1 have relatively small error margins. For example, when comparing the *qua2* mutant with the wild-type sample, even the relatively weak peaks of i4 (89 ppm) and R6 (18 ppm) still have reasonably decent error bars below 5%. However, due to the insufficient resolution, 1D spectra can only be used for initially screening these plant materials and in-depth structural information can only be obtained using 2D/3D correlation experiments [141]. Also, *Arabidopsis* seedlings change dramatically in polymer composition (Supplementary Figure 4.4); therefore, the wild-type control and different mutants are always grown under identical conditions. Some mutants exhibit significant changes with certain polymers fully or largely depleted while other samples may only have minor changes of 10-20% in carbohydrate composition[19,148].

All three samples had similar intensities for the methyl ester peak at 53 ppm, which agree with the results showing that the relative degree of methyl-esterification did not change drastically in the mutants [132]. These observations collectively indicate that QUA2 is likely not the only regulator of pectin methyl-esterification, although QUA2 itself is a methyltransferase for homogalacturonan [132]. Based on the cellulose-deficient phenotypes of *qua2* and *tsd2* mutants [132], it has been hypothesized that QUA2 might play a more prominent role in facilitating the production of HG forms that contribute to pectin-cellulose interactions.

To further resolve the structures of matrix polysaccharides, we measured 2D ^{13}C-^{13}C refocused J-INADEQUATE spectra, which rely on ^{13}C-^{13}C J-coupling to detect correlations between covalently bonded carbons (Figure 4.2a). With an additional dimension, the 2D spectra

provide higher resolution than their 1D counterparts, allowing for the unambiguous assignment of carbon connectivities in biomolecules. These spectra selectively probe mobile wall components; therefore, the cellulose signals are suppressed, and pectin signals are unambiguously detected. All of the ^{13}C chemical shifts are summarized in Supplementary Table 4.1. The assignment of cellulose and pectin signals was based on a series of published studies of *Arabidopsis* primary cell walls [19,20,22,61,81,148]. All these studies relied on high-resolution 2D/3D ^{13}C-^{13}C correlation spectra collected for uniformly ^{13}C-labeled cell wall samples, occasionally assisted by the use of mutants or chemical treatments that selectively remove certain wall components. The signals of cellulose, GalA, Rha, and Ara were unambiguously assigned. These chemical shifts were indexed in the Complex Carbohydrate Magnetic Resonance Database (CCMRD) [124].

The chemical structure of arabinan is highly complex, with major covalent linkages at carbons 1 and 5, and linkages at carbons 2 and 3 also possible. This structural polymorphism has inevitably resulted in spectroscopic complexity, resulting in 8 types of arabinose units (annotated using superscript a to h) as we recently reported [148]. In addition to the arabinan signals being increased in the *qua2* and *tsd2* mutants (Figure 4.1), they were also more branched in the pectin mutants as both *tsd2* and *qua2* showed higher signals for 2-Ara residues (type-f and -g in Figure 4.2b), which are responsible for creating additional, branched linkages at C2 in addition to C1 and C5 linkages for linear structures (Figure 4.2c). In addition, *qua2* also showed a new type of Ara (type-b) signal that is absent in the wild-type and *tsd2* samples (Figure 4.2, Supplementary Figure 4.5). In addition, the rhamnose carbon 6 showed three distinct peaks in *qua2* but showed a single peak in the wild-type and *tsd2* samples (Figure 4.2a and Supplementary Figure 4.5), indicating a more complex environment experienced by the rhamnose residues in the *qua2* mutant.

The signals of $A1^{b}$ and $A1^{f,g}$ are beyond the noise level as confirmed by analysis of the 1D ^{13}C cross sections (Supplementary Figure 4.6). Although major A1 signals resonate at 108 ppm, a minor form is also present at 110 ppm (Figure 4.2b), which is unresolvable in 1D quantitative spectra (Figure 4.1) due to the limited resolution and the dominance of cellulose peaks. These arabinose forms have been repeatedly observed in *Brachypodium* seedlings as well as the seedlings and inflorescence stems of *Arabidopsis* [62,81,148].

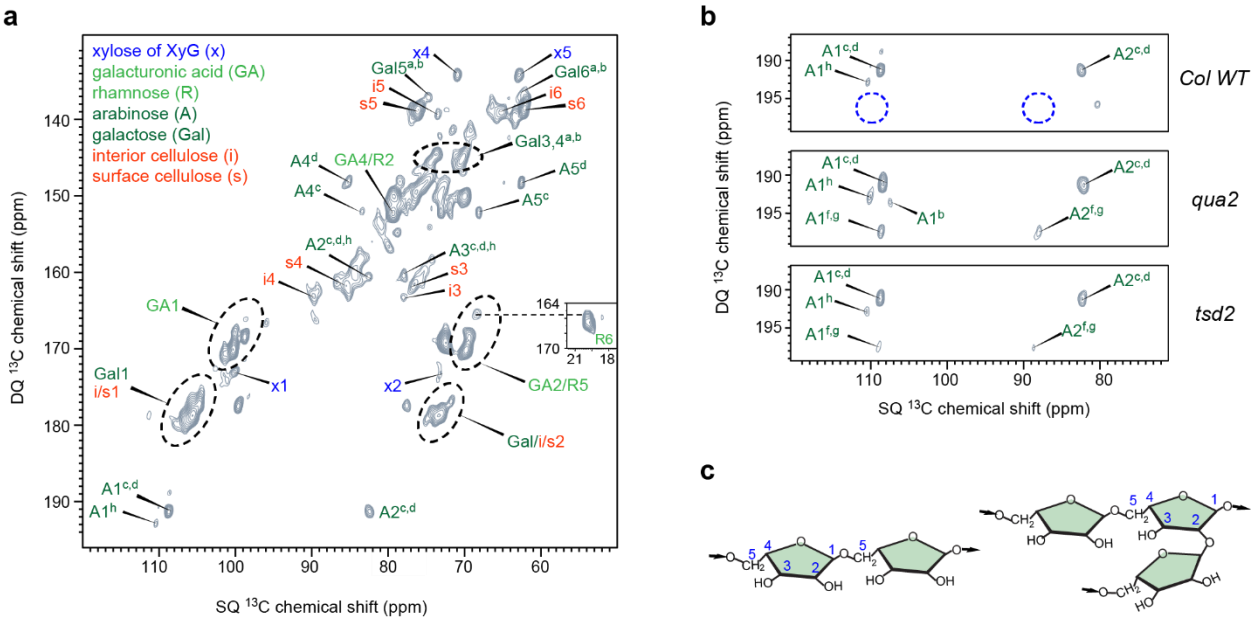

Figure 4.2. Structural change of matrix polysaccharides pinpointed by 2D INADEQUATE spectra. (a) 2D ^{13}C DP J-INADEQUATE spectrum of *Arabidopsis* wild-type cell walls. (b) Comparison of arabinose C1-C2 regions of wild-type, *qua2* and *tsd2* samples. The *qua*2 and *tsd2* samples showed stronger $A1^{f,g}$ and $A2^{f,g}$ signals (carbon 1 and 2 of type f and g arabinose units), which belong to branched arabinans with additional linkage at carbon 2. (c) Representative structure of linear (left) and branched (right) arabinan.

4.3.2. Cellulose and Pectin are Tightly Associated in *qua2* and *tsd2* Mutants

To investigate the physical packing of polysaccharides, we carried out a 2D ^{13}C-^{13}C correlation experiment using a 1.5-s PDSD mixing time. This method has been employed to investigate non-covalent interactions between cellulose and matrix polysaccharides as well as between cellulose and lignin in plant biomass [8,10,160-162]. With this long mixing time, strong

intermolecular cross peaks can be identified bridging cellulose carbon sites, namely 89 ppm for i4 and 65 ppm for i6, with pectic Rha and GalA C1 signals at 101 ppm and 100 ppm (Figure 4.3a). These cross peaks originate from the sub-nanometer spatial correlations of carbons in different polysaccharides, which allows for polarization transfer from pectin to the surface chains and then to the internal chains of cellulose microfibrils. Such physical associations between cellulose and pectin have been found to be robust in *Arabidopsis* primary cell walls, regardless of the history of sample hydration and chemical treatment [61]. Even alkaline treatment does not affect these pectin-cellulose cross peaks. We previously found that alkali only digests the mobile portion of pectin, without perturbing the rigid domain of pectin that is associated with cellulose microfibrils [61]. It is impractical to precisely define intermolecular distance, but an upper limit could be provided for the observed correlations. Despite the use of a long mixing time and low temperature, the intermolecular ^{13}C-^{13}C correlations should still fall within 1 nanometer. Therefore, the direct contacts between pectin and cellulose surface should be closer than 4-5 Å, considering the cross peaks observed between pectin and interior cellulose, which are spaced by the surface layer of glucan chains in cellulose.

Key 1D ^{13}C cross sections were extracted to provide a better view of the relative intensities of these intermolecular contacts (Figure 4.3b). In the 89 and 65 ppm cross sections that are characteristic of the interior glucan chains of cellulose microfibrils, both *qua2* and *tsd2* mutants showed stronger pectin cross-peaks with GalA/Rha C1 (101 ppm) than the wild-type sample. Consistently, in the 101 ppm cross sections of pectin, both pectin mutants showed stronger cellulose intensities at 89 ppm and 65 ppm, as well as the cellulose-dominant 105 ppm peaks. The 99 ppm cross section showed similar intensities of interior cellulose peaks (i4 at 89 ppm and i6 at 65 ppm) in the mutant and control samples, but with stronger intensities observed at the surface

cellulose (84 and 62 ppm) positions in the mutants. Compared with the wild-type cell walls, the *qua2* and *tsd2* mutations displayed stronger or more extensive interactions between cellulose and the GalA/Rha residues in the rigid domains of HG and RG-I backbones (Figure 4.3c).

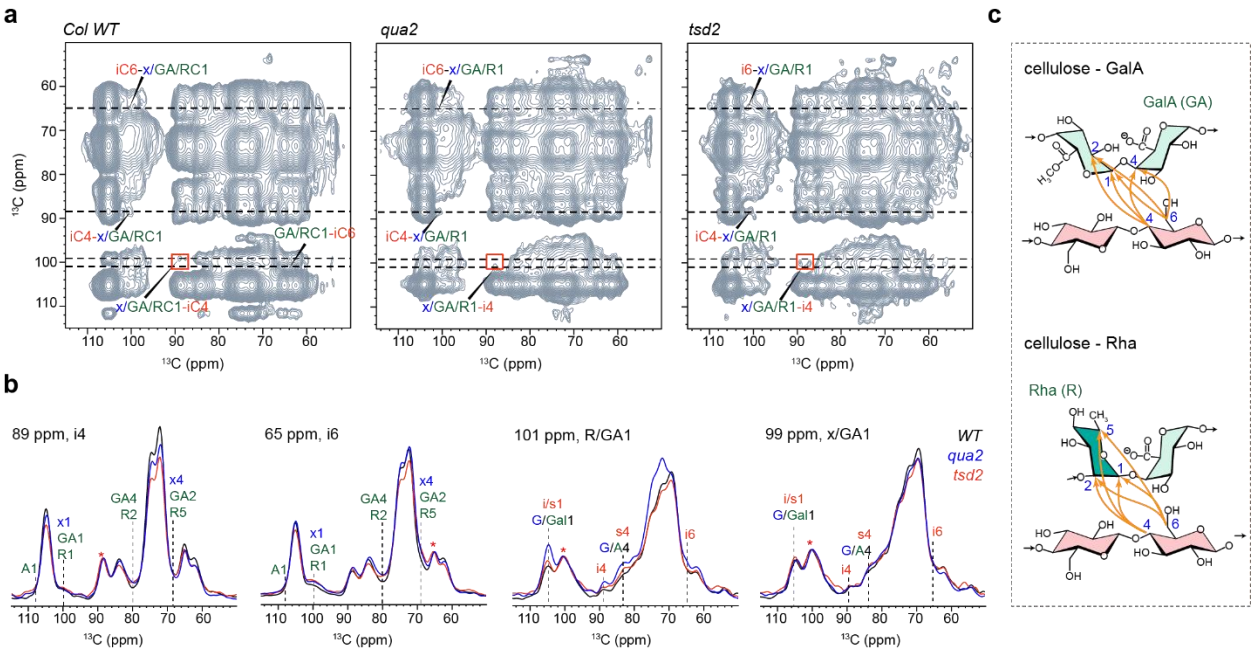

Figure 4.3. Cellulose-pectin interactions are stronger in *qua2* and *tsd2* mutants. (a) 1.5-s PDSD spectra measured at 253 K under 10 kHz MAS using 1.5 s mixing time on the wild-type (WT) sample and mutants. (b) Representative cross sections for cellulose (89 ppm and 65 ppm) and pectin (101 ppm and 99 ppm) compared among the three samples, with normalization by the diagonal peaks (asterisk). Dashed lines indicate cellulose-pectin cross peaks of interest. (c) Representative physical contacts between cellulose and the GalA and Rha residues of pectin backbones (HG and RG-I). The carbon sites are labeled in blue.

4.3.3. Polysaccharides Have Different Motional Dynamics in Wild-type and Pectin-Deficient Walls

Because the plant cell wall is a composite of interconnected but dynamic molecular networks, we hypothesized that the alteration in intermolecular interactions between pectin and cellulose in *qua2* and *tsd2* cell walls would be accompanied by abnormal motional characteristics of these polysaccharides in the mutants. Thus, motional rates on the microsecond (μs) and nanosecond (ns) timescales were probed using ^{1}H-$T_{1\rho}$ and ^{13}C-T_1 relaxation measurements,

respectively (Figure 4.4 and Supplementary Figure 4.7). The ^{1}H-$T_{1\rho}$ relaxation curves of cellulose exhibited a slower decay than those of pectin because cellulose microfibrils are much more rigid than matrix polysaccharides (Figure 4.4a). Compared to the wild-type sample, both *qua2* and *tsd2* mutants exhibited faster ^{1}H-$T_{1\rho}$ relaxation, both for cellulose and pectin. The ^{1}H-$T_{1\rho}$ relaxation time constants of cellulose peaks were 39-63 ms in the wild-type sample but dropped to 11-24 ms in the *tsd2* and *qua2* mutants (Figure 4.4b). Consistently, the ^{1}H-$T_{1\rho}$ of pectin dropped from 13 ms in the control sample to less than 7 ms in the mutants. These halved relaxation times indicate that local disorder is higher in these pectin-deficient mutants, facilitating collective motions among several sugar units on the microsecond timescale.

Although all the relaxation curves in Figure 4.4 were fit using single-exponential functions for the ease of comparison, the pectin relaxation data for all three genotypes displayed a feature of double-exponential decay, with a noticeable kink in the middle. As a result, the initial data points were underneath the single-exponential curve (faster relaxation), while the latter ones were higher than the curve (slower relaxation). We hypothesize that this double-exponential pattern is induced by the separation of pectin into two domains consisting of a rigid fraction tightly associated with cellulose microfibrils and a more mobile fraction filling the more open spaces between cellulose microfibrils. Another possible explanation is the structural heterogeneity of pectic polymers. This double-exponential feature has been observed for pectin in *Arabidopsis* and for the hemicellulose glucuronoarabinoxylan (GAX) in *Brachypodium distachyon*; the weighting factor of the slow-relaxing component has been used to estimate the fraction of matrix polymers that are closely associated with cellulose microfibrils [61,62]. For our samples, the double-exponential decay is particularly pronounced in the *tsd2* and *qua2* mutants (Figure 4.4a and Supplementary Figure 4.4b), potentially due to the stronger packing between cellulose and pectin (RG-I and HG). As CP-

based measurements are already specific to the rigid portion of pectin, the observation of a multi-exponential feature further suggests the presence of two distinct populations of pectic polymers in the relatively rigid domain.

To examine faster motions occurring on the nanosecond timescale, we measured ^{13}C-T_1 relaxation using a CP-based method that preferentially detects rigid molecules (Figure 4.4c) and a quantitative DP method that probes all molecules without bias (Figure 4.4d). The latter generally has shorter ^{13}C-T_1 relaxation times than the former due to the co-existence of both rigid and mobile molecules. In the rigid phase, pectin had longer ^{13}C-T_1 in the mutants than in wild-type samples (Figure 4.4c). For example, ^{13}C T_1 of the 100-ppm peak of Rha/GalA C1 increased from 0.7 s in wild-type sample to 1.1 s in both *tsd2* and *qua2* mutants (Figure 4.4c and Supplementary Table 4.2). In contrast, the trend was inverted for cellulose peaks. This is mainly due to the ^{13}C-^{13}C spin-exchange, which happens efficiently in uniformly labeled materials during the ^{13}C-T_1 measurements. The smaller difference in relaxation times between pectin and cellulose confirmed the stronger interactions of these two polysaccharides in the mutants. Under quantitative detection, this trend was no longer detected: for both pectin and cellulose, the ^{13}C-T_1 was longer in wild-type than in the mutants (Figure 4.4d). For example, ^{13}C T_1 for the 100-ppm peak of Rha/GalA C1 decreased from 0.4 s in the wild-type sample to 0.2 s in the mutants (Supplementary Table 4.2). This finding indicates that the mobile phase of pectin is even more dynamic in *tsd2* and *qua2* walls.

To project the motional amplitudes of cellulose and pectin, we measured ^{13}C-^{1}H dipolar couplings using the dipolar chemical-shift (DIPSHIFT) correlation experiment. Figure 4.5a shows the C-H dipolar dephasing curves and the corresponding order parameters (S_{CH}) of major polysaccharides. A more pronounced decay, in general, presents a larger C-H dipolar coupling, a larger order parameter, and a higher rigidity, but this trend does not hold across different chemical

motifs (for example, CH or CH_2). Cellulose was highly rigid in all three samples, showing deeply dephased curves and large dipolar order parameters ranging from 0.8-1.0 for various carbon sites (Figure 4.5a, top row). In contrast, the order parameters of pectin carbon sites were generally in the range of 0.5-0.8, with only two exceptions happening at 101 ppm and 79 ppm in the *qua2* mutant, which are in the range of 0.85-0.90 (Figure 4.5b).

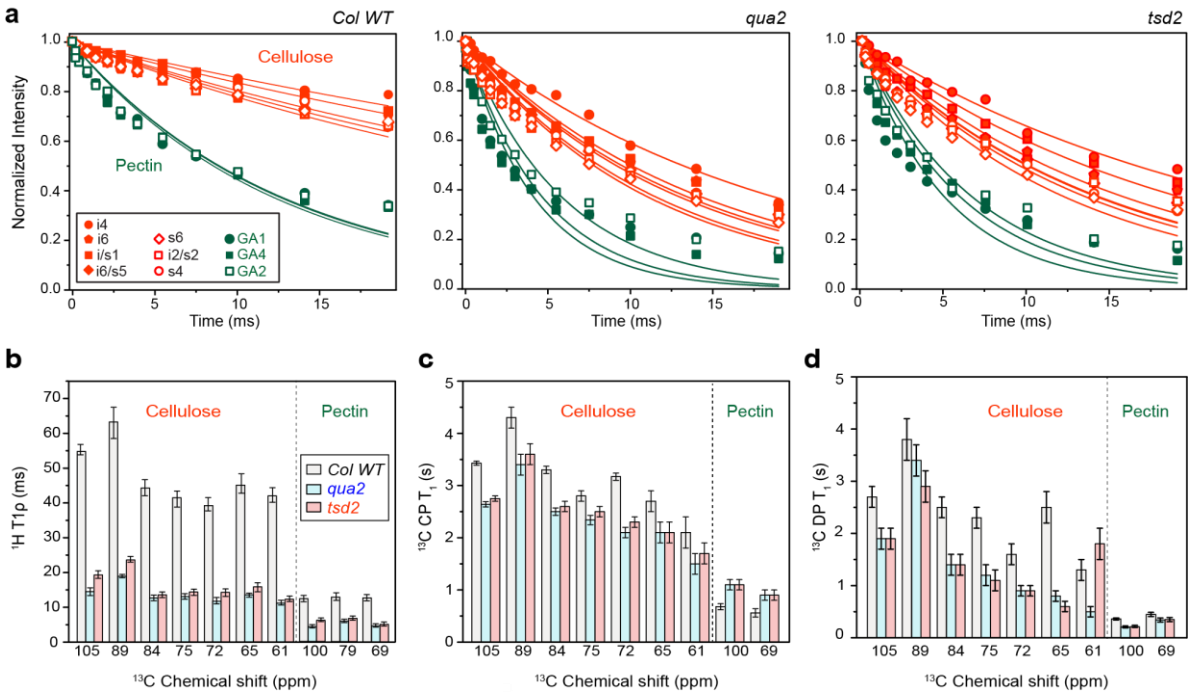

Figure 4.4. Change of polysaccharide dynamics revealed by NMR relaxation. (a) ^{1}H $T_{1\rho}$ of wild-type (left), *qua2* (center) and *tsd2* (right) cell walls. Pectin has faster relaxation than cellulose. Polymers in the pectin mutants have faster ^{1}H-$T_{1\rho}$ relaxation than those in the wild-type sample. b-d, Relaxation time constants of (b) ^{1}H $T_{1\rho}$, (c) ^{13}C-T_1 of rigid molecules as probed using CP, and (d) ^{13}C-T_1 of all molecules as probed using quantitative DP and inversion recovery pulse sequence. Error bars represent the standard deviation of the fit parameters.

Since this CP-based experiment preferentially detects more rigid components, the large dipolar order parameters of pectin in the *qua2* and *tsd2* mutants (Figure 4.5b) indicated a very small fluctuation angle of the CH bonds, which are likely due to the restriction imposed by tighter pectin-cellulose packing in this mutant. Therefore, the rigid domain of pectin that interacts with cellulose might become even more rigid in the mutants. This hypothesis is supported by the

stronger pectin-cellulose cross peaks in the mutants (Figure 4.3b). At the same time, other possible mechanisms, such as alternations in pectin-pectin interactions and supramolecular assemblies of pectic polymers, might also contribute to these dynamical changes. In addition, arabinan and galactan sidechains of pectic polymers are invisible in these experiments due to their high mobility. If more prominent interactions with cellulose are present, these pectic sidechains should have detectable signals. Therefore, our observations support the hypothesis that it is pectin backbones rather than side chains that primarily interact with rigid cellulose microfibrils [148].

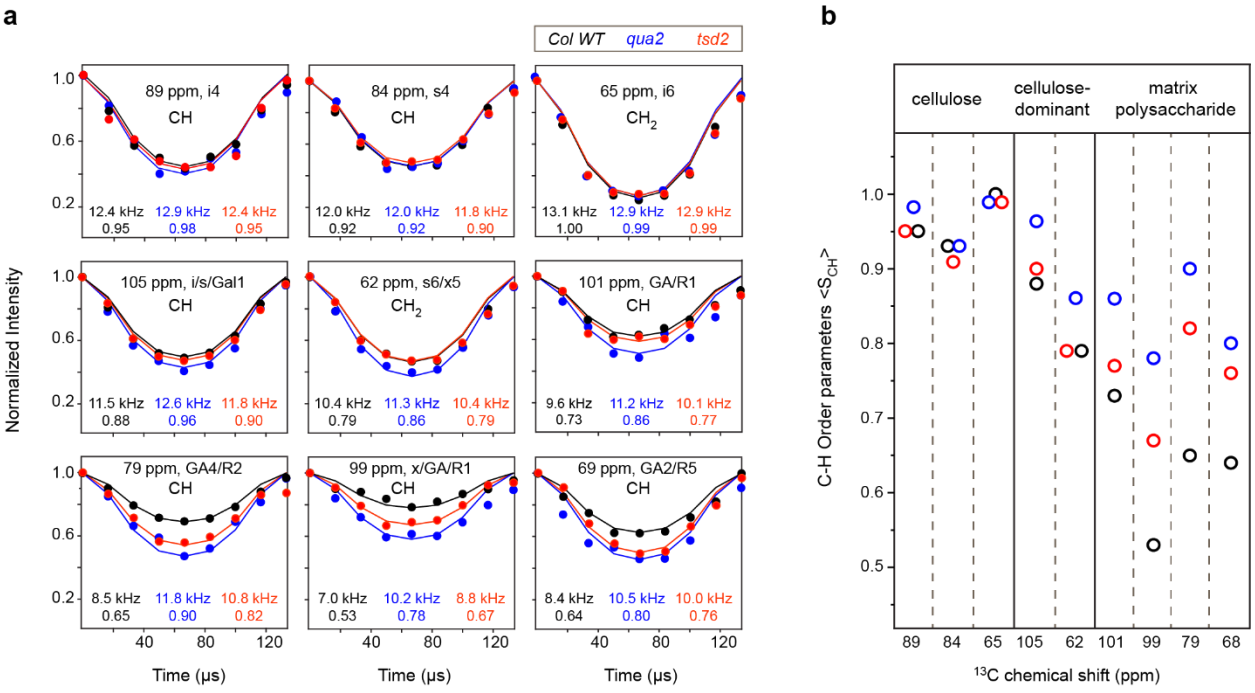

Figure 4.5. ^{13}C-^{1}H dipolar order parameters of polysaccharides in intact cell walls. (a) ^{13}C-^{1}H dipolar dephasing curves of cellulose and pectin. DIPSHIFT spectra were measured at 297 K under 7.5 kHz MAS. Best fit dipolar couplings and the corresponding order parameters are indicated in each panel. The chemical motif (CH or CH_2) is indicated in each panel. (b) C-H dipolar order parameters. Matrix polysaccharides (mainly RG-I and HG signals here) are generally more rigid in *qua2* (blue) and *tsd2* (red) mutants than in the wild-type sample (black).

4.3.4. Postulated Molecular Rationale for Mechanical Defects in Pectin Mutants

Despite evidence for disorganization of cell wall ultrastructure and defects in pectin content in the *tsd2* and *qua2* mutants [132], the direct molecular cause of the shorter hypocotyls and cell

adhesion defects observed in these mutants has remained elusive. Because QUA2 is a HG methyltransferase, it is natural to suspect that changes in polysaccharide structure, in particular, the chemistry associated with GalA residues, might lead to the phenotype changes. In fact, several recent studies have suggested a structural role of HG backbones in primary cell walls [5,61,81,163]. In particular, chemical changes in GalA units, while subtle, may substantially affect the structural properties of HG. These variations include the protonation and deprotonation of carboxylates mediated by pH, as well as the methyl-esterification that hinders the formation of calcium cross-linked pectin networks. Recently, the crucial role of these chemical modifications has been confirmed by ssNMR studies of the seedlings of *PGX1*^{AT} and *pgx1-2* mutants [148], in pH-regulated primary cell walls [164], as well as along the inflorescence stem of *Arabidopsis* [81]. An increased degree of methyl esterification has been connected to stronger pectin-cellulose interactions and slower plant growth [81]. However, it is intriguing that the *qua2* mutant retains a similar apparent level of HG methyl esterification as the wild-type sample (Figure 4.1). In fact, both *qua2* and *tsd2* seedlings retain a polymer composition resembling that of wild-type sample as shown by their similar spectral patterns. The compositional difference is relatively trivial, typically within the range of 10-20% for each polymer, which was consistently revealed by solid-state NMR data and monosaccharide composition analysis [132]. Therefore, other mechanisms are likely to alter cell wall and tissue mechanics in these mutants.

In a recent study, *GAUT4* knockdown (KD) plant biomass had lower levels of HG and RG-II, suggesting that *GAUT4*-produced HG might serve as precursor for RG-II synthesis. RG-II has an HG backbone, unlike RG-I, which has an alternating Rha/GalA backbone, and hence might have been affected in *GAUT4*-KD plants by the absence of a specific HG subtype. As a result of the reduced HG- and RG-II-mediated cross-linking, overall wall integrity was hypothesized to be

compromised, resulting in an increase in biomass saccharification and plant growth [149]. This idea indicates that HG and RG-II are required for maintaining normal wall integrity.

The supramolecular structure of the plant cell wall is stabilized by numerous physical interactions between different polysaccharides [110]. Extensive data derived from Sum Frequency Generation (SFG), Atomic Force Microscopy (AFM) and Field Emission Scanning Electron Microscopy (FESEM) have consistently shown that cellulose is disorganized in *qua2* and *tsd2* cell walls [132]. Unlike the well-bundled fibrils arranged in a uniform direction in wild-type walls, microfibrils in these two mutants appear more separated from each other, with shorter lengths and a broader distribution of orientations within a lamella. This has been attributed to compromised wall integrity and attenuated cellulose deposition in the mutants [132]. These microscopic observations can help explain the stronger cross peaks between cellulose and pectin observed in the mutants by ssNMR (Figure 6): with cellulose microfibrils more dispersed in the matrix, the surface of cellulose should become more accessible to pectin, which will enhance sub-nanometer physical interactions between these two polysaccharides. As anticipated for reduced microfibril bundling, both cellulose and pectin might become more dynamic on the relatively slow, microsecond timescale (Figure 4.4a, b). However, likely due to stronger pectin-cellulose interactions, the motional amplitudes of wall polysaccharides have been restricted, in particular for the rigid portion of pectin that should be tightly associated with cellulose microfibrils (Figure 4.5). In this way, the mutations might substantially modulate the nanoscale organization of cell walls despite inducing only relatively minor changes in the chemical structure and composition of carbohydrate polymers.

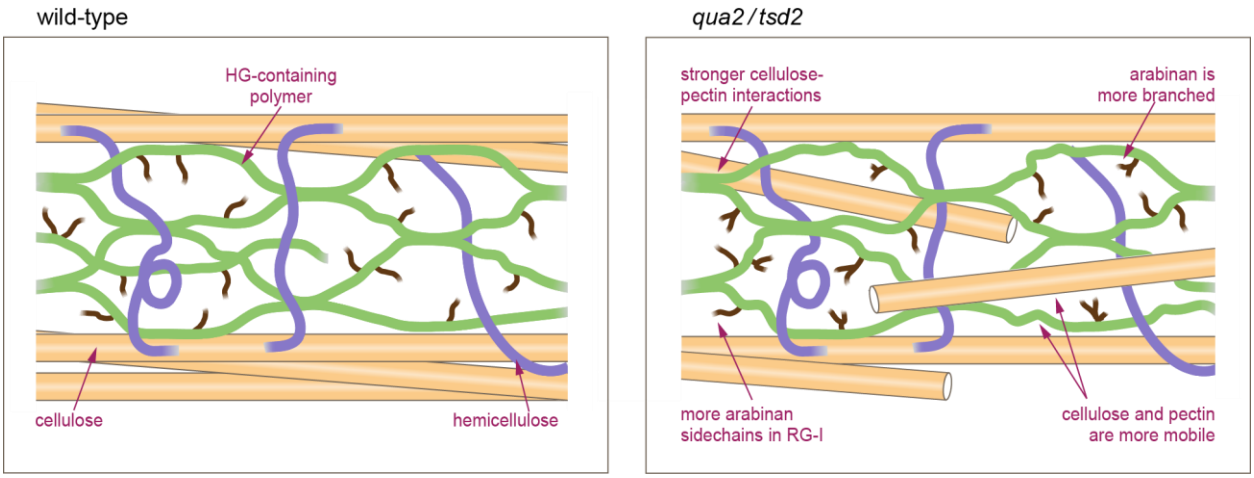

Figure 4.6. Schematic models of wild-type and mutant cell walls. The HG-containing polymers (green) primarily include the HG polysaccharide and HG-domains connected to RG-I, with possible minor contributions from the HG domains connected to RG-II and proteoglycans. This conceptual structure of pectin is adapted from [149]. In the mutants, more arabinan sidechains are included in the pectic polymers. These arabinans also exhibit a higher degree of branching. Cellulose microfibrils (yellow) become shorter and orientationally diverse, which results in more extensive contacts with pectin and increased cell wall dynamics. The hemicellulose xyloglucan (purple) is not discussed here. Other mechanisms, such as pectin-pectin interactions, are possible but are not included in the current discussion. This illustrative figure is not intended to be to scale.

4.4. Conclusions

In this work, we have evaluated the abundance, molecular structure, physical packing, and motional characteristics of pectic polymers and cellulose in the *qua2* and *tsd2* mutants of *Arabidopsis.* Using high-resolution solid-state NMR spectroscopy, we have shown that in both mutants the pectin extensively associates with cellulose microfibrils, which correlates with the restricted motional amplitudes of pectic polysaccharides. In addition, both cellulose and pectin backbones become more dynamic on the microsecond timescale, which is supportive of a model where cellulose microfibrils are dispersed in the soft matrix, with extensive intermolecular contacts and enhanced disorder of cell wall polymers. This study provides a clearer structural picture of the cell walls of *tsd2* and *qua2* mutants and sheds light on the nature of cellulose-pectin contacts, supporting a potential role of RG-I and HG pectic backbones in stabilizing these polysaccharide interactions.

CHAPTER 5. LIGNIN-POLYSACCHARIDE INTERACTIONS IN PLANT SECONDARY CELL WALLS REVEALED BY SOLID-STATE NMR

5.1. Introduction

The secondary cell wall comprises the majority of plant biomass and is a sophisticated composite of cellulose, hemicellulose (mainly xylan and glucomannan) and lignin[49,50]. This supramolecular network formed by complex carbohydrates and aromatic polymers provides the cell with sufficient mechanical strength and rigidity, but it also makes the lignocellulosic materials inherently recalcitrant to chemical and enzymatical treatments during biofuel production[48]. Decades of efforts have been devoted to genetically engineering the plants to improve the composition and structure of cell wall polymers, aiming at increased digestibility[165-167]. This method offers the potential for effectively generating sustainable bioenergy, however, a major hurdle here is our inadequate understanding of the cell wall architecture on the molecular level.

In secondary cell walls of woody materials, bundles of cellulose microfibrils, typically 10-20 nm across[109], are proposed to be coated by a xylan-lignin complex and crosslinked by glucomannans[3,168-170]. However, due to the inherent, technical constraints of traditional analytical methods, detailed molecular information about secondary cell wall organization has remained scarce. Conventional methods either rely on sequential extractions followed by compositional analysis or require partial dissolution of the lignocellulosic materials using organic solvents and ionic liquids for solution-NMR characterization[11-13]. These procedures substantially perturb the physical state and molecular interactions of biomolecules, introducing considerable uncertainty to

---

This chapter was previously published as X Kang, A Kirui, MC Dickwella Widanage, F Mentink-Vigier, DJ Cosgrove, T Wang, "Lignin-Polysaccharide Interactions in Plant Secondary Cell Walls Revealed by Solid-State NMR", in *Nature Commununications*, January 21, 2019, copyright 2019, The Authors. https://dx.doi.org/10.1038%2Fs41467-018-08252-0

our understanding of the cell wall structure. This limitation has been partially alleviated by the recent solid-state NMR (ssNMR) work that characterized xylan polymorphism in native secondary cell walls of *Arabidopsis*, revealing a two-fold helical screw symmetry with a regular pattern of acetate or glucuronate substitutions in cellulose-bound xylan[10,18,63]. However, many structural aspects still await investigation and a key question, examined here, is how lignin and polysaccharides are packed in intact secondary cell walls.

The atomic resolution of ssNMR spectroscopy and the sensitivity enhancement provided by the dynamic nuclear polarization (DNP) technique have enabled us to clarify and substantiate our ambiguous view of lignocellulose structure with detailed molecular evidence. The ^{13}C-labeled stems from three energy and agricultural crops (maize, rice, switchgrass) as well as the model plant *Arabidopsis* were investigated. Dominant interactions between xylan with non-flatten conformations and lignin units rich in methyl ethers are observed whereas direct lignin-cellulose interactions are less prominent. Because the degree of hydration and timescale of motions are distinct between the lignin and polysaccharides, we propose that lignin self-aggregates in distinctive nanodomains with extensive surface contacts to hemicelluloses. These results provide a substantial revision of our understanding of the supramolecular architecture of secondary plant cell walls, which can facilitate the development of crops with higher digestibility and improve the efficiency of biomass deconstruction and conversion to biofuels.

5.2. Results

5.2.1. Polysaccharides and Lignin are Structurally Polymorphic

Uniformly ^{13}C-labeled stems of maize, rice, switchgrass, and *Arabidopsis* were produced for ssNMR analysis by growing the plants in a closed growth chamber with continuous supply of $^{13}CO_2$. Isotopic enrichment provides adequate sensitivity for systematically measuring two-

dimensional (2D) ^{13}C-^{13}C spectra, which provide atomic resolution for determining the composition, sub-nanometer packing, site-specific hydration and ns-μs motion of lignin and polysaccharides in the near-native state.

Figure 1 shows representative 2D ^{13}C-^{13}C correlation INADEQUATE spectra and molecular structures of biomolecules in intact maize stems. These samples contained predominantly secondary cell walls, as xyloglucan (a primary wall component) was negligible (Figure 5.1a). The major hemicellulose, xylan, is dominated by its 2-fold, extended conformers (Xn^{2f}), accounting for ~70 mol% as indicated by the peak volume (Figure 5.1b). This is potentially due to the extensive interaction of xylan with cellulose microfibrils, which promotes the 2-fold, flat conformation. The interactions with cellulose rigidifies the 2-fold xylan and further enhance its signal in the current spectrum that relies on the ^{1}H-^{13}C cross-polarization (CP) to preferentially detect rigid components. These 2-fold xylans are structurally polymorphic (Figure 5.1a) and only a subgroup is in close contact with lignin as shown later. The 2- and 3-fold xylan conformers are both heavily acetylated and mixed on the sub-nanometer scale because a moderate cross peak exists between the C1 of 2-fold xylan and the C4 of the 3-fold conformer ($Xn1^{2f}$-$Xn4^{3f}$) (Supplementary Figure 5.1a**)**.

The glucan chains in cellulose microfibrils of secondary cell walls are highly polymorphic in structure. Among the six major allomorphs, types a-d are the internal chains while types g and f originate from surface residues (Figure 5.1a). With the high resolution attained here, NMR further reveals subtle differences in cellulose organization in cell walls from growing coleoptiles versus mature stems (Figure 5.1c) where microfibrils aggregate extensively[109,112]. The increase in relative intensities of the deeply embedded allomorph (type-c) and the reduced number of surface chains (Figure 5.1c and Supplementary Table 5.1) collectively indicate the restructuring of elementary

microfibrils on the aggregation interface, likely enabled by cooperative activity of multiple cellulose synthase complexes during secondary wall formation[171,172].

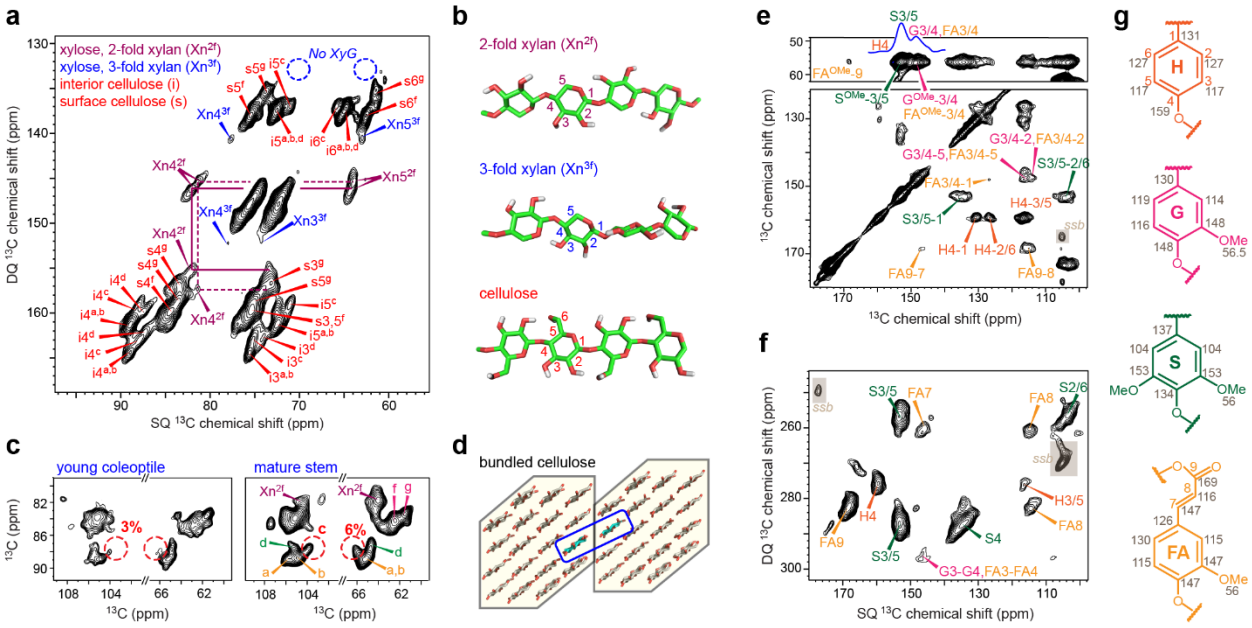

Figure 5.1. The polymorphic structure of lignin and polysaccharides in intact maize stems. (a) Representative 2D ^{13}C-^{13}C correlation spectrum resolves the polymorphic signals of cellulose and xylan. The xyloglucan (XyG) signals are missing (blue circles), indicating a negligible amount of primary cell walls. Abbreviations are used for assignment, e.g. $s4^{g}$ is carbon 4 of glucose type-g on the microfibril surface. (b) Representative polysaccharide structures. (c) Cellulose signals in maize coleoptile and mature stems. The six cellulose allomorphs are labeled using letters a-g. The intensity of type-c cellulose is 2X greater in mature stems compared with coleoptiles. (d) An illustrative figure of two adjacent microfibrils, with the restructured chains boxed in blue, which increase the intensity of type-c cellulose in panel c. These chains restructure by changing the hydroxymethyl conformation. The number of glucan chains in the figure may not represent the actual microfibril structure. The aromatic signals of lignin are resolved using 2D ^{13}C-^{13}C spectra measured using (e) 53-ms CORD and (f) INADEQUATE methods. (g) Representative structures and ^{13}C chemical shifts of lignin.

Maize lignin is mainly composed of *p*-hydroxyphenyl (H), guaiacyl (G), syringyl (S) and ferulate (FA) residues (Figure 5.1e-g). The H, G and S lignin units differ in the number of methoxyl substitutions at carbon 3 and 5, which results in well-resolved signals for the ring carbons. These aromatics bear conformational heterogeneity since they show broad linewidth and peak multiplicity (Supplementary Figure 5.1). The ^{13}C NMR chemical shifts are documented in

Supplementary Table 5.2, and the well-resolved signals of aromatics and carbohydrates enable further determination of their intermolecular packing as detailed below.

5.2.2. Lignin Binds Xylan Through Electrostatic Interactions

Both native and modified lignins have been extensively studied using solution NMR[12,13,52,173], but native interactions with other wall components are lost in the ball-milled, fractioned and dissolved samples. Using the intact maize stems, we have measured a long-mixing (1.0 s) 2D spectrum, which displays 74 intermolecular cross peaks that are absent in the 0.1-s short-range correlation spectrum (Figure 5.2a). This experiment provides exquisite details on the spatial proximities (instead of covalent bonding) of cell wall polymers as each cross peak represents a unique sub-nanometer contact between two distinct atoms in adjacent molecules. These intermolecular interactions are well-resolved in the NMR spectra and can be classified into four major categories depending on the interaction site and the structural motifs. First, cross peaks may occur between two different lignin units, for instance, the H4-S3/5 cross peak at (159, 153 ppm). Second, the methyl ethers of lignin may be spatially proximal to xylan and cellulose. Notable examples include the OMe-s4 at (57, 84 ppm) and the OMe-Xn4^{3f} at (57, 78 ppm) caused by the contacts between lignin methyl ethers and surface cellulose carbon 4 and 3-fold xylan carbon 4. Third, the aromatic carbons of lignin may correlate with the ring carbons of carbohydrates, for example, the S3/5-Xn4^{3f} cross peak at (153, 78 ppm). Fourth, the xylan acetyl group may correlate with lignin as reflected by the Ac^{Me}-FA9 cross peak at (21, 169 ppm) and the Ac^{Me}-S3/5 cross peak at (21, 153 ppm), which originate from physical contacts between the methyl carbon of xylan acetyl groups with the carbon 9 of ferulate and the carbon 3/5 of syringyl units.

All intermolecular correlations are categorized by the interacted molecules and the relative intensities of these cross peaks (Figure 5.2b). Xylan is the primary polysaccharide interactor of

lignin with 47 cross peaks (Figure 5.2b) and tightly contacts S-lignin (<5 Å), evidenced by cross peaks with only a short mixing period (Figure 5.2c). Although cellulose-lignin contacts have been proposed in-silico[174], the scarcity of cross peaks indicate few direct interactions in these non-woody samples (Figure 5.2b).

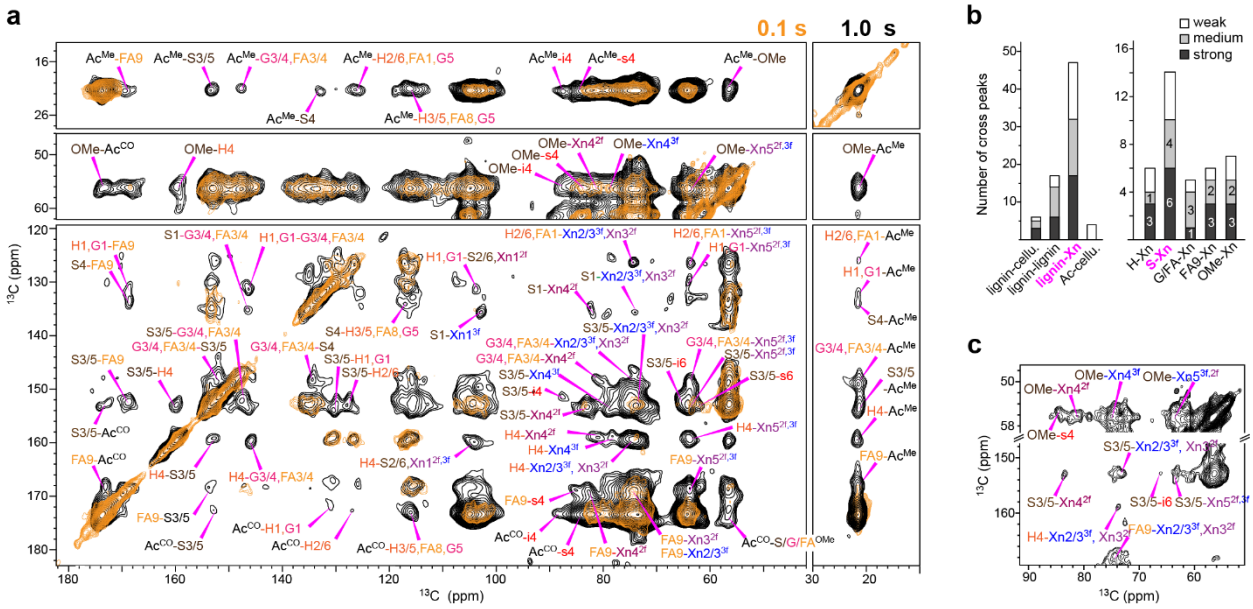

Figure 5.2. Electrostatic interactions of xylan and S units dominate lignin-polysaccharide interactions in maize. (a) Representative ^{13}C-^{13}C spectra measured with short (0.1 s, orange) and long (1 s, black) mixing times on maize. The 1-s spectrum shows many long-range intermolecular cross peaks that are absent in the 0.1-s spectrum. Only intermolecular cross peaks are labeled. (b) Summary of the 74 intermolecular cross peaks in maize. For each category, the peaks are grouped by their strength. Cellulose is abbreviated as cellu. Lignin-xylan contacts dominate, with the most cross peaks for S. (c) The Xn-S and Xn-OMe cross peaks in the 100-ms spectrum reveal close contacts.

We have extended these experiments to two other economically important grasses, switchgrass, and rice, and to *Arabidopsis*, a model dicot (Figure 4.3 and Supplementary Figure 5.2). The lignin composition varies substantially among species: maize contains all the four units; in *Arabidopsis* S and G predominate; switchgrass lacks S and rice lacks H (Figure 5.3a, b and Supplementary Figure 5.1c). In these plants, we have identified 234 distinctive intermolecular cross peaks, and the large number of correlations identified here allows us to conduct statistical

analysis of polymer contacts in this collection of plant species. Lignin has 155 cross peaks with xylan but only 25 contacts with cellulose, confirming the anchoring role of xylan (Figure 5.3c). Despite its modest abundance (29% on average) (Figure 5.3b), the S-residue has the most abundant cross peaks with xylan (Figure 5.3d). The amount of G and FA (52%) is almost twice that of S but their xylan cross peaks are less prevalent. The number of physical contacts with polysaccharide correlates with the number of methyl ether groups (OMe) in lignin and decreases in the order: S > G/FA > H. Consistently, 80% of the OMe-Xn cross peaks are either strong or medium (Figure 5.3d), indicating that electrostatic interactions between lignin methoxy groups and xylan polar functionalities dominate their physical contacts. The strong polysaccharide interaction of S units may be related to its early deposition during lignification[175] and the weak H-Xn interaction enlightens the higher lignin extractability in H-rich plants[176].

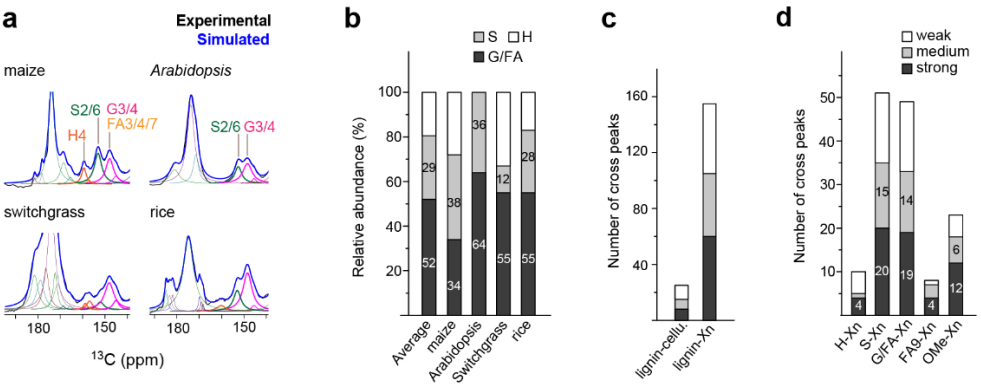

Figure 5.3. Lignin composition and carbohydrate interactions in four species. (a) Spectral deconvolution of quantitative ^{13}C spectra for compositional analysis of lignin. (b) The molar composition of lignin from different species. Note that the FA/G is only G in *Arabidopsis*. (c) Summary of lignin-carbohydrate interactions. Lignin mainly interacts with xylan instead of cellulose. (d) The 155 xylan-lignin cross peaks categorized by the lignin type and peak intensities.

5.2.3. Xylan With a Non-Flatten Conformation Binds Lignin

The lignin-binding capacity of xylan is found to be conformation-dependent. We measured a lignin-edited spectrum to selectively probe the interface between lignin and polysaccharide (Supplementary Figures 5.3 and 5.4). This challenging experiment is enabled by a 23-fold

sensitivity enhancement (Figure 5.4a) that is achieved using the Dynamic Nuclear Polarization (DNP) technique, which transfers polarization from electrons to NMR-active nuclei[23-25,177]. The lignin-bound polysaccharides contain xylan and part of the cellulose surface (Figure 5.4b). In these maize walls, xylan in 3-fold conformation constitutes less than one-third of all xylans but accounts for almost half of the lignin-bound xylans; therefore, 3-fold conformation facilitates xylan-aromatic interactions. In contrast, the 2-fold xylans are structurally polymorphic and lignin only binds subtypes b and c, whose signals are sandwiched between the flat conformer (type-a) and the 3-fold allomorph. Since the xylan ^{13}C4 chemical shift indicates glycosidic bond conformation, it shows that the flat ribbon structure of the 2-fold conformation is not favorable for binding the intrinsically disordered lignin polymer.

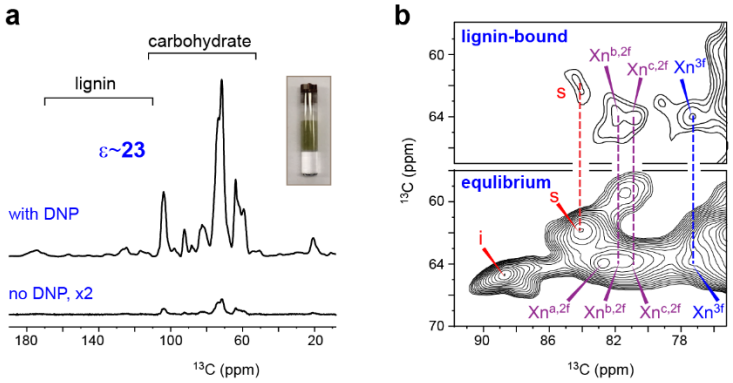

Figure 5.4. DNP reveals the conformational selectivity of xylan for lignin-binding. (a) DNP enhances the NMR sensitivity by 23-fold on maize. The inset shows a representative DNP sample. (b) Lignin-edited (top) and control (bottom) ^{13}C-^{13}C correlation spectra measured using DNP. The lignin-edited spectrum only shows polysaccharides spatially proximal to lignin, including 3-fold and a subset of 2-fold xylan (type b and c) and surface cellulose (s).

5.2.4. Lignin Self-Aggregates to Form a Highly Hydrophobic Domain

To probe the hydration profile of secondary cell walls, we have compared the intensities of water-associated molecules with those of the whole cell wall (Supplementary Figure 5.5). The relative intensities correlate with the extent of water retention and reveal a decreasing hydration gradient in the order: 3-fold xylan > 2-fold xylan ~ cellulose surface > cellulose internal chains >

lignin (Figure 5.5a). This experimental observation dovetails with a simulation reporting 50% faster diffusion for water molecules in lignin than those bound to xylan[178]. The distinctive hydration of lignin and 3-fold xylan excludes homogeneous mixing, instead suggesting proximity of separate domains: lignin nanodomains close to a well-hydrated matrix of 3-fold xylan (Figure 5.6). The hydrated matrix further connects the junctions of 2-fold xylan and surface cellulose[179], two molecules with comparable hydration (Figure 5.5a), thus bridging lignin with cellulose (Figure 5.6).

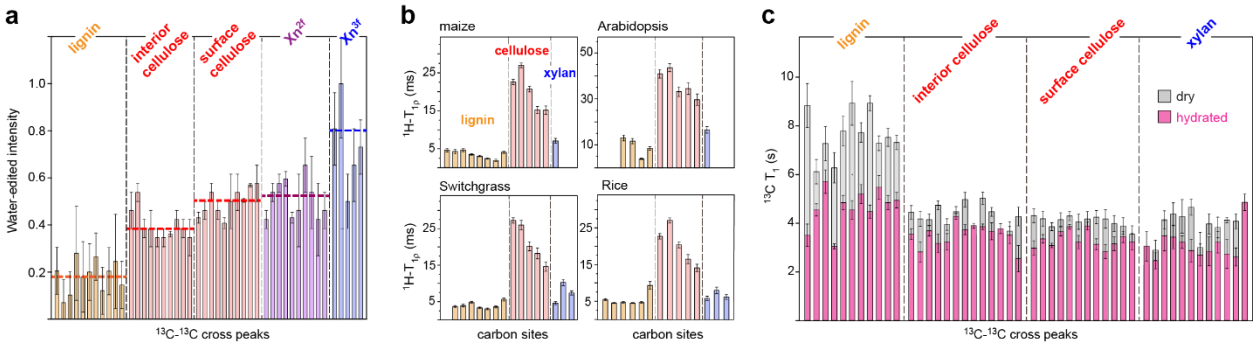

Figure 5.5. Lignin is highly hydrophobic and dynamically distinct from polysaccharides. (a) Water-edited intensities showing the hydration level of molecules in maize. Error bars are standard deviations propagated from NMR sensitivity. The hydration level decreases in the order of 3-fold xylan, 2-fold xylan, surface cellulose, interior cellulose, and lignin. (b) ^{1}H-T$_{1\rho}$ relaxation times of four plants detect molecular motions on the microsecond timescale. (c) ^{13}C-T$_1$ relaxation times of hydrated (magenta) and dried (grey) maize reflect nanosecond timescale motions. Distinct from the polysaccharide, lignin has long ^{13}C-T$_1$ but short ^{1}H-T$_{1\rho}$ relaxation. Error bars are standard deviations of the fit parameters. The x-axis corresponds to well-resolved cross peaks or carbon sites as tabulated in Supplementary Table 5.7-5.10.

Compared with primary cell walls[82], secondary walls have considerably weaker water associations, evidenced by 2-4 times slower ^{1}H polarization transfer from water to macromolecules (Supplementary Figure 5.6). The lignin and polysaccharide peaks in maize secondary cell walls only reached 20-30% of the equilibrium intensity within 4-ms ^{1}H mixing (Supplementary Figure 5.6). This water buildup rate is notably slower than in the primary cell walls of *Arabidopsis*, which, at 4-ms, exhibits as high as 60-80% and 30-40% intensities for pectins and cellulose,

respectively[82]. This can be attributed to the deposition of hydrophobic lignin, decreased water content[3], tighter packing of polymers, and lack of pectins with their water-stabilizing action. Tight packing also explains the unexpectedly large number of spatial contacts that are more prominent than those of highly porous primary cell walls[5,61].

5.2.5. Lignin and Polysaccharides are Dynamically Distinct

The domain separation of lignin and polysaccharide is confirmed by their distinct dynamics. Lignin has the shortest ^{1}H-$T_{1\rho}$ relaxation times of all wall polymers (Figure 5.5b) and its fast relaxation can be attributed to μs motions similar to the ring flips of protein tyrosine or phenylalanine sidechains[180] or the collective motions of multiple rings. Similar motions are not feasible in the hydrogen-bonded glucan chains of cellulose microfibrils, which exhibit the longest ^{1}H-$T_{1\rho}$ relaxation times. This trend is fully reversed for the ^{13}C-T_1 relaxation, with the longest times for lignin, ~5 s for hydrated sample and 8 s for dried materials (Figure 4.5c), indicating that aromatics resist rapid local reorientation on the ns timescale. In contrast, the ^{13}C-T_1 relaxation is markedly shorter for all polysaccharides due to efficient spin diffusion across the tightly packed polysaccharides. These dynamical heterogeneities support the concept of inhomogeneous mixing on the nm scale. The aromatic rings exhibit pronounced μs motion, thus are unlikely to adopt the partial alignment observed in woods using Fourier-Transform Infrared (FTIR) and Raman spectroscopy[94,181]. In addition, lignin contains both rigid and mobile components (Supplementary Figure 5.7, 5.8), indicative of the coexistence of aggregated rings and polysaccharide interfaces.

The fact that pronounced ^{13}C-T_1 differences between lignin and carbohydrates still exist in dehydrated samples suggests a large domain size far beyond the reach of relayed spin diffusion, a process that reduces relaxation heterogeneity for molecules within a few nanometers. Therefore,

lignin domains may be as large as a few to tens of nanometers across so that the unique characteristics of motion and hydration can be fully retained.

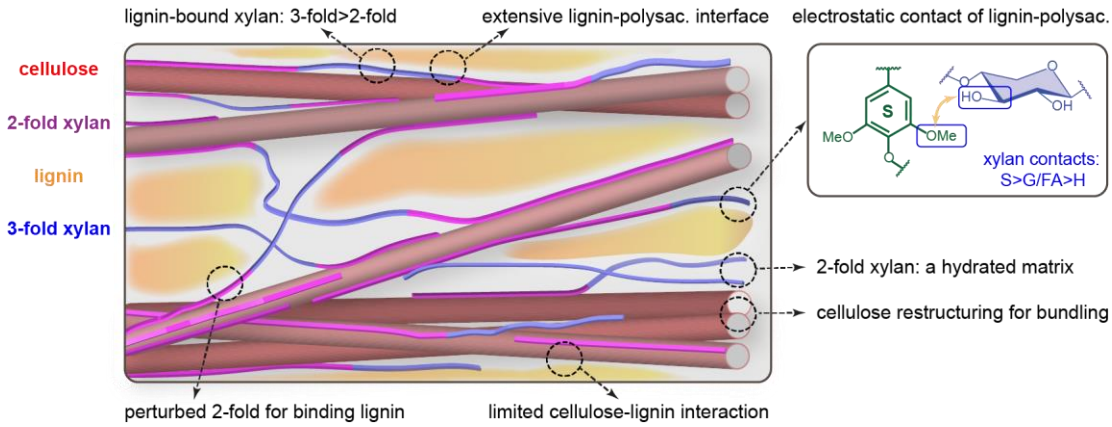

Figure 5.6. A revised model of lignin-polysaccharide packing and secondary cell wall architecture. Cellulose microfibrils, 2-fold and 3-fold xylan, and lignin are depicted in red, purple, blue and yellow, respectively. The secondary cell wall adopts much tighter packing than the primary cell walls, and the two hydrophobic cores of lignin and cellulose are bridged by xylans in a conformation-dependent manner. The key findings of this study have been annotated in the model. Polysaccharides are abbreviated as polysac. The depiction may not be to scale.

5.3. Discussion

This study provides heretofore unavailable molecular evidence to define the 3D architecture of secondary cell walls. The exceptional resolution and sensitivity of ssNMR and DNP, assisted by a novel experiment for analyzing the lignin-carbohydrate interface, allow us to identify 234 intermolecular cross peaks that pinpoint the packing interactions, 325 relaxation curves that probe polymer mobilities on microsecond and millisecond timescales, and 62 site-specific hydration data (Supplementary Tables 5.3-5.10). This large dataset markedly alters the paradigm for lignocellulose structure. The two hydrophobic cores of lignin and bundled cellulose are bridged by xylan in a conformation-dependent manner (Figure 5.6): the dehydrated 2-fold xylan with a flat-ribbon structure coats the microfibril surface[63] and the remaining, well-hydrated xylans with uneven conformations connect the lignin nanodomains via extensive interfaces, along which electrostatic interactions occur between lignin methyl ethers and sugar polar groups. This

well-defined boundary between aromatics and polysaccharides validates the modeling results in which lignin and xylans tend to self-aggregate to form separate phases, between which only limited interpenetration can happen[178].

The numerous cross peaks between xylan and lignin, and between different carbon sites, mainly represent through-space, sub-nanometer contacts rather than covalent linkages. In fact, the lack of through-bond correlations between the arabinose sidechains of xylan and the ferulate lignin in the INADEQUATE spectrum (Figure 5.1a, f) refines the hypothesis that xylan sidechains are crosslinked to lignin via ferulate or diferulate residues[182,183]. Such covalent bonding may only occur at limited spots, well below the detection limit of ssNMR. The abundant noncovalent interactions documented here predominate the physical interactions between xylan and lignin.

Pectin has also been assumed to be covalently connected to lignin via ester or ether linkages and bridge the lignin to hemicellulose[184]. Pectin has also been proposed to play a crucial role in lignification, especially in the initiation steps, as evidenced by biomimetic polymerization process of coniferyl alcohol in pectin solutions[185-187]. The intact stems analyzed here only contain a minor fraction of pectic substances and we have not identified any lignin-pectin cross peaks. Therefore, the proposed covalent linkages between lignin and pectin are scarce, if they exist, or only happening at the early stage of lignin deposition. These two molecules are not extensively co-localized within the sub-nanometer scale in the mature plant stems.

The structure that emerges from this ssNMR study differs substantially from contemporary views of complex lignocellulose in four aspects. First, lignins are found to bind mainly xylans rather than cellulose. For decades, lignin has been considered as the glue that connects cellulose microfibrils with hemicellulose[188]. The minor cellulose-lignin interactions observed here largely discounts previous models in which cellulose aggregates are proposed to be directly coated by

lignin[169] but rather suggests that lignin and cellulose are spaced and joined by xylan. Second, the phase-separation of lignin and xylan have revised an earlier model, where these two polymers are depicted to be well-mixed via entanglements and covalent linkage[170]. Third, we have emphasized the importance of electrostatic interactions over the hydrophobic contact, which is another possible mechanism proposed by simulation[174]. Finally, we have revealed, for the first time, that distorted xylan structure favors lignin-binding. This discovery, integrated with the previous finding that flat xylan conformers bind cellulose[10], has fully revealed the structure-function relationship for xylan and resolved how this versatile hemicellulose can bridge different molecules with diverse conformational structures. These novel molecular characteristics provide the structural basis for designing more digestible crops and further optimizing the biomass degradation process to facilitate the production of biorenewable energy. Similar approaches can be applied to biomasses from other plants and organisms.

5.4. Methods

5.4.1. Isotope Labeling and Preparation of Plant Materials

The uniformly ^{13}C-labeled stems (97% ^{13}C) of four plants were prepared by IsoLife (Wageningen, The Netherlands) using the following protocol. Briefly, uniformly ^{13}C-enriched (97 atom % ^{13}C) plant stems of maize (*Zea mays*; Age 2 months after sowing), rice (*Oryza sativa*; Age 7 months), switchgrass (*Panicum virgatum*; Age 3.5 months), and *Arabidopsis thaliana*, (ecotype Columbia-O; Age 1 months) were produced under identical growth conditions in custom-designed, air-tight, high-irradiance labelling chambers of the Experimental Soil Plant Atmosphere System. Plants were grown hydroponically under controlled environmental conditions: photosynthetic photon flux density 900 (700 for *A. thaliana*) µmol m^{-2} s^{-1} (top of plants), 16 h (*A.th.* 14 h) day length, day/night temperature 24/16 °C, RH 75%, in a closed atmosphere containing 97 atom% $^{13}CO_2$ (CO_2 enriched with the stable isotope ^{13}C; from pressurized cylinders, Cambridge Isotope

Laboratories) from germination till harvest. Minerals and water were supplied as a modified Hoagland-type nutrient solution with micronutrients[189] and iron as Fe(III)-EDTA[190], modified to contain a maximum of 25% of total N as ammonium, maintaining pH between 5 (maize: 4) and 6. At harvest, immediately after removing the plants from the growth chamber, plant shoots were dissected into leaves and stems, cut to 2-4 cm pieces, weighed, packaged in food-grade PE pouches, and stored at -30°C. After freeze-drying, representative subsamples were prepared for ^{13}C analysis by high-abundance isotope ratio mass spectrometry (IRMS; Stable Isotope Facility, UC-Davis, CA, USA). ^{13}C abundance of CO_2 in the chamber atmosphere was kept close to 97 atom% ^{13}C, continuously monitored during culture by non-dispersive infra-red detection. All the four plant samples were hydrated to ~40 wt % and 80-100 mg were sliced and packed into a 4 mm Bruker magic-angle spinning (MAS) NMR for ssNMR experiments. Around 30 mg of maize were packed into a 3.2-mm Revolution NMR rotor. Another 28 mg of maize was proceeded in DNP matrix and transferred to a 3.2-mm sapphire rotor for MAS DNP experiments as detailed below.

5.4.2. Solid-State NMR Experiments for Resonance Assignment

Solid-state experiments were conducted on a Bruker Avance 600 MHz (14.1 Tesla) spectrometer and a 400 MHz (9.4 Tesla) Bruker Avance spectrometer using 3.2-mm and 4-mm MAS HCN probes respectively. Most experiments except those with MAS-DNP were collected under 10-14 kHz MAS at 294-298 K. ^{13}C chemical shifts were externally referenced to adamantane CH_2 signal at 38.48 ppm on the TMS scale. Typical radiofrequency field strengths were 80-100 kHz for ^{1}H decoupling and hard pulse, 62.5 kHz for ^{1}H CP and 50-62.5 kHz for ^{13}C.

To assign the NMR signals of polysaccharides and lignin, 2D double-quantum (DQ) correlation spectra were recorded using the refocused CP J-INADEQUATE pulse sequence[25,36], which relies upon the scalar coupling between two ^{13}C nuclei to obtain through-bond information

regarding directly couple ^{13}C nuclei. A 2D ^{13}C-^{13}C correlation spectrum is also measured with 53-ms CORD mixing[157]. All the assigned ^{13}C chemical shifts of both polysaccharides and lignin have been summarized in Supplementary Table 5.2.

To analyze the lignin composition in four different plants, spectral deconvolution of the ^{13}C quantitative DP spectra was conducted using the software DMfit[191]. The peak area of the 159 ppm, 153 ppm and 147 ppm were assigned to the H4, S2/6 and the mixture of G3/4 and FA3/4/7, respectively (Supplementary Figure 5.1c). To convert the peak area into molar percentage, the carbon numbers of each peak and the residue multiplicity need to be considered. We have thus divided the relative intensity of S2/6 by 2, and the G3/4 and FA3/4/7 peak intensity by either 2 or 3 to account for the two extreme conditions. The resulting error margin was well below 3% for the H and S residues in all plants and below 5% for the G/FA residues.

The aromatic signals of lignin are typically difficult to analyze in solids due to the signal suppression caused by large chemical shift anisotropy. Here we employ a modified version of the standard proton-driven ^{13}C spin diffusion (PDSD) method that reintroduces ^{13}C-^{1}H dipolar coupling via a gated decoupling period to enhance lignin signals against the proton-rich polysaccharides (Supplementary Figures 5.3 and 5.4)[192]. A total dipolar dephasing period of 68 μs is employed to reintroduce ^{13}C-^{1}H dipolar couplings that selectively suppress the signals of protonated carbons. This dipolar dephasing period is asymmetric with respect to the π pulse in the Hahn echo, containing two undecoupled delays of 46 μs and 22 μs[193]. A 100 ms mixing period is applied to both the gated-PDSD and the standard DARR experiment. The standard DARR experiment better detects the protonated carbons due to the use of CP while the gated-PDSD preferentially detects the nonprotonated carbons. Adding these two spectra with the same number

of scans better presents the lignin signals due to the compensation of spectral asymmetry caused by the proton density heterogeneity in the aromatic motifs.

5.4.3. Solid-State NMR Experiments for Structural Determination

To determine lignin-carbohydrate interactions, 2D gated proton-driven ^{13}C spin diffusion (PDSD) experiments were measured on all four plant samples using 100 ms mixing time for detecting intramolecular cross peaks and 1 s for long-range intermolecular cross peaks. 74, 62, 59 and 39 intermolecular cross peaks have been identified for the rice, *Arabidopsis*, switchgrass, and rice, respectively. These 234 long-range cross peaks were categorized into 87 strong, 68 medium and 79 weak cross peaks according to the relative area of each single cross peak within a whole 1D ^{13}C cross-section. For the 74 cross peaks in maize, they include 26 strong, 24 medium and 24 weak cross peaks. The intensity cutoff is set to >5.0% for strong restraints, 2.5-5.0% for medium restraints, and <2.5% for weak restraints (Supplementary Table 5.3-5.6). This strategy has been recently employed to determine the structure of fungal cell walls[14]. These structural restraints, together with the lignin-edited spectra measured using MAS-DNP, provide site-specific information of the cell wall packing.

To determine the site-specific hydration of lignin and polysaccharides, we conducted the water-edited 2D ^{13}C–^{13}C correlation experiment (Supplementary Figure 5.4c)[82,194], which generated 62 hydration restraints. This experiment uses a ^{1}H-T_2 relaxation filter of 0.71 ms × 2 to suppress the polysaccharide signals to less than 2% but retains 75% of water magnetization. The water-polarization is further transferred to spatially proximal polysaccharides using a 2.25-ms ^{1}H mixing period and a 1 ms ^{1}H-^{13}C CP for ^{13}C detection. A 100-ms DARR mixing period is used for both the water-edited spectrum and the control 2D ^{13}C-^{13}C correlation spectrum showing full intensity. Both the control and water-edited 2D spectra are plotted with normalization to the worst

hydrated iC4-iC6 cross peaks at (89, 65 ppm). Both spectra are plotted using a bottom level that is set to 20% of the iC4-iC6 peak height, a level increment for multiplication of 1.2 and 28 contour lines. The intensity ratio between the 2D water-edited spectrum and the control spectrum is quantified, which is further normalized by that of the $Xn^{3f}2/3$-4 cross peak with the highest water-edited intensity (Supplementary Table 5.7). The 2D spectra are processed using QSINE window function (SSB 2.5) for the polysaccharide region and Gaussian Multiplication (LB, GB: -30, 0.03) for the lignin region. A series of 1D water-buildup curves are also measured using a ^{1}H-T_2 relaxation filter of 1 ms × 2 and a ^{1}H mixing period that varies from 0.1 μs to 100 ms to obtain the water-to-polysaccharide/lignin buildup curves.

To systematically determine the molecular mobility, we have generated 325 relaxation curves (Supplementary Table 5.8-5.10) by measuring 1D/2D ^{13}C spin-lattice (T_1) relaxation and ^{1}H rotating-frame spin-lattice relaxation ($T_{1\rho}$) relaxation at 298 K under 10 kHz MAS on the 400-MHz spectrometer. The ^{1}H- $T_{1\rho}$ is measured using a 62.5 kHz for spin-lock. The ^{13}C-T_1 is measured using both the standard inversion recovery and the z-filter versions[195]. The inversion recovery experiment is measured using a long recycle delay of 30 s, thus providing quantitative detection of all molecules. The Torchia T_1 measurement is CP-based, thus preferentially probes the rigid molecules. Furthermore, we have measured a series of 2D ^{13}C-^{13}C correlation experiment with a variable z-filter time to probe the ^{13}C-T_1 relaxation with enhanced resolution (Supplementary Figure 5.4d)[160]. For the dried sample, 9 of 2D spectra were measured using z-filter times of 0, 0.1, 0.4, 1, 2, 3.5, 5, 7.5 and 10.5 s, and the total experimental time is 89 hours. For the hydrated sample, 7 spectra were measured using z-filter times of 0, 0.1, 0.4, 1, 2, 3.5 and 5.5 s, and the total experimental time is longer, 118 hours, due to an increase in the number of scans. The intensity of

each cross peak in the 2D spectra was quantified and plotted as relaxation curves. These data were fit using a single exponential decay function to obtain the site-specific relaxation times.

The dynamical profile of cell wall components is also examined using a series of one-dimension (1D) ^{13}C spectra measured using four different methods on a 600 MHz spectrometer under 14 kHz MAS. Refocused INEPT[28] were measured using a total polarization of 5.74 ms, which consists of two delays of 1.72 ms followed by two delays of 1.15 ms. 1D ^{13}C direct polarization (DP) spectra were measured using a 2 s recycle delay for the detection of dynamic components and a 40 s recycle delay to obtain quantitative detection of cell wall molecules. The difference spectrum was obtained by subtracting the 2 s DP spectrum from the 40 s DP spectrum with normalization by the number of scans, and this difference spectrum only reports rigid molecules. 1D ^{13}C cross polarization (CP) spectra were measured with 1-ms contact time, which preferentially improves the sensitivity of the rigid molecules.

5.4.4. MAS-DNP Sample Preparation

The maize stem sample was processed for MAS-DNP experiments[102,196,197]. The stock solution of AMUPol radical[198], the DNP matrix, was prepared using a solvent mixture of d_8-glycerol/D_2O/H_2O (60/30/10 Vol%) and a radical concentration of 10 mM. About 28 mg of the ^{13}C maize sample was impregnated into 60 µL of the AMUPol solution and grinded for 15-20 minutes to allow the radical to penetrate through the plant cell wall. 28 mg of well-hydrated plant sample was then transferred into a 3.2-mm sapphire rotor. The NMR sensitivity has been enhanced by 23-fold with and without microwave irradiation. The lignin has shorter DNP buildup time (2.1 s) compared with polysaccharides (3.7 s), indicating a better association with the paramagnetic radicals. Three possible reasons might account for this preferential binding: 1) radicals may be better trapped in the aromatic network of lignins during the hand grinding of biomass in DNP

matrix; 2) the polysaccharide cores are so tightly packed that the radicals, with the largest dimension of ~13 Å[198], cannot effectively penetrate through; 3) the lignin-coating on the carbohydrate cores substantially decrease the surface-to-volume ratio of polysaccharide complex, which also explains the decrease in polysaccharide accessibility upon lignin deposition.

5.4.5. MAS-DNP Experiments

The DNP experiments were carried out on a 600 MHz/395 GHz MAS-DNP spectrometer using a 3.2 mm probe under 10 kHz MAS frequency. The cathode currents of the gyrotron were 120 mA and the temperature was 104 K with microwave on. The gyrotron microwave source was equipped with a shutter to program the duration of microwave irradiation during the experiments[106].

With the sensitivity enhancement from DNP, we are able to design a novel spectral editing experiment that combines dipolar and frequency filter to achieve clean selection of the aromatic signals of lignin over the signals (Supplementary Figure 5.4b), the highest peak of which is 270 times higher than lignin peaks (Supplementary Figure 5.3d-g). The microwave is on during the recycle delay and the CP excitation but turned off by the shutter after CP to prevent repolarization of the dominant signals. A short recycle delay of 2.7 s is also applied to further enhance the lignin signals over the polysaccharides that have a longer DNP buildup time of 3.7 s. The selected lignin polarization is transferred to polysaccharides using a 0.5-s PDSD mixing period and the signals of these lignin-proximal polysaccharides are detected as a 2D ^{13}C-^{13}C correlation spectrum with 20-ms PDSD mixing. The carrier frequency was set to 153 ppm for dipolar and frequency filters but changed to 114 ppm during the t_1 evolution and t_2 detection. A control spectrum with 20-ms PDSD is also measured for comparison. The DNP measurement time is 41 h for the lignin-edited 2D and 2 h for the control spectrum.

CHAPTER 6. CARBOHYDRATE-AROMATIC INTERFACE AND MOLECULAR ARCHITECTURE OF LIGNOCELLULOSE

6.1. Introduction

With solar energy and carbon dioxide transformed into carbohydrate-rich cell walls, terrestrial plants constitute eighty percent of the biomass distributed in the biosphere[199]. The secondary cell wall is a lignocellulosic composite deposited once the cellular expansion has ceased, which has evolved into a major source of biopolymers and biofuels[50,200]. Lignification mechanically strengthens secondary walls, however, the presence of these intractable polyphenols and their association with carbohydrate components contributes to the biomass recalcitrance that renders the feedstock resistant to enzymatic hydrolysis during its conversion to liquid transportation fuel[201,202]. To cost-effectively access structural polysaccharides for ethanol fermentation, vast efforts have been dedicated to tailoring plants to produce more digestible walls and optimizing deconstruction procedures in biorefineries[167,203,204]. These efforts have not yet reached the full potential due to our limited understanding of cell wall architecture.

The secondary cell wall is assembled by carbohydrate and aromatic constituents, with remarkable complexity and variability. Each elementary cellulose microfibril contains eighteen 1,4-β-glucan chains, which are held together by a hydrogen-bonding network[1,205]. The exact organization of these glucan chains is unresolved, but recent density functional theory (DFT) calculations suggest a six-layered organization, likely with 2, 3, 4, 4, 3, and 2 chains in each layer (Figure 6.1a)[206]. Elementary microfibrils frequently coalesce, forming large fibrils that often span across tens of nanometers[109,207]. Hemicelluloses, such as xylan, glucuronoxylan, arabinoxylan, and glucomannan, are highly variable in their monosaccharide composition and linkage pattern. Xylan is among the most found hemicelluloses, and its backbone comprises β-1,4-xylose units in a wide range of conformations, with substitutions by arabinose (Ara) or glucuronic acid (GlcA), and

modifications by acetyl (Ac) groups. Lignin contains guaiacyl (G), syringyl (S), and *p*-hydroxyphenyl (H) phenolic residues, which are interconnected by different types of covalent linkers such as β-O-4 ether-O-aryl, β-β' resinol, and β-5' phenylcoumaran[208,209].

Conceptually, the mechanical scaffold of crystalline cellulose is dispersed in a matrix formed by hemicellulose and lignin[3]. Our understanding of cell wall organization is supported by many studies that employed diffraction methods to reveal the spatial arrangement of cellulose microfibrils, imaging techniques to map out cell wall meshes and the microscopic distribution of lignin, and solution NMR spectroscopy to identify lignin-carbohydrate linkages[210-212]. However, the interface between lignin and polysaccharides, the focus of this study, is not yet well understood. This is partially due to the hardly accessible length scale (angstrom to nanometer) and the requirement of both chemical and atomic resolutions. In addition, only a small number of molecules reside on this lignin-carbohydrate interface, which needs to be deconvoluted from the bulk of the cell wall. As both lignin and polysaccharide exist in the solid state, conventional separation methods often perturb their structures and interactions, making it difficult to investigate this polymer interface.

Recently, multidimensional solid-state NMR spectroscopy of *Arabidopsis* and *Zea mays* (maize) has spotlighted a structure-function relationship of the molecules involved in the lignocellulosic interface[141,213]. Lignin tends to form hydrophobic and disordered nanodomains, the surface of which binds the xylan in a three-fold helical screw conformation (three sugar residues per helical turn: a non-flat structure; Figure 6.1a) through non-covalent interactions. The three-fold domain is connected to its two-fold flat-ribbon region, which is coating the smooth surface of cellulose microfibrils[8,10,18,63]. To generalize these structural principles, we need to examine other plant systems to evaluate three critical aspects: (i) the conformational bias of hemicellulose's

function, (ii) the absence of cellulose-lignin contact, and (iii) the self-aggregating nature of aromatic polymers.

The combination of solid-state NMR and DNP methods has allowed us to unveil the structural and chemical principles underlying the formation of lignocellulosic materials. We investigated the ^{13}C-labeled stems of two hardwoods, eucalyptus (*Eucalyptus grandis*) and poplar (*Populus x canadensis*), and the softwood spruce (*Picea abies*). These plants are non-food energy candidates for the development of second-generation biofuels to reduce our dependence on grain crops[214]. Despite lignin's preference for binding non-flat xylan, direct contacts are also observed between the aromatics and the junctions of cellulose surface and flat-ribbon xylan, which is probably enforced by molecular crowding. In these woody plants, molecules experience a highly homogeneous mixing on the nanoscale, which inevitably involves polymer interpenetration and entanglement. Consequently, the counter-intuitive hydration of aromatics is observed, where water is retained and stabilized by the polysaccharides closely packed to lignin. These molecular insights have brought our understanding of lignocellulose architecture to an unprecedented level of detail, allowing us to envision better biomass-conversion schemes for sustainable energy production.

6.2. Results

6.2.1. Polymorphic Structure of Carbohydrates in Woody Stems

We obtained ^{13}C-labeled plant stems by providing poplar, eucalyptus (gum tree), and spruce with $^{13}CO_2$. Free from chemical treatments, the hydrated lignocellulosic materials were directly analyzed using solid-state NMR. Therefore, all biomolecules have fully retained their chemical structure and physical packing. Atomic-level information of polysaccharide structure was obtained using two-dimensional (2D) ^{13}C-^{13}C correlation experiments (Supplementary Figure

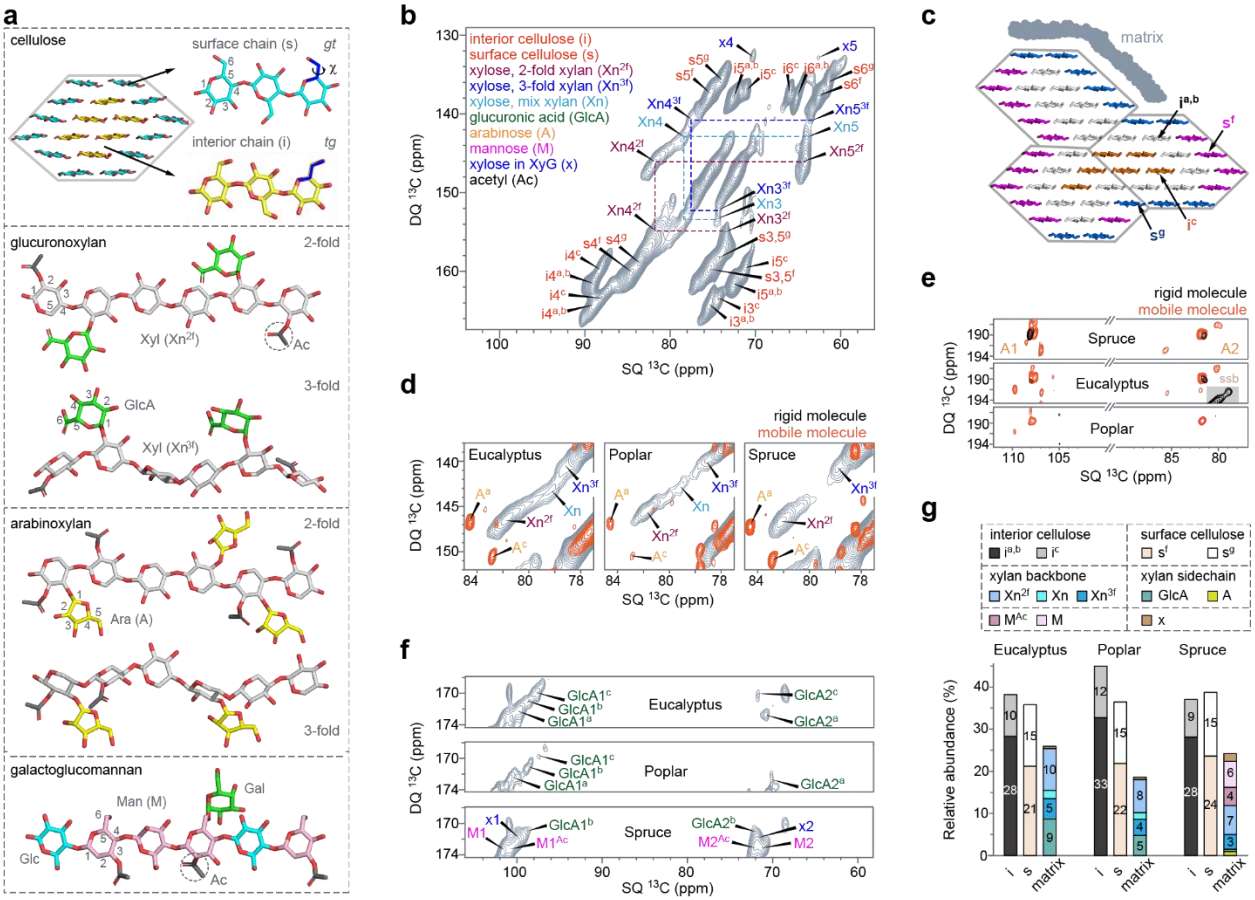

Figure 6.1. Solid-state NMR resolves the polymorphic structure of polysaccharides using intact wood cells. a) Representative structures of cellulose and major types of hemicellulose (xylan and galactoglucomannan). The cross-section of an elementary cellulose microfibril is shown, with a close view of an individual glucan chain and the hydroxymethyl conformation of surface (gauche-trans, gt) and internal (trans-gauche, tg) glucan chains. Xylan has two-fold or three-fold helical screw conformation in the backbone, with glucuronic acid (GlcA) or arabinose (Ara or A) sidechains. Acetyl motifs (Ac) are present in hemicelluloses. b) Representative 2D ^{13}C J-INADEQUATE spectrum of eucalyptus, which is based on ^{13}C cross polarization selecting rigid molecules. Dash lines track the carbon connectivity of xylan conformers. c) A model of three elementary cellulose microfibrils fitting the NMR observables. The hydrophilic (s^f) and hydrophobic (s^g) surfaces, the embedded chains (i^c), and the middle layer ($i^{a,b}$) are color-coded. d) Carbon-4 regions measured using ^{13}C direct polarization (orange spectra selecting mobile molecules) and cross polarization (grey spectra selecting rigid molecules). Both two- and three-fold xylan backbones are rigid while arabinose is mobile. e) Arabinose carbon-1 and carbon-2 regions. The only rigid arabinose is the terminal one in xylan sidechain. f) Eucalyptus has a high content of GlcA and spruce is rich in mannose (M). g) Composition of the rigid molecules in cell walls determined by peak volumes from 2D spectra.

6.1), which spotted 69 allomorphs of monosaccharide residues in three samples (Supplementary Tables 6.1 and 6.2).

These sugar units, with a wide range of linkages and conformations, were mainly found in cellulose and four hemicelluloses, including glucuronoxylan, arabinoxylan, galactoglucomannan, and a very low amount of xyloglucan (Figure 6.1a). The remarkable resolution is evidenced by the narrow ^{13}C linewidths of 0.5-0.9 ppm, which allowed us to inspect the multifaceted polymorphism of polysaccharide structures. Locally, the structural variation of cellulose happens to the glucose hydroxymethyl conformations defined by the O5−C5−C6−O6 (χ) torsional angle (Figure 6.1a)[98]. The surface (s) and internal (i) chains primarily and respectively adopt gauche-trans (gt, χ=+60°) and trans-gauche (tg, χ=180°) conformations[98], which resulted in well-resolved signals (Figure 6.1b). Upon bundling, the averaged structure of a fibril was restrained using the number of glucan chains residing in different environments, including the hydrophilic (s^f) or hydrophobic (s^g) surface, the inaccessible core (i^c), and the middle layer ($i^{a,b}$) sandwiched in between (Figure 6.1c)[22]. A satisfactory fit includes three elementary microfibrils, with 15, 12, 6, and 21 chains for the s^f, s^g, i^c, and $i^{a,b}$ forms, respectively. Assuming uniform interfibrillar association, this averaged structure only designates the minimal bundle size, without considering loose packing. Other arrangements disagree with spectral observables (Supplementary Figure 6.2).

Hemicellulose structure is highly complex as evidenced by the peak multiplicity. The backbones of hardwood xylan encompass two-fold (Xn^{2f}), three-fold (Xn^{3f}), and mixed (Xn) conformations (Figure 6.1d). The mixed form is absent in spruce; therefore, softwood xylan has higher homogeneity. Xylan was found to be rigid, suggestive of a close association with the stiff cellulose microfibrils. This observation differs from previous findings in *Arabidopsis*, where three-fold xylan remained mobile due to its spatial separation from cellulose[10]. Four types of arabinose

(A) signals were identified, likely induced by the varied linkage sites at carbon 1, 2, 3, and 5 (Figure 6.1e). Only a single type is partially rigid, which is attributed to the terminal arabinose of xylan sidechains in secondary cell walls, whereas the mobile ones are from pectic polymers in primary walls. Hardwoods showed a high content of glucuronic (GlcA), while the softwood spruce exhibited unique signals of mannoses (M), one of the major constituents of galactoglucomannan (Figure 6.1f)[161].

Analysis of the spectral intensities led to the molar composition of rigid polysaccharides (Figure 6.1g). Around three quarters (74-81%) are cellulose, making it the most abundant polymer in woody stems (Supplementary Table 6.3). Xylan makes up 18-26% of hardwood polysaccharides. Spruce has equal shares of xylan and mannan, each accounting for 10-12%. Consistent across these samples, the amount of two-fold xylan has doubled that of the three-fold counterpart, likely due to their promoted interactions with cellulose. Xylan sidechains are predominantly GlcA (therefore, glucuronoxylan) in hardwoods but mainly Ara (that is, arabinoxylan) in spruce.

6.2.2. Complex Structure and Linkage of Lignin

Wood lignin mainly contains guaiacyl (G) and syringyl (S) residues, with a single and two methoxyl groups, respectively (Figure 6.2a, b). The unsubstituted ring, *p*-hydroxyphenyl (H), was not observed in solid-state NMR spectra due to its low abundance in these plants. The aromatic signals are dispersed over an extensive range of chemical shifts. For instance, four types of S/S' residues and four forms of G units were identified in eucalyptus and spruce, respectively. The multiplicity should be triggered by the varied oxidation states (for example, S' is a Cα-oxidized form of S unit), the assorted linkages, and presumably, the wide-ranging conformation and packing in native solids.

Aromatic rings are interconnected by a diverse array of covalent linkers. For example, β-ethers (A), with a characteristic one-bond cross peak between carbons β and γ at (85, 59) ppm (Figure 6.2a), have the β-O-4 linkages that are readily cleavable during degradation. Other signals emerged from resinol (B) that has β-β connections, phenylcoumaran (C) that encompasses β-5 and α-O-4 linkages and spirodienone (E) that contains β-1 and α-O-α links (Figure 6.2c). These signals are detectable by two experimental schemes based on ^{1}H-^{13}C cross polarization (CP) and ^{13}C direct polarization (DP) methods, indicating the distribution of these linkers in the rigid and mobile phases of lignin (Supplementary Figure 6.3). Despite the low intensity, we managed to detect several cross peaks between these linkers and aromatic carbons (Figure 6.2a). For example, the connection between the carbon α of β-ethers and the carbon 1 of S residues yielded a cross peak at (72, 135) ppm in eucalyptus and poplar. Similar correlations were also found between the carbon 1 of S residues and the carbon α of B and E linkers. In spruce, analogous connections were observed for G units. These junctions typically evade solution-NMR characterization because the aromatic carbon 1 of lignin is non-protonated. These results demonstrated the feasibility of using solid-state NMR to characterize lignin structure and linkage, but the technical capability still requires further development.

Hardwood samples are rich in S residues (63-86 mol%) while the softwood only contains G units (Figure 6.2d). This observation agrees with our freshly collected solution NMR data of ball-milled and dissolved lignocellulose (Supplementary Figure 6.4 and Table 6.4), average S/G ratios found in the literature (Supplementary Table 6.5) as well as the quantification using deconvoluted 1D solid-state NMR spectra (Supplementary Figure 6.5 and Table 6.6). Both solid-state and solution NMR results (Figure 6.2e) suggest that these woody plants contain a large amount of β-ethers[215]. Solution NMR spectra also show considerable signals of both resinol and

phenylcoumaran in poplar and spruce (Figure 6.2e), while the phenylcoumaran peaks become very weak in eucalyptus[209,215-221]. Since these linkers respond differently to degradation, such analysis helps identify the plant candidates for saccharification.

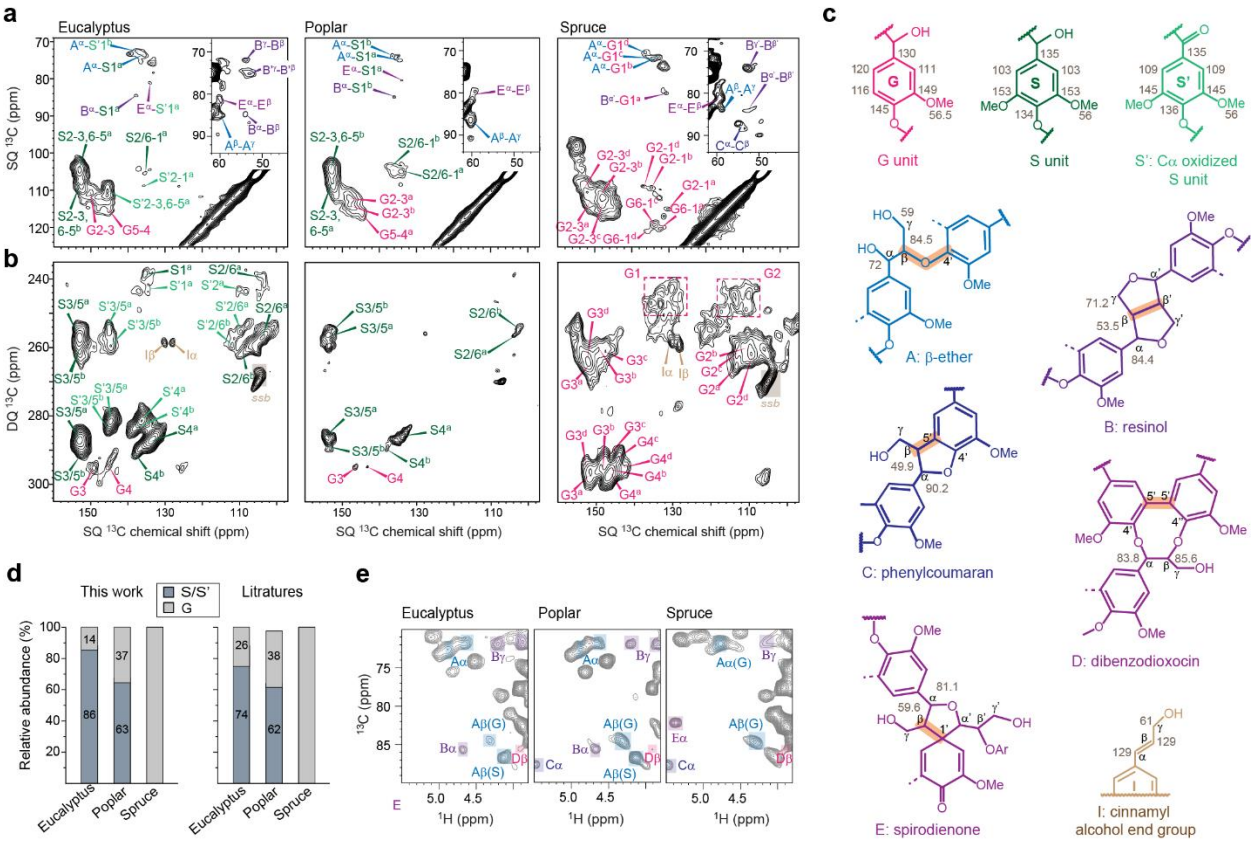

Figure 6.2. Chemical structure of lignin determined using solid-state and liquid NMR. Lignin signals are resolved using the aromatic regions of a) 2D ^{13}C-^{13}C RFDR spectra and b) 2D ^{13}C J-INADEQUATE spectra of intact plant cells of eucalyptus, poplar, and spruce. c) The structure of lignin units and linkages resolved in wood stems. The observed ^{13}C chemical shifts are labeled for each carbon site. Key inter-residual linkages are highlighted. d) Composition of lignin units quantified using the integration of one-bond cross peaks in 2D ^{13}C RFDR spectra (left panel) and using solution NMR as reported in the literature (right panel)[215,217,218,220,222-224]. Eucalyptus and poplar are S-rich while spruce is G-rich. Source Data files are provided. e, Molar fractions of the major linkage types quantified using the integration of one-bond cross peaks in 2D ^{13}C RFDR spectra. e) Representative lignin linkages detected by 2D ^{1}H-^{13}C HSQC spectra of ball-milled biomass in d_6-DMSO.

6.2.3. Distinct Patterns of Lignin-Carbohydrate Packing across Plant Species

The supramolecular architecture of lignocellulose differs dramatically in hardwood and softwood. In both eucalyptus and poplar, the use of a long-mixing period (1.0 s) in 2D ^{13}C-^{13}C

correlation spectra has generated many long-range intermolecular cross peaks that are absent in the short-mixing (0.1 s) spectrum (Figure 6.3a and Supplementary Figure 6.6). Puzzlingly, these two spectra showed a comparable pattern in spruce, which signified that ^{13}C magnetization was already equilibrated among polymers within 0.1 s. This is not caused by variations of spin diffusion coefficients or polymer dynamics in hardwood and softwood as validated experimentally (Supplementary Figures 6.7 and 6.8). Therefore, the rapid equilibrium observed in spruce indicates that lignin and polysaccharides are well-mixed on the nanoscale in spruce but stay apart in hardwoods.

The spatial association of polymers was pinpointed by 272 intermolecular cross peaks, each of which represents a sub-nanometer, physical contact between two carbons from different molecules (Figure 6.3b and Supplementary Figure 6.9). For example, the methyl carbon in the acetyl group of xylan (Ac^{Me}) exhibited cross peaks with the carbon 3 or 5 of S-lignin (S3/5) at (21, 153) ppm and with the carbon 3 of G-lignin (G3) at (21, 148) ppm (Figure 6.3b). These interactions happen between i) acetyl groups and lignin, ii) xylan and lignin, iii) acetyl and cellulose, iv) acetyl and lignin methyl, v) lignin methoxyl group and cellulose, and vi) different lignin residues (Supplementary Figure 6.10)[141].

switchgrass)[8], validating the principal role of xylan-lignin interaction in stabilizing lignocellulose. Mannan has a small number of resolvable sites; therefore, it only showed a few cross peaks with lignin. However,

the equilibrated pattern in Figure 6.3a supports a widespread association of mannan and lignin in

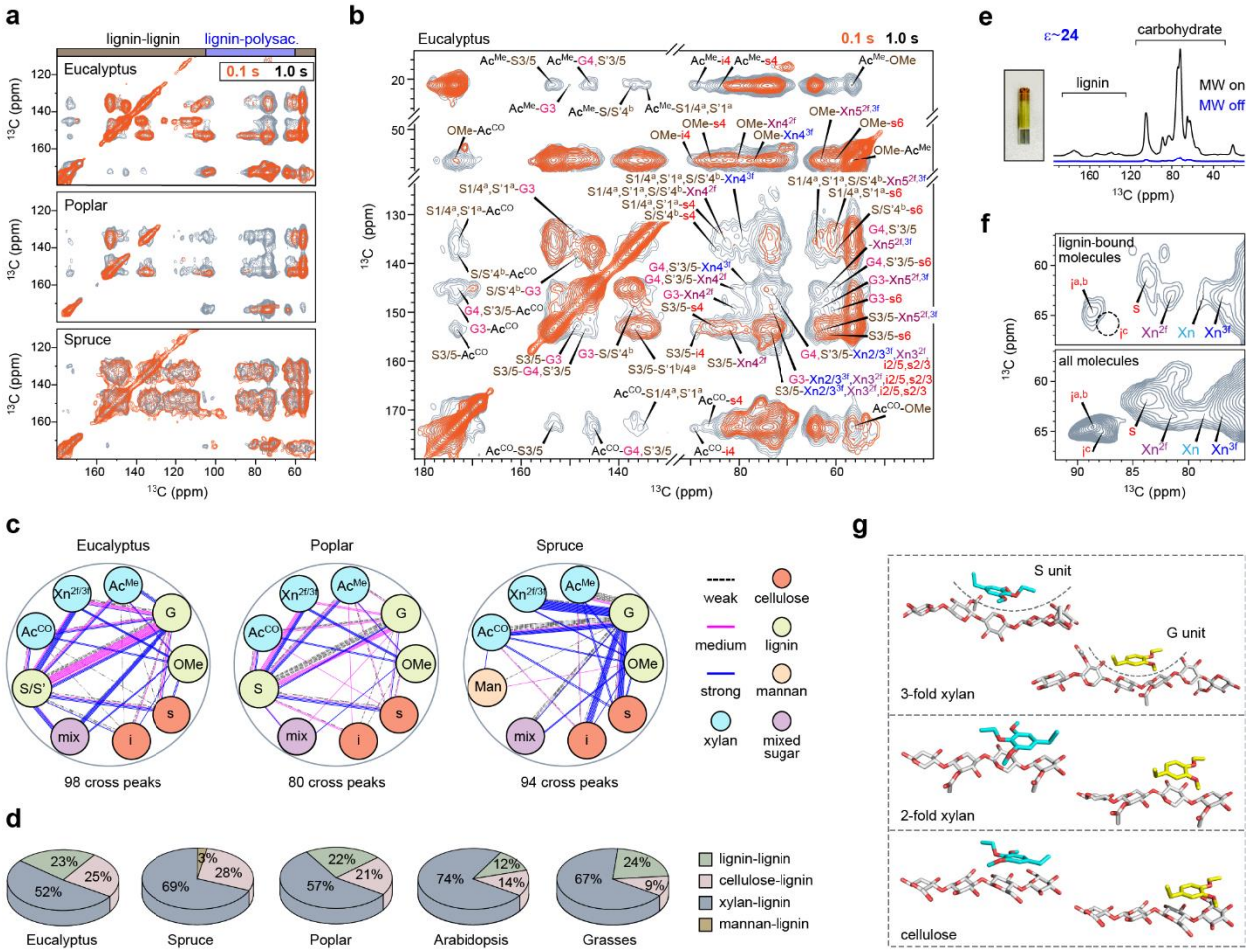

Figure 6.3. DNP-assisted detection of long-range interactions defines lignin-carbohydrate packing. a, Overlay of long-range (1.0 s mixing; grey) and short-range (0.1 s mixing; orange) 2D ^{13}C-^{13}C correlation spectra. The long- and short-range spectra showed similar spectral patterns in spruce: softwood polymers are homogeneously mixed on the molecular level. b, Dipolar-gated 2D ^{13}C-^{13}C correlation spectra showing 98 intermolecular cross peaks in eucalyptus. c, Summary of 272 intermolecular interactions identified in eucalyptus, poplar, and spruce. d, The count of lignin-lignin, cellulose-lignin, and xylan-lignin interactions in eucalyptus, poplar, spruce, *Arabidopsis*, and grasses (maize, rice, and switchgrass). Lignin-cellulose interactions are scarce in *Arabidopsis* and grasses but become abundant in woods. e, DNP enhancing NMR sensitivity of eucalyptus by 24-fold. Inset shows a picture of the plant material in a sapphire DNP-NMR rotor. f, Comparison of the equilibrium spectrum (bottom) of eucalyptus that detects all components with the aromatic-edited spectrum (top) that only shows lignin-bound molecules. The lignin-bound polysaccharides include the two-fold, three-fold, and mixed conformers of xylan as well as the surface and interior cellulose. The deeply embedded glucan chains in cellulose (i^c) are absent as highlighted using the dash line circle. g, DFT energy-minimized structures showing the possible packing between lignin units and polysaccharides.the equilibrated pattern in Figure 6.3a supports a widespread association of mannan and lignin in spruce.

A statistical view of the number and intensities of intermolecular contacts (Supplementary Tables 6.7-6.10) designated xylan as the major interactor with lignin, which is manifested by the extensive correlations between G/S and xylan carbons, including the carbonyl and methyl carbons of acetyl (Ac^{CO} and Ac^{Me}) and xylose ring carbons (Figure 6.3c). This result echoes with the recent findings in *Arabidopsis* and commelinid monocots (grasses, for example, maize and

Unexpectedly, wood lignin also exhibited extensive correlations with cellulose (Figure 6.3c), which accounts for 20-30% of all intermolecular cross peaks (Figure 6.3d). Such interactions are particularly abundant in spruce, consistent with the homogeneous mixing of molecules in this sample. In contrast, cellulose-lignin contacts only account for 9-14% of polymer interactions in *Arabidopsis* and grasses[8]. Thus, cellulose-lignin interaction is a unique feature of woody plants, which should contribute, at least in part, to the mechanical strengths of their stiff stems.

6.2.4. Visualization of the Polysaccharide-Lignin Interface

The unanticipated lignin-cellulose interactions were verified using the sensitivity-enhancing DNP technique[23,225,226]. The eucalyptus stem showed a 24-fold enhancement of NMR intensity (Figure 6.3e), which was achieved by transferring the polarization of electrons in the stable biradical AMUPol to the protons of biopolymers. This sensitivity enhancement shortens the measurements by 576 times (a 1.5-year experiment in a day), allowing us to take snapshots of the lowly populated boundaries between polysaccharides and lignin. Eucalyptus cellulose was found in the lignin-bound part of polysaccharides (Figure 6.3f), but such signals were missing in maize[8]. Only the surface glucan chains of cellulose (s) or those chains right underneath the surface layer ($i^{a,b}$) correlated with lignin, while the embedded core (i^{c}) lacked such interaction. The three-fold xylan (Xn^{3f}) is still favorable for binding lignin, showing stronger signals than the two-fold (Xn^{2f}) and the mixed (Xn) conformers.

Favorable lignin-polysaccharide interactions were revealed using quantum mechanical geometry optimizations conducted using the DFT method in continuum solvation models (Figure 6.3g). The three-fold xylan formed a packet to enclose aromatics. Conversely, the flat chains from cellulose surface or two-fold xylan relied on their pyranose/furanose rings to align with an aromatic unit. Examination of recently reported DFT structures[227] showed that S-units preferentially aligned to carbohydrate rings as stabilized by the two methoxyl groups on both sides of the aromatic ring (Supplementary Figure 6.11). The G unit, on the other hand, typically has its single methoxyl group closer to the carbohydrates. Such orientational preference supports the strong interactions experimentally observed between lignin methoxyl groups and xylan acetyls (Supplementary Figure 6.10). Consequently, the methoxyl-rich S-residues correlate better with xylan in space. Therefore, non-covalent interactions between these polar groups are essential to the existence of lignin-xylan complex.

6.2.5. Landscape of Biomolecular Hydration and Dynamics

Biopolymers have sophisticated dynamics and variable water-association in their native environments. Among the three plants, poplar turned out to be the worst hydrated sample as shown by its slowest water-to-polymer ^{1}H polarization transfer buildup curves, which were consistent for both cellulose and xylan (i4 and Xn^{3f}1, Figure 6.4a), as well as lignin (Supplementary Figure 6.12). The relative intensities (S/S_0) of a hydration heatmap reflect the degree of water association (Figure 6.4b and Supplementary Figure 6.13). Plots of the S/S_0 ratios against 127 carbon sites show that the hydration level increases sequentially from poplar to eucalyptus and spruce (Figure 6.4c). Within each sample, polymer hydration generally increases from cellulose to xylan, and then to mannan, if present.

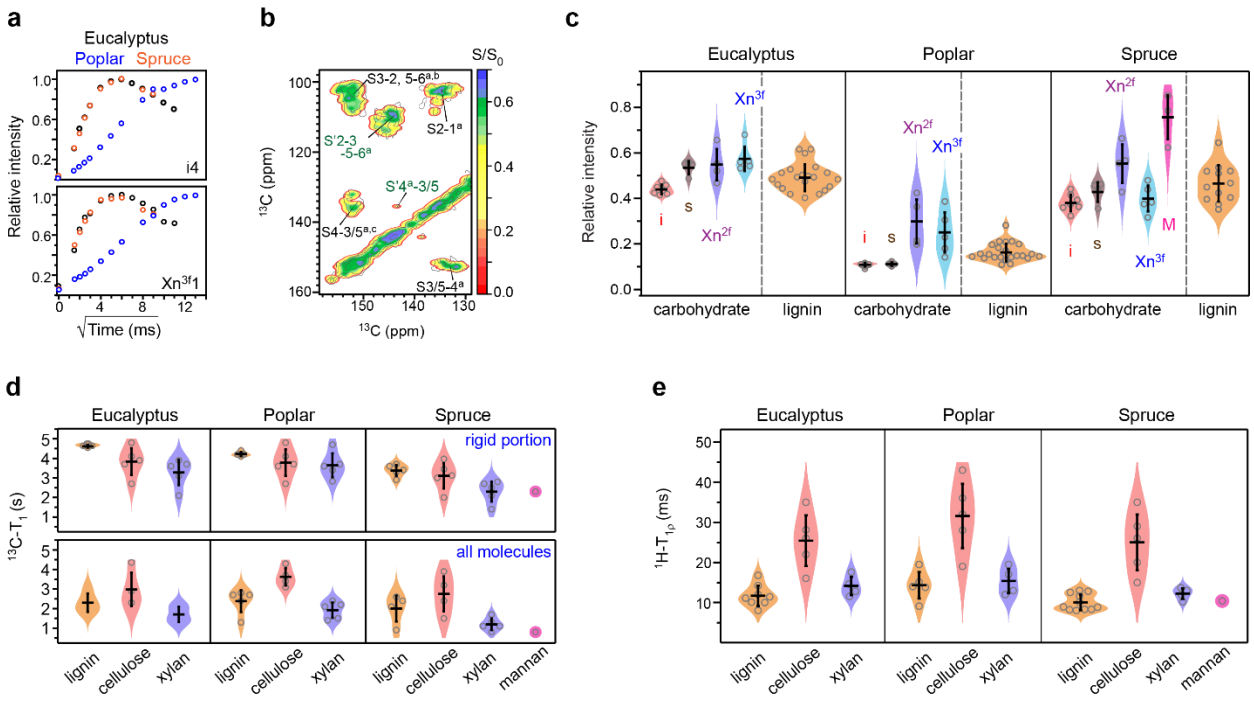

Figure 6.4. Site-specific hydration and dynamic landscape of biomolecules. a) Representative water-to-biomolecule ^{1}H polarization transfer buildup curves. The data of interior cellulose carbon 4 (i4) and three-fold xylan carbon 1 ($Xn^{3f}1$) are compared across plants. Poplar has slow buildup due to the limited water contact. b) Hydration map on top of a 2D spectrum plotting the ratio (S/S_0) of water-edited intensity (S) to the equilibrium intensity (S_0). A larger S/S_0 ratio indicates better polymer hydration. c) Distribution of the relative water-edited intensities (S/S_0) of polysaccharides and lignin in eucalyptus, poplar, and spruce. Molecules with better water retention show higher water-edited intensities. Poplar is poorly hydrated. d) ^{13}C-T_1 relaxation times of rigid (blue rectangles) and all molecules (colored as yellow, red, purple, and magenta for different molecules) in three woody plants, which represent nanosecond timescale motions. e) ^{1}H-$T_{1\rho}$ relaxation times reflecting microsecond timescale dynamics. The average value and standard deviation (error bars) are presented for each violin plot in panels c-e, the dataset of which are tabulated in Supplementary Tables 6.11-6.15.

Surprisingly, wood lignin retained high S/S_0 ratios, typically on the same range as those of xylan, indicating a high level of hydration (Figure 6.4c). This is intriguing because these aromatic polymers are perceived as relatively hydrophobic, which by expectation, should hinder water retention. For example, maize lignin was previously found to self-aggregate, forming nanodomains that are largely separated from water[8]. The water contact observed here should originate from lignin's tight association with those carbohydrates that kept water localized. Likewise, wood

biopolymers should experience frequent entanglement and interpenetration instead of domain separation.

Polymer dynamics were examined using ^{13}C-T_1 and ^{1}H-$T_{1\rho}$ relaxation measurements, which generated 150 relaxation curves (Supplementary Figures. 6.14 and 6.15). When all molecules were considered, the ^{13}C-T_1 relaxation time decreased in the order of cellulose, lignin, xylan, and mannan, if any (Figure 6.4d). The short ^{13}C-T_1 time constants of lignin and hemicellulose revealed the efficient ^{13}C-T_1 relaxation in these non-cellulosic polymers, and furthermore, their enhanced motion on the nanosecond timescale. Such differences became indistinguishable if only rigid molecules were focused on, for example, all rigid molecules of eucalyptus showed ^{13}C-T_1 time constants of 4-5 s. This observation contradicts previous results in which maize lignin showed substantially longer ^{13}C-T_1 than any polysaccharide[8]. This can be comprehended using the efficient spin-exchange between lignin and carbohydrates (mediated by the better molecular mixing), which has averaged the ^{13}C-T_1 relaxation times in wood. On the microsecond timescale, cellulose had the longest ^{1}H-$T_{1\rho}$ relaxation times (30-40 ms) due to the restricted motion in the massively hydrogen-bonded microfibrils (Figure 6.4e). Both lignin and hemicellulose had short ^{1}H-$T_{1\rho}$ times of 10-15 ms, like the counterparts in maize[8]. Compared to G residues, S units exhibited slower ^{1}H-$T_{1\rho}$ relaxation, indicating attenuated dynamics due to interactions with polysaccharides (Supplementary Figure 6.15). Among the three samples, spruce displayed the shortest ^{13}C-T_1 and ^{1}H-$T_{1\rho}$ relaxation times, revealing a unique profile of molecular dynamics in softwood.

6.2.6. Effects of Rehydration on Water-Retention and Polymer Dynamics

Water molecules are important for stabilizing the nanostructure of cell wall biomaterials, and the complete removal of water could potentially cause irreversible changes. In a recent NMR

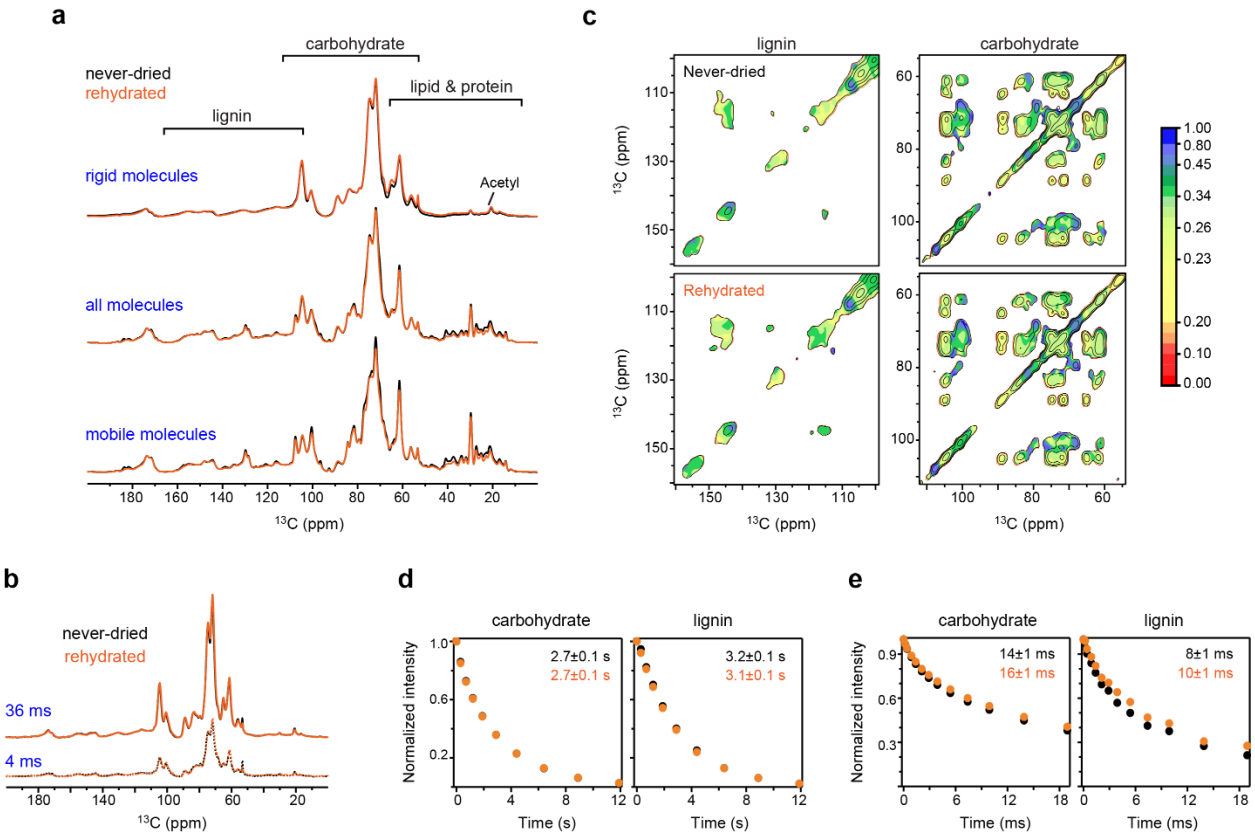

Figure 6.5. Molecular-level dynamics and water association after dehydration and rehydration. A never-dried spruce sample was first measured, and then freeze-dried and rehydrated for direct comparison. a) Overlay of spectra collected using never-dried (black) and lyophilized and then rehydrated (orange) spruce stem samples showing high similarity for polysaccharides and lignin. From top to bottom are the CP, quantitative DP, and short recycle-delay DP spectra. The key regions of lignin, carbohydrate, and lipid are marked. b) 1D water-to-carbohydrate polarization transfer spectra revealing similar water association for never-dried and rehydrated samples. The well-hydrated molecules are selected using a short ^{1}H mixing time of 4 ms while the equilibrated state is measured using 36 ms ^{1}H mixing. c) Water-edited 2D hydration map showing comparable water-edited intensities for both lignin and carbohydrate regions in the never-dried and the rehydrated samples. d) Average ^{13}C-T_1 relaxation plot, using the integrals of spectral regions for carbohydrates (left) and lignin (right). e) Average $T_{1\rho}$ relaxation of carbohydrates and lignin in never-dried (black) and rehydrated (orange) samples. Error bars are standard deviations of the fitting derived parameters.

study of the softwood *Pinus radiata*, oven-drying (for complete dehydration) and rehydration were found to promote polymer association (e.g. xylan-cellulose and lignin-cellulose packing) and irreversibly alter the dynamics and conformation of mannan in the secondary cell walls[228]. Similarly, the lyophilized-rehydrated grass sorghum (*Sorghum bicolor* L. Moench) has shown

permanent changes of hemicellulose, with enhanced mobility for the three-fold xylan backbone and some arabinose residues[162]. Differently, dehydration only caused reversible structural changes to the primary cell walls of *Arabidopsis*, likely due to the high content of pectic polymers that can efficiently associate with water molecules[229].

We measured the never-dried samples of spruce and eucalyptus, followed by re-examination of the same materials after lyophilization and rehydration. In spruce, the lignocellulosic complex was not dramatically affected by the rehydration process, which differs from lipids and proteins (Figure 6.5a). The structure of the carbohydrates and lignin, as well as their distribution in dynamically distinct domains, can be efficiently retained in the rehydrated biomass, occasionally with minor intensity variations that are well below 10% for each carbohydrate or lignin carbon site (Figure 6.5a). The retention of water molecules can also be fully restored, as shown by the identical spectral patterns in 1D water-edited spectra (Figure 6.5b) and the comparable 2D heatmap representation for both carbohydrates and aromatics in the never-dried and rehydrated samples (Figure 6.5c). The nanosecond-timescale motion and the subnanometer polymer packing (reflected by spin-exchange) are unaffected since there is no deviation of ^{13}C-T_1 relaxation within the well-controlled error margin (Figure 6.5d). Both lignin and carbohydrates showed a 10-20% increase in the ^{1}H-$T_{1\rho}$ relaxation time constants; therefore, the only notable change happened to the microsecond scale motions of biopolymers (Figure 6.5e). Eucalyptus behaves differently: this plant fully restored the structural and dynamical features but moderately improved polymer-water association after rehydration (Supplementary Figure 6.16).

6.3. Discussion

The abundant molecular-level evidence presented four novel features of lignocellulosic materials, each exploring a structural or chemical foundation of the supramolecular architecture

(Figure 6.6). First, even though three-fold xylan is favored for binding lignin, in wood, other xylan conformers can also coexist with lignin in part. Accompanying with this functional resemblance is the hydration equivalence of these xylan forms (Figure 6.4c). These results have extended the conceptual model of lignocellulose derived from maize, in which lignin mainly interacts with the three-fold xylan, and *vice versa*. Actually, interactions between three-fold xylan and cellulose have been reported in a grass *Sorghum*[162], which also implies the interchangeable roles of xylan conformers. Uniquely, wood xylan is mainly in two-fold helical screw, which is energetically unfavorable unless forced by the binding to cellulose surface. Therefore, the unanticipated proximity of lignin to the two-fold xylan, as well as its associated cellulose surface, might be a destined consequence of spatial crowding in densely packed lignocellulosic materials.

Second, the packing between cellulose and lignin is plant-specific and only serves as a secondary interaction. In *Arabidopsis* and grasses, lignin and cellulose are spatially separated[8]. The situation has changed for woody biomass, where lignin and cellulose become colocalized. Although *Arabidopsis* is widely used as a model system for investigating the biophysical traits of hardwoods, it becomes apparent that these plants differ in their cell wall organization. Our DFT results and a recent molecular simulation study[230] consistently suggest that lignin is mainly docked on the hydrophobic surface of cellulose, with aligned phenyl and pyranose rings. The increased coverage of cellulose surface by aromatic polymers might reduce enzyme accessibility and contribute to biomass recalcitrance.

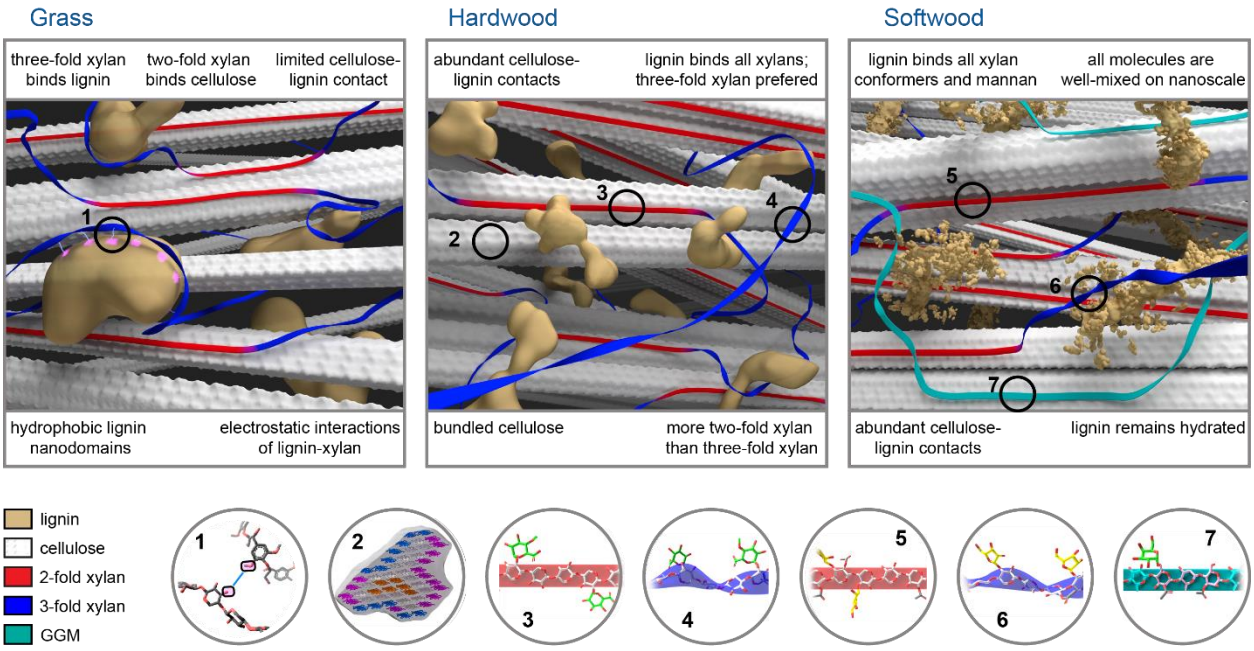

Figure 6.6. Comparative schemes of secondary cell walls in grass, hardwood, and softwood. The figure shows the spatial arrangement of lignin (yellow), cellulose (white fibrils), two-fold xylan (red flat ribbons), three-fold xylan (blue twisted ribbons), mixed forms of xylan (magenta), and mannan (GGM; green) in secondary plant cell walls. Numbered spheres highlight the structural features of (1) lignin-xylan interaction in all plants, (2) cellulose bundles in woody plants, (3-6) twofold and threefold xylan with different sidechains, and (7) galactoglucomannan. The molecular fraction of polysaccharides is considered in the depiction, but the illustration may not be strictly to scale. The model of grass cell wall is generated using the data recently reported[8], for comparison with the models of woody plants. Lignin and carbohydrates are much better mixed in woody plants than in grass, resulting in the binding of lignin to both three-fold and two-fold xylan as well as to cellulose microfibrils. The structural assembly of woody cell walls is thus different from the domain-separation scheme of grass cell walls.

Third, the structural feature of aromatic polymer needs reconsideration. Lignin nanodomains observed in maize are absent in woody plants due to the promoted polymer mixing on the nanoscale (Figure 6.3). Accordingly, polymer entanglements and inter-penetration, rather than superficial contact between domain surfaces, should govern lignin-carbohydrate interactions in wood[170]. Once well-mixed with polysaccharides, even the aromatics could effectively retain and immobilize water molecules (Figure 6.4c). The thermodynamical driving force of this peculiar phenomenon awaits inputs from modeling methods.

Finally, the ultrastructure of softwood is featured by homogeneous molecular mixing (Figure 6.3a). This structural hallmark has revised the prevailing model in which well-aligned and partially crystalline glucomannans were perceived as being sandwiched between an internal cylinder of cellulose microfibrils and an outside tubular domain of lignin, with xylan forming an outermost layer[169]. Actually, our results better align with a recent study reporting that glucomannan and xylan could potentially associate with both cellulose and lignin[161].

Although the focus of this exploratory study is to understand the chemical and physical principles underlying polymer packing and lignocellulose architecture, the structural foundation and methodology established here would inspire more in-depth investigations for understanding the structural diversity and mechanical properties presented by numerous plant species and mutants, various cell types, and different growth stages[231]. These structural insights will guide the utilization of forestry resources for the production of biomaterials and biofuels[232], and the spectroscopic toolbox will stimulate structural investigations of polymer assemblies in other organisms, such as bacteria, fungi, and algae, as well as bio-inspired materials[14,233-240].

6.4. Methods

6.4.1. Plant Material.

Uniformly ^{13}C-enriched stems (97% ^{13}C) of eucalyptus (*Eucalyptus grandis*; age 16 weeks), poplar wood (*Populus x canadensis*; 27 weeks), and spruce (*Picea abies*; 16 weeks) were obtained for structural characterization from IsoLife (The Netherlands). Eucalyptus and spruce were obtained from seeds while poplar was obtained from stem cutting. Poplar plants were saplings of close to 1 m height at harvest. Immediately after removing the plants from the growth chamber, plant shoots were dissected into leaves and stems. The stem-sections were split, cut, and debarked after freeze-drying. Debarking was strived to be complete, which was conducted through the

longitudinal cutting of the bark followed by separation from the xylem at the cambium interface. Debarked stems were hydrated for NMR analysis. The material was briefly hand-grinded using a pestle and a mortar, resulting in small pieces on the range of a few mm across. The homogeneity helps to avoid potential issues during magic-angle spinning. The technical details of isotope labeling are presented in the Supplementary Methods.

To test the effect of freeze-drying, we obtained never-dried ^{13}C-labeled spruce and eucalyptus wood from IsoLife, without lyophilization. The debarking process is finished manually by carefully removing the outside soft bark layer with tweezers. Around 104 mg of debarked spruce was cut into mm scale pieces, packed into 4-mm rotor, and measured under 10 kHz MAS on a 400 MHz Bruker NMR spectrometer. The never-dried samples were first measured freshly. After ssNMR measurements, overnight lyophilization was conducted, giving 43.5 mg of freeze-dried spruce stem. The sample is then sufficiently rehydrated (with a final weight of 107 mg), and all ssNMR experiments were conducted again on the rehydrated material for direct comparison with never-dried samples (Figure 6.5). Besides, never-dried (96 mg) eucalyptus stem, and the dehydrated and then rehydrated material (94mg including 68 wt% H_2O) were also examined (Supplementary Figure 6.16).

6.4.2. Solid-State NMR Experiments for Assignment.

The plant stems were packed into MAS rotors for measurements on 600 MHz and 400 MHz Bruker spectrometers using 3.2-mm and 4-mm MAS probes, respectively. Most experiments were collected under 10-14 kHz MAS at 293 K unless otherwise stated. ^{13}C chemical shifts were referenced to the tetramethylsilane (TMS) scale. Radiofrequency field strengths were 80-100 kHz for ^{1}H decoupling, 62.5 kHz for ^{1}H CP contact pulse, and 50–62.5 kHz for ^{13}C. The technical parameters of all solid-state NMR experiments were summarized in Supplementary Tables 6.16

and 6.17 for the initial batch of rehydrated samples, and in Supplementary Table 6.18 for the more recently obtained never-dried and the subsequent freeze-dried and rehydrated samples.

To assign NMR signals, 2D correlation spectra were recorded using the refocused CP J-INADEQUATE sequence[37], which was coupled with ^{13}C DP for detecting mobile molecules or ^{1}H-^{13}C CP for detecting rigid polymers. A 2D ^{13}C radio frequency-driven recoupling (RFDR) correlation experiment was measured under 10 kHz MAS and 83 kHz ^{1}H decoupling to assign intra-residue cross peaks[241]. A recoupling time of 1.6 ms was used to detect one-bond ^{13}C–^{13}C cross peaks. An additional set of ^{13}C-DP PDSD experiments were conducted to examine the structure of lignin in the mobile phase, which were selected through the short recycle delay of 2 s. The standard flow chart of resonance assignment is presented in Supplementary Figure 6.17. All chemical shifts are validated by comparison with literature-reported values (Supplementary Table 6.19).

To enhance aromatic signals, we measured a dipolar-coupling-gated version of the proton-driven spin diffusion (PDSD) experiment[8,192,193]. A dipolar-dephasing period of 48 μs was employed to efficiently suppress the signals of protonated carbons, allowing the preferential detection of non-protonated carbons in the aromatic lignin. This period was asymmetric with respect to the π pulse in the Hahn echo, containing two undecoupled delays of 32 μs and 16 μs. A 0.1-s PDSD mixing was used to report intramolecular cross peaks in all samples. A 20-ms mixing was also used for spruce. The observed chemical shifts were compared with values deposited in the Complex Carbohydrate Magnetic Resonance Database to facilitate resonance assignment[242].

6.4.3. Solid-State NMR Experiments for Structural Analysis.

The 2D gated PDSD experiment was also conducted to determine lignin-carbohydrate packing, with a long mixing time (1 s) for intermolecular polarization transfer. We have identified

98, 80, and 94 cross peaks for eucalyptus, poplar, and spruce, respectively. These 272 correlations were categorized as 112 strong, 75 medium, and 85 weak restraints according to their relative intensities (area of a peak relative to that of the 1D cross-section), with cutoffs set to >4.0% (strong), 2.0–4.0% (medium), and <2.0 (weak) as tabulated in Supplementary Tables 6.7-6.10. Polymer hydration was determined using water-edited 2D ^{13}C–^{13}C correlation experiment at 277 K (Figure 6.4 a, b)[82,243], which generated 44, 48, and 37 datasets for eucalyptus, poplar, and spruce, respectively. This experiment used a ^{1}H-T_2 relaxation filter of 120 μs × 2 to suppress the polysaccharide signals to <5% and retain >85% of water magnetization. Water-polarization was transferred to spatially proximal polymers using a 4-ms ^{1}H mixing period, followed by a 1-ms CP for ^{13}C detection. A 100-ms DARR mixing was used for both water-edited and control spectra. 1D buildup curves were measured at 277 K using a ^{1}H-T_2 filter of 120 μs × 2 and a ^{1}H mixing of 0-81 ms for spruce, 0-121 ms for eucalyptus, and 0- 169 ms for poplar.

To probe dynamics, we measured ^{13}C spin-lattice relaxation (T_1) and ^{1}H rotating frame spin-lattice relaxation ($T_{1\rho}$). ^{13}C-T_1 was measured using Torchia-CP [195] and standard ^{13}C DP inversion recovery schemes. Torchia-CP preferentially detected rigid molecules, with a z-filter of 0-12 s. A 30-s recycle delay was used in the DP inversion recovery experiment for quantitatively detecting all molecules, with a z-period of 0-35 s. ^{1}H–$T_{1\rho}$ was measured using an effective ^{1}H spin-lock field of 62.5 kHz with a duration of 0-19 ms. Relaxation data were fit using single exponential functions (Supplementary Tables 6.14 and 6.15). Also, the dipolar-chemical shift (DIPSHIFT) experiment[244] was conducted under 7.5 kHz MAS, to report dipolar order parameters of biopolymers in three wood samples. Frequency-Switched Lee Goldburg (FSLG) ^{1}H homonuclear decoupling sequence was utilized, the scaling factor was verified to be 0.577.

6.4.4. Solution NMR Sample Preparation and Experiments.

To validate the lignin assignment obtained using the solid-state method, we conducted solution NMR analysis, which has well-documented chemical shifts of lignin polymers. A summary of the lignin chemical shifts is included in Supplementary Table 6.4. Wood samples were ball-milled for 1 h with a motor running at 1750 rpm. About 30 mg of each powdered wood sample was dissolved in 10 mL DMSO-d_6 with constant stirring using a magnetic stirrer for 2 h at 60°C for solution NMR experiments. To identify linkages in lignin, we conducted 2D ^{1}H-^{13}C HSQC spectra conducted on a Bruker Avance III 500 MHz ^{1}H Larmor frequency and equipped with a 5 mm *z*-gradient Prodigy TCI probe. Both the ^{1}H and the ^{13}C chemical shifts gave indications of the linkage types using the chemical shifts reported previously[13,52,224,245-247].

6.4.5. MAS-DNP Experiment.

About 30-35 mg of eucalyptus stems were impregnated into 50 µL DNP matrix solution containing 10 mM AMUPol[198] radical in d_8-glycerol/D_2O/H_2O (60/30/10 Vol%). The material was softly ground for 10-15 min to allow radical distribution and packed into a 3.2-mm sapphire rotor. The NMR sensitivity was enhanced by 24-fold with microwave irradiation on a 600 MHz/395 GHz MAS-DNP spectrometer under 10 kHz MAS. DNP analysis has been applied to various carbohydrate and plant systems using different protocols[25,92,248]. Recently, we have demonstrated that the radical can effectively and homogeneously polarize all molecules in cell wall materials[249]. Lignin had a slightly shorter DNP buildup time (1.8 s) compared with polysaccharides (2.2 s). The recycle delay was set to 2.3 s to facilitate the selection of lignin against carbohydrates in the 2D experiments. A lignin-edited 2D ^{13}C-^{13}C experiment was measured to detect the signals of lignin-bound carbohydrates, with a 0.5-s PDSD mixing to transfer lignin polarization to carbohydrates,

followed by a 20-ms PDSD mixing for 2D ^{13}C-^{13}C correlation[8]. For comparison, a 20-ms PDSD spectrum was measured as a control.

6.4.6. DFT Calculation.

DFT calculations were used to investigate the interactions between the S or G units in lignin and cellulose, or xylan with two- and three-fold conformations. Tetramers of β-1,4-linked glucose and xylose were built to represent cellulose and two-fold xylan, respectively. Hexamers of β-1,4-linked xylose were built to represent three-fold xylan, based on a crystal structure of three-fold xylopentaose (PDB ID: 1GNY).[250] Six models were constructed: G unit-cellulose, G unit-xylan (two-fold), G unit-xylan (three-fold), S unit-cellulose, S unit-xylan (two-fold), and S unit-xylan (three-fold). Previously, it has been shown that for lignin-cellulose and lignin-xylan interactions, the stacked configurations tend to have the largest interaction energies[227]. Therefore, the initial starting configurations of the six models were constructed by positioning the G/S units parallel to the surface of the glucose/xylose residues, ~4 Å away. The geometry optimizations were conducted using the DFT method, M05-2X/6-31+G*[251] with the integral equation formalism for the polarizable continuum model (IEFPCM)[252] solvation model in Gaussian 09[253]. Although other methods may be available, this exchange-correlation functional with dispersion corrections performs reasonably well for carbohydrate and carbohydrate-aromatic interactions[206,254,255].

CHAPTER 7. MOLECULAR ARCHITECTURE OF FUNGAL CELL WALLS REVEALED BY SOLID STATE NMR

7.1. Introduction

Fungi are a group of eukaryotic microorganisms, some of which are capable of causing superficial infections or serious systemic diseases in humans. Superficial infections affect nearly a quarter of humans, but more importantly, invasive infections caused by fungi such as unicellular *Candida* species and filamentous *Aspergillus fumigatus* often result in fatality in individuals with immunodeficiency. To date, life-threatening fungal infections affect more than two million people worldwide, with an exceptionally high mortality rate of 20-95%[256]. As one of the most prevalent airborne fungi, *Aspergillus fumigatus* causes fatal invasive aspergillosis in more than 200,000 patients, including a quarter of all leukemia patients, with an overall mortality rate of 50% for patients with treatment and nearly 100% for those left untreated[47,257-260]. The high mortality rate is also coupled with a substantial rise in occurrence due to a fast-growing population with immunodeficiency and the wide application of immunosuppressive agents in medical treatments such as cancer therapy or organ transplantation.

Despite the above-described medical significance, effective antifungal agents remain very limited. Most available antifungals target ergosterols in the cell membranes and therefore are highly toxic to humans [261,262]. In addition, these antifungal drugs have limited efficacy. For example, Amphotericin B fails to prevent death in more than half of the patients with invasive aspergillosis[263]. Moreover, a substantial increase in drug resistance has been observed during the

---

This chapter was previously published as X Kang, A Kirui, A Muszyński, MC Dickwella Widanage, A Chen, P Azadi, P Wang, F Mentink-Vigier, T Wang, "Molecular Architecture of Fungal Cell Walls Revealed by Solid-State NMR" ", in *Nature Commununications*, July 16, 2018, copyright © 2018, The Authors. https://doi.org/10.1038/s41467-018-05199-0

last decades [260,262]. Recent efforts have been devoted to developing agents that bind to the fungal cell wall since the fungal polysaccharides are absent in human cells [264,265]. Echinocandins are such new compounds that disrupt glucan-synthesis and perturb cell wall integrity with reduced toxicity[266-268]. However, echinocandins are not broad-spectrum drugs and very expensive. All this makes it imperative to develop new compounds with better functional mechanisms or different primary targets such as the polysaccharides in the cell walls. One of the major challenges is that the fungal cell wall structure is poorly understood, placing a barrier to the development of cell wall-targeted antifungal agents.

Fungal cell walls typically contain, by weight, 50-60% glucans, 20-30% glycoproteins, and a small portion of chitin, for example, 10-20% for *A. fumigatus*[264,269]. Fungal glucans contain the predominantly linear β-1,3-linkage, and a small portion, typically 10% or less, of β-1,6- and β-1,4-linkages. The supramolecular assembly of these biomolecules remains vague due to the lack of a non-destructive and high-resolution technique for characterizing the insoluble, complex and amorphous biomolecules within the intact cell wall[2]. To date, chitin microfibrils are thought to be deposited next to the plasma membrane following the biosynthesis of individual chain and the fibril formation process through hydrogen bonding. These microfibrils may be covalently linked to β-1,3-glucans[54] that extend through the cell wall and tether mannoproteins on the cell wall surface through branched networks with β-1,6-linked glucans[55]. The current understanding of the spatial packing has been shaped by the evidence from enzymatic digestion, fractional solubilization and isolation of cell wall components followed by sugar analysis[55,270]. These chemical and enzymatic methods, however, are destructive and often fail to reveal the complicated polymer assembly generated by biosynthesis machinery.

Recently, magic-angle spinning (MAS) solid-state NMR (ssNMR) spectroscopy has been employed to elucidate the structure, spatial proximities and ligand binding of native or genetically modified polysaccharides in intact tissues including the bacterial biofilm, plant biomass, and fungal pigment assemblies[10,18,21,63,65,66,97,238,271]. Here, by integrating glucosyl linkage analysis, 2D ^{13}C-^{13}C/^{15}N correlation ssNMR spectroscopy and the sensitivity-enhancing dynamic nuclear polarization (DNP)[23,24,74,105,226,272-275] technique, we have successfully revealed the structural frame of the cell wall in uniformly ^{13}C, ^{15}N-labeled *A. fumigatus*. We found that chitin and α-1,3-glucans closely interact to form a rigid and hydrophobic scaffold that is surrounded by a soft and well-hydrated matrix of β-glucans. Glycoproteins and a minor fraction of α-1,3-glucans form a highly dynamic shell coating the cell wall surface. In addition, we have revealed that fungal cell wall molecules adopt polymorphic structures and heterogeneous dynamics in order to perform versatile functions. Our findings also shed lights onto the machinery and mechanisms of cell wall component biosynthesis and their assembly. The methods presented in this study enables the investigation of complex carbohydrates in intact cells and will allow the direct detection of fungal responses to antifungal agents through in-situ assessment of cell wall structures.

7.2. Results

7.2.1. Chitin and Glucans Form the Stiff Fungal Cell Wall

Uniformly ^{13}C, ^{15}N-labeled *A. fumigatus* samples were grown on a ^{13}C/^{15}N liquid medium for 14 days. For ssNMR experiments, the *A. fumigatus* samples are analyzed in the intact and native state with minimal perturbation. We rely on the adequate sensitivity provided by isotope labeling and the resolution from a series of two-dimensional (2D) ^{13}C-^{13}C and ^{13}C-^{15}N correlation spectra for assigning the NMR resonances and analyzing the composition, mobility, intermolecular packing, and site-specific water-interactions of these complex carbohydrates *in muro*.

Glycosyl compositional analysis, assisted by ssNMR, demonstrated a major component of glucan (71%), chitin (9%), mannan (6%) and galactan (13%) and traces of chitosan and arabinan in *A. fumigatus* (Supplementary Table 7.1). A gas chromatography-mass spectrometry (GC-MS) glycosyl linkage analysis of partially methylated alditol acetates (PMAA) (Supplementary Figure 7.1) further revealed the highly diverse linkage patterns of fungal glucans. The major form 3-linked glucopyranosyl (3-Glc*p*) accounts for 73% of all neutral sugars and 86% of Glc*p* residues, indicating the dominance of 1,3-glucans (Table 7.1). Another five types of Glc*p* linkages are also identified, comprising 11% of all neutral sugars. Since glucans are better solubilized in the linkage analysis than in classical alditol acetates method of the compositional analysis, minor discrepancies between these two methods are possible.

Table 7.1. ^{13}C-glycosyl linkages of fungal neutral sugars. The percentages reported are peak area from relative EI detector response (%). The intact cell walls of *A. fumigatus* and the alkali-insoluble portion of *A. niger* cell walls are reported.

glycosyl residue	*A. fumigatus*	*A. niger*
terminally linked mannopyranosyl (t-Man*p*)	1.4	0.1
terminally linked glucopyranosyl (t-Glc*p*)	2.6	2.5
terminally linked galactofuranosyl (t-Gal*f*)	1.8	0.4
3-linked glucopyranosyl (3-Glc*p*)	72.8	81.1
4-linked glucopyranosyl (4-Glc*p*)	3.9	4.3
2,3-linked glucopyranosyl (2,3-Glc*p*)	2.3	4.0
2,6-linked glucopyranosyl (2,6-Glc*p*)	0.5	0.3
3,6-linked glucopyranosyl (3,6-Glc*p*)	2.1	2.8
2-linked mannopyranosyl (2-Man*p*)	1.7	0.8
6-linked mannopyranosyl (6-Man*p*)	0.8	0.5
4-linked galactopyranosyl (4-Gal*p*)	10.0	3.4

To assign the NMR resonances of cell wall polysaccharides, we measured 2D ^{13}C-^{13}C correlation spectra using 53-ms CORD mixing[157,276] for through-space correlations (Figure 7.1a) and refocused ^{13}C INADEQUATE pulse sequence[36,37] for through-bond correlations (Figure 7.1b). These 2D ^{13}C-^{13}C correlation experiments preferentially detect the stiff cell wall due to the use of ^{1}H-^{13}C cross polarization (CP). The *A. fumigatus* cell wall exhibits exceptionally high resolution and the typical ^{13}C full-width at half-maximum (FWHM) linewidths range from 0.4 ppm to 0.7

ppm. Major signals are from chitin, β-1,3-glucan, and α-1,3-glucan (Figure 6.1a, b), consistent with the dominance of 3-Glc*p* in linkage analysis. The unique downfield ^{13}C chemical shift of 80-87 ppm at the linkage site of carbon 3 (C3) resolves the signals of 1,3-glucans, and the C1 chemical shift tells the two anomers apart: 99-101 ppm and 102-105 ppm for α- and β-1,3-glucans, respectively. Weaker signals from β-1,4- and β-1,6-glucans have also been identified, with downfield ^{13}C chemical shifts of 85 ppm and 67 ppm at the linkage sites of C4 and C6, respectively.

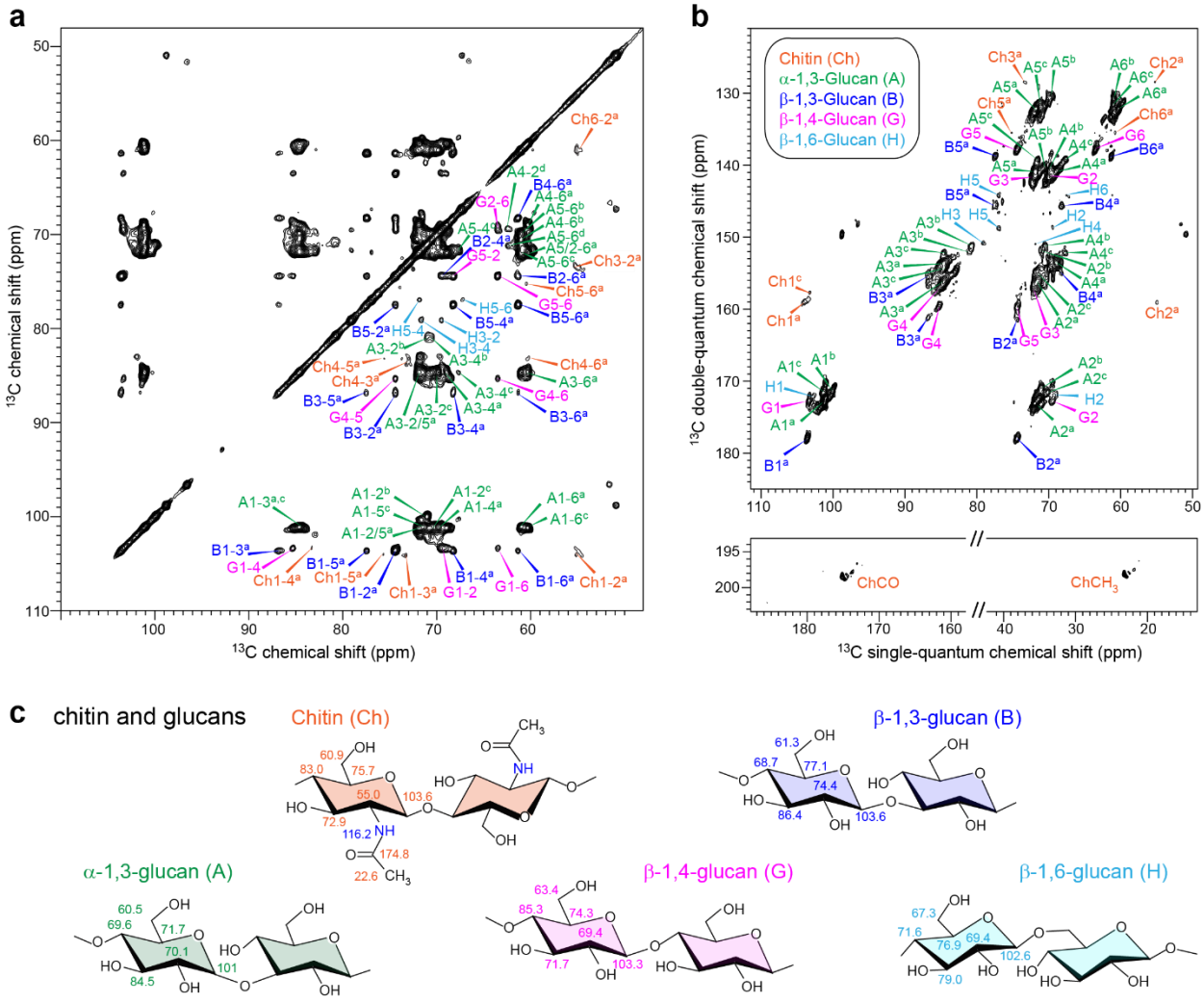

Figure 7.1. Chitin and glucans form the rigid domain of intact *A. fumigatus* cell walls. (a) 2D ^{13}C-^{13}C correlation spectrum measured with 53-ms CORD mixing detects all intramolecular cross peaks of chitin and four types of glucans. Abbreviations are used for resonance assignment and different polysaccharide signals are color coded. (b) ^{13}C CP J-INADEQUATE spectrum resolves the ^{13}C through-bond connectivity for each polysaccharide. (c) Identified polysaccharides and

representative chemical shifts. All spectra were measured on an 800 MHz solid-state NMR spectrometer.

The low intensity of β-1,4- and β-1,6-glucans is also in good agreement with the glycosyl linkage analysis: only 7% of neutral sugars are glucans with linkages at C4 or C6 (Table 7.1). The representative structures are shown in Figure 6.1c and the ^{13}C and ^{15}N chemical shifts are documented in Supplementary Table 7.2. These sugar units may be covalently linked to form branched structures such as the β-1,3/-1,6-glucan

Interestingly, the 2D ^{13}C-^{13}C correlation spectrum of the alkali-insoluble portion of cell walls from *Aspergillus niger*, a related but non-pathogenic fungus, also shows a comparable pattern to that of the intact *A. fumigatus*, with signals primarily from chitin, β-1,3-glucan and α-1,3-glucan (Supplementary Figure 7.2). Linkage analysis confirmed that more than 80% of neutral sugars are 3-Glc*p* residues (Table 7.1). Therefore, the dominance of chitin, β-1,3-glucan, and α-1,3-glucan in the stiff core of cell walls is a conserved feature in *Aspergillus*.

7.2.2. Fungal Polysaccharides are Highly Polymorphic in Structure

The decent ^{13}C resolution of the *A. fumigatus* sample allows the unambiguous assignment of seven types of polysaccharides, including chitin, α-1,3-glucan, three types of β-glucans, mannan, and arabinan. In total 23 allomorphs have been identified for these molecules. 1D ^{15}N spectrum revealed multiple major types of nitrogenated polysaccharides, with two peaks of chitin amides at 123 and 128 ppm and a sharp amine peak at 33 ppm from other amino sugars such as chitosan. Chitosan is an enzymatically derivative of chitin and the degree of deacetylation (DD)[277] is 10% as determined using the well-resolved ^{15}N signals (Figure 7.2a).

Chitin is found to be the most polymorphic molecule in fungal cell walls. 2D ^{15}N-^{13}C correlation spectrum resolves three major forms of chitin (Figure 7.2b), and simply for the type-a chitin, we can resolve at least six C2-N_H cross peaks, each representing a different sub-form. With

another three minor types identified using DNP, we have discovered 11 types of chitins (Supplementary Table 7.2). This level of structural polymorphism is beyond our current knowledge obtained from X-ray and NMR studies on model chitins, and the 11 types of signals could *not* be explained using the known ways of packing: the antiparallel α-chitin, parallel β-chitin, and the mixed γ-chitin [278,279]. Signals from the known structures, both the α- and β-allomorphs[119], can be found within the signals of type-a chitin, with a per-carbon chemical shift difference as low as 0.3 ppm. In contrast, types-b and c do not correlate with any known structures, and the chemical shift difference increased to at least 0.7 ppm and 1.2 ppm, respectively. Thus, Chitin-b and c belong to two structures that have never been reported before. This unexpected level of structural polymorphism is potentially caused by sophisticated patterns of hydrogen-bonds through the N-H and C=O groups in chitin when multiple chains are put together outside the plasma membrane after the biosynthesis.

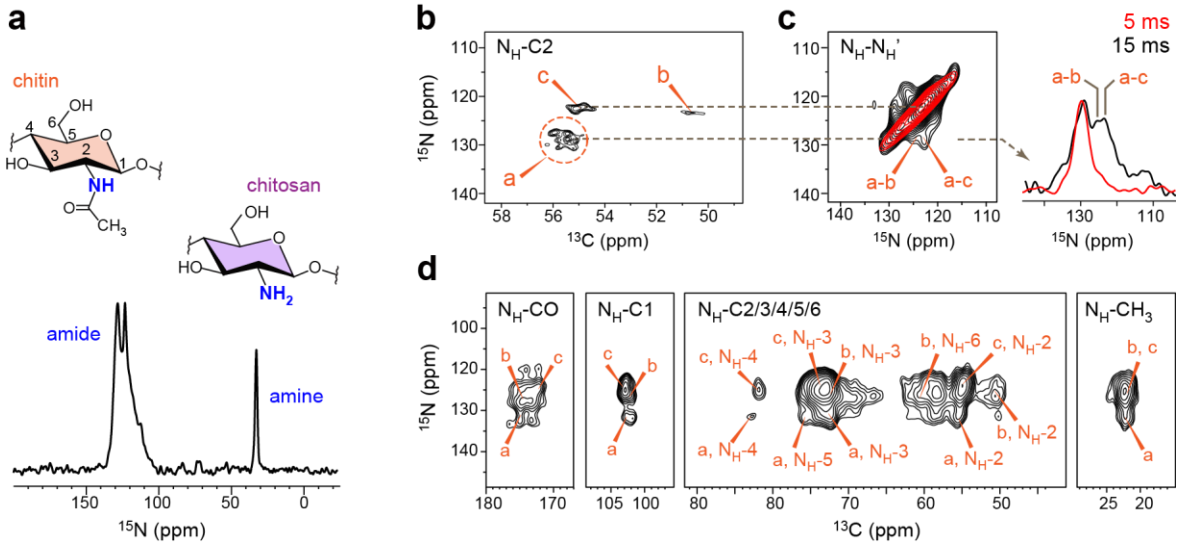

Figure 7.2. Chitin is structurally polymorphic in intact *A. fumigatus* cell walls. (a) 1D ^{15}N spectrum resolved multiple amide and amine signals. (b) High-resolution ^{15}N-^{13}C correlations spectra resolved three major types of chitins. (c) DNP-assisted ^{15}N-^{15}N PAR spectra measured using 5-ms (red) and 15-ms (black) mixing times revealed extensive cross peaks between different chitin allomorphs. (d) DNP-assisted ^{15}N-^{13}C correlation spectra measured using 3-mg *A. fumigatus*.

It is striking that the three major forms of chitin identified in this study are thoroughly mixed on the subnanometer scale in intact *A. fumigatus* cell walls. This is revealed by the strong off-diagonal cross peaks between types-a and b and between types-a and c observed in the 15-ms ^{15}N-^{15}N Proton Assisted Recoupling (PAR) spectrum (Figure 7.2c) [280,281]. For these interactions to happen in the microfibrils, chitin allomorphs should coexist as tightly packed chains in the fibrillar cross-section rather than as separated domains associated longitudinally along the fibril. This organization of chitin bears a resemblance to the assembly of glucan chains in plant cellulose, in which seven types of glucan chains are found to coexist in the cross-section of a single microfibril [22]. It should be noted that the presence of amide, methyl and carbonyl groups substantially facilitated the resonance assignments of chitin allomorphs (Figure 7.2d) and this unique chemical structure further serves as the basis for spectral editing to determine the chitin-glucan packing (*vide infra*).

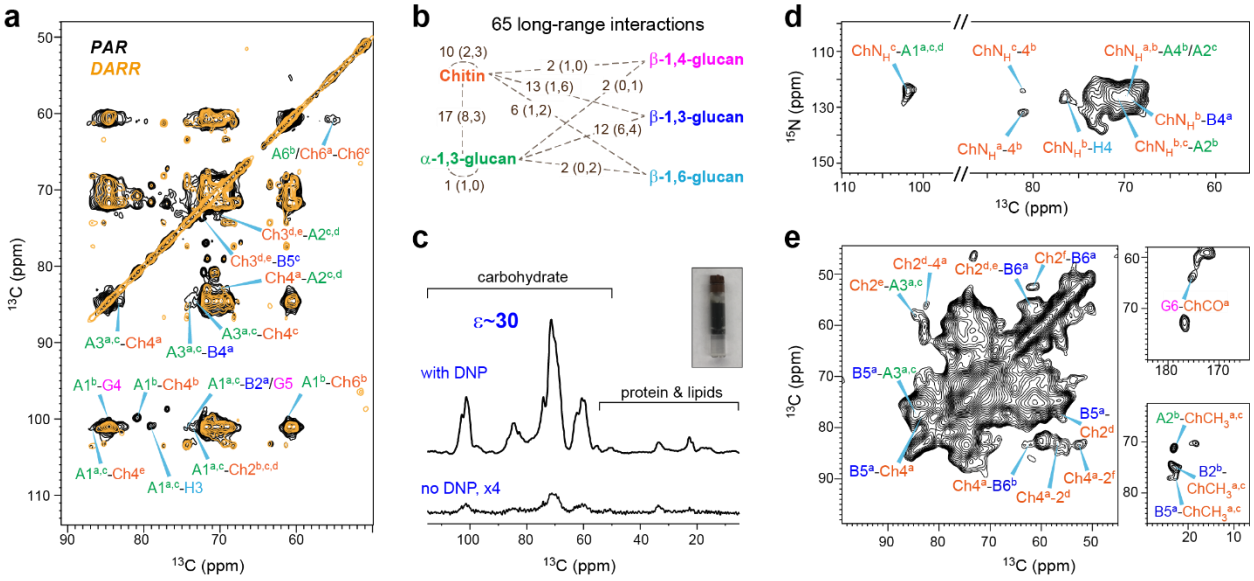

Figure 7.3. MAS-DNP solid-state NMR reveals the tight packing of chitin and α-1,3-glucan. (a) 15 ms ^{13}C-^{13}C PAR spectrum (black) reports many intermolecular cross peaks, mainly between chitin and α-1,3-glucans. A 100-ms DARR spectrum (orange) that primarily detects intra-molecular correlations is overlaid for comparison. (b) Summary of 65 long-range restraints. For each category, the number of all cross peaks and the number of strong and intermediate restraints (in parenthesis) are listed. (c) Sensitivity enhancement $\varepsilon_{on/off}$ 30-fold was obtained on *A. fumigatus*. A picture of a DNP sample is also included. (d) DNP-assisted intermolecular-only ^{15}N-^{13}C

correlation spectrum unambiguously detected several chitin-glucan cross peaks. (e) DNP-assisted chitin-edited spectrum only shows signals from chitin itself or the glucans that are spatially proximal. All DNP experiments were conducted on a 600 MHz/395 GHz spectrometer.

7.2.3. MAS-DNP Reveals a Tight Packing of Chitin and α-1,3-Glucans

It has been a long-standing question of how cell wall biomolecules interact to form the polymer network. To address this question, we measured 15-ms ^{13}C-^{13}C PAR spectrum and discovered 23 long-range (5-10 Å) intermolecular cross peaks (Figure 7.3a and Supplementary Figure 7.3). Most of these cross peaks originate from intermolecular interactions between chitin (Ch) and α-1,3-glucans (A), for instance, between type-b α-1,3-glucan carbon 1 and type-b chitin carbon 4 ($A1^b$-$Ch4^b$) and between type-a/c α-1,3-glucan carbon 3 and type-a chitin carbon 4 ($A3^{a,c}$-$Ch4^a$). In addition, several cross peaks are also found between the chitin-α-1,3-glucan complex and β-glucans. Noteworthy examples include the α-1,3-glucan carbon 1 to β-1,6-glucan carbon 3 (A1-H3) cross peak at (101, 79) ppm and α-1,3-glucan carbon 3 to β-1,3-glucan carbon 4 (A3-B4) cross peak at (85, 73) ppm. Therefore, despite the close packing of chitin and α-1,3-glucans, these two molecules are still crosslinked by β-glucans.

To concurrently improve the sensitivity and resolution, we combined the DNP technique[92,282] with spectral-editing methods and successfully identified another 35 long-range interactions. The magic-angle spinning DNP (MAS-DNP) enhances the NMR sensitivity by tens to hundreds of fold by transferring the polarization from the electrons in radicals to NMR-active nuclei in biomolecules under microwave (μW) irradiation[24]. With an optimized protocol ensuring homogeneous mixing of radicals with cell wall biomolecules, a sensitivity enhancement ($\varepsilon_{on/off}$) of 30-fold has been achieved using the intact cells of ^{13}C, ^{15}N-labeled *A. fumigatus* on a 600 MHz/395 GHz DNP spectrometer (Figure 7.3c). The feasible sensitivity not only facilitates the detection of long-range cross peaks with weak intensities but also allows us to employ spectral-editing methods

to alleviate the signal overlapping issue in intact cells. Briefly, the ^{15}N magnetization of chitin amide is first selected through a ^{15}N-^{13}C dipolar filter [283,284] and then transferred to spatially proximal glucans via a proton-driven spin diffusion (PDSD) mixing period (Supplementary Figure 6.4). By subtracting two parent ^{15}N-^{13}C correlation spectra measured with short (100 ms) and long (1 s) mixing times, we can eliminate all intramolecular signals[160] (Supplementary Figure 7.5). The resulted spectrum only contains long-range intermolecular cross peaks that are structurally important (Figure 7.3d). Using this method, we have identified seven additional cross peaks between different chitin allomorphs, between the chitin and α-glucan, such as the chitin nitrogen to α-1,3-glucan carbon 1 (ChN_H-A1) cross peak, and between chitin amides and β-glucan carbons such as the ChN_H-H4 and ChN_H-B4 cross peaks. The same strategy is extended to measure chitin-edited 2D ^{13}C-^{13}C correlation spectrum, which enables the identification of another 25 long-range cross peaks, for instance, between chitin carbonyl/methyl groups to β-1,3- or β-1,6-glucans (Figure 6.3e).

Overall, these experiments have generated 65 long-range cross peaks, among which 54 are intermolecular interactions and 11 are inter-allomorph cross peaks within chitin or α-1,3-glucans (Figure 7.3b). The cross peaks are further categorized into 20 strong, 21 medium and 24 weak restraints according to the relative intensity and the experimental methods (Supplementary Table 7.3). Eight out of the 17 cross peaks between chitin and α-1,3-glucan are strong, constituting 40% of all strong restraints, supporting the proposed complex formed by tightly packed chitin and α-1,3-glucans. These two molecules further exhibit 25 through-space cross peaks to β-1,3-glucans, among which only 7 are strong restraints, therefore, the β-1,3-glucan, assisted by β-1,4- and β-1,6-glucans, may serve as tethers between multiple chitin-α-1,3-glucans segments. This finding is further supported by the high hydration level and mobility of β-1,3-glucans (*vide infra*).

7.2.4. Chitin and α-1,3-Glucans Form the Hydrophobic Core

To investigate carbohydrate-water interactions, we conducted the water-edited 2D ^{13}C-^{13}C correlation experiment[82,243,285]. This experiment relies on a ^{1}H-T_2 relaxation filter to eliminate all original polysaccharide signals and then transfer the water ^{1}H magnetization to carbohydrates so that only carbohydrates with bound water can be detected. The water-edited signals are compared with the equilibrium intensities of a control spectrum (Figure 7.4a, b), and the intensity ratios tell the polymer hydration in a site-specific manner. Among all the complex carbohydrates, α-1,3-glucan and chitin are most hydrophobic and have the lowest water-transferred intensity. For instance, all α-1,3-glucan cross peaks, including A4-1 (carbons 4 to carbon 1), A4-3, A4-2 and A4-6, show substantial dephasing in the 2D water-edited spectrum (Figure 7.4a) and its 69.5-ppm ^{13}C cross section (Figure 7.4b).

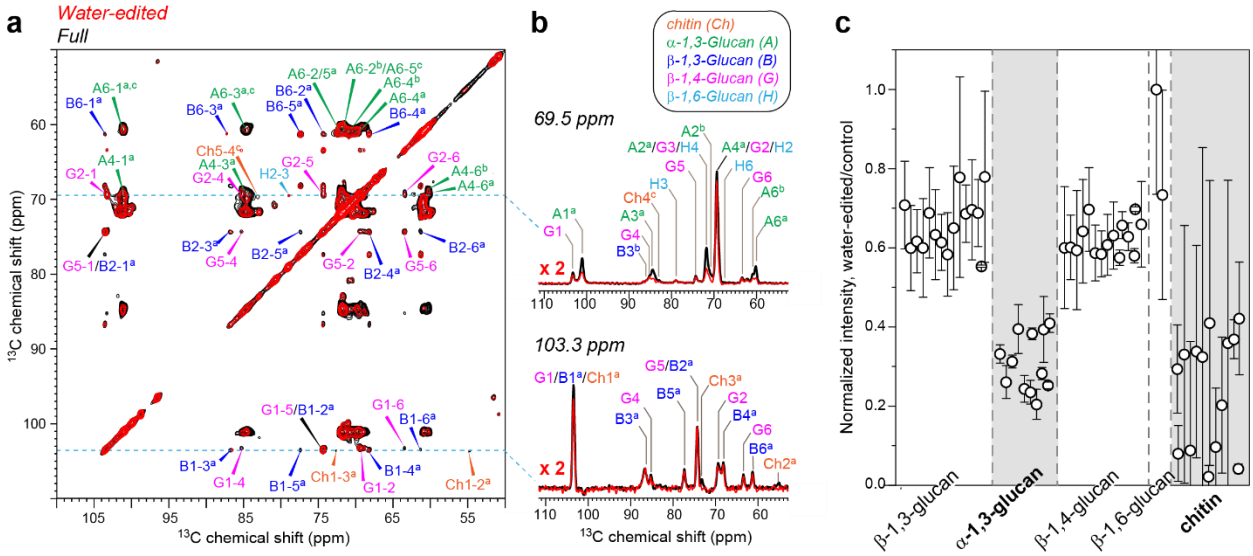

Figure 7.4. Chitin and α-1,3-glucans form the hydrophobic core of A. fumigatus cell walls. (a) Overlay of 2D water-edited (red) and control (black) ^{13}C-^{13}C correlation spectra and (b) 1D ^{13}C cross sections. (c) Relative intensities of different polysaccharides in water-edited spectra. The water-edited spectrum preferentially detects well-hydrated molecules. Error bars are standard deviations propagated from NMR signal-to-noise ratios. Chitin and α-1,3-glucans have the lowest intensities in water-edited spectra (shaded).

The residual intensities are below 40% for chitin and α-1,3-glucan but are higher than 60% for all the well-hydrated β-glucans (Figure 6.4c and Supplementary Table 7.4).

The hydration data dovetail nicely with the long-range correlation results, collectively indicating that chitin and α-1,3-glucan tightly pack to form the hydrophobic domains that are surrounded by a well-hydrated matrix formed of β-glucans. The formation of this dehydrated domain might be facilitated by the assembly of chitin microfibrils, with α-1,3-glucans occasionally deposited on the fibrillar surface or between multiple chains or several microfibrils to further reduce the water accessibility.

7.2.5. Rigid Chitin and α-Glucan are Enclosed by Mobile β-Glucans

To systematically examine the dynamics of cell wall biomolecules, we measured NMR relaxations and a series of 1D ^{13}C spectra that select components with different mobilities. 1D ^{13}C spectrum measured using ^{13}C direct polarization (DP) and a long recycle delay of 35-s provides quantitative detection all cell wall components including polysaccharides, proteins, lipids and small molecules (Figure 7.5a). This quantitative spectrum differs substantially from the spectrum that favorably detects mobile molecules through the combined use of ^{13}C DP and short recycle delays of 2-s. The difference between these two DP spectra is comparable to the ^{13}C cross polarization (CP) spectrum that favors the rigid components with stronger ^{1}H-^{13}C dipolar couplings (Figure 7.5b, c). The major peaks in this difference spectrum are from chitin and α-1,3-glucan, unveiling the stiffness of these two molecules. At the same time, signals from relatively mobile components, such as proteins, lipids, β-glucans and small molecules, are substantially suppressed (Figure 7.5b).

When compared with the quantitative detection, α-1,3-glucans have the highest CP intensity in the CP spectrum selecting stiff polymers, doubling that of quantitative DP, but the

lowest signals in the 2-s DP spectrum that favors mobile molecules (Figure 7.5d). Accordingly, α-1,3-glucan is the most rigid polysaccharides in *A. fumigatus*. Two subtypes, a and b, of chitin are found to be the second rigid molecules, with 50% higher signals in CP but 0-50% less intensity in 2-s DP spectrum than the quantitative spectrum. All the β-glucans, together with another two types of chitins, fully retain their signals in 2-s DP spectrum, thus are dynamic (Figure 7.5d and Supplementary Table 7.5).

.

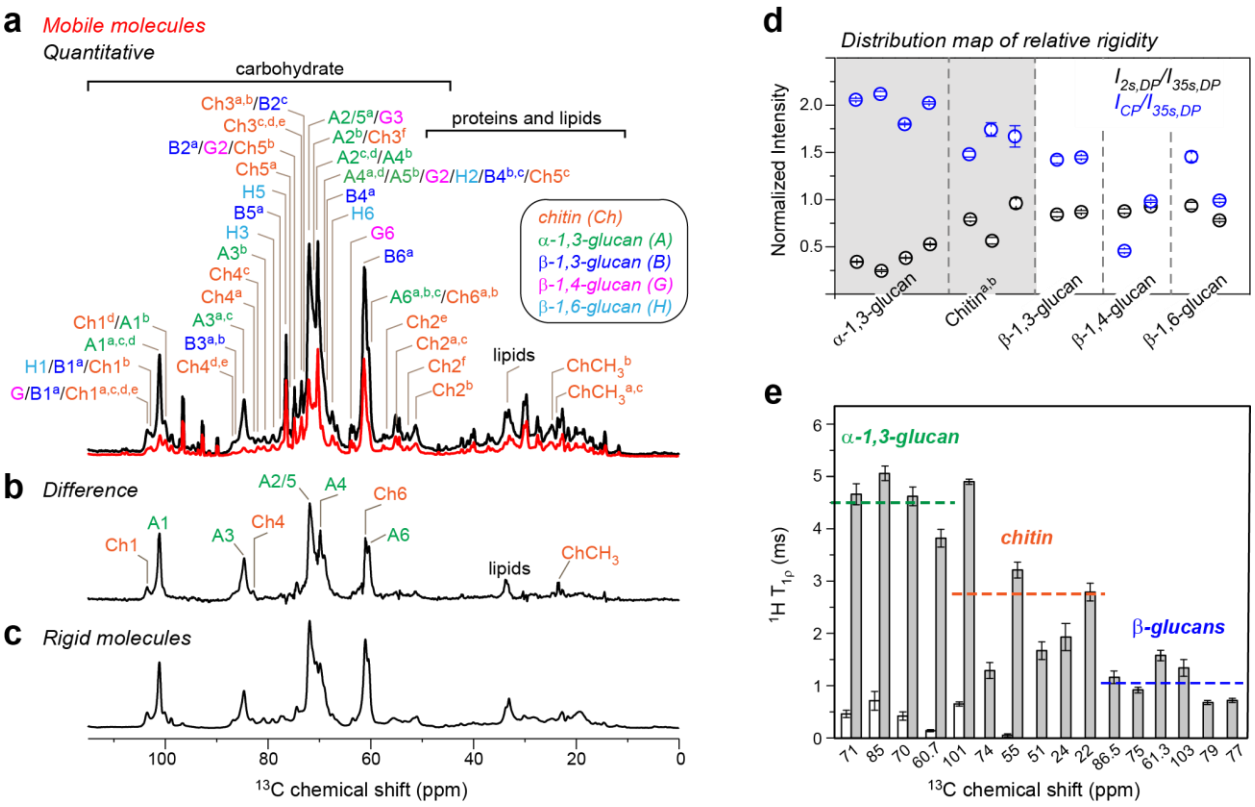

Figure 7.5. Fungal cell walls are dynamically heterogeneous. (a) 1D ^{13}C DP spectra of intact *Aspergillus fumigatus* cells with quantitative detection of all molecules (black) or selective detection of the mobile components (red). Abbreviations of carbohydrate names, carbon numbers and subtypes (superscripts) are included for the assignments. (b) Difference spectrum obtained by subtraction of the two 1D DP spectra. (c) ^{13}C CP spectrum that favors rigid molecules. (d) Peak intensity ratios between different DP spectra and CP spectra show that α-1,3-glucan, and a subset of chitins are relatively rigid. Error bars are standard deviations propagated from NMR signal-to-noise ratios. (e) ^{1}H-$T_{1\rho}$ relaxation times. The open and filled bars represent the short and long-components of ^{1}H-$T_{1\rho}$ relaxation. Error bars are standard deviations of the fit parameters. Dashlines indicate the average value of the longer ^{1}H-$T_{1\rho}$ component for each type of polysaccharides.

The molecular motional rates are quantified by measurements of ^{13}C-T_1 relaxation that probes local reorientation and ^{1}H-$T_{1\rho}$ for larger-scale motions such as cooperative movement of multiple sugar rings. Cell wall polysaccharides exhibit distinct ^{1}H-$T_{1\rho}$ relaxation times, signifying a highly heterogeneous profile of dynamics (Supplementary Figure 7.6a and Table 7.6). The average ^{1}H-$T_{1\rho}$ is 4.5 ms, 2.8 ms and 1.1 ms for α-1,3-glucans, chitin, and β-glucan, respectively (Figure 7.5e). Consistently, α-1,3-glucans also have the slowest ^{13}C-T_1 relaxation among all types of glucans (Supplementary Figure 7.6b and Table 7.7). Therefore, α-1,3-glucan is the most rigid molecule, followed by chitins and then β-glucans

Interestingly, chitin has the largest variance in relaxation times (Figure 7.5e), which, together with the allomorph-specific 1D ^{13}C intensities, suggests a functional-relevant structural polymorphism: a subgroup of chitin allomorphs is responsible for forming rigid microfibrils whereas the remainder retains considerable disorder due to unfavored conformations or unstable hydrogen bonding patterns. Type-a chitin has similar chemical shifts as the α- and β-chitins, and these allomorphs clearly bear high rigidity in the intact cell walls. It should be noted that for most α-1,3-glucan peaks the satisfactory fit of ^{1}H-$T_{1\rho}$ data can only be achieved using double exponential equations. It suggests a two-domain distribution: 70-90% of α-1,3-glucans interact with chitins to form a stiff and hydrophobic scaffold conferring rigidity to the cell wall (the long ^{1}H-$T_{1\rho}$ component of 3.8-5.0 ms) while the other 10-30% have very short ^{1}H-$T_{1\rho}$ relaxation of less than a millisecond due to the interactions with the mobile β-glucans (Figure 7.5e, Supplementary Figure 6.6a). Particularly, β-1,3-glucan is the major binding target of α-1,3-glucans as they have 12 intermolecular cross peaks, among which half are strong interactions (Figure 7.3b).

7.2.6. Glycoproteins and α-1,3-Glucans Forms a Highly Mobile Shell

While the previous 2D experiments are CP-based and primarily focus on the relatively rigid polysaccharides that are mechanically important, a ^{13}C DP J-INADEQUATE spectrum with short recycle delays of 2-s is also measured to highlight the mobile domain of the cell wall (Figure 6.6a). The primary signals have been attributed to proteins that are absent in CP-based experiments and some polysaccharides. The very sharp ^{13}C linewidths of 0.3-0.5 ppm confirmed the rapid motional averaging of these molecules. Unambiguous signals of mannan and arabinan are observed (Figure 7.6b). Since mannan is a major component of fungal glycoproteins purposely forming an outmost layer of fungal cell walls [256,269], our results revealed that this outer shell is highly dynamic and spatially separated from the relatively rigid inner domain of chitin and glucans. Despite the fact that most α-1,3-glucans participate in the formation of stiff and hydrophobic cores, a considerable amount of α-1,3-glucan signals remain in the dynamic domain (Figure 7.6b), which supports a hypothesis that α-1,3-glucans may form the outmost layer of cell walls to block the immune recognition of β-glucan receptors in the host cells[265,286]. Thus, α-1,3-glucan is bi-functional: supporting cell walls through the formation of hydrophobic scaffolds and increasing fungal virulence by disabling the detection of invading microbes.

In addition to this mobile domain, we have also identified a rigid component of proteins (Supplementary Figure 7.7a and Supplementary Table 7.8). These proteins are as hydrophobic as the fatty acid chains of membrane and are apparently more hydrophobic than any polysaccharides (Supplementary Figure 7.7b and Supplementary Table 7.9). These rigid proteins are mainly membrane proteins but may also exist in the hydrophobin rodlet protein layer, a hydrophobic coating preventing immune recognition[287,288].

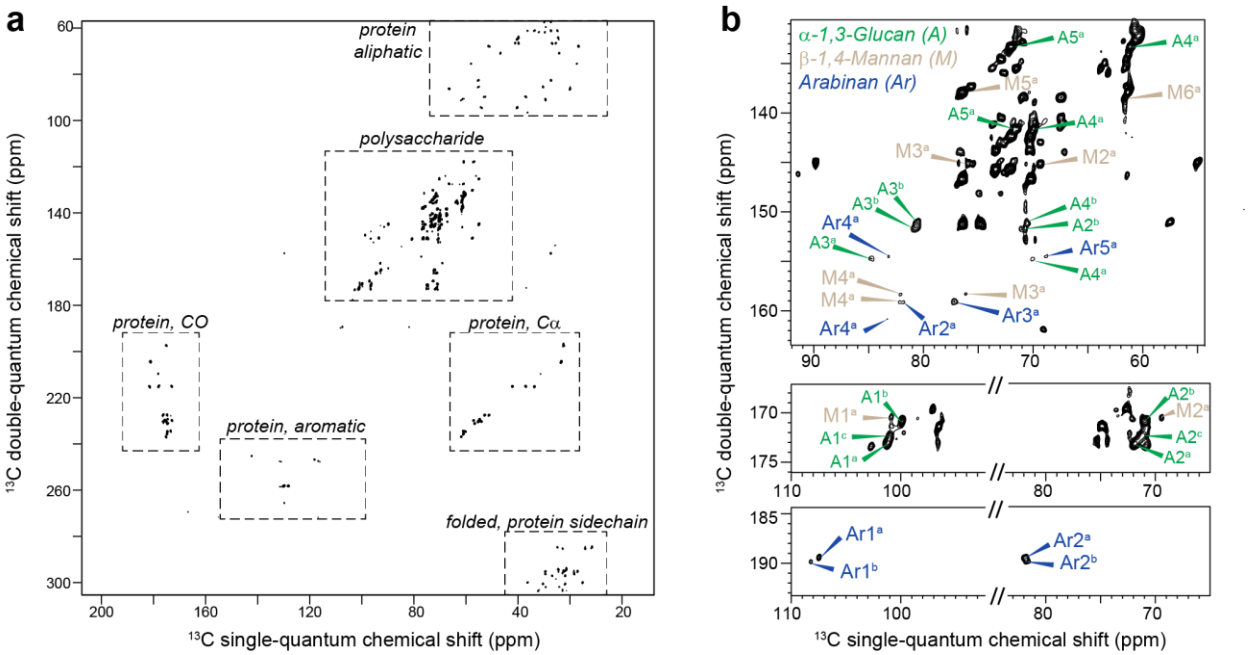

Figure 7.6. Glycoprotein and α-1,3-glucan form a highly mobile shell. (a) 2D ^{13}C DP J-INADEQUATE spectrum selects only the very mobile molecules of proteins and polysaccharides. (b) The polysaccharide region reveals the presence of β-1,4-mannan, arabinan and α-1,3-glucans.

7.3. Discussion

This study presents a high-resolution and non-destructive method for determining fungal cell wall architecture. Solid-state NMR and MAS-DNP results of 64 intermolecular and inter-allomorph interactions, site-specific hydration, and molecular mobility steadily indicate a two-domain distribution of molecules: glucans and chitins form a relatively rigid and inner portion of cell walls, while mannoproteins and α-1,3-glucan form the extremely mobile outer shell. In the inner domain, α-1,3-glucan and chitin are tightly packed as the most rigid and hydrophobic cores that are embedded in a well hydrated and relatively mobile matrix formed by β-1,3-, β-1,4- and β-1,6-glucans (Figure 7.7).

Compared with previous biochemical analyses, this NMR-derived model has both consistency and revisions. For decades, we have been solubilizing different components using chemical or enzymatical treatment, for example, alkali solubilization, and then determine the composition and covalent linkages of the extracted portions[54,55,289-293]. A conserved skeleton of

branched β-1,3 and 1,6-glucans with β-1,4-linkages to chitins is found in the alkali insoluble component of most fungi, while the other molecules vary substantially in mould and yeast[2,289]. Mannoproteins are found in the cell wall surface and connected to the cell wall via either non-covalent connections or covalent linkages to β-1,6-glucans[294,295]. These biochemical data and our ssNMR analysis dovetail well considering the structural roles of chitin and β-glucans and the outer layer of proteins.

The current model also shifted the prevailing paradigm of fungal cell wall from three aspects. First, we have identified the molecules that determine cell wall rigidity. As the most abundant building unit of the fungal cell wall, β-glucans, especially the multi-branched polymers of β-1,3/-1,6-glucan, have long been proposed to form the rigid network[2,269]. However, the high-level of hydration and the intermediate mobility of β-glucans we found have clearly excluded this structural role but suggest a rigid scaffold formed by chitin and α-1,3-glucan. The structural role of α-1,3-glucan is unexpected since it is usually defined as the major alkali-soluble polysaccharide in previous studies[2]. Second, the current model reveals the bridging role of β-1,3-glucans to a great detail. At present, all β-glucans are indistinguishable in dynamics and hydration but among the three types of β-glucans, β-1,3-glucan absolutely has more pronounced interactions with other molecules, in particular, with α-1,3-glucan. This can be seen from the 12 intermolecular cross peaks between β-1,3-glucan and α-1,3-glucan in which half are strong restraints (Figure 7.3b). β-1,3-glucan and chitin also have a large number of cross peaks, 13 in total, but mostly weak or intermediate in strength. Thus, chitin may serve as a secondary anchor, right after α-1,3-glucan, for β-1,3-glucan to link the rigid and mobile domains (Figure 7.7). Third, the dual functions of α-1,3-glucan have been emphasized. The high rigidity of α-1,3-glucan has not been expected and we propose that stiffening by covalent or physical interactions with β-1,3-glucans and chitin grant α-

1,3-glucan with the capability of performing structural roles. Linkages between α-1,3- and α-1,4-glucose units have been reported before[290] but it is unclear whether covalent interactions exist between α-1,3-glucans and chitin or β-1,3-glucans. Interestingly, the occurrence of α-1,3-glucans in two distinct domains, the outer surface, and the inner rigid cores, demonstrated the structural and functional versatility of this molecule.

A. fumigatus produces a low amount of chitosan, a cationic molecule with various biomedical and industrial applications due to its antimicrobial, anti-tumor, wound-healing and cholesterol lowering properties[296]. Previously, structural roles have been assumed for chitosan since chitosan-deficient strains of *Cryptococcus neoformans* have compromised cell wall integrity in vitro and reduced virulence[297]. But in *A. fumigatus*, chitosan accounts for less than 1% of all carbohydrates (Supplementary Table 7.1) and is mobile as revealed by the sharp ^{15}N linewidth of 1.5 ppm (Figure 7.2a). Therefore, chitosan contributes negligibly to cell wall rigidity.

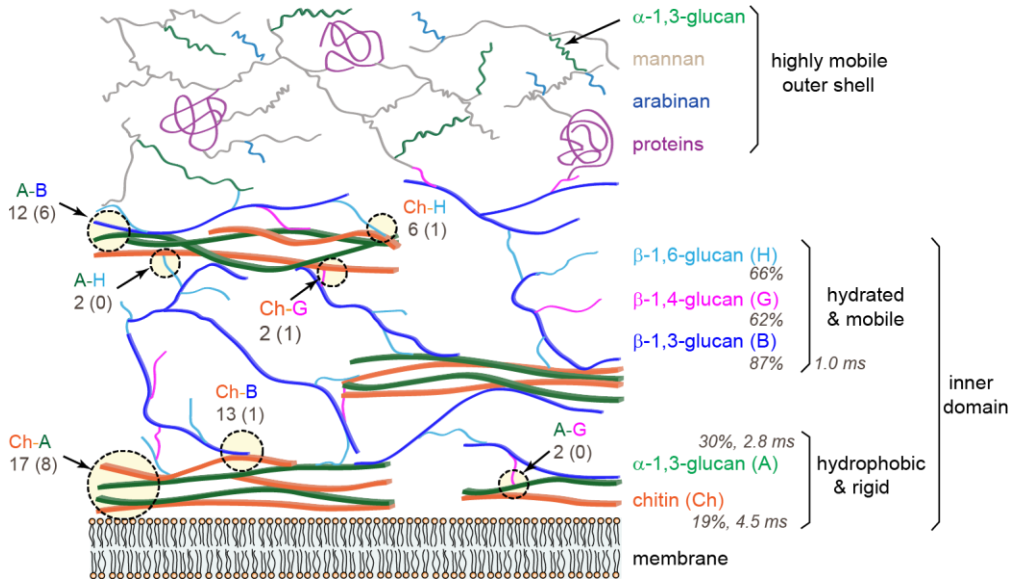

Figure 7.7. Illustrative model of the supramolecular architecture of *A. fumigatus* cell walls. Dashline circles highlight the intermolecular interactions with the total numbers of NMR restraints indicated. The number of strong restraints is in parenthesis. The average hydration levels (percentage values) and the average ^{1}H-$T_{1\rho}$ relaxation times of each polymer are in italic.

The current study provides insights on the polysaccharide scaffold for pigment deposition. The insoluble pigment of melanin is present in many fungi and it increases cell hydrophobicity and reduces cell wall porosity, which was proposed to be the cause of drug resistance[298-301]. Recent ssNMR studies of melanin "ghosts", the isolated and purified particles, indicate that melanin may be integrated into the cell wall via association with polysaccharides in *C. neoformans*[65,66] but the scaffold that holds the pigment in place was unclear. Chitin has been proposed to be the supporting polysaccharide, but our results revealed a stiff and hydrophobic frame of α-1,3-glucans and chitins, which could accommodate the aromatic assembly of pigments, which, in turn, may explain the high hydrophobicity of these two polysaccharides (Figure 7.4c).

Notably, the fungal wall is significantly more dynamic than its counterparts in plants. The narrow ^{13}C linewidth of fungal polysaccharides is comparable to that of the matrix polysaccharides, hemicellulose and pectins, in the fast-growing primary plant cell walls, but is apparently narrower than that of rigid cellulose microfibrils[22]. Upon maturation, plant cell walls are further rigidified and dehydrated by the deposition of aromatic lignins and coalescence of cellulose microfibrils[302]. Therefore, despite the presence of a relatively rigid scaffold formed by chitin fibrils and α-1,3-glucans, the polymer network in fungi still retains considerable plasticity, which allows fungal cell wall to reshape its molecular architecture to survive through different external stress and to fulfill diverse functions. The lack of need for vertical growth and the limited size of microbes may also explain the high mobility of fungal cell walls. In addition, the fungal cell wall also has a substantially larger number of intermolecular cross peaks than the plant cell walls. This may be caused by the extensive covalent cross-linking of glucans and chitin in fungi, while plants principally rely on non-covalent interactions, such as van der Waals forces and electrostatic interactions, as well as the entanglement and entrapment of polymers. Given the high

mobility of fungal biomolecules, it may be crucial to have chemical linkages instead of physical contacts as the primary interactions so that this dynamic structure could remain intact under external and internal stress.

Although this study builds a frame for fungal cell wall structure, in particular, for the complex carbohydrates, more structural details await systematic investigations. Emerging questions include the correlation of linkage patterns with structural or mechanical functions for β-glucans and the developmental changes of cell wall architecture, for example, during conidial outgrowth. A detailed and dynamic understanding of the supramolecular assembly of fungal cell walls and future studies on drug response will substantially facilitate the design of better antifungal compounds that inhibit a broader spectrum of invasive fungal infections with minimal or no side toxicity.

7.4. Methods

7.4.1. Preparation of Fungal Materials

Uniformly ^{13}C,^{15}N-labeled mycelium was prepared by IsoLife (Wageningen, The Netherlands) using the following protocol. *Aspergillus fumigatus* cultures (strain RL 578, a wild strain obtained from compost) were grown on a $^{13}C/^{15}N$ liquid medium (a modified Czapek-Dox medium) under still cultivation at 30 °C for 14 days in the dark on 50-mL medium in 250 mL capacity Erlenmeyer flasks. At the end of the cultivation the mycelium was flash-frozen in liquid nitrogen and stored at -80 °C. The resulting materials were further dialyzed for 6 times over 3 days to remove the majority of small molecules from the isotope-labeled media and reduce the ion concentration. For solid-state NMR experiments, 30 mg and 100 mg of this whole-cell material were packed into 3.2-mm and 4-mm magic-angle spinning (MAS) rotors, respectively. Another 5 mg was proceeded in DNP matrix for DNP experiments and 3 mg was finally transferred into a

3.2-mm sapphire rotor. The hydration level is 90% for the initial culture and has been decreased to 50% in the NMR samples by multiple times of compression.

To verify the composition of the rigid portion of fungal cell walls and compare it with the whole cells, the alkali-insoluble polysaccharides were extracted by IsoLife from *Aspergillus niger* mycelium by deproteinization with 2% w/v sodium hydroxide solution (30:1 v/w, 90 °C, 2 h), separation of alkali-insoluble fraction by centrifugation (4000xg, 15 min), extraction of chitosan under reflux (10% v/v acetic acid, 40:1 v/w, 60 °C, 6 h), separation of crude cell wall by centrifugation (4000×g, 15 min). The crude was washed with water, ethanol and acetone and air-dried at 20 °C. 70 mg of the extracted polysaccharides was packed in a 4-mm rotor for solid-state NMR experiments, which clearly indicate the dominance of chitin and glucans in this alkali-insoluble portion.

7.4.2. Glycosyl Composition Analysis

Glycosyl composition analysis of neutral sugars constituting the cell wall was achieved after dispersion of 600 µg dry samples in 0.5 mL 2 M TFA (v/v) in sealed reaction tubes, by 20 min sonication in ultrasound water bath at RT, followed with 2 h hydrolysis at 121 ºC, overnight reduction with $NaBD_4$, and 1 h acetylation with acetic anhydride and pyridine at 80 ºC. Inositol was used as an internal standard. The glycosyl constituents were assigned based on the retention time of the derivatives of original sugar standards and unique EI-MS fragments of ^{13}C alditol acetates derivatives identified in the fungal samples. We used the same GLC-MS equipment and temperature program as for linkage analysis.

7.4.3. Glycosyl Linkage Analysis

The glycosyl linkage of ^{13}C, ^{15}N uniformly labeled cell polysaccharides was obtained by GC-MS analysis of partially methylated alditol acetates (PMMA)[303] after 2 h hydrolysis with 2 M

(v/v) TFA at 121 ºC, overnight reduction with $NaBD_4$ and acetylation with acetic anhydride and pyridine. The inositol was used as an internal standard. GLC-MS analysis was performed on an HP-5890 GC interfaced to a mass selective detector 5970 MSD using a Supelco SP2330 capillary column (30 × 0.25 mm ID, Supelco) with temperature program: 60 ºC for 1 min, then ramp to 170 ºC at 27.5 ºC/min, and to 235 ºC at 4 ºC/min with 2 min hold and finally at to 240 ºC at 3 ºC/min with 12 min hold.

Because the organism was grown on media supplemented with ^{13}C and ^{15}N as sole carbon and nitrogen source, respectively, one could expect these isotopes to incorporate in the cell wall polysaccharides. Consequently, GC-MS analysis of partially methylated alditol acetates (PMAA) generated a set of unique EI-MS diagnostic fragments that differed from fragments predicted for classical PMAAs (Supplementary Figure 6.1). It should be noted that the complex glucan samples solubilize better during the linkage analysis (DMSO solvent and permethylation step prior to TFA hydrolysis) than in classical alditol acetates method of compositional analysis (only TFA hydrolysis). Thus, we have a better detection of glucan in the PMMA analysis.

7.4.4. Solid-State NMR Experiments

Solid-state NMR experiments were conducted on a Bruker Avance 800 MHz (18.8 Tesla) spectrometer and a 400 MHz (9.4 Tesla) Bruker Avance spectrometer using 3.2-mm and 4-mm MAS HCN probes, respectively. Most experiments except those with MAS-DNP were collected under 10-13.5 kHz MAS at 290 K. ^{13}C chemical shifts were externally referenced to the adamantane CH_2 signal at 38.48 ppm on the TMS scale. ^{15}N chemical shifts were referenced to the liquid ammonia scale either externally through the methionine amide resonance (127.88 ppm) of the model peptide N-formyl-Met-Leu-Phe-OH[304] or using the ratio of the gyromagnetic ratios of ^{15}N and ^{13}C. Typical radiofrequency field strengths, unless specifically mentioned, were 80-100

kHz for ^{1}H decoupling, 62.5 kHz for ^{1}H CP and hard pulses, 50-62.5 kHz for ^{13}C and 41 kHz for ^{15}N.

To assign the ^{13}C and ^{15}N resonances of cell wall biomolecules, five types of experiments were measured: (1) 2D refocused ^{13}C J-INADEQUATE[36,37] spectra with DP and short recycle delays of 2 s for selective detection of the very mobile phase in the outer layer of cell walls (2) ^{13}C CP J-INADEQUATE for the detection of rigid molecules located inside the cell wall. (3) ^{13}C-^{13}C RFDR[241] for the detection of one-bond cross peaks; (4) 2D ^{13}C-^{13}C spectra using 53 ms CORD[157,276] or 50 ms DARR for the detection of intramolecular cross peaks; (5) 2D ^{15}N-^{13}C N(CA)CX heteronuclear correlation spectra[305] to select the amide signals of chitins. The N(CA)CX is measured using a 0.6 ms ^{1}H-^{15}N CP contact time, a 5 ms ^{15}N-^{13}C CP and a 100 ms ^{13}C-^{13}C DARR mixing period. The ^{15}N and ^{13}C spin-lock field strengths for the ^{15}N-^{13}C CP were 20 kHz and 33 kHz, respectively. The ^{13}C and ^{15}N carrier frequencies were 55 ppm and 70 ppm, respectively. A strong ^{1}H decoupling of 100 kHz is applied during the ^{15}N-^{13}C CP.

To determine the spatial proximities of biomolecules in intact cell walls, we measured 15-ms ^{13}C-^{13}C proton-assisted recoupling (PAR)[306] using ^{13}C field strengths of 53 kHz and ^{1}H field strengths of 50 kHz. 23 intermolecular cross peaks have been identified in the PAR spectra, which, in combination with 7 long-range cross peaks in 3-s PDSD and 35 long-range cross peaks in DNP experiments, restrain the spatial packing of molecules in intact cell walls.

To site-specific determine the water accessibilities of different polysaccharides, we conducted water-edited 2D ^{13}C–^{13}C correlation spectra [82,194,285]. This experiment initiates with ^{1}H excitation followed by a ^{1}H-T_2 filter of 0.88 ms x 2 that eliminated 97% of polysaccharide signals but retains 80% of water magnetization, a 4-ms ^{1}H mixing period for water-to-polysaccharide transfer and a 1 ms ^{1}H-^{13}C CP for ^{13}C detection. 50 ms DARR mixing is used for both the water-

edited spectrum and a control 2D spectrum showing full intensities. The intensity ratio between the water-edited spectrum and the control spectrum is quantified, which is further normalized by that of the C2-C3 cross peak of β-1,6-glucan, the highest value among all the peaks, to reflect the relative degree of hydration.

To examine the dynamics of wall polysaccharides, we measured a series of 1D ^{13}C spectra with different methods for the creation of initial magnetization. 1D ^{13}C direct polarization (DP) spectra were measured using a 35 s recycle delay to obtain the quantitative signals and a 2 s recycle delay to selectively detect the dynamic components. The difference spectrum was obtained by subtracting the 2 s DP spectrum from 35 s DP spectrum, without scaling. 1D ^{13}C CP spectrum that preferentially detects the rigid components were also conducted using 1-ms contact time. Furthermore, we measured both ^{13}C spin-lattice (T_1) relaxation and ^{1}H rotating-frame spin-lattice relaxation ($T_{1\rho}$) relaxation at 298 K under 10 kHz MAS on a Bruker Avance 400-MHz Spectrometer. The spin-lock field was 62.5 kHz for the measurement of ^{1}H- $T_{1\rho}$. The relaxation data were fit using either a double or single exponential decay function.

7.4.5. MAS-DNP Sample Preparation

The stock solution of AMUPol[198] was freshly prepared in the d_8-glycerol/D_2O/H_2O (60/30/10 Vol%) solvent mixture referred as the DNP-matrix, and a final radical concentration of 10 mM. To prepare the DNP sample, 50 µL of the stock solution was added into 5 mg of the ^{13}C,^{15}N-*A. fumigatus* sample, grinded for 10-15 minutes to allow the radical solution to penetrate into the cell walls. 3-mg of well-hydrated samples were transferred into a 3.2-mm sapphire rotor. A 30-fold enhancement factor of NMR sensitivity with and without microwave irradiation ($\varepsilon_{on/off}$) has been achieved. Relatively short buildup times of 3-5 s indicate a good mixing of the radicals and biomolecules in these whole-cell samples. It should be noted that simply mixing the materials

with the DNP matrix failed to give any enhancement regardless of the mixing time. Therefore, grinding the fungi in DNP matrices thoroughly for several minutes is needed to ensure homogeneous mixing of radicals and biomolecules in these whole-cell samples.

7.4.6. MAS-DNP Solid-State NMR Experiments

All the experiments were performed on a 600 MHz/395 GHz 89 mm-bore MAS-DNP spectrometer equipped with a gyrotron microwave source (National High Magnetic Field Laboratory, Tallahassee). The cathode currents of the gyrotron were 160 mA. All DNP spectra were measured using a 3.2 mm probe under 8 kHz MAS frequency. The temperature was 103.6 K with the microwave (μW) off and 106 K with the μW on.

To select chitin signals and identify chitin-glucan interactions, 2D ^{15}N-^{13}C TEDOR[284] correlation experiments were implemented by a mixing period with 100-ms DARR or 3-s PDSD. Spectral subtraction generates a difference spectrum that clearly revealed seven intermolecular cross peaks. The total experimental time is 22 hours. Second, to further improve the spectral resolution, we conducted a ^{15}N,^{13}C filtered 2D ^{13}C-^{13}C correlation spectra[21], which benefits from the presence of two ^{13}C dimensions and provide unambiguous detection of chitin-proximal biomolecules. It took 4.5 hours to measure this experiment on 3 mg ^{13}C, ^{15}N-fungi and 25 intermolecular cross peaks have been identified. In addition, a ^{13}C-^{13}C dipolar-INADEQUATE-PDSD spectrum was measured to identify the signals of minor species and further detect long-range correlations. To determine the packing of different chitin allomorphs, we measured 2D ^{15}N-^{15}N homonuclear correlation spectra using 5 ms and 15 ms PAR mixing[280,281]. The radiofrequency field strengths for PAR were 34 kHz for ^{15}N and 56 kHz for ^{13}C.

APPENDIX A. SUPPORTING INFORMATION FOR CHAPTER 4

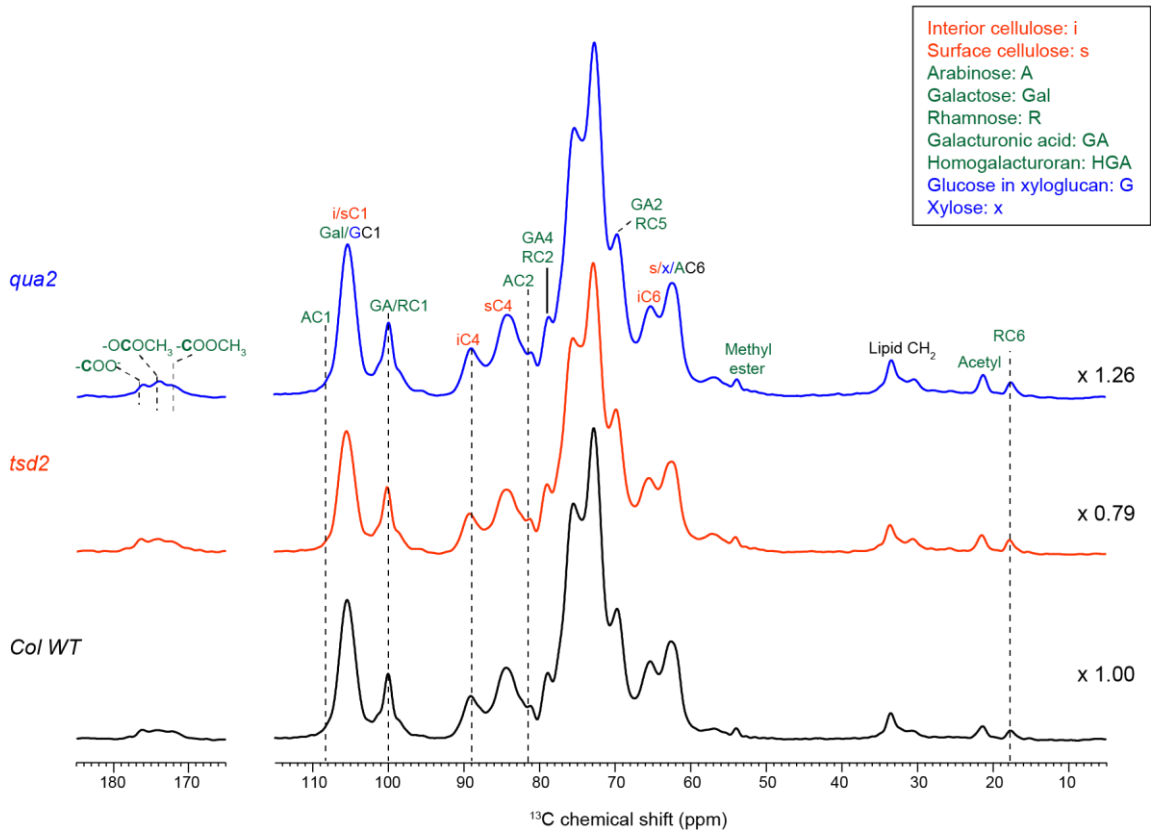

Figure A.1. 1D ^{13}CP spectra of wild type, *tsd2*, and *qua2* seedlings primary cell walls at 293 K. The CP spectra selectively detect the signals of rigid polysaccharides. The spectra are scaled to account for the difference of sample amount.

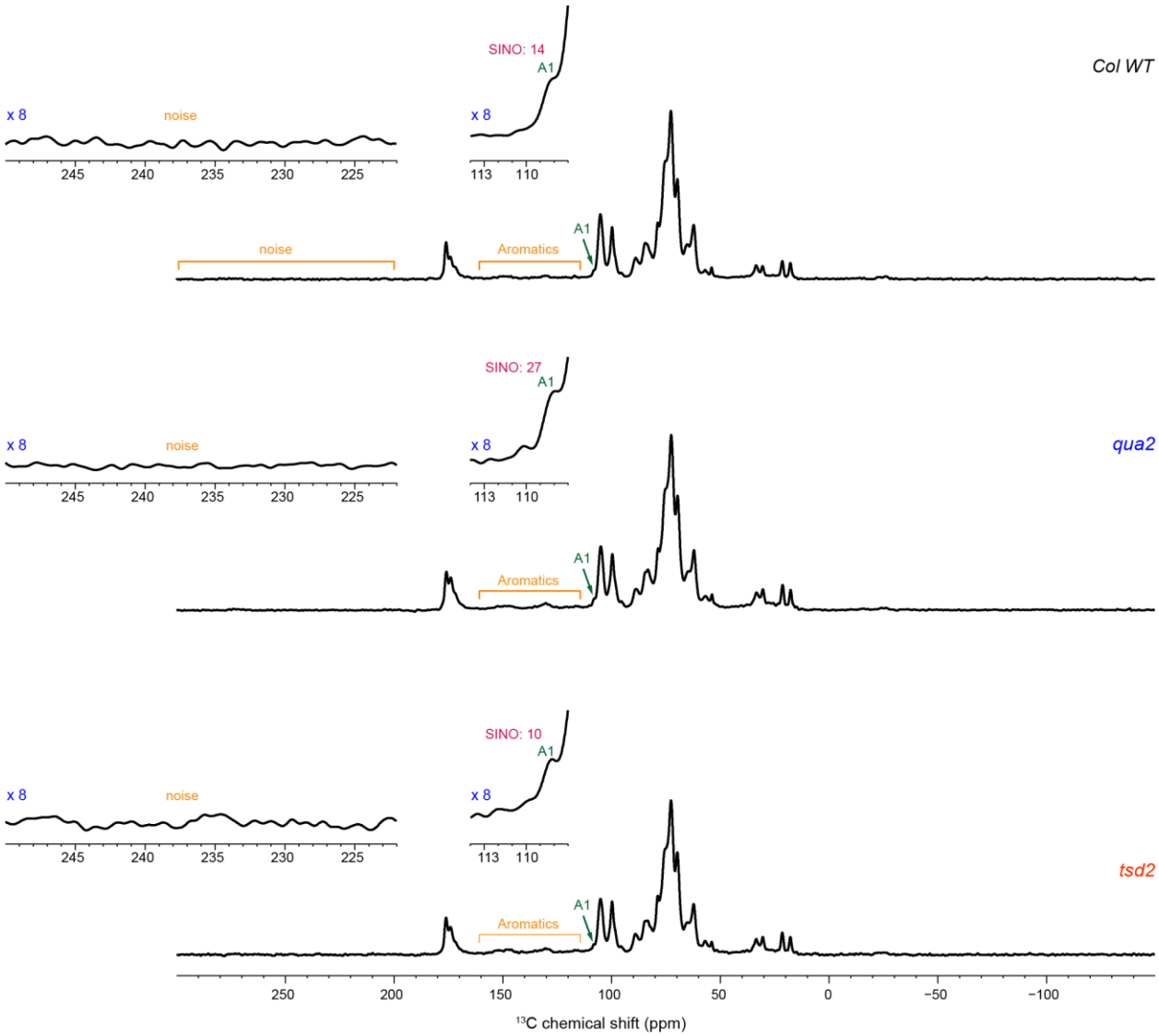

Figure A.2. Quantification of the signal-to-noise ratios of arabinose carbon 1 peak. The full ^{13}C spectra are shown for each sample, showing biomolecular signals as well as the noise regions. All spectra are processed using Topspin window function of GM, with parameters of LB = -10 and GB =0.05. The resulting spectra are almost "noiseless". Insets show the representative regions of noise and the weakest signal of the full spectra, arabinose carbon 1. The arabinose carbon 1 peak has signal-to-noise (SINO) ratios between 10 and 27 for the three samples. These numbers are obtained using the standard Topspin command: .SINO. Error bars can be propagated from the signal-to-noise ratios: $y = \frac{S}{S_0}\sqrt{\frac{1}{SINO(S)^2} + \frac{1}{SINO(S_0)^2}}$, where S/S0 is the intensity ratio of A1 peak between mutant (S) and WT (S_0). The error bars are 10% for qua2 mutant (the ratio of A1 in qua2 and WT is 1.2±0.1) and 12% for the tsd2 mutant.

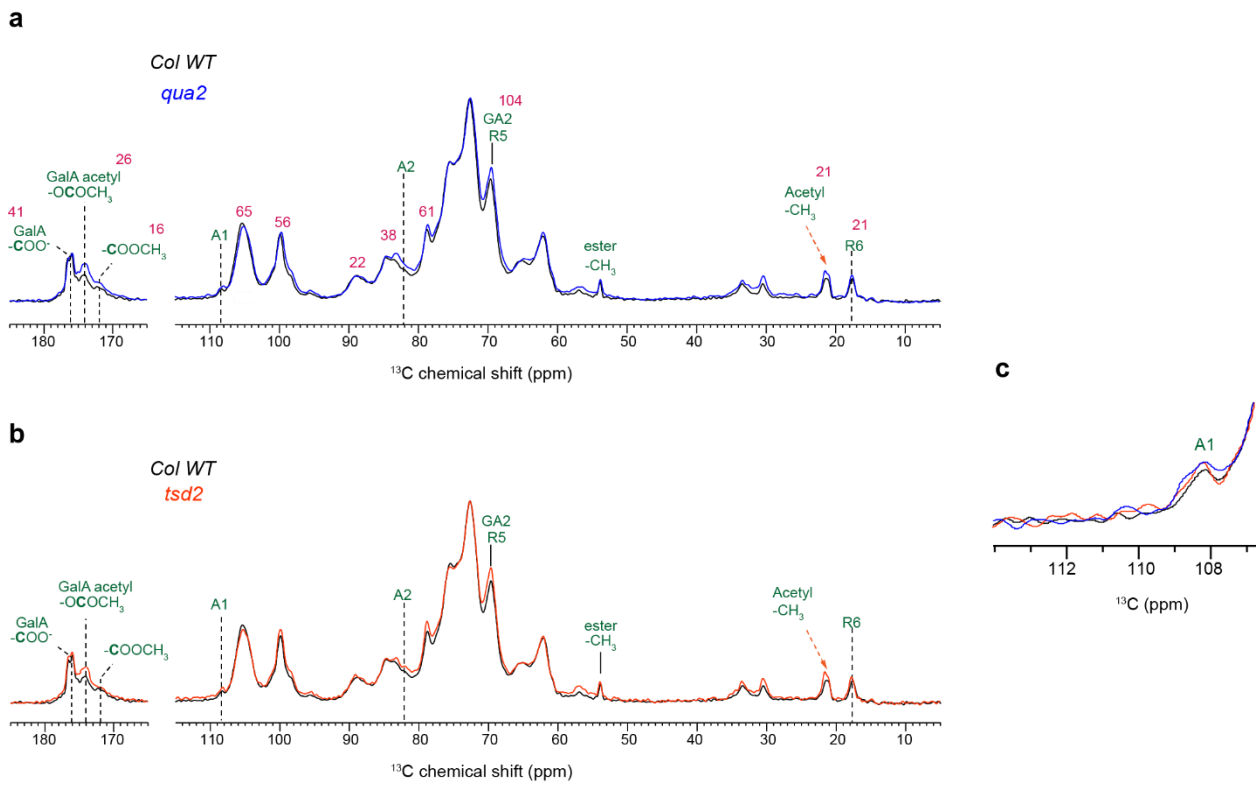

Figure A.3. Comparisons of quantitative ^{13}C DP spectra. Spectral overlays are shown for comparison between a, wild-type and *qua2* samples, and between b, wild-type and *tsd* samples. c, Zoomed-in region of Ara C1 showing the change of arabinose content in different samples. All spectra are processed using the Topspin window function of GM, with parameters of LB = -5 and GB = 0.1. The numbers in magenta are the signal-to-noise ratios at representative carbon sites of the wild-type sample. To account for sample amount differences, spectra were plotted after multiplying the *tsd2* spectral intensities by 1.26 and *qua2* spectral intensities by 0.79.

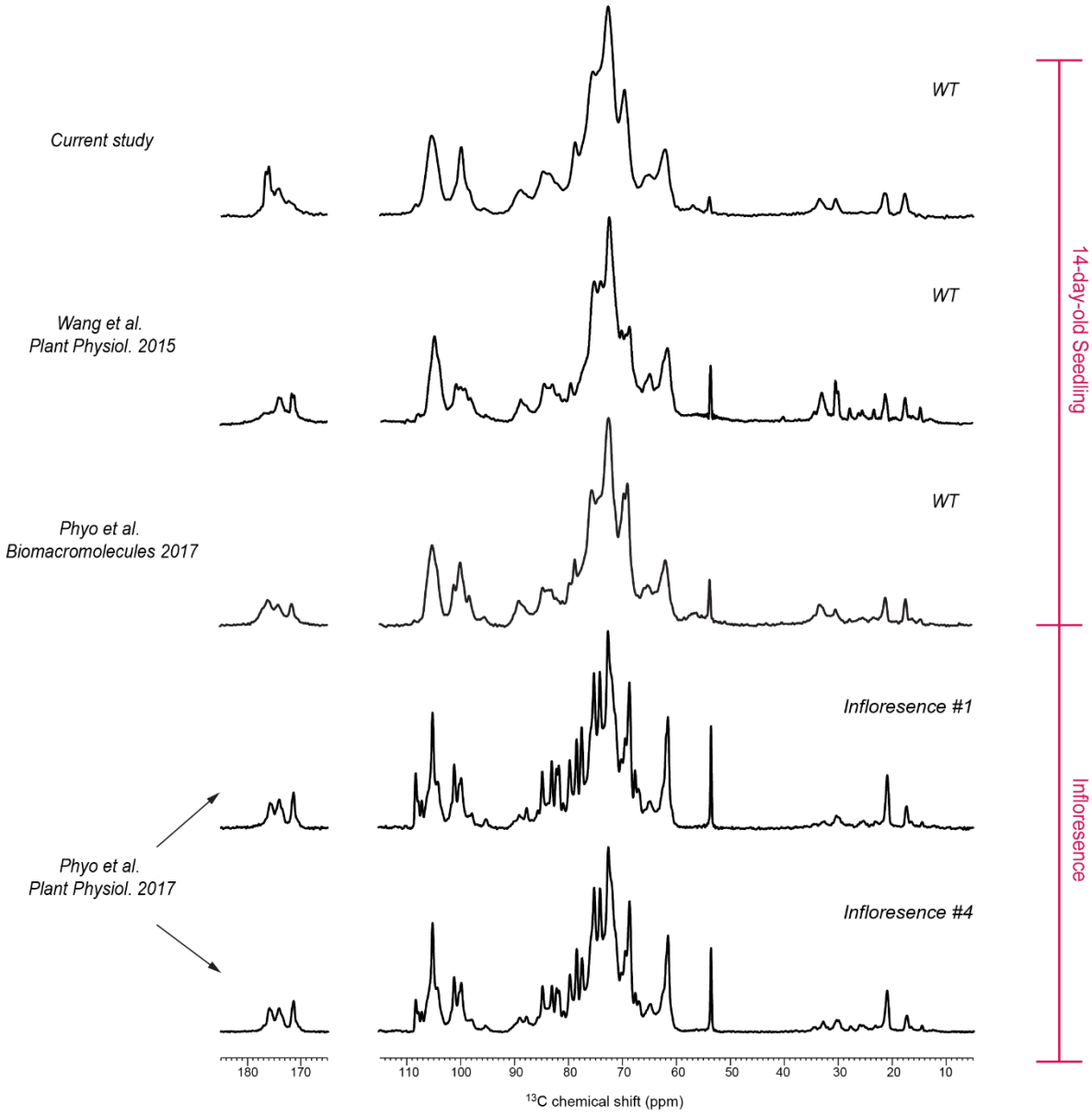

Figure A.4. 1D ^{13}C quantitative DP spectra collected on the seedlings and inflorescence stems of *Arabidopsis*. The spectra were adapted from [61,81,148] with permission.

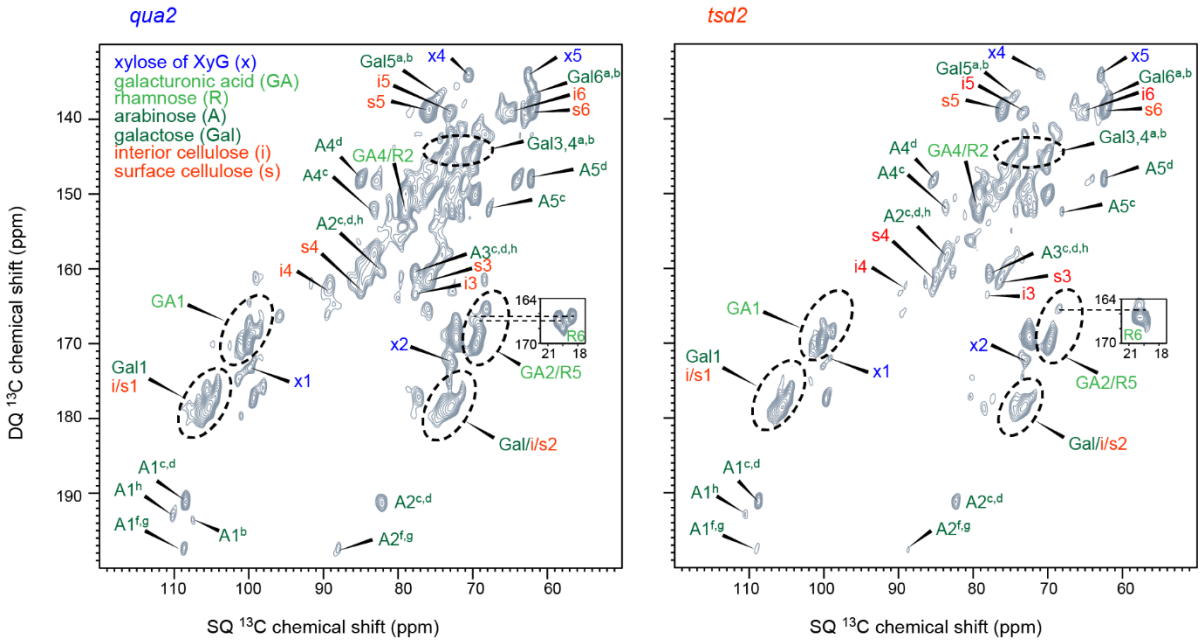

Figure A.5. 2D ^{13}C-DP J-INADEQUATE spectra of pectin mutants. The spectra of *qua2* and *tsd2* samples are shown.

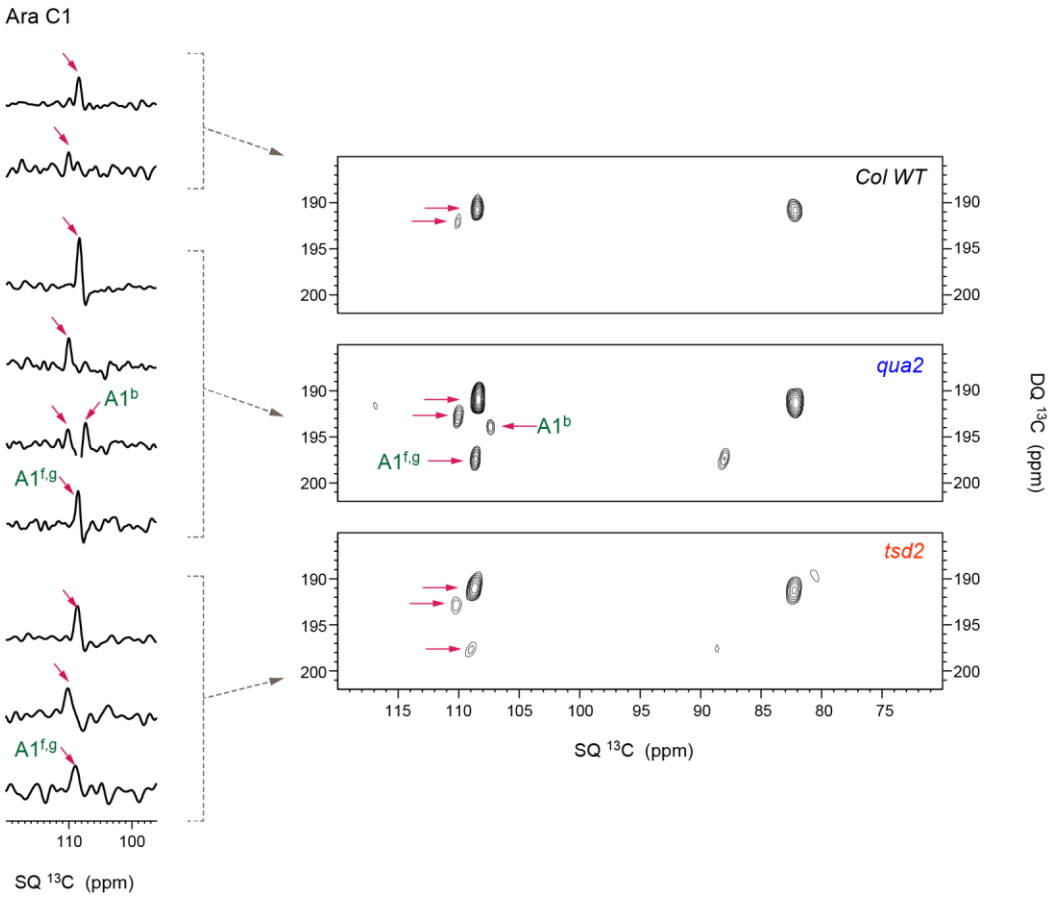

Figure A.6. Arabinose cross sections of ^{13}C-DP J-INADEQUATE spectra. The representative Ara carbon 1 cross sections are extracted from the 2D spectra of wild-type (top), *qua2* (middle), and *tsd2* (bottom) samples to show the typical sensitivity of arabinose peaks. The key residues, such as type-b and type-f,g forms of arabinose are beyond the noise level. Magenta arrows are used to indicate the positions of A1 peaks in the 1D cross sections and corresponding 2D spectra.

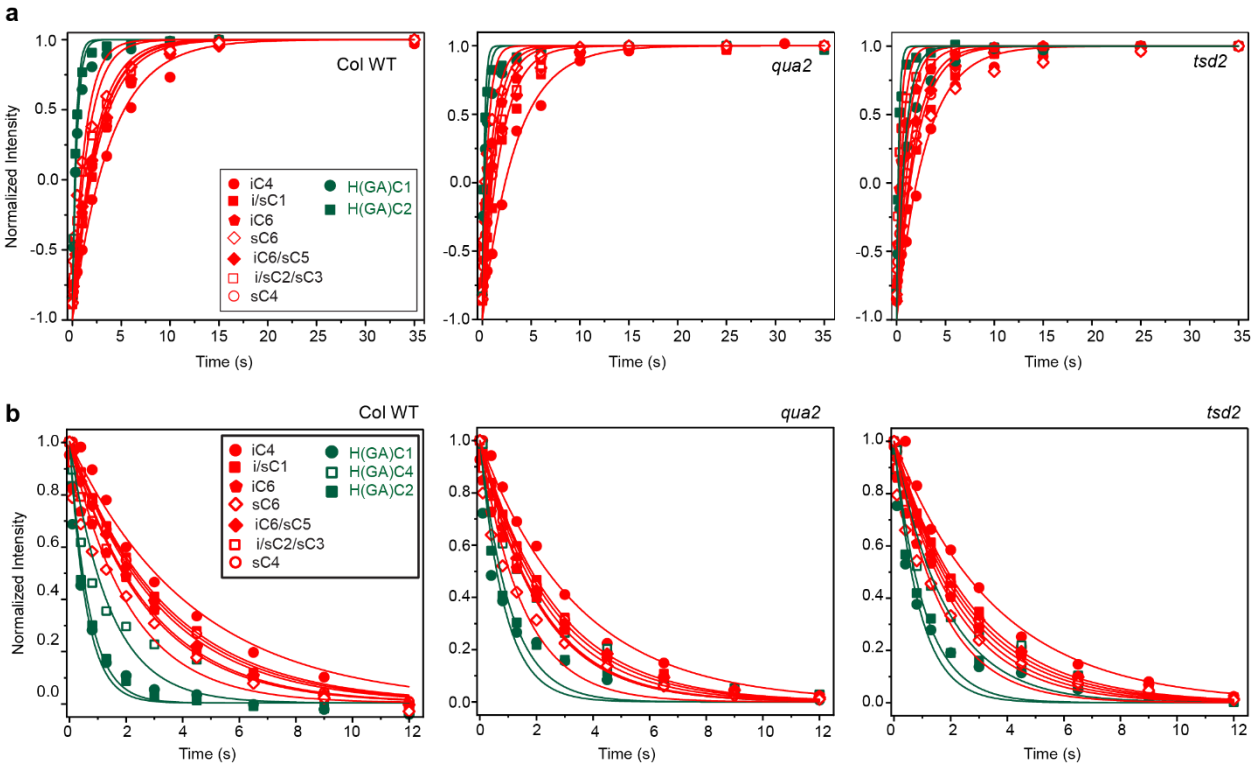

Figure A.7. Relaxation curves of cell wall polysaccharides. a, ^{13}C T_1 measured with Quantitative-DP and the inversion recovery sequence. b, Torchia-CP ^{13}C T_1. Three samples are compared, including the wild-type (left), *qua2* (center), and *tsd2* (right) samples. The fast-relaxing components (dark green) are pectin carbons while the rigid components (red) are from cellulose.

Table A.1. ^{13}C chemical shifts of polysaccharides in primary cell walls. All chemical shifts are referenced to the TMS scale. Not applicable (/). Unidentified (-). The error margin of resonance assignments is typically within 0.5 ppm. The ambiguous assignments due to spectral overlap are underlined.

Carbohydrates		C1	C2	C3	C4	C5	C6	Cell Wall
interior cellulose	i	105.7	73.2	77.9	89.8	73.3	65.1	Col WT
surface cellulose	s	105.7	73.2	77.9	85.1	76.5	62.0	Col WT
interior cellulose	i	105.2	72.9	77.8	89.2	73.0	64.9	*qua2*
surface cellulose	s	105.2	72.9	76.8	84.8	75.8	61.9	*qua2*
interior cellulose	i	105.3	73.1	78.0	89.1	73.1	65.1	*tsd2*
surface cellulose	s	105.3	73.1	76.2	85.0	76.1	62.1	*tsd2*
xylose of xyloglucan	x	100.1	73.1	-	70.8	62.8	/	Col WT
	x	99.9	72.9	-	70.7	62.5	/	*qua2*
	x	99.2	72.9	-	71.0	62.9	/	*tsd2*
galacturonic acid	GA	100.1	69.8	-	-	-	-	Col WT
	GA	100.0	69.5	-	-	-	-	*qua2*
	GA	100.1	69.8	-	-	-	-	*tsd2*
rhamnose	R	100.1	79.3	-	-	69.8	17.6	Col WT
	R	100.1	79.0	-	-	69.5	17.7	*qua2*
	R	100.0	79.1	-	-	69.8	17.6	*tsd2*
galactose	Gal[a,b]	105.7	73.2	70.1	-	74.8	62.6	Col WT
	Gal[a,b]	105.2	72.9	72.9	-	74.9	61.9	*qua2*
	Gal[a,b]	105.3	73.1	73.1	-	74.8	61.9	*tsd2*
arabinose	a	-	-	-	-	-	/	Col WT
	b	-	-	-	-	-	/	
	c	108.8	82.3	-	83.4	68.0	/	
	d	108.8	82.3	-	85.1	62.5	/	
	f	-	-	-	-	-	/	
	g	-	-	-	-	-	/	
	h	110.3	82.3	-	-	-	/	
arabinose	a	-	-	-	-	-	/	*qua2*
	b	107.5	-	-	-	-	/	
	c	108.5	82.1	77.8	-	67.9	/	
	d	108.5	82.1	77.8	-	62.1	/	
	f	108.8	88.1	-	-	-	/	
	g	108.8	88.1	-	-	-	/	
	h	110.4	82.1	77.8	-	-	/	
arabinose	a	-	-	-	-	-	/	*tsd2*
	b	-	-	-	-	-	/	
	c	108.8	82.3	78.9	83.8	68.1	/	
	d	108.8	82.3	78.9	-	-	/	
	f	109.0	88.8	-	-	-	/	
	g	109.0	88.8	-	-	-	/	
	h	110.6	-	78.9	-	-	/	

Table A.2. ^{13}C-T_1 and ^{1}H-$T_{1\rho}$ relaxation times of matrix polysaccharides in primary walls of *qua2* and *tsd2* mutants as well as wild type. The data are fit using single exponential equation: $I\ (t) = e^{-t/T1}$ for ^{13}C-T_1 Torchia CP and ^{1}H-$T_{1\rho}$, and $I\ (t) = 1 - 2e^{-t/T1}$ for standard inversion recovery with quantitative DP. Error bars are standard deviations of the fitting parameters.

	^{1}H $T_{1\rho}$ (ms)				^{13}C T_1 Inversion Recovery (s)			^{13}C T_1 Torchia CP (s)		
	ppm	wild type	*qua2*	*tsd2*	wild type	*qua2*	*tsd2*	wild type	*qua2*	*tsd2*
i/s1	105	55±2	15±1	19±1	2.7±0.2	1.9±0.2	1.9±0.2	3.43±0.04	2.64±0.05	2.75±0.05
GA/R/x1	100	12.3±0.9	4.2±0.5	6.1±0.5	0.36±0.02	0.21±0.02	0.22±0.02	0.68±0.06	1.1±0.1	1.1±0.1
i4	89	63±5	18.9±0.5	23.6±0.8	3.8±0.4	3.4±0.3	2.9±0.3	4.3±0.2	3.4±0.2	3.6±0.2
s4	84	44±2	12.7±0.8	13.6±0.8	2.5±0.2	1.4±0.2	1.4±0.2	3.3±0.2	2.5±0.07	2.6±0.1
GA4/R2	79	12.8±0.8	5.9±0.5	6.7±0.6	-	-	-	1.4±0.2	2.1±0.1	1.8±0.2
i/s3	75	42±2	13.1±0.6	14.4±0.9	2.3±0.2	1.2±0.2	1.1±0.2	2.8±0.1	2.34±0.09	2.5±0.1
i/s5	72.5	39±2	11.7±0.9	14±1	1.6±0.2	0.9±0.1	0.9±0.1	3.17±0.07	2.1±0.1	2.3±0.1
GA/R5	69	12.7±0.9	4.7±0.5	5.1±0.6	0.45±0.04	0.34±0.04	0.35±0.04	0.56±0.08	0.9±0.1	0.9±0.1
i6	65	45±3	14±1	16±1	2.5±0.3	0.8±0.1	0.6±0.1	2.7±0.2	2.1±0.2	2.1±0.2
s6	62.5	42±2	11.2±0.7	12.3±0.8	1.3±0.2	0.5±0.1	1.8±0.3	2.1±0.3	1.5±0.2	1.7±0.2

APPENDIX A. LETTER OF PERMISSION FOR CHAPTER 2

From: JoVE <no-reply@jove.com>

Sent: Friday, November 26, 2021 9:09 PM

To: Alex K Kirui <akirui1@lsu.edu>

Subject: JoVE Reprint Permissions: Article 59152

jove

Hi Alex,

Thank you for publishing your article Preparation of Fungal and Plant Materials for Structural Elucidation Using Dynamic Nuclear Polarization Solid-State NMR with JoVE.

You have permission to reuse the following material from it in your thesis or dissertation, pursuant to your Author License Agreement:

Figure(s):
1, 2

Table(s):
1

Text:
All

Please ensure that JoVE is properly cited in the legends as well as the References: "This is adapted from Kirui, A., Dickwella Widanage, M. C., Mentink-Vigier, F., Wang, P., Kang, X., Wang, T. Preparation of Fungal and Plant Materials for Structural Elucidation Using Dynamic Nuclear Polarization Solid-State NMR. *J. Vis. Exp.* (144), e59152, doi:10.3791/59152 (2019)."

Best regards,

Review
JoVE
617.674.1888
Follow us: Facebook | Twitter | LinkedIn
About JoVE

This message was sent to you by JoVE, the Journal of Visualized Experiments.
JoVE, 625 Massachusetts Ave., 2nd Floor, Cambridge, MA 02139 | tel: 617.945.9051 | fax: 866.381.2236

Click the following links if you no longer want to receive emails from JoVE or to learn more about our policies.

APPENDIX B. LETTER OF PERMISSION FOR CHAPTER 3

SPRINGER NATURE LICENSE
TERMS AND CONDITIONS

Dec 07, 2021

This Agreement between Louisiana State University -- Alex Kirui ("You") and Springer Nature ("Springer Nature") consists of your license details and the terms and conditions provided by Springer Nature and Copyright Clearance Center.

License Number	5203910325224
License date	Dec 07, 2021
Licensed Content Publisher	Springer Nature
Licensed Content Publication	Cellulose
Licensed Content Title	Atomic resolution of cotton cellulose structure enabled by dynamic nuclear polarization solid-state NMR
Licensed Content Author	Alex Kirui et al
Licensed Content Date	Nov 11, 2018
Type of Use	Thesis/Dissertation
Requestor type	academic/university or research institute
Format	print and electronic
Portion	full article/chapter

APPENDIX C. LETTER OF PERMISSION FOR CHAPTER 4

12/7/21, 7:53 PM RightsLink® by Copyright Clearance Center

RightsLink

Home | Help | Email Support | Sign in | Create Account

A pectin methyltransferase modulates polysaccharide dynamics and interactions in Arabidopsis primary cell walls: Evidence from solid-state NMR

Author:
Alex Kirui,Juan Du,Wancheng Zhao,William Barnes,Xue Kang,Charles T. Anderson,Chaowen Xiao,Tuo Wang

Publication: Carbohydrate Polymers

Publisher: Elsevier

Date: 15 October 2021

© 2021 Elsevier Ltd. All rights reserved.

Journal Author Rights

Please note that, as the author of this Elsevier article, you retain the right to include it in a thesis or dissertation, provided it is not published commercially. Permission is not required, but please ensure that you reference the journal as the original source. For more information on this and on your other retained rights, please visit: https://www.elsevier.com/about/our-business/policies/copyright#Author-rights

BACK CLOSE WINDOW

© 2021 Copyright - All Rights Reserved | Copyright Clearance Center, Inc. | Privacy statement | Terms and Conditions
Comments? We would like to hear from you. E-mail us at customercare@copyright.com

APPENDIX D. SUPPORTING INFORMATION FOR CHAPTER 5

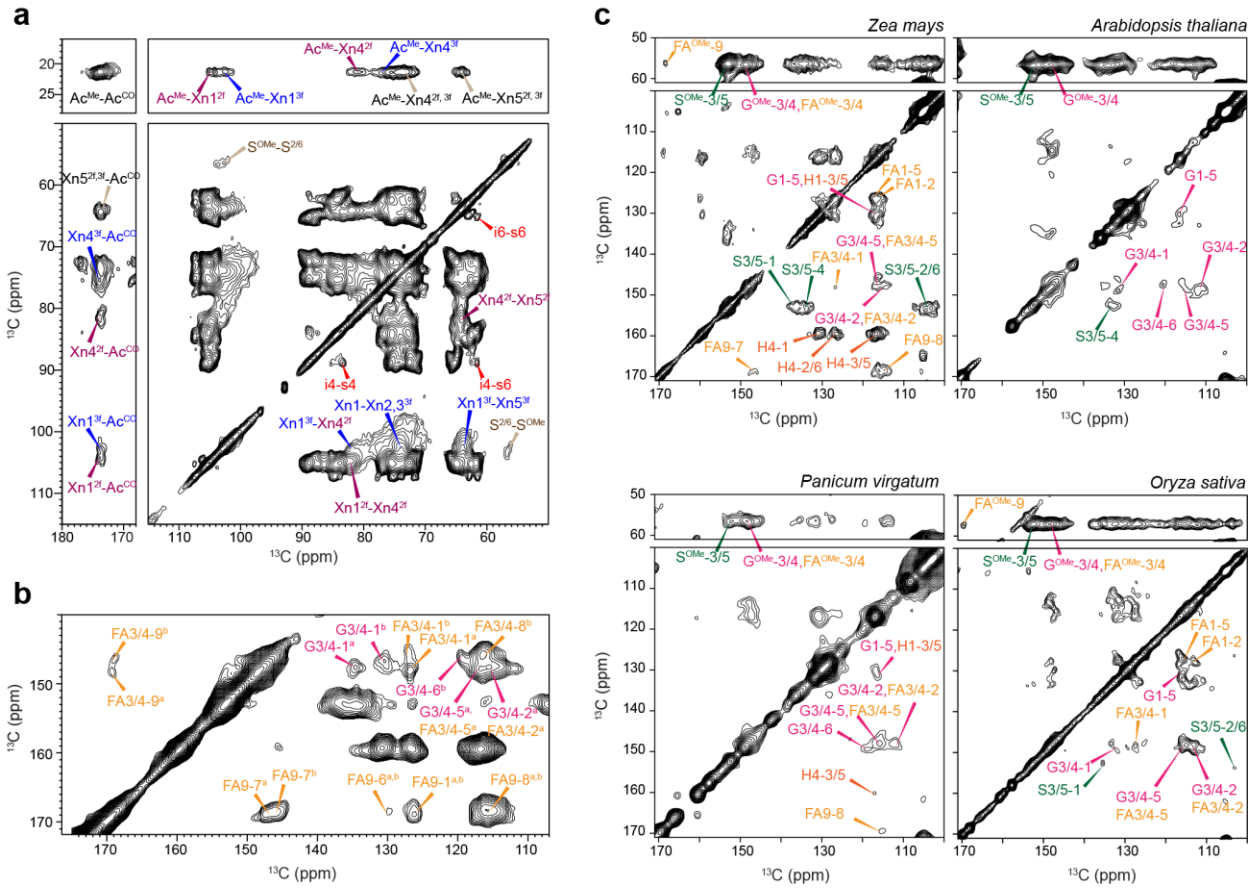

Figure D.1. Structural and compositional heterogeneity of secondary cell walls. (a) Two-fold and three-fold xylan have distinct chemical shifts as shown in 100 ms DARR spectra of *Zea mays*. The well-resolved signals of 2-fold and 3-fold xylans are labeled in purple and blue, respectively. (b) Structural polymorphism of lignin residues. Two subtypes have been resolved for both G and FA as annotated using superscript a and b. (c) The lignin regions of 2D DARR spectra of the secondary cell walls of four different plants. Compared with the *Zea mays* (maize), *Arabidopsis thaliana* does not have FA, the *Panicum virgatum* (switchgrass) has reduced amount of S and the *Oryza sativa* (rice) has negligible H signals.

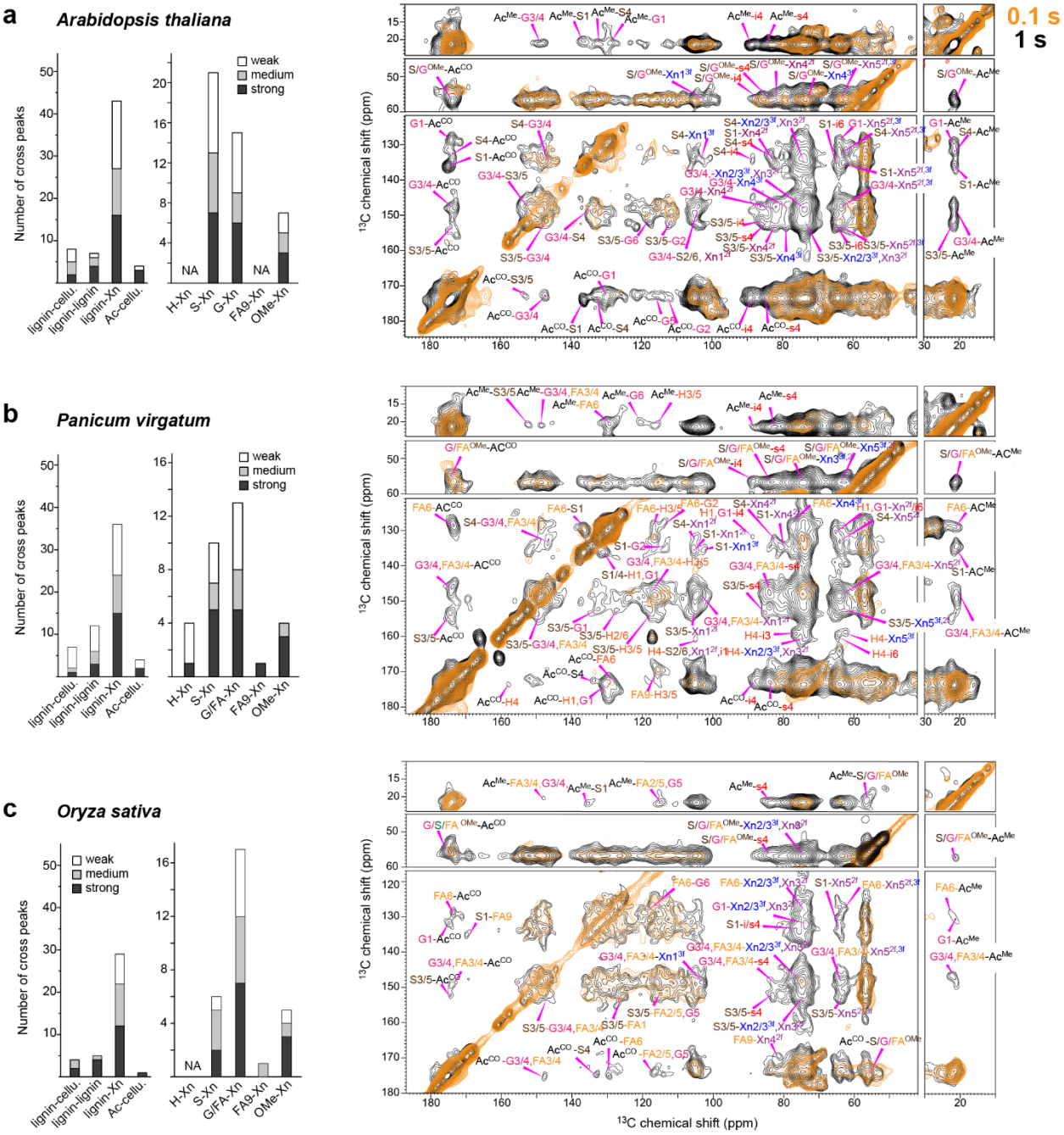

Figure D.2. Intermolecular interactions of polymers in intact plant stems. The summary bar diagrams and the gated 2D ^{13}C-^{13}C correlation spectra are shown for (a) *Arabidopsis thaliana*, (b) *Panicum virgatum* (switchgrass), and (c) *Oryza sativa* (rice). 100 ms spectra (yellow) mainly detect the intramolecular correlations, and the 1 s (black) spectra show many intermolecular cross peaks. Note that the FA/G is only G in *Arabidopsis*. Only the intermolecular cross peaks are labeled. Source data are provided as a Source Data file.

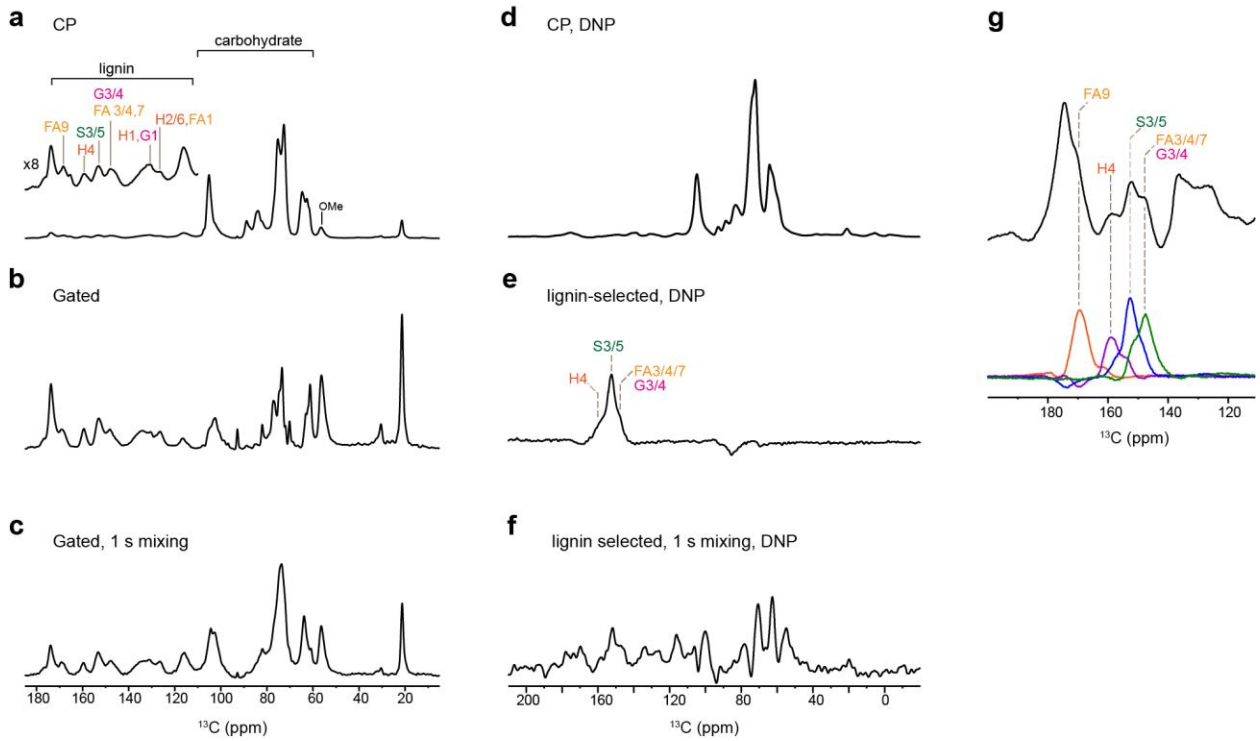

Figure D.3. Selection of lignin signals using dipolar and frequency filters. (a) Representative 1D ^{13}C CP spectrum shows predominant signals of carbohydrates. (b) The gated spectrum enhances the relative intensity of lignins. (c) Gated spectrum with 1 s PDSD mixing time to transfer polarization from lignins to carbohydrates. (d) DNP-enhanced ^{13}C CP spectrum. (e) DNP-assisted lignin edited spectrum using dipolar and frequency filters cleanly select the lignin signals against the dominant carbohydrate peaks. (f) DNP-assisted lignin selected spectra with 1 s mixing time. The selected signals have contributions from all the four major lignin units and is used for measuring lignin-edited 2D ^{13}C-^{13}C correlation spectra. (g) DNP-assisted single-site selection using the dipolar and frequency filters. The DNP spectra were measured on a 600 MHz/395 GHz spectrometer under 10 kHz MAS.

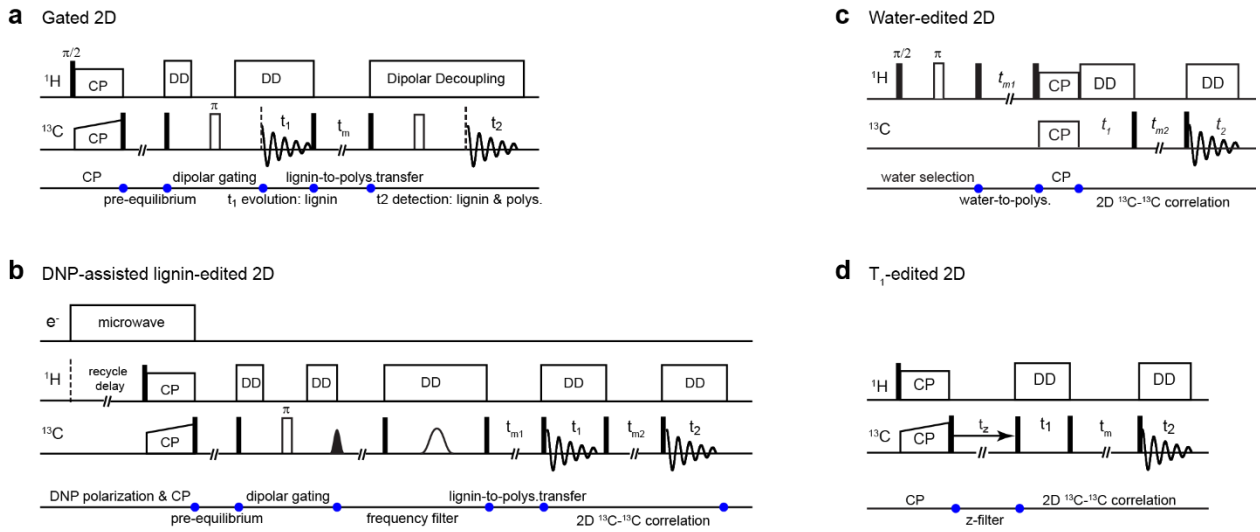

Figure D.4. NMR pulse sequences for determining lignin-carbohydrate interactions. (a) Gated 2D ^{13}C-^{13}C correlation experiment for detecting lignin-carbohydrate correlations, (b) DNP-assisted lignin-edited 2D ^{13}C-^{13}C correlation experiment that shows the signals of lignin-proximal carbohydrates. A shutter is used to regulate the duration of microwave. (c) Water-edited 2D ^{13}C-^{13}C correlation experiment, (d) 2D ^{13}C-^{13}C correlation experiment with z-filter time for measuring ^{13}C-T_1.

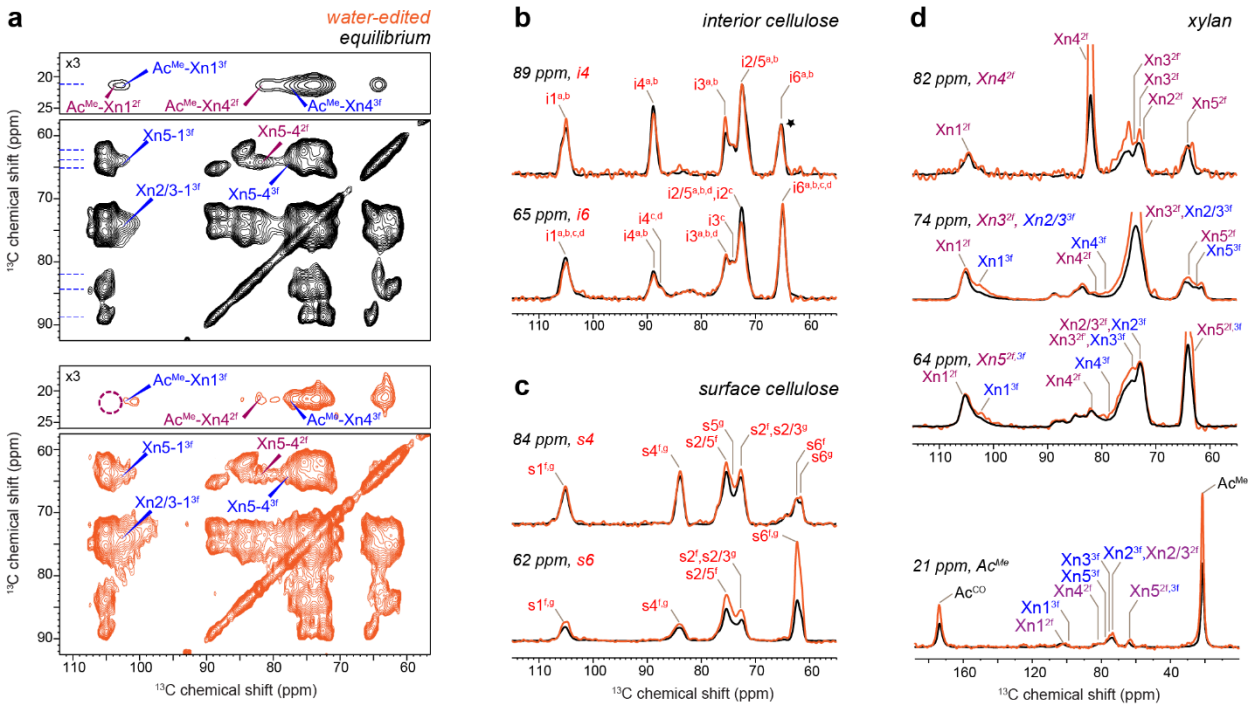

Figure D.5. Water-edited 2D ^{13}C-^{13}C correlation spectra of maize**.** (a) Comparison of 2D water-edited (orange) and control (black) ^{13}C-^{13}C correlation spectra. The plotting base level is 3-times higher for polysaccharides than the acetyl region. The blue dash lines indicate the positions at which the ^{13}C cross sections are extracted and compared. The Representative 1D ^{13}C cross sections are categorized as (b) interior cellulose, (c) surface cellulose and (d) xylan. All the cross sections are normalized by the i4-6 peak (asterisk). The 3-fold xylan has enhanced intensity in the water-edited spectra, indicating better interactions with water molecules.

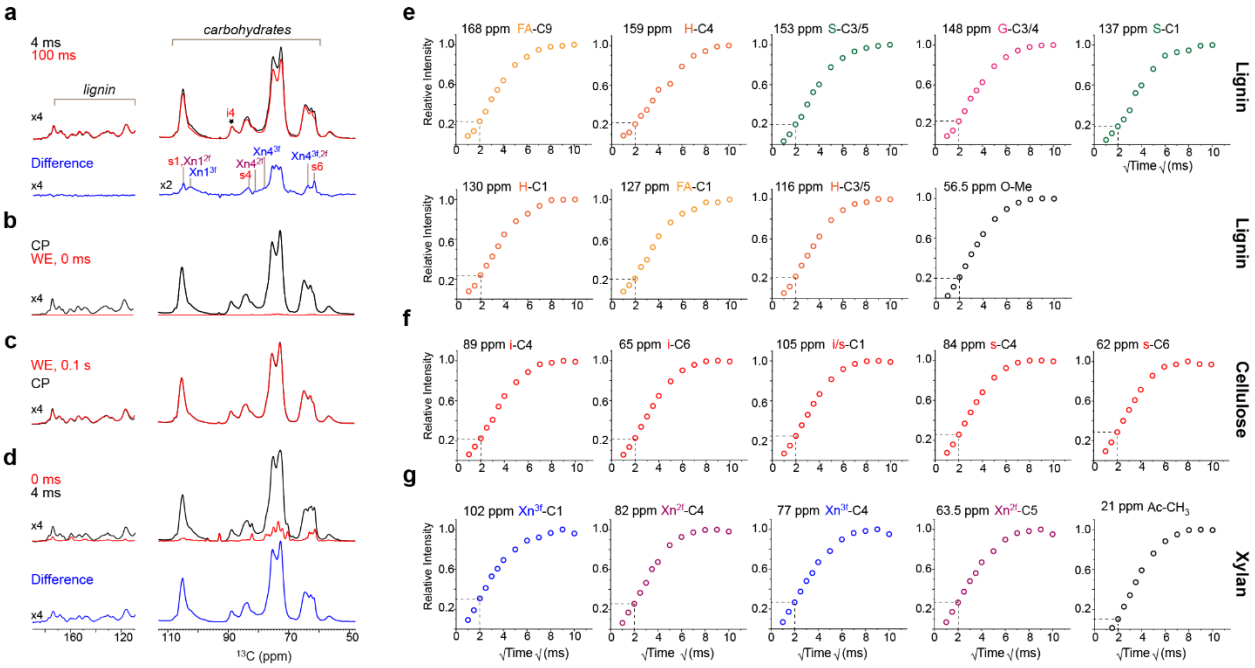

Figure D.6. Water-to-polysaccharide/lignin buildup curves of *Zea mays*. (a) Water-edited (WE) spectra measured with different mixing times. The 4-ms spectrum detects the hydrated molecules and the 100-ms spectrum report equilibrium intensities. the difference spectrum only shows well-hydrated molecules, thus are lacking the hydrophobic lignin and cellulose. (b) More than 98% of cell wall signals are removed by a ^{1}H-T_2 filter in the water-edited spectrum without ^{1}H-mixing. (c) The 100 ms ^{1}H-mixing restores the equilibrium intensity in the water-edited ^{13}C spectrum (red) with a spectral pattern identical to the equilibrium intensity of the CP spectrum (black). (d) Subtraction of 1D water-edited ^{13}C spectra with 0 (red) and 4 ms (black) helps eliminate the original signal that survives through the ^{1}H-T_2 filter. The water ^{1}H spin diffusion curves for (e) lignin, (f) cellulose and (g) xylan are shown. Dashlines indicate the intensities of 4-ms spectra. The best-hydrated 3-fold xylan has the fastest spin diffusion from water, with ~30% of the equilibrium intensity detected at 4-ms 1H mixing, followed by the 2-fold xylan and surface cellulose (~25%), and then interior cellulose and lignin (~20%). Lignin and internal cellulose are most hydrophobic. These intensities are clearly weaker than those of pectin (60-80%) and cellulose (30-40%) in primary cell walls.

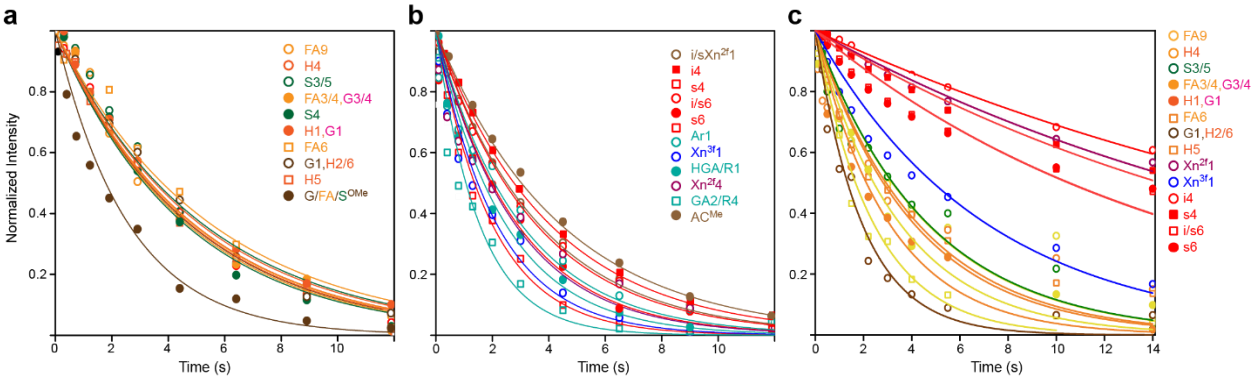

Figure D.7. Representative ^{13}C-T_1 and ^{1}H-$T_{1\rho}$ relaxation curves for *Zea mays*. The ^{13}C-T_1 relaxation curves of (a) lignin and (b) polysaccharides are shown. (c) ^{1}H-$T_{1\rho}$ relaxation curves of lignin and polysaccharides. The data are collected on a 400 MHz spectrometer and are fitted using single exponential equations: $I(t) = 1 - e^{-t/T_{1b}}$. The fit parameters are summarized in Supplementary Table 5.8-5.10. Source data are provided as a Source Data file.

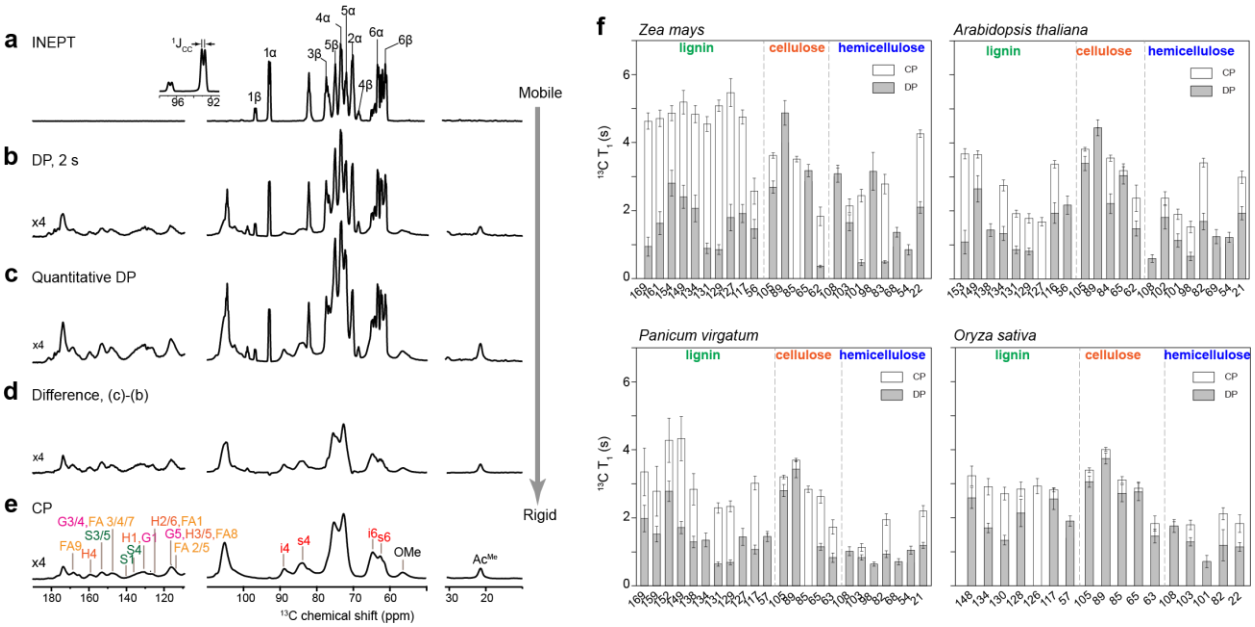

Figure D.8. The dynamical profile of molecules in intact *Zea mays* stems as resolved using 1D ^{13}C spectra and NMR relaxations. (a) ^{13}C INEPT spectrum shows only the signals of highly mobile carbohydrates such as the α- and β-glucose. ^{13}C-^{13}C J-couplings can be resolved as shown. (b) ^{13}C DP spectrum measured with 2-s recycle delays detects mobile molecules showing major signals from glucose, moderate signals of lignins and starch, and minor signals of polysaccharides. (c) Quantitative ^{13}C DP measured with 40-s recycle delays. (d) The difference of ^{13}C DP spectra with 35-s and 2-s recycle delays shows signals of the rigid components. (e) ^{13}C CP spectrum detects the rigid molecules of the cell walls. Substantial signals of lignins are identified in both 2-s DP and CP spectra, thus lignin is dynamically heterogeneous. (f) ^{13}C-T_1 relaxation times of lignin and polysaccharides in four plants. The open and filled bars represent the ^{13}C-T_1 relaxation times measured using Torchia CP (open) and the standard inversion recovery with quantitative DP (filled). The CP version preferentially detects the rigid molecules and the DP version provides quantitative detection. Error bars are standard deviations of the fitting parameters. Lignins show the highest variation of ^{13}C-T_1 in the CP and quantitative DP detection, indicating the presence of both highly mobile and rigid domains.

Table D.1. Cellulose composition in the primary and secondary cell walls of *Zea mays.* The percentages are calculated using the integrated intensities of C4-C1 and C4-C6 cross peaks. The glucose C6 conformation is an indicator of the hydrogen bonding pattern among glucan chains within the microfibril[307]. Among the seven major cellulose allomorphs, the internal chains a-e adopt trans-gauche (tg) conformation while surface residues g and f primarily adopt the gt conformation, with minor contributions from gg conformers[98]. The increased intensity of type-c cellulose, the dehydrated chains in tg conformation[22,98], indicate conversion of surface chains in gt/gg conformation into tg conformers on the aggregation interface of two cellulose microfibrils.

crystalline and disordered cellulose							
	a	b	c	d	e	f	g
coleoptile	9%	11%	**3%**	8%	2%	31%	36%
stem	9%	19%	**6%**	5%	1%	27%	34%
crystalline cellulose							
	a	b	c	d	e		
coleoptile	27%	32%	**10%**	24%	6%		
stem	22%	47%	**15%**	12%	4%		

Table D.2. ^{13}C chemical shifts of polysaccharides and lignins in secondary plant cell walls. Superscripts are used to denote different allomorphs. Underline denotes the ^{13}C connectivity with ambiguity. Weak signals or minor species are indicated using "w." Not applicable (/). Unidentified (-).

	Lignins	C1	C2	C3	C4	C5	C6	OMe	C7	C8	C9	Plant
H	*p*-hydroxyphenyl	131.0	126.9	116.0	159.4	116.0	126.9	/	/	/	/	*Z. mays*
H		130.2	127.0	116.3	159.5	116.3	127.0	/	/	/	/	*P. virgatum*
G^a		130.1	113.8	148.5	148.5	115.0	-	56.1	/	/	/	*Z. mays*
G^b	guaiacyl	134.6	-	148.5	148.5	-	-	56.1	/	/	/	*Z. mays*
G^a		132.1	114.5	146.2	146.2	114.5	-	56.7	/	/	/	*A. thaliana*
G^b		134.8	111.5	147.4	147.4	115.8	120.4	56.7	/	/	/	*A. thaliana*
G		132.7	113.3	148.4	148.4	-	120.5	57.0	/	/	/	*P. virgatum*
G		131.6	-	148.2	148.2	115.5	119.6	56.9	/	/	/	*O. sativa*
S	syringyl	136.5	104.1	153.1	134.3	153.1	104.1	56.1	/	/	/	*Z. mays*
S		136.2	105.5	152.7	134.5	152.7	105.5	56.7	/	/	/	*A. thaliana*
S		137.5	104.9	153.4	133.5	153.4	104.9	57.0	/	/	/	*P. virgatum*
S		135.3	-	153.4	133.3	153.4	-	56.9	/	/	/	*O. sativa*
FA^a	ferulate	126.0	114.7	147.8	147.8	114.7	130.4	56.5	147.8	116.0	168.8	*Z. mays*
FA^b		126.3	115.0	145.5	145.5	115.0	130.6	56.4	145.5	116.3	168.0	*Z. mays*
FA		128.9	-	148.0	148.0	-	-	57.0	148.0	-	169.4	*P. virgatum*
FA		129.0	115.5	147.9	147.9	115.5	127.4	56.9	-	116.7	169.7	*O. sativa*
	Polysc.	C1	C2	C3	C4	C5	C6	AC^{CO}	AC^{Me}			
Xn^{2f}	2-fold xylan	-	-	74.4	82.7	64.9	/	-	-			*Z. mays*
Xn^{2f}	2-fold xylan	105.1	72.5	73.5	82.3	64.6	/	174.0	21.0			
Xn^{2f}	2-fold xylan	105.1	72.5	74.0	81.5	64.0	/	-	-			
Xn^{3f}	3-fold xylan	102.5	73.5	74.5	78.0	62.5	/	174.0	21.0			
	Cellulose	C1	C2	C3	C4	C5	C6					
i	type a	105.8	71.5	75.8	89.1	72.5	64.9					*Z. mays*
i	type b	105.1	72.9	74.1	89.1	72.5	65.0					
i	type c	104.2	71.1	-	87.9	-	65.8					
i	type d	105.4	72.8	75.2	87.2	72.5	64.9					
i	type e (w)	105.4	72.1	-	89.9	72.1	65.3					
s	type f	105.2	72.7	75.8	84.3	75.4	62.5					
s	type g	106.1	73.0	73.1	83.5	74.6	61.5					

Table D.3. Relative intensities of intermolecular cross peaks of *Zea mays*. The intensities are relative ratios of the peak area normalized by the integral of a ^{13}C cross-section. For gated 1-s PDSD peaks higher than 5% are categorized as strong restraints (s, in bold), >2.5% for medium (m) restraints and below 2.5% for weak (w) restraints. All the peaks in the gated 100-ms PDSD spectrum are strong restraints. In total, 74 restraints are identified, including 26 strong restraints, 24 medium ones and 24 weak restraints.

	Atom1 (ω_1)	Atom2 (ω_2)	Gated 100 ms PDSD (%)	Gated 1s PDSD (%)	Type
lignin-cellulose	$S/G/FA^{OMe}$	i4		0.69	w
	S3/5	i4		2.66	m
	S3/5	i6	**1.91**	3.44	s
	$S/G/FA^{OMe}$	s4	**0.79**	1.25	s
	S3/5	s6	**1.27**	2.19	s
	FA9	s4		2.21	w
xylan-cellulose	Ac^{Me}	i4		0.79	w
	Ac^{Me}	s4		2.01	w
	Ac^{CO}	i4		0.50	w
	Ac^{CO}	s4		1.90	w
lignin-lignin	$S/G/FA^{OMe}$	H4		0.63	w
	H1,G1	FA9		4.57	m
	H1,G1	G3/4,FA3/4		**7.84**	s
	H1,G1	S2/6		**5.13**	s
	S4	FA9		**5.37**	s
	S4	H3/5,FA8,G5		**5.42**	s
	S1	G3/4,FA3/4		4.81	m
	G3/4,FA3/4	S3/5		**7.25**	s
	G3/4,FA3/4	S4		**5.57**	s
	S3/5	FA9		2.71	m
	S3/5	H4		1.49	w
	S3/5	G3/4,FA3/4		3.54	m
	S3/5	H1,G1		2.84	m
	S3/5	H2/6		3.31	m
	H4	S3/5		4.40	m
	H4	G3/4,FA3/4		4.20	m
	FA9	S3/5		2.27	w
syringyl-xylan	Ac^{Me}	S3/5		0.83	w
	Ac^{Me}	S4		0.66	w
	S4	Ac^{Me}		3.49	m
	S1	$Xn1^{3f}$		**8.46**	s
	S1	$Xn4^{2f}$		3.66	m
	S1	$Xn2/3^{3f}$,$Xn3^{2f}$		**5.96**	s
	S3/5	Ac^{CO}		1.60	w
	S3/5	$Xn1^{3f}$		**5.77**	s
	S3/5	$Xn4^{2f}$	**2.88**	**5.49**	s
	S3/5	$Xn4^{3f}$		3.09	m
	S3/5	$Xn2/3^{3f}$,$Xn3^{2f}$	**4.40**	**7.57**	s
	S3/5	$Xn5^{2f,3f}$	**2.58**	**5.57**	s
	S3/5	Ac^{Me}		3.25	m
	Ac^{CO}	S3/5		0.47	w

(table cont'd.)

	Atom1 (ω_1)	Atom2 (ω_2)	Gated 100 ms PDSD (%)	Gated 1s PDSD (%)	Type
p-hydroxyphenyl-xylan	H4	$Xn4^{2f}$		4.18	m
	H4	$Xn4^{3f}$		1.99	w
	H4	$Xn2/3^{3f}$,$Xn3^{2f}$	**2.47**	**17.40**	s
	H4	$Xn5^{2f,3f}$		**7.36**	s
	H4	Ac^{Me}		**5.33**	s
	Ac^{CO}	H2/6		0.46	w
ferulate-xylan	Ac^{Me}	FA9		1.19	w
	FA9	Ac^{CO}		2.65	m
	FA9	$Xn4^{2f}$		3.22	m
	FA9	$Xn2/3^{3f}$,$Xn3^{2f}$	**5.93**	**27.46**	s
	FA9	$Xn5^{2f,3f}$		**12.04**	s
	FA9	Ac^{Me}	**4.65**	**5.00**	s
OMe-xylan	Ac^{Me}	$S/G/FA^{OMe}$		2.09	w
	$S/G/FA^{OMe}$	Ac^{CO}		1.28	w
	$S/G/FA^{OMe}$	$Xn4^{2f}$	**1.48**	2.76	s
	$S/G/FA^{OMe}$	$Xn4^{3f}$	**0.94**	2.33	s
	$S/G/FA^{OMe}$	$Xn5^{2f,3f}$	**1.99**	**10.26**	s
	$S/G/FA^{OMe}$	Ac^{Me}		3.00	m
	Ac^{CO}	$S/G/FA^{OMe}$		3.07	m
G/FA (ring)-xylan	Ac^{Me}	G3/4,FA3/4		0.48	w
	G3/4,FA3/4	$Xn4^{2f}$		2.63	m
	G3/4,FA3/4	$Xn4^{3f}$		2.54	m
	G3/4,FA3/4	$Xn5^{2f,3f}$		4.23	m
	G3/4,FA3/4	Ac^{Me}		**5.18**	s
lignin (mixed)-xylan	Ac^{Me}	H2/6,FA1,G5		1.14	w
	Ac^{Me}	H3/5,FA8,G5		2.26	w
	H2/6,FA1	$Xn2/3^{3f}$,$Xn3^{2f}$		**5.16**	s
	H2/6,FA1	$Xn5^{2f,3f}$		3.91	m
	H2/6,FA1	Ac^{Me}		2.33	w
	Ac^{CO}	H3/5,FA8,G5		1.58	w
	H1,G1	$Xn5^{2f,3f}$		2.68	m
	H1,G1	Ac^{Me}		3.13	m
	Ac^{CO}	H1,G1		0.46	w

Table D.4. Relative intensities of intermolecular cross peaks of *Arabidopsis thaliana*. The intensities are relative ratios of the peak area normalized by the integral of a ^{13}C cross-section. For gated 1-s PDSD, a peak higher than 5% is categorized as a strong restraint (s, in bold), >2.5% for medium (m) restraints and below 2.5% for weak (w) restraints. All the peaks in the gated 100-ms PDSD spectrum are strong restraints. In total, 62 restraints are identified, including 23 strong restraints, 16 medium ones and 23 weak restraints.

	Atom1 (ω_1)	Atom2 (ω_2)	100 ms Gated PDSD (%)	1s Gated PDSD (%)	Type
G/S-cellulose	S/G^{OMe}	i4	**1.70**	1.01	s
	S/G^{OMe}	s4	**1.48**	2.19	s
	S4	i4		2.10	w
	S4	s4		4.39	m
	S1	i6		2.11	w
	S3/5	i4		1.05	w
	S3/5	s4		4.33	m
	S3/5	i6		2.53	m
xylan-cellulose	Ac^{Me}	i4		1.06	w
	Ac^{Me}	s4	**0.62**	4.73	s
	Ac^{CO}	i4		1.65	w
	Ac^{CO}	s4		1.79	w
lignin-lignin	S4	G3/4	**5.31**	**5.94**	s
	G3/4	S3/5	**1.04**	1.47	s
	G3/4	S4	**1.09**	1.68	s
	G3/4	$S2/6,Xn1^{3f}$		3.72	m
	S3/5	G3/4	**4.31**	2.59	s
	S3/5	G6		3.02	m
	S3/5	G2		0.78	w
Guaiacyl (ring)-xylan	Ac^{Me}	G1		0.50	w
	G1	Ac^{CO}		**5.37**	s
	G1	$Xn5^{2f,3f}$		**5.34**	s
	G1	Ac^{Me}		**5.83**	s
	Ac^{CO}	G3/5		0.63	w
	Ac^{CO}	G1	**0.45**	1.53	s
	Ac^{CO}	G5		0.34	w
	Ac^{CO}	G2		0.46	w
	G3/4	Ac^{CO}		4.46	m
	G3/4	$Xn4^{2f}$		4.11	m
	G3/4	$Xn4^{3f}$		1.73	w
	G3/4	$Xn5^{2f,3f}$	**0.89**	**8.42**	s
	G3/4	$Xn2/3^{2f,3f},Xn3^{3f}$		**19.52**	s
	G3/4	Ac^{Me}		3.43	m
	Ac^{Me}	G3/4		1.00	w
syringyl-xylan	Ac^{Me}	S1		0.50	w
	Ac^{Me}	S4		0.74	w
	S4	Ac^{CO}		4.13	m
	S4	$Xn1^{3f}$		1.93	w
	S4	$Xn2/3^{2f,3f},Xn3^{3f}$		**11.68**	s
	S4	$Xn4^{3f}$		**6.70**	s
	S4	$Xn5^{2f,3f}$		**6.81**	s
	S4	Ac^{Me}		3.10	m

(table cont'd.)

.

	Atom1 (ω_1)	Atom2 (ω_2)	100 ms Gated PDSD (%)	1s Gated PDSD (%)	Type
syringyl-xylan	S1	Ac^{CO}		**6.77**	s
	S1	$Xn4^{2f}$		4.29	m
	S1	$Xn5^{2f,3f}$		4.14	m
	S1	Ac^{Me}		3.22	m
	S3/5	Ac^{CO}		2.07	w
	S3/5	$Xn4^{2f}$		2.51	m
	S3/5	$Xn4^{3f}$		1.97	w
	S3/5	$Xn5^{2f,3f}$	**2.37**	**5.75**	s
	S3/5	$Xn2/3^{2f,3f}$,$Xn3^{3f}$		**20.69**	s
	S3/5	Ac^{Me}		**5.26**	s
	Ac^{CO}	S3/5		0.57	w
	Ac^{CO}	S1		0.59	w
	Ac^{CO}	S4		0.86	w
OMe-xylan	S/G^{OMe}	Ac^{CO}		4.55	m
	S/G^{OMe}	$Xn1^{3f}$		2.23	w
	S/G^{OMe}	$Xn4^{2f}$		2.05	w
	S/G^{OMe}	$Xn4^{3f}$	**2.02**	1.90	s
	S/G^{OMe}	$Xn2/3^{2f,3f}$,$Xn3^{3f}$	**3.89**	**18.07**	s
	S/G^{OMe}	$Xn5^{2f,3f}$	**2.04**	**7.06**	s
	S/G^{OMe}	Ac^{Me}		2.62	m

Table D.5. Relative Intensities of intermolecular cross peaks of *Panicum virgatum.* The intensities are relative ratios of the peak area normalized by the integral of a ^{13}C cross-section. For gated 1-s PDSD, a peak higher than 5% is categorized as a strong restraint (s, in bold) and >2.5% for medium (m) restraints and below 2.5% for weak (w) restraints. All the peaks in the gated 100-ms PDSD spectrum are strong restraints. In total, 59 restraints are identified, including 19 strong restraints, 13 medium ones and 25 weak restraints.

	Atom1 (ω_1)	Atom2 (ω_2)	Gated 100 ms PDSD (%)	Gated 1s PDSD (%)	Type
lignin-cellulose	$S/G/FA^{OMe}$	i4		1.76	w
	H1,G1	i4		1.46	w
	H4	i3		**11.06**	s
	H4	i6		2.60	w
	G3/4,FA3/4	i4		2.17	w
	$S/G/FA^{OMe}$	s4		2.85	w
	S3/5	s4		3.28	m
xylan-cellulose	Ac^{Me}	i4		0.94	w
	Ac^{Me}	s4		2.60	m
	Ac^{CO}	i4		0.70	w
	Ac^{CO}	s4		4.00	m
lignin-lignin	S1	G2		3.45	m
	S1/4	H1,G1		**6.34**	s
	S3/5	G3/4,FA3/4		1.98	w
	S3/5	G1		2.19	w
	S3/5	H2/6		2.25	w
	S3/5	H3/5		3.80	m
	S4	FA3/4		3.45	m
	G3/4,FA3/4	H3/5		**5.97**	s
	FA6	S1	**5.46**	2.42	s
	FA6	H3/5		1.16	w
	FA6	G2		1.22	w
	FA9	H3/5		1.53	w
guaiacyl-xylan	Ac^{Me}	G6		0.46	w
syringyl-xylan	Ac^{Me}	S3/5		0.73	w
	S1	Ac^{Me}		**5.46**	s
	S3/5	$Xn1^{2f}$		**7.55**	s
	S3/5	AC^{CO}		2.47	w
	S3/5	$Xn5^{2f,3f}$		**11.35**	s
	S4	$Xn1^{2f}$		**7.39**	s
	S4	$Xn4^{2f}$		**7.56**	s
	S1	$Xn4^{2f}$		2.55	m
	S1	$Xn1^{2f}$		2.95	m
	AC^{CO}	S4		0.19	w
p-hydroxyphenyl-xylan	AC^{Me}	H3/5		0.93	w
	AC^{CO}	H4		0.39	w
	H4	$Xn2/3^{3f}$,$Xn2^{2f}$		**11.06**	s
	H4	$Xn5^{3f}$		1.89	w
ferulate-xylan	Ac^{Me}	FA6		1.57	w
	Ac^{CO}	FA6		0.24	w
	FA6	AC^{CO}		3.71	m
	FA6	$Xn4^{3f}$		**7.05**	s

(table cont'd.)

	Atom1 (ω1)	Atom2 (ω_2)	Gated 100 ms PDSD (%)	Gated 1s PDSD (%)	Type
ferulate-xylan	FA9	$Xn5^{2f,3f}$		**6.48**	s
	FA6	Ac^{Me}	**6.14**	4.21	s
OMe-xylan	$S/G/FA^{Ome}$	Ac^{CO}		3.70	m
	$S/G/FA^{Ome}$	H3/5		2.66	m
	$S/G/FA^{Ome}$	$Xn3^{2f,3f}$		**12.35**	s
	$S/G/FA^{Ome}$	$Xn5^{2f,3f}$		**6.23**	s
	$S/G/FA^{Ome}$	AC^{Me}	**0.30**	2.59	s
G/FA (ring)-xylan	Ac^{Me}	G3/4,FA3/4		0.63	w
	G3/4,FA3/4	$Xn1^{2f}$	**3.23**	**8.96**	s
	G3/4,FA3/4	$Xn3^{2f,3f}$		**11.83**	s
	G3/4,FA3/4	$Xn5^{2f}$		**8.03**	s
	G3/4,FA3/4	Ac^{Me}		4.91	m
	G3/4,FA3/4	Ac^{CO}		2.66	m
	G3/4,FA3/4	$Xn4^{2f}$		2.17	w
lignin (mixed)-xylan	H1,G1	$Xn5^{2f}$/i6		4.04	m
	H4	S2/6,$Xn1^{2f}$,i1		4.72	m
	AC^{CO}	H1,G1		0.72	w

Table D.6. Relative Intensities of intermolecular cross peaks of *Oryza sativa*. The intensities are relative ratios of the peak area normalized by the integral of a ^{13}C cross-section. For gated 1-s PDSD, the peaks higher than 5% are categorized as strong restraints (s, in bold) and 2.5% for medium (m) restraints and below 2.5% for weak (w) restraints. All the peaks in the gated 100-ms PDSD spectrum are strong restraints. In total, 39 restraints are identified, including 19 strong restraints, 13 medium ones and 7 weak restraints.

	Atom1 (ω_1)	Atom2 (ω_2)	Gated 100 ms PDSD (%)	Gated 1s PDSD (%)	Type
lignin-cellulose	S/G/FA^{Ome}	s4	**0.91**	3.32	s
	G3/4,FA3/4	s4		3.23	m
	S1	i3,s3		**17.2**	s
	S3/5	s4		4.63	m
xylan-cellulose	Ac^{Me}	s4	**0.95**	**3.68**	s
lignin-lignin	FA6	G6		**6.47**	s
	S1	FA9		2.80	m
	S3/5	G3/4,FA3/4	**1.78**	**11.67**	s
	S3/5	FA1		**8.04**	s
	S3/5	G5,FA2/5		**6.48**	s
guaiacyl-xylan	G1	Ac^{CO}		3.16	m
	G1	Xn3^{2f},Xn2/3^{3f}		**8.02**	s
	G1	Ac^{Me}		1.50	w
syringyl-xylan	S3/5	Ac^{CO}		0.63	w
	S3/5	Xn5^{2f,3f}		**8.60**	s
	S3/5	Xn3^{2f},Xn2/3^{3f}		**21.71**	s
	S1	Xn5^{2f,3f}		**4.95**	m
	Ac^{CO}	S4		2.54	m
	Ac^{Me}	S1		2.51	m
ferulate-xylan	FA9	Xn^{2f}4		2.73	m
	FA6	Ac^{CO}		**5.57**	s
	FA6	Xn3^{2f},Xn2/3^{3f}		**13.37**	s
	FA6	Xn^{2f,3f}5		**6.05**	s
	FA6	Ac^{Me}		3.24	m
	Ac^{CO}	FA6		1.14	w
Ome-xylan	S/G/FA^{Ome}	Ac^{CO}	**2.04**	**3.40**	s
	S/G/FA^{Ome}	Xn3^{2f},Xn2/3^{3f}	**0.43**	**17.51**	s
	S/G/FA^{Ome}	AC^{Me}		1.10	w
	Ac^{CO}	S/G/FA^{Ome}	**3.00**	**4.47**	s
	Ac^{Me}	S/G/FA^{Ome}		3.01	m
G/FA (ring)-xylan	G3/4,FA3/4	Ac^{CO}		2.13	w
	G3/4,FA3/4	Xn5^{2f,3f}		**7.55**	s
	G3/4,FA3/4	Xn3^{2f},Xn2/3^{3f}		**16.96**	s
	G3/4,FA3/4	AC^{Me}		2.50	m
	G3/4,FA3/4	Xn1^{2f}		**6.86**	s
	Ac^{CO}	G3/4,FA3/4		2.40	w
	Ac^{CO}	G5,FA2/5		3.08	m
	Ac^{Me}	G3/4,FA3/4		1.22	w
	Ac^{Me}	FA2/5,G5		3.39	m

Table D.7. Water-edited intensities of polysaccharide cross peaks from 2D ^{13}C-^{13}C correlations spectra. The relative intensities are obtained by comparing the water-edited and control spectra. Error bars are standard deviations propagated from NMR signal-to-noise ratios.

Type	cross peaks	Intensities	Type	cross peaks	Intensities
Interior cellulose	i4-1[a,b]	0.46±0.08	Surface cellulose	s4-1[f,g]	0.43±0.02
	i4-3[a,b]	0.54±0.04		s4-2/5[f]	0.46±0.04
	i4-2/5[a,b]	0.38±0.04		s4-s5g	0.54±0.04
	i4-6[a,b]	0.38±0.08		s4-2[f],4-2/3[g]	0.46±0.04
	i6-1[a,b,c,d]	0.35±0.04		s4-6[f]	0.41±0.02
	i6-4[a,b]	0.35±0.04		s4-6[g]	0.5±0.1
	i6-4[c,d]	0.36±0.01		s6-1[f,g]	0.54±0.08
	i6-3[a,b,d]	0.42±0.04		s6-4[f,g]	0.50±0.01
	i6-3[c]	0.38±0.04		s6-2/5[f]	0.57±0.01
	i6-2/5[a,b,d],i6-2[c]	0.35±0.08		s6-2[f],s6-2/3[g]	0.58±0.08
Xn^{2f}	Xn^{2f}4-1	0.42±0.04	$Xn^{2f,3f}$ Ac^{Me}	$Xn^{3f}Ac^{Me}$-2, $Xn^{2f}Ac^{Me}$-2/3	0.54±0.08
	Xn^{2f}4-3’	0.54±0.04		$Xn^{2f,3f}Ac^{Me}$-5	0.9±0.2
	Xn^{2f}4-3	0.58±0.04	Lignin	FA8-9	0.3±0.2
	Xn^{2f}4-2	0.60±0.03		FA1-3/4	0.2±0.1
	Xn^{2f}4-5	0.43±0.02		FA3/4/7-9	0.1±0.1
	Xn^{2f}3-1	0.5±0.2		FA^{Ome}-9	0.1±0.1
	Xn^{2f}3-4	0.7±0.1		H1-4	0.4±0.2
	Xn^{2f}3-5	0.5±0.2		H5-4	0.2±0.1
	Xn^{2f}5-1	0.4±0.2		H2-4	0.2±0.1
	Xn^{2f}5-4	0.46±0.08		H3-2	0.3±0.1
$Xn^{2f}Ac^{Me}$	$Xn^{2f}Ac^{Me}$-1	0.30±0.02		S4-3	0.1±0.1
	$Xn^{2f}Ac^{Me}$-4	0.34±0.02		S2/6-3/5	0.2±0.1
Xn^{3f}	Xn^{3f}2/3-1	0.8±0.2		S^{Ome}-2/6	0.3±0.2
	Xn^{3f}2/3-4	**1.0±0.2**		S^{Ome}-5	0.1±0.1
	Xn^{3f}2/3-5	0.5±0.1	Lignin (mixed)	FA5-3/4,G5-3/4	0.2±0.1
	Xn^{3f}5-1	0.7±0.2		G1-3/4,FA6-3/4	0.1±0.1
	Xn^{3f}5-4	0.7±0.1		FA8-1,H5-2	0.3±0.1
$Xn^{3f}Ac^{Me}$	$Xn^{3f}Ac^{Me}$-1	0.31±0.08		FA^{Ome}-3/4,G^{Ome}-3/4	0.1±0.1
	$Xn^{3f}Ac^{Me}$-5	0.46±0.04		H^{Ome}-5,G^{Ome}-5,FA^{Ome}-5	0.1±0.1
	$Xn^{3f}Ac^{Me}$-3	0.5±0.2		G^{Ome}-1,S^{Ome}-4	0.1±0.1
Xn^{2f}/Xn^{3f}	$Xn^{2f,3f}$5-3	0.50±0.08			
	Xn^{2f}5-2/3,Xn^{3f}5-2	0.42±0.04			

Table D.8. ^{13}C-T_1 relaxation times of polysaccharides in the hydrated secondary cell walls of four plants. The experiments are measured using Torchia CP or the standard inversion recovery with quantitative DP. The data are fit using single exponential equation: $I(t)=1-e^{-t/T_{1b}}$. Error bars are standard deviations of the fitting parameters. Ar stands for the arabinose, GA stands for galacturonic acid, GlcA stands for glucuronic acid, and R stands for rhamnose, the other names are consistent with that from the main figures.

	Zea mays				*Arabidopsis thaliana*				*Panicum virgatum*				*Oryza sativa*			
	Atom (ppm)	T1, CP (s)	Atom (ppm)	T1, DP (s)	Atom (ppm)	T1, CP (s)	Atom (ppm)	T1, DP (s)	Atom (ppm)	T1, CP (s)	Atom (ppm)	T1, DP (s)	Atom (ppm)	T1, CP (s)	Atom (ppm)	T1, DP (s)
FA9	168	4.6±0.2	168	0.9±0.3	-	-	-	-	169	3.4±0.7	169	2.0±0.4	-	-	-	-
H4	160	4.7±0.2	159	1.6±0.3	-	-	-	-	159	2.8±0.7	159	1.5±0.2	-	-	-	-
S3/5	154	4.9±0.2	154	2.8±0.4	153	3.7±0.2	153	1.1±0.4	152	4.3±0.7	153	2.8±0.3	-	-	-	-
G3/4,FA3/4	149	5.2±0.3	149	2.4±0.3	149	3.7±0.1	149	2.7±0.4	149	4.3±0.7	149	1.7±0.2	148	3.2±0.3	148	2.6±0.3
S1	138	-	-	-	-	-	136	1.4±0.2	138	2.8±0.5	137	1.3±0.2	-	-	-	-
S4	134	4.8±0.3	134	2.1±0.4	134	2.8±0.2	133	1.3±0.2	-	-	135	1.4±0.2	134	2.9±0.2	134	1.7±0.1
H1,G1	131	4.5±0.2	131	0.9±0.2	131	1.9±0.1	130	0.9±0.1	130	2.3±0.2	130	0.64±0.06	130	2.7±0.2	130	1.3±0.1
FA6	129	5.1±0.2	129	0.9±0.1	129	1.8±0.1	129	0.8±0.1	129	2.3±0.2	129	0.69±0.07	128	2.8±0.2	128	2.1±0.4
FA1,H2/6	127	5.5±0.4	126	1.8±0.4	127	1.7±0.1	-	-	-	-	126	1.4±0.3	126	2.9±0.2	-	-
H5	117	4.8±0.2	117	1.9±0.3	116	3.4±0.1	117	1.9±0.3	117	3.0±0.2	116	1.1±0.1	117	2.82±0.06	117	2.6±0.3
FA/G/S-O^{Me}	56	2.6±0.4	56	1.5±0.3	56	1.8±0.2	57	2.2±0.3	57	1.3±0.2	57	1.5±0.2	57	1.4±0.2	57	1.9±0.2
i/s/Xn^{2f}1	105	3.62±0.08	105	2.7±0.2	105	3.82±0.06	105	3.4±0.2	106	3.20±0.05	105	2.8±0.2	105	3.40±0.07	105	3.1±0.2
i4	89	4.00±0.07	89	3.9±0.4	89	4.41±0.04	89	4.5±0.2	89	3.70±0.05	89	3.4±0.3	89	4.01±0.06	89	3.7±0.2
s4	85	3.51±0.08	-	-	84	3.55±0.09	83	2.2±0.3	85	2.84±0.09	-	-	85	3.1±0.1	85	2.7±0.3
i/s6	65	2.9±0.3	65	2.6±0.2	65	3.2±0.2	65	3.0±0.3	65	2.2±0.2	64	1.2±0.1	65	2.9±0.2	65	2.8±0.3
s6	62	1.8±0.3	61	0.36±0.04	62	2.4±0.4	62	1.5±0.2	63	1.7±0.2	62	0.8±0.1	63	1.8±0.2	63	1.5±0.2
Ar1	108	3.0±0.3	108	2.6±0.3	-	-	108	0.6±0.1	-	-	109	1.0±0.1	108	1.7±0.2	108	1.8±0.2
Xn^{3f}1	103	2.1±0.2	103	1.6±0.2	102	2.4±0.2	102	1.8±0.3	103	1.1±0.1	103	0.83±0.08	103	1.8±0.1	103	1.3±0.1
GA/R1	101	2.4±0.2	101	0.47±0.09	101	1.9±0.2	101	1.1±0.2	-	-	-	-	-	-	100	0.7±0.2
GlcA1	98	-	99	3.2±0.6	98	1.5±0.2	98	0.7±0.1	-	-	97	0.64±0.06	-	-	-	-
Xn^{2f}4	82	2.8±0.3	82	0.49±0.04	82	3.4±0.1	82	1.7±0.3	82	2.0±0.2	81	0.9±0.1	82	2.1±0.2	82	1.2±0.5
GA2,R4	68	0.9±0.2	68	1.4±0.1	69	0.9±0.1	69	1.2±0.2	-	-	68	0.71±0.09	-	-	-	-
--	54	-	54	0.9±0.2	54	1.02±0.08	54	1.2±0.2	54	0.7±0.1	54	1.1±0.1	-	-	-	-
$Xn^{2f/3f}AC^{Me}$	22	4.3±0.1	22	2.1±0.2	21	3.0±0.2	21	1.9±0.2	21	2.2±0.2	21	1.19±0.09	21	1.8±0.3	21	1.1±0.1

Table D.9. ^{1}H-$T_{1\rho}$ relaxation times of polysaccharides in the hydrated secondary cell walls of four plants. The data are fit using single exponential equation: $I(t) = e^{-t/T_{1\rho,b}}$. Error bars are standard deviations of the fitting parameters.

	Zea mays		*Arabidopsis thaliana*		*Panicum virgatum*		*Oryza sativa*	
	Atom (ppm)	T_1 (ms)	Atom (ppm)	T_1 (ms)	Atom (ppm)	T_1 (ms)	Atom (ppm)	T_1(ms)
FA9	169.2	4.6±0.5	168.9	-	169.8	3.7±0.3	168.0	-
H4	160.4	4.2±0.6	160.4	-	160.4	-	159.0	-
S3/5	153.4	4.6±0.4	152.5	13±1	152.8	3.9±0.4	153.0	-
G3/4,FA3/4	147.5	3.5±0.3	148.6	12±1	148.1	4.8±0.3	148.0	5.4±0.3
H1,G1	130.4	3.1±0.2	130.7	4.2±0.3	130.0	3.3±0.2	129.6	4.5±0.2
FA6	128.9	2.4±0.2	128.9	-	128.5	3.0±0.2	128.0	4.7±0.2
FA1,H2/6	127.3	1.9±0.3	127.3	-	127.3	-	126.3	4.5±0.2
H5	116.6	4.1±0.3	116.6	-	116.8	3.6±0.3	116.5	4.7±0.2
FA/S/G-Ome	57.0	-	57.0	8.4±0.8	56.8	5.7±0.5	57.0	9±1
i/s/Xn1^{2f}	105.0	22.6±0.7	105.0	41±2	105.0	27.4±0.7	105.1	22.7±0.7
i4	89.0	26.9±0.6	89.0	44±2	89.0	26±1	88.9	27.1±0.7
s4	84.5	20.7±0.7	84.1	33±2	84.5	20±1	84.5	20.4±0.8
i/s6	64.8	15.2±0.9	65.2	35±3	64.8	18±2	65.0	17±1
s6	61.5	15±1	62.5	30±3	62.7	15±1	62.5	14±1
Ar1	108.0	-	108.0	-	108.0	-	108.2	7.9±0.8
Xn1^{3f}	102.2	7.1±0.7	102.2	-	102.0	4.6±0.4	103.0	5.8±0.6
GA/R1	100.2	-	100.2	-	100.2	-	100.2	1.7±0.2
Xn4^{2f}	82.0	-	82.0	-	81.8	10.3±0.9	82.5	7.9±0.9
GA2,R4	68.3	-	68.3	-	68.3	-	68.3	2.6±0.3
Xn^{2f,3f}-AC^{Me}	21.0	-	21.0	17±1	21.5	7.4±0.6	-	6.2±0.7

Table D.10. ^{13}C-T_1 relaxation times of polysaccharides in dried and hydrated *Zea mays*. The data are obtained by measuring a series of 2D ^{13}C-^{13}C correlation spectra with various z-filter time. The data are fit using single exponential equations: $I(t)=1-e^{-t/T_{1b}}$. Error bars are standard deviations of the fitting parameters.

Type	Cross peaks	Dry T1 (s)	Hydration T1 (s)
Interior cellulose (i)	i5-1	4.5±0.3	3.5±0.2
	i3-4	4.2±0.3	2.8±0.4
	i2/5-4	4.2±0.2	3.7±0.2
	i4-1	4.7±0.2	3.2±0.4
	i1-4	4.0±0.2	3.2±0.3
	i1-6	4.5±0.2	4.3±0.1
	i6-3	5.0±0.3	3.7±0.2
	i5-2	3.5±0.1	3.9±0.1
	i5-6	5.0±0.3	3.9±0.1
	i4-6	4.5±0.2	3.7±0.4
	i4-2/5	3.6±0.1	3.8±0.2
	i6-4	3.7±0.4	3.5±0.4
	i3-4	4.3±0.4	2.5±0.5
Surface cellulose (s)	s6-3/5	4.3±0.3	3.0±0.3
	s4-1	4.2±0.3	3.4±0.2
	s4-3	3.9±0.2	3.08±0.09
	s4-5	4.2±0.3	3.7±0.2
	s1-6	4.3±0.2	3.9±0.1
	s1-4	4.1±0.3	3.2±0.3
	s4-6	4.2±0.3	3.9±0.2
	s4-6	4.3±0.3	3.1±0.2
	s6-4	4.2±0.4	2.8±0.3
	s3/5-4	4.0±0.3	3.2±0.3
	s2-3/5	3.9±0.3	3.4±0.2
	s2-4	3.6±0.4	3.2±0.3
i/s	i3-1,s3/5-1	4.3±0.3	3.7±0.4
	i1-3,s1-3/5	4.0±0.3	3.6±0.2
Xn	$Xn^{2f,3f}1\text{-}AC^{Me}$	2.3±0.6	3.1±0.6
	$Xn^{2f}6\text{-}AC^{Me}$	4.1±0.4	3.5±0.6
	$Xn^{2f,3f}3\text{-}AC^{Me}$	4.4±0.5	3.4±0.5
	$Xn^{2f}3\text{-}AC^{CO}$,$Xn^{3f}2/3\text{-}AC^{CO}$	4.7±0.3	2.9±0.5
	$Xn^{2f,3f}6\text{-}AC^{CO}$	3.0±0.6	2.7±0.5
	$Xn^{2f}5$-4	4.1±0.1	2.7±0.6
	$Xn^{3f}5$-1	4.1±0.3	2.6±0.4
	$Xn^{2f}5\text{-}AC^{Me}$	2.9±0.4	2.5±0.3
	$Xn^{2f,3f}3\text{-}AC^{Me}$	4.3±0.7	3.2±0.3
	$Xn^{2f,3f}3\text{-}AC^{CO}$	4.0±0.4	2.8±0.6
	$Xn^{2f}5\text{-}AC^{CO}$	3.8±0.4	3.2±0.4
	$Xn^{2f}4$-5	4.5±0.2	4.9±0.3
Xn/i/s	$Xn^{3f}5$-2,s6-2	4.27±0.08	2.8±0.3
	$Xn^{2f}2$-1,i2/5-1,s2-1	4.0±0.3	3.9±0.2
	$Xn^{2f}1$-3,s1-3	4.1±0.3	4.07±0.03
	$Xn^{3f}2$-5,s2-6	4.5±0.2	4.7±0.5
	$Xn^{2f}2$-5,i2-6	4.5±0.2	4.7±0.2
	$Xn^{3f}3$-5,s3/5-6	4.7±0.2	3.1±0.1
	$Xn^{2f}5$-2,i6-2/5	4.6±0.4	4.2±0.2

(table cont'd.)

Type	Cross peaks	Dry T1 (s)	Hydration T1 (s)
Lignin	H2/6-4	8.8±0.9	3.5±0.5
	FA1-3/4	6.1±0.5	4.5±0.3
	S1-3/5	7.3±0.7	5.7±0.5
	S3/5-1	6.3±0.6	3.0±0.1
	FA3/4-1	7.8±0.6	4.8±0.3
	H4-2	8.9±0.9	4.5±0.4
	FA2/5-9	7.7±0.4	5.2±0.4
	H3/5-4	8.9±0.3	4.5±0.3
	G5-3/4,FA5-3/4	7.3±0.3	5.5±0.5
	G3/4-5,FA3/4-5	7.5±0.4	4.8±0.3
	H4-3/5	7.3±0.3	4.9±0.3

APPENDIX E. LETTER OF PERMISSION FOR CHAPTER 5

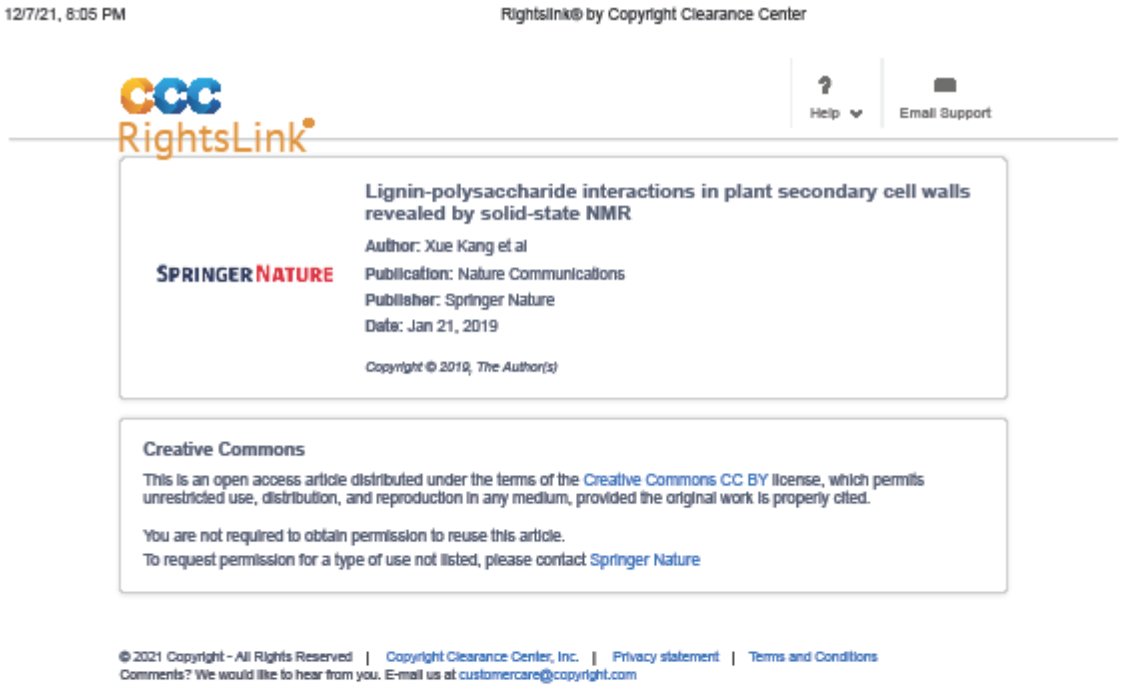

12/7/21, 8:05 PM RightsLink® by Copyright Clearance Center

RightsLink

Help Email Support

SPRINGER NATURE

Lignin-polysaccharide interactions in plant secondary cell walls revealed by solid-state NMR

Author: Xue Kang et al
Publication: Nature Communications
Publisher: Springer Nature
Date: Jan 21, 2019

Copyright © 2019, The Author(s)

Creative Commons

This is an open access article distributed under the terms of the Creative Commons CC BY license, which permits unrestricted use, distribution, and reproduction in any medium, provided the original work is properly cited.

You are not required to obtain permission to reuse this article.
To request permission for a type of use not listed, please contact Springer Nature

© 2021 Copyright - All Rights Reserved | Copyright Clearance Center, Inc. | Privacy statement | Terms and Conditions
Comments? We would like to hear from you. E-mail us at customercare@copyright.com

APPENDIX F. SUPPORTING INFORMATION FOR CHAPTER 6

F.1. Supplementary Methods.

F.1.1. Isotope Labeling.

Plant samples from eucalyptus, poplar, and spruce were produced under identical growth conditions in custom-designed, air-tight, high-irradiance labeling chambers of the Experimental Soil Plant Atmosphere System at IsoLife (Wageningen, The Netherlands). Under regulated environmental conditions, these plants were grown hydroponically in a closed atmosphere containing 97 atom% $^{13}CO_2$ from germinated seed or rooted stem cutting till harvest: photosynthetic photon flux density (PPFD) 800 µmol m^{-2} s^{-1} (top of plants); CO_2 concentration (Day); 400 ppm (v/v); 15 h (eucalyptus), 21 h (poplar), and 16 h (spruce) day lengths; day/night temperature of 22/16 °C (eucalyptus), 22/15 °C (poplar), and 24/20 °C (spruce). The day/night relative humidity is 75/75% for eucalyptus, 70/80% for poplar, and 70/75% for spruce. Minerals and water were supplied as aerated modified Hoagland nutrient solutions with micronutrients and iron[308,309], maintaining nitrogen concentration between 25 and 200 mg/L; pH close to 5; EC between 0.4 – 0.7 mS/cm; 25% of total nitrogen was supplied as ammonium. Plant shoots were dissected into leaves and stems after removing the plants from the growth chamber. After freeze-drying, these plant stems were kept stored at -20°C, in the dark with silica-gel drying bags. All plants were rehydrated for solid-state NMR analysis.

F.1.2. Effects of Plant Age on Cell Walls.

Given our ever-increasing knowledge on plant secondary cell wall, impacts of the plant age at which the material is harvested relative to its natural growth cycle can be considered. Our 6.5-months old poplar can be put in perspective of 3-, 6- and 18-month-old poplar samples reported in literature[209]. Overall, there is no significant change in cellulose to hemicellulose proportions,

and cellulose crystallinity has become a stable parameter after 6 months. However, a slight increase in

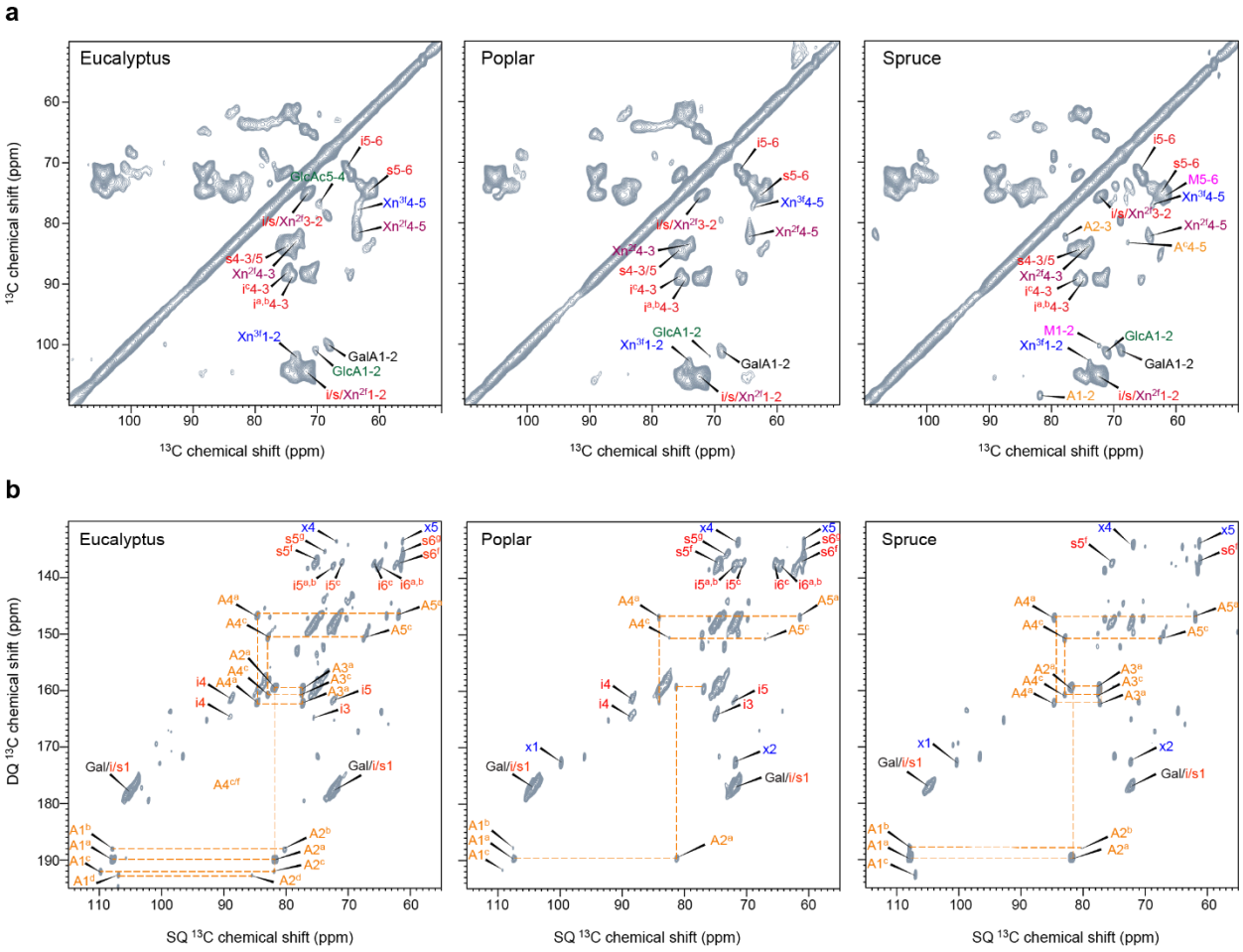

Figure F.1. 2D ^{13}C-^{13}C spectra of polysaccharides in softwood and hardwood. a) 2D ^{13}C-^{13}C RFDR spectra showing the rigid components of eucalyptus, poplar, and spruce. Uniquely, spruce has mannan and arabinose signals in the CP-based RFDR spectrum. b) 2D ^{13}C DP J-INADEQUATE spectra of eucalyptus, poplar, and spruce. The combination of ^{13}C DP with a short recycle delay of 2 s selectively detects the mobile molecules. Arabinose (A) signals dominate the spectra, and the four major types of arabinose are distinguished by the superscript, from A^a to A^d. The carbon connectivity of arabinose is highlighted by yellow lines. Poplar has relatively weak signals of arabinose. The ^{13}C chemical shifts are summarized in Supplementary Tables 1 and 2.

lignin content with age has been consistently reported for both poplar and eucalyptus[215]. Solution NMR data have demonstrated that lignin structure undergoes substantial evolution over a longer period of time, in both unit nature. For example, S lignin is deposited at later stages and the

proportions of different linkage types. In-depth analyses of polysaccharide structure, lignin composition and linkage types, the consequential effect on lignocellulose architecture is thus of significant interest for future solid-state NMR research.

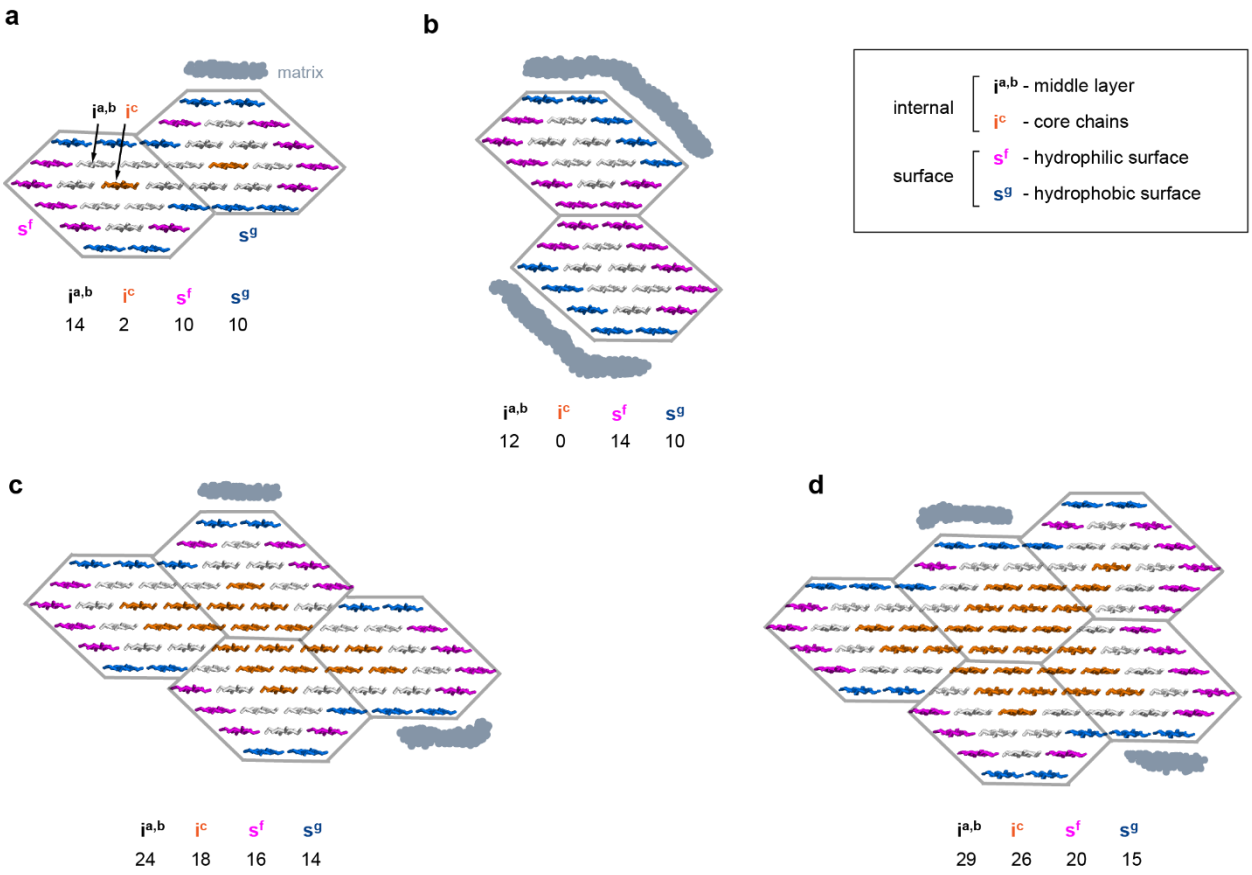

Figure F.2. Cellulose bundling models that violate the NMR constraints. The cartoon illustrations include a and b) two elementary microfibrils, c) four elementary microfibrils, and d) five elementary microfibrils. Each elementary microfibril is depicted to contain 18 glucan chains following the current biochemical evidence[205,206]. The number of hydrophobic surface chains (s^g), hydrophilic surface chains (s^f), middle layer internal chains ($i^{a,b}$), and the deeply embedded core chains (i^c) are labeled[22,98]. The matrix polymers are added to better fit the NMR constraints, but major violations still exist for all these models.

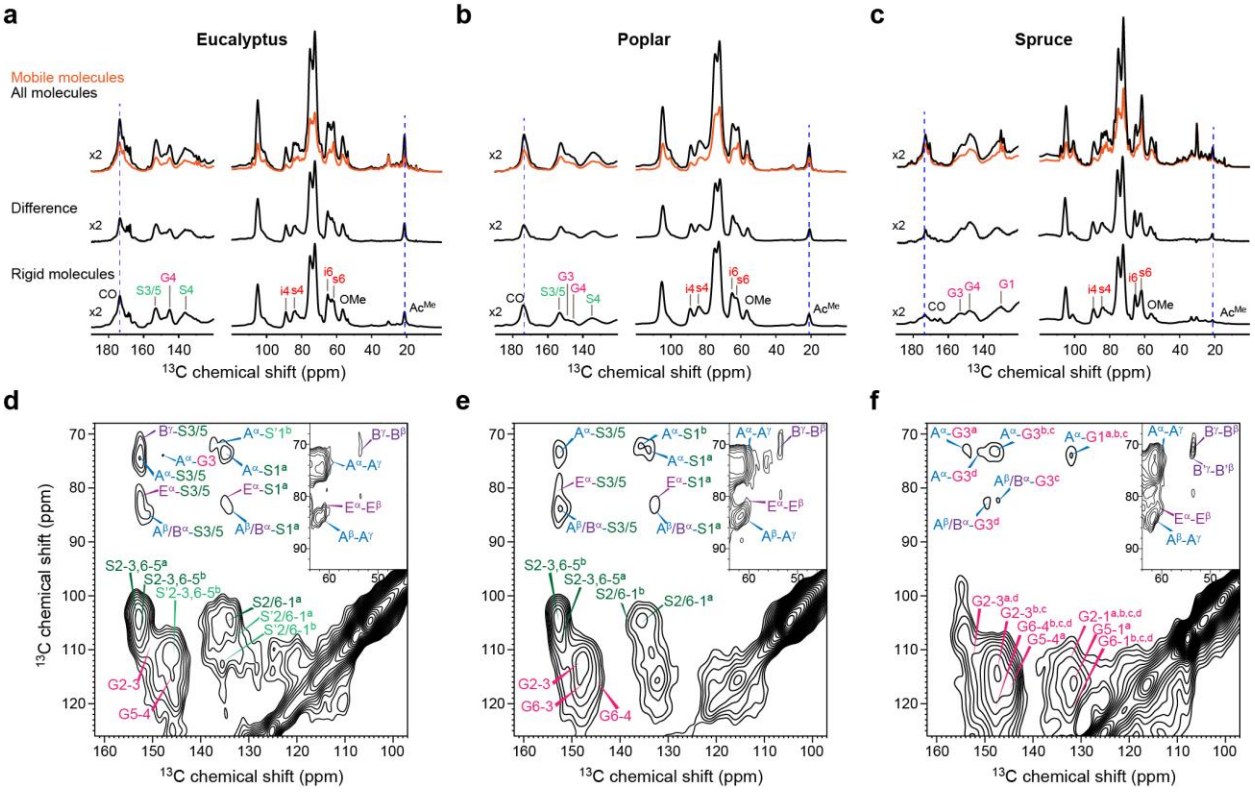

Figure F.3. Lignin distributed in the mobile and rigid phases. The top row is the quantitative-detected DP (orange), mobile molecule detected DP, rigid component detected CP spectra of a) eucalyptus, b) poplar, and c) spruce. All the three difference spectra of ^{13}C DP spectra with long and short recycle delays showing peaks of the rigid components, are comparable to the corresponding CP spectra. Both 2-s DP and CP spectra give well-resolved aromatic peaks, indicating dynamically heterogeneous lignin components. The bottom row is DP-PDSD spectra (1.7s recycle delay) of d, eucalyptus, e) poplar, and f) spruce. Abundant signals of aromatics and linkers are identified, suggesting that these linkers are also revolved at mobile phases of lignin.

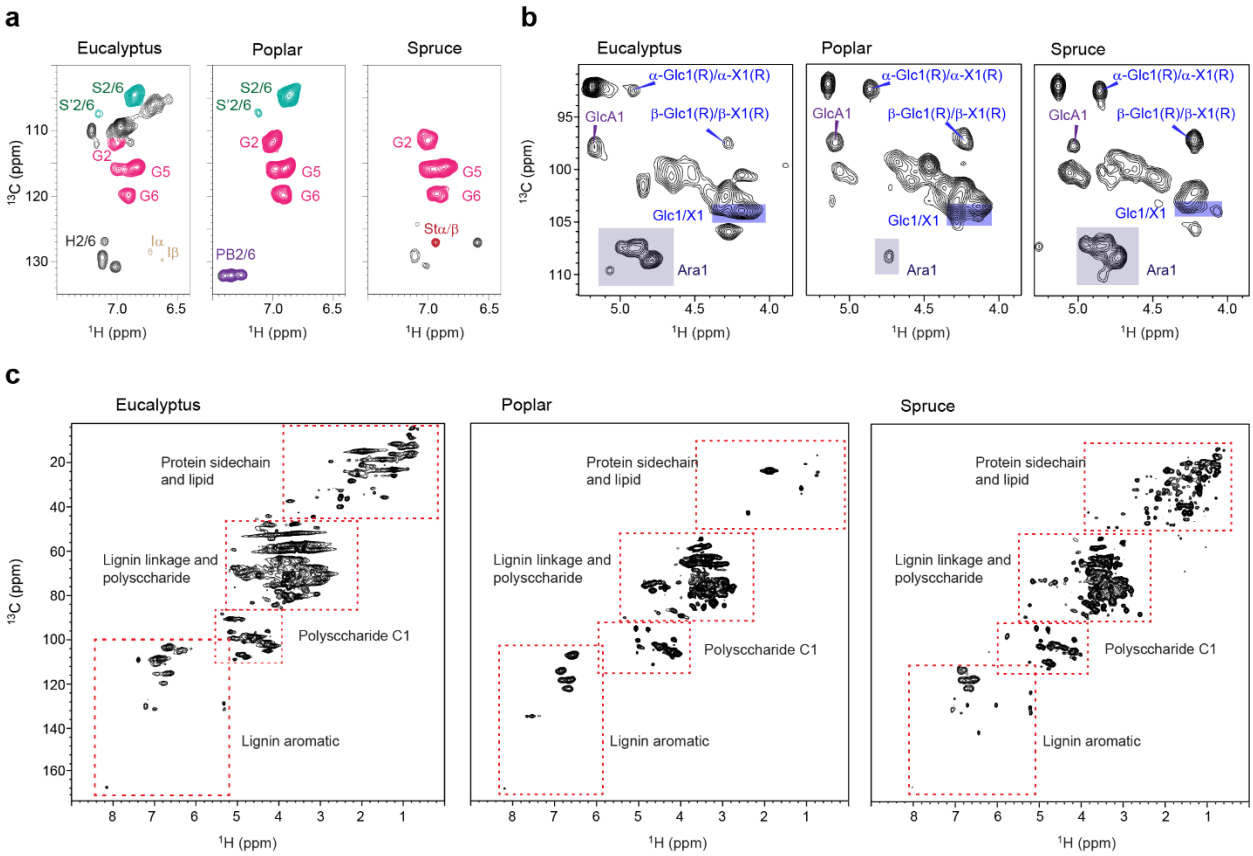

Figure F.4. Solution NMR of lignin and polysaccharides in woody stems. 2D ^{1}H-^{13}C HSQC spectra showing selected regions of a) mainly lignin signals and b) mainly polysaccharide peaks. Arabinose (Ara) is more predominant in spruce than in eucalyptus and poplar. c) Full HSQC spectra of the three samples. The ^{13}C and ^{1}H chemical shifts are documented in Supplementary Table 4 and supported by a literature surveil compiled in Supplementary Table 5.

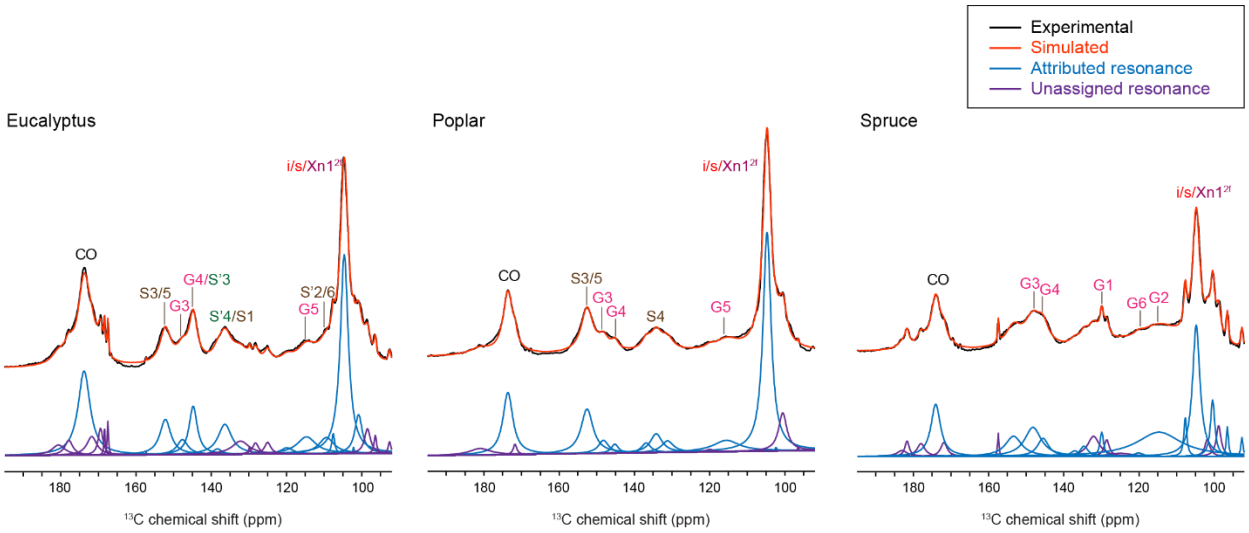

Figure F.5. Spectral deconvolution reveals the lignin composition. Deconvolution is conducted on 1D quantitative ^{13}C DP spectra collected with long recycle delays of 35-40 s. The experimentally measured spectra (black) is overlaid with the simulated spectra (red) for eucalyptus, poplar, and spruce. The bottom panels show the deconvoluted peaks. Attributed resonances are plotted in blue and uncertain resonances are in purple. Deconvolution is conducted using the DMfit software[191], using a Lorentzian model on a 92-195 ppm chemical shift window. The fitting parameters are summarized in Supplementary Table 6.6.

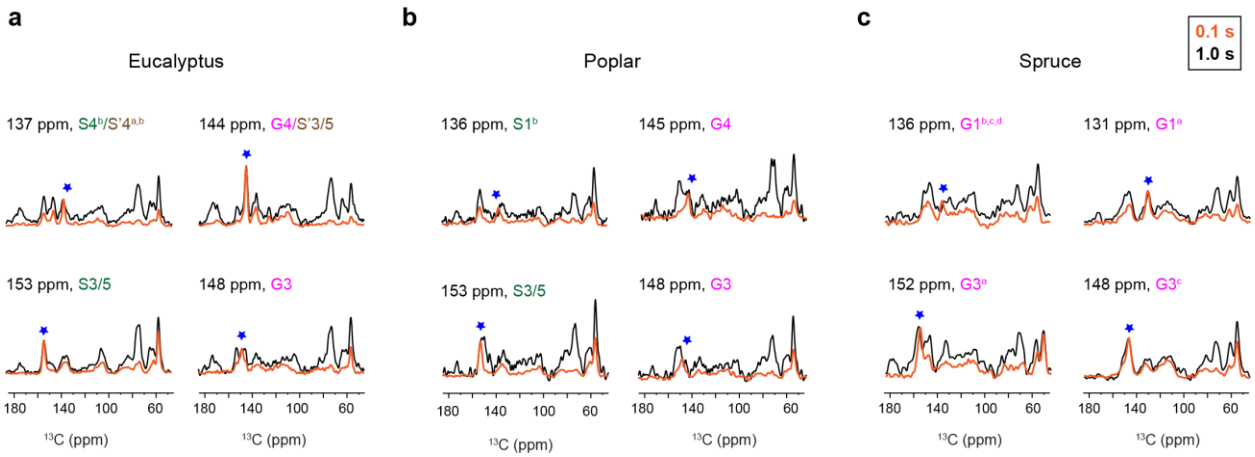

Figure F.6. 1D ^{13}C cross sections of lignin region reveal the polymer mixing patterns. Representative cross sections are obtained from dipolar gated 2D ^{13}C-^{13}C correlation spectra (Figure 3a) of a) eucalyptus, b) poplar, and c) spruce. For eucalyptus and poplar, the first column shows the cross sections from S-lignin units and the second column shows those from G units. All the cross sections are normalized by the diagonal peaks (blue asterisks). The more similar the spectral pattern between 0.1 s and 1.0 s, the more homogeneous the polymers are mixed on the sub-nanometer scale. The spruce cross sections are more equilibrated.

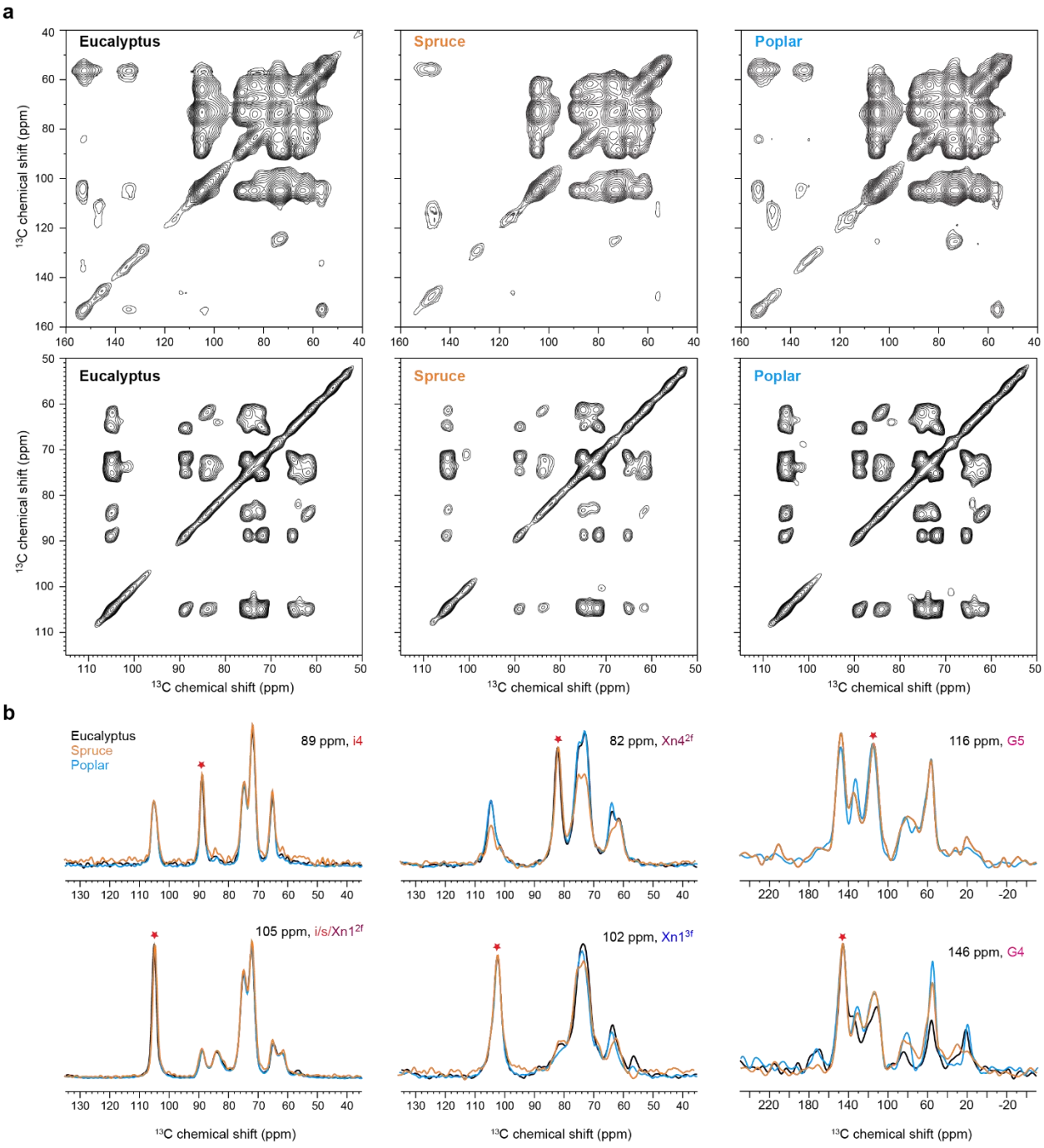

Figure F.7. Comparable spin diffusion rates of biopolymers in three wood samples. a) Aromatics regions (top row) and carbohydrates regions (second row) of 0.1s PDSD spectra of three woody plants. b) Representative cross peaks for cellulose, xylan, and lignin are obtained from 0.1s PDSD spectra, which are normalized by the diagonal peaks (red asterisks). The similar spectral patterns among three wood samples indicates the spin diffusion rates of lignin and carbohydrates are comparable in all three woody stems.

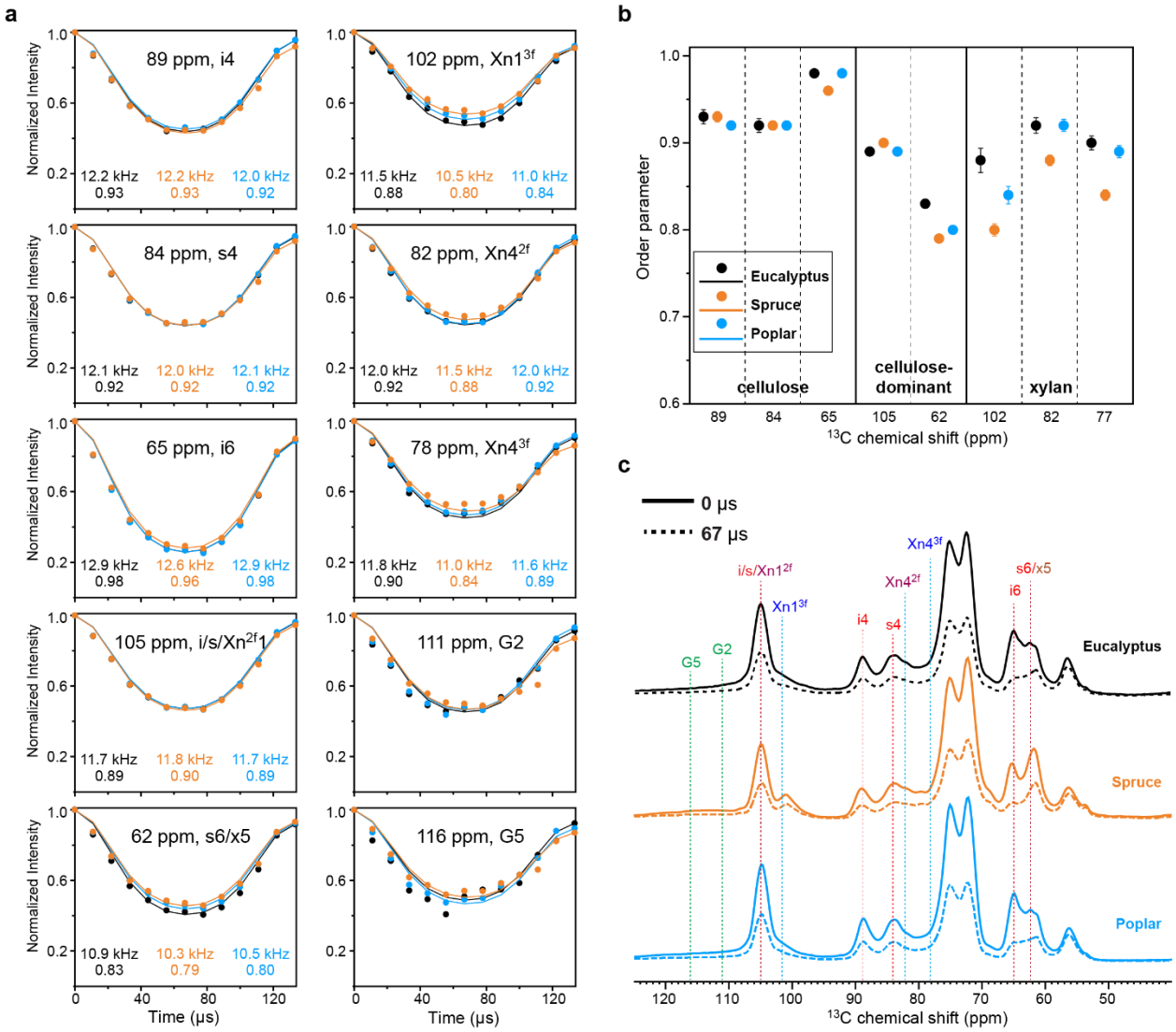

Figure F.8. ^{13}C–^{1}H dipolar order parameters of biopolymers in wood cell walls. a) Dipolar dephasing curves of carbohydrates and lignin processed from DIPSHIFT spectra. The spectra were collected under 7.5 kHz MAS with a 0.577 scaling factor for C-H bond. b) Summary of C–H dipolar order parameters with error bars. Spruce shows a relatively smaller order parameter for xylan. c) The first (0 μs dipolar dephasing) and middle (67 μs dipolar dephasing) slices of the 2D DIPSHIFT experiment imply how much the spectra are suppressed at a half rotor period.

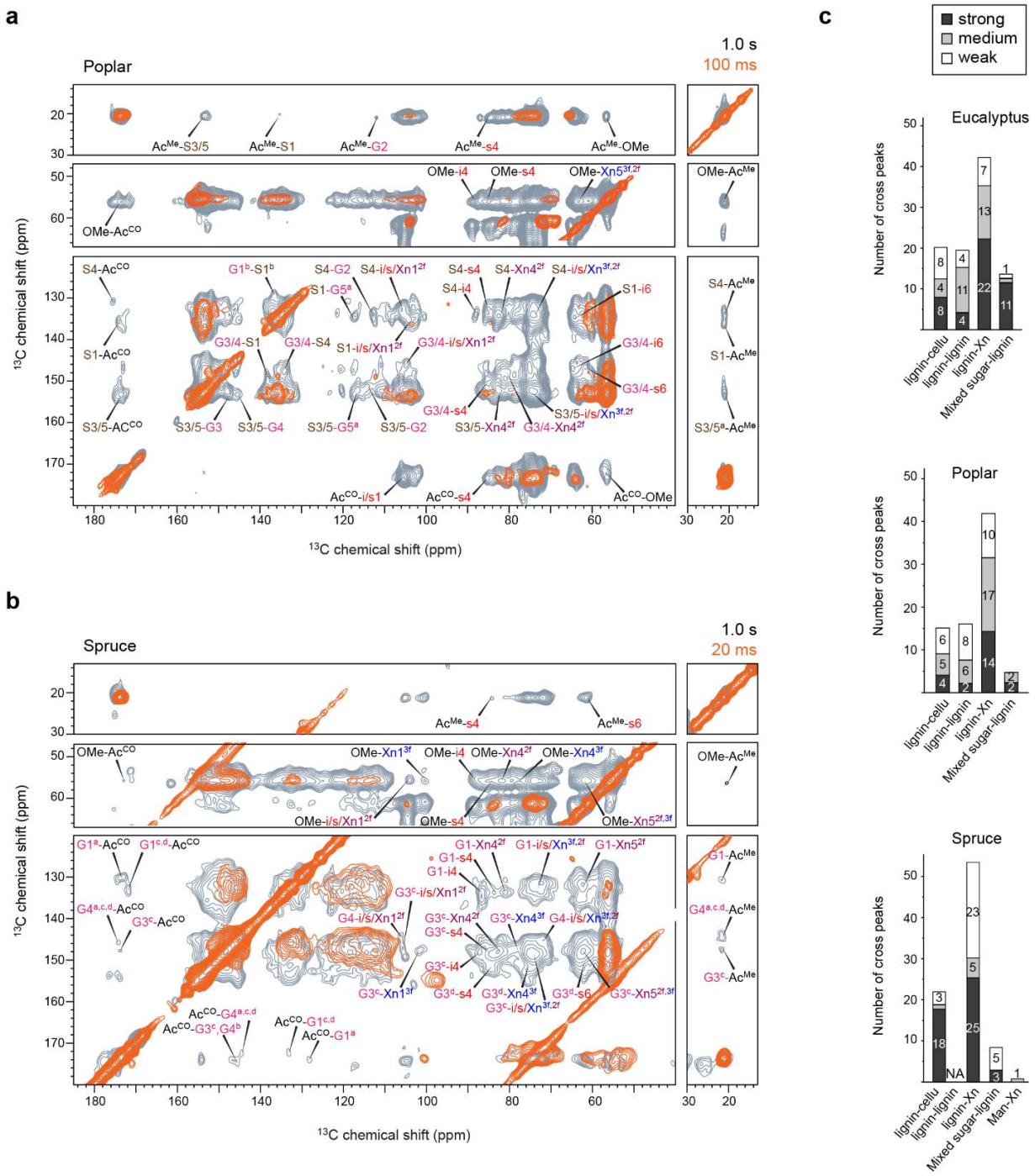

Figure F.9. Intermolecular interactions of polymers in woody plants. Dipolar-gated 2D ^{13}C-^{13}C correlation spectra measured with 1.0 s and 100 ms (poplar), 1.0 s and 20 ms (spruce) are overlaid for a) poplar and b) spruce. 100 ms (poplar) and 20 ms (spruce) spectra mainly detect the intramolecular correlations, and the 1 s spectra show many intermolecular cross peaks. Only the intermolecular cross peaks are labeled. c) The bar diagrams show the number of interactions between different molecules in the woods. The interactions are categorized according to the peak intensity. The details of the short-range and long-range cross peaks are summarized in Supplementary Tables 6.7-6.10

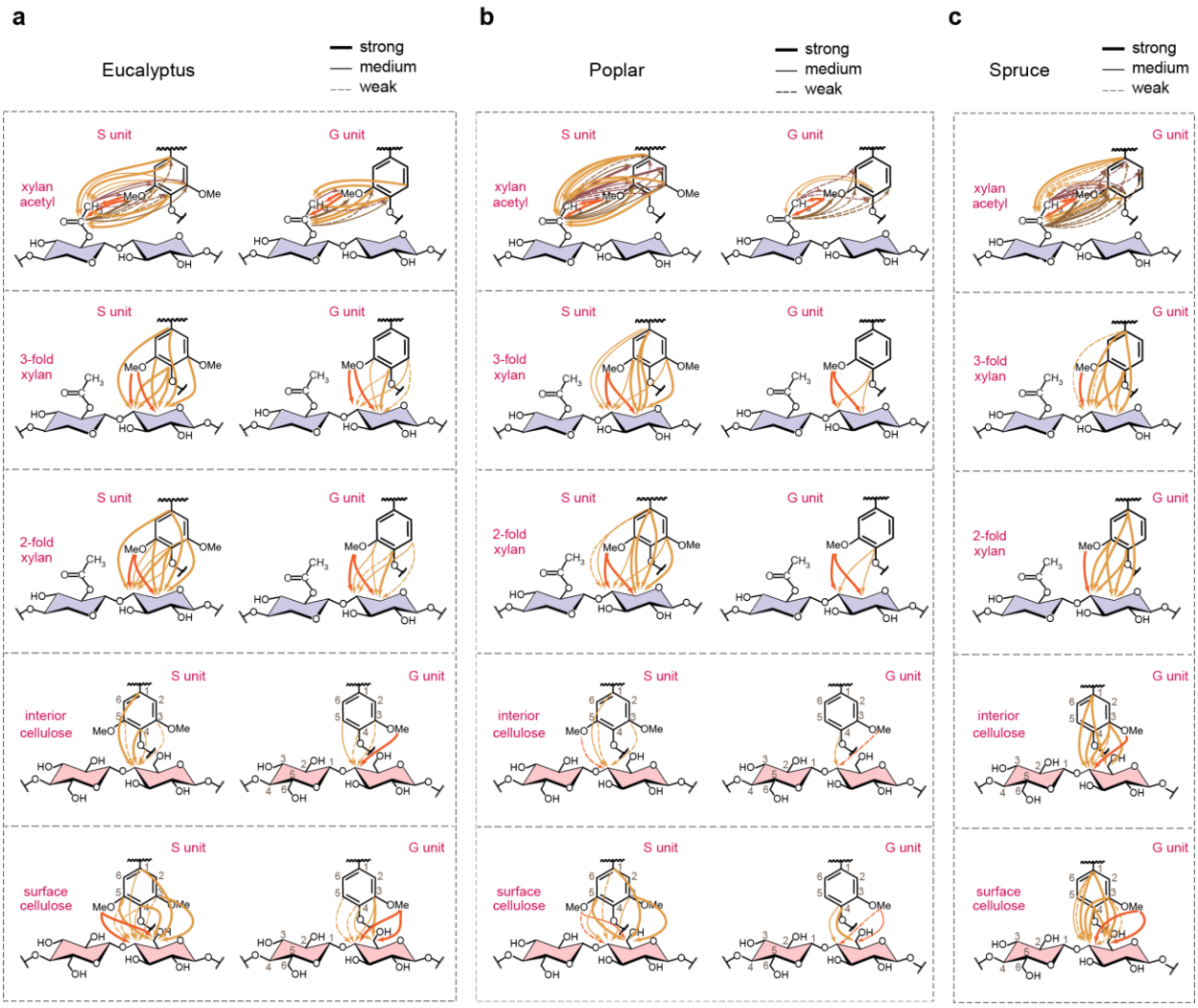

Figure F.10. NMR restraints of polymer packing in secondary cell walls. Thick lines, thin lines, and dash lines are used to represent strong, medium, and weak cross peaks observed in solid-state NMR spectra, respectively. Three major types of interactions happen between xylan acetyl and lignin (brown), between lignin methyl ether and carbohydrates (orange), and between lignin aromatics and carbohydrates (yellow). The details of these cross peaks are tabulated in Supplementary Tables 6.7-6.10.

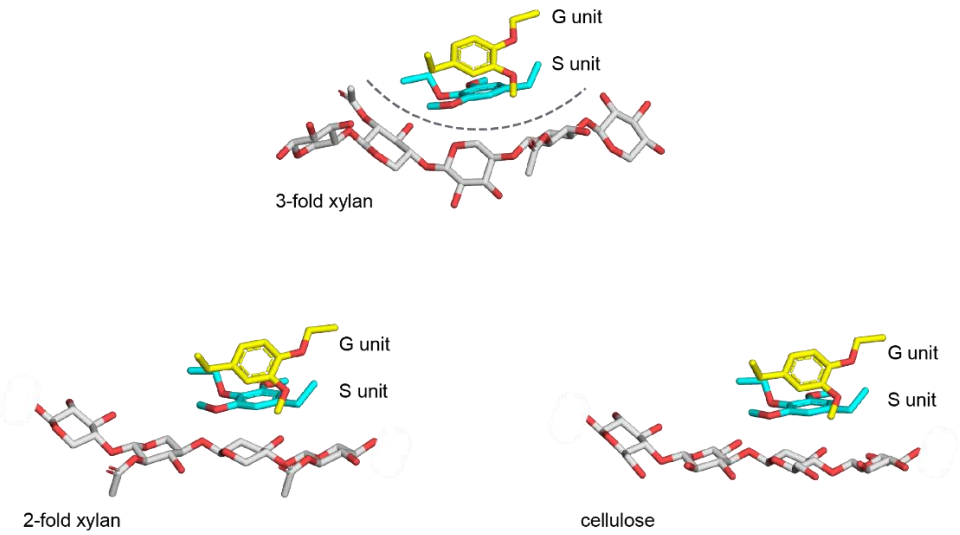

Figure F.11. DFT structures of lignin-carbohydrate packing. The structure includes the complex formed between G (yellow) or S (cyan) unit of lignin and three types of polysaccharides. The structures were adapted from an earlier study.[227]

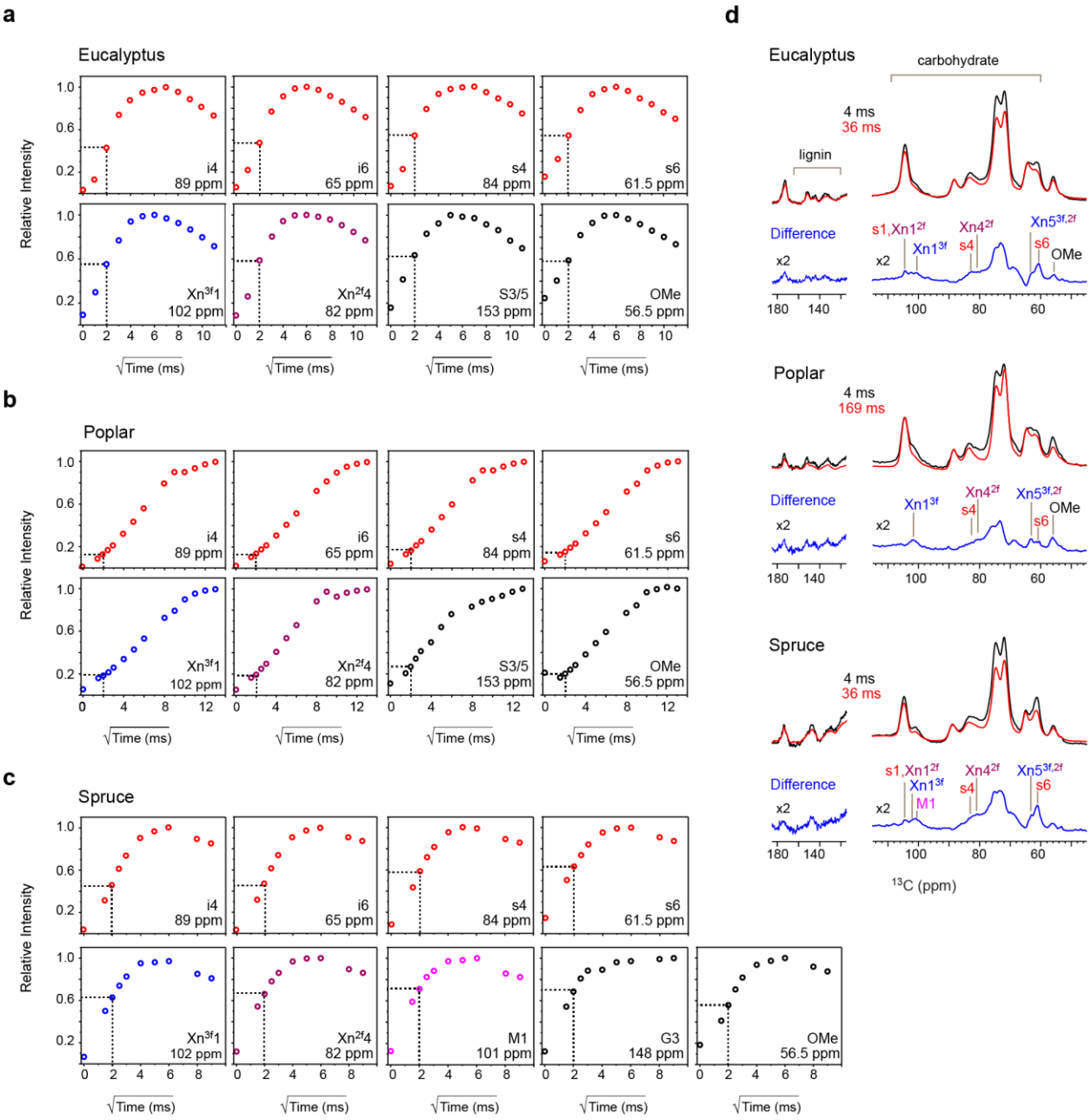

Figure F.12. Buildup curves for water-to-polysaccharides/lignin. The water ^{1}H spin diffusion curves for cellulose, xylan, and lignin for a) Eucalyptus, b) poplar and c) spruce. Dash lines indicate the intensities of 4-ms ^{1}H mixing. Poplar has the slowest spin diffusion from water among the three woods, with ~15-20% of the equilibrium intensity detected at 4-ms ^{1}H mixing. Eucalyptus and spruce have the fastest spin diffusion with ~45-60% of the equilibrium intensity detected at 4-ms ^{1}H mixing. d) Water-edited spectra measured with different mixing times. The 4-ms spectrum detects the hydrated molecules and the 36-ms (eucalyptus and spruce) and 169-ms (poplar) spectra report equilibrium intensities. The difference spectrum only shows well-hydrated molecules.

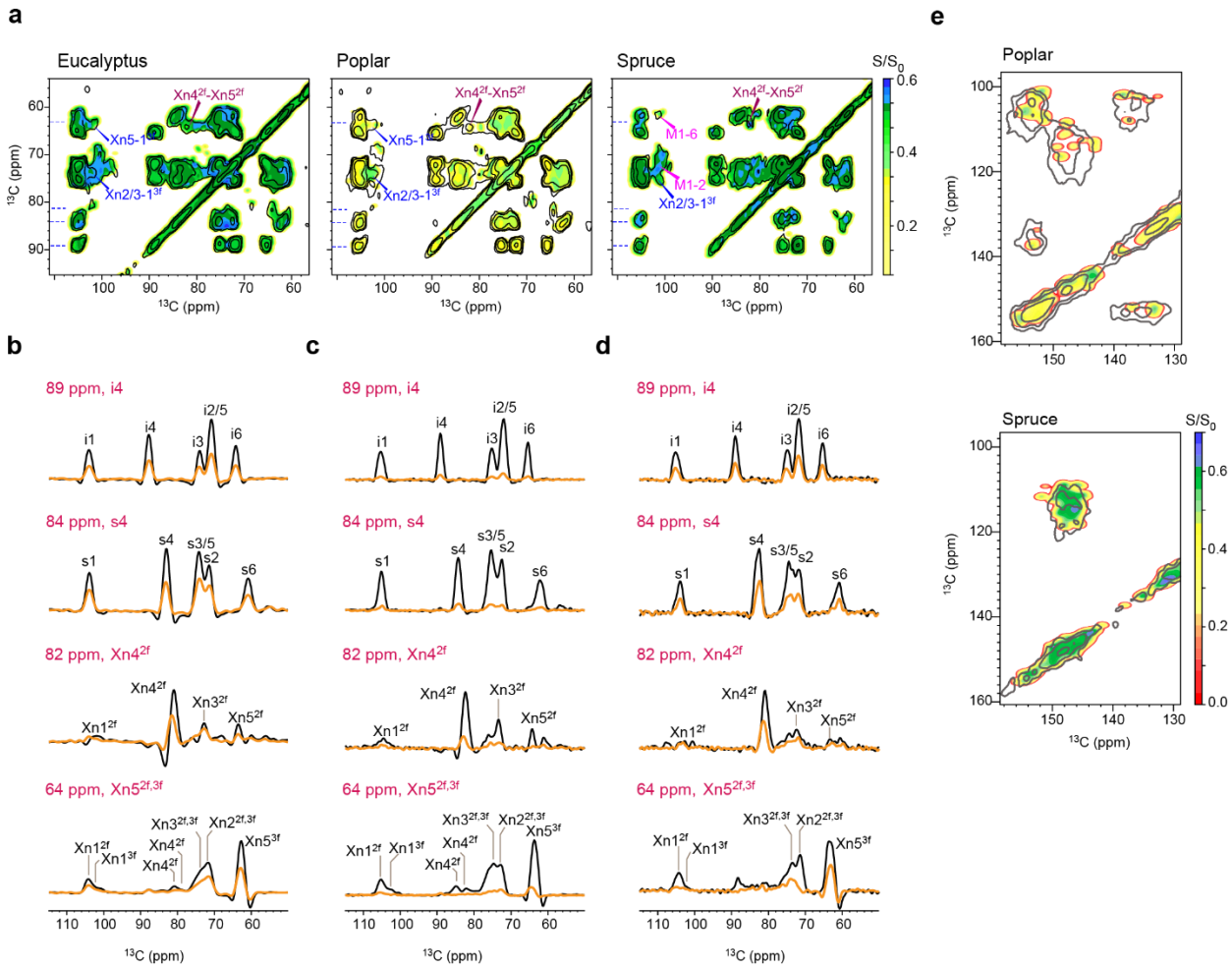

Figure F.13. Water-edited 2D ^{13}C-^{13}C correlation spectra of polysaccharides. Overlay of water-edited and equilibrium spectra showing hydration maps with S/S_0 values for a) eucalyptus, b) poplar, and c) spruce. The blue dash lines indicate the positions at which the ^{13}C cross sections are extracted. The representative 1D ^{13}C cross sections of cellulose (interior: i4; surface: s4) and xylan (Xn4 and Xn5) are shown for a, Eucalyptus, b, poplar, and c, spruce. The water-edited spectra and the equilibrium spectra are plotted in orange and black, respectively. The 3-fold and 2-fold xylans have enhanced intensity in the water-edited spectra, indicating better interactions with water molecules. e) Hydration maps of lignin regions with S/S_0 values for poplar (top) and spruce (bottom). Spruce is well hydrated compared to poplar as it shows higher S/S_0 values. The water-edited intensities are summarized in Supplementary Tables 6.11-6.13.

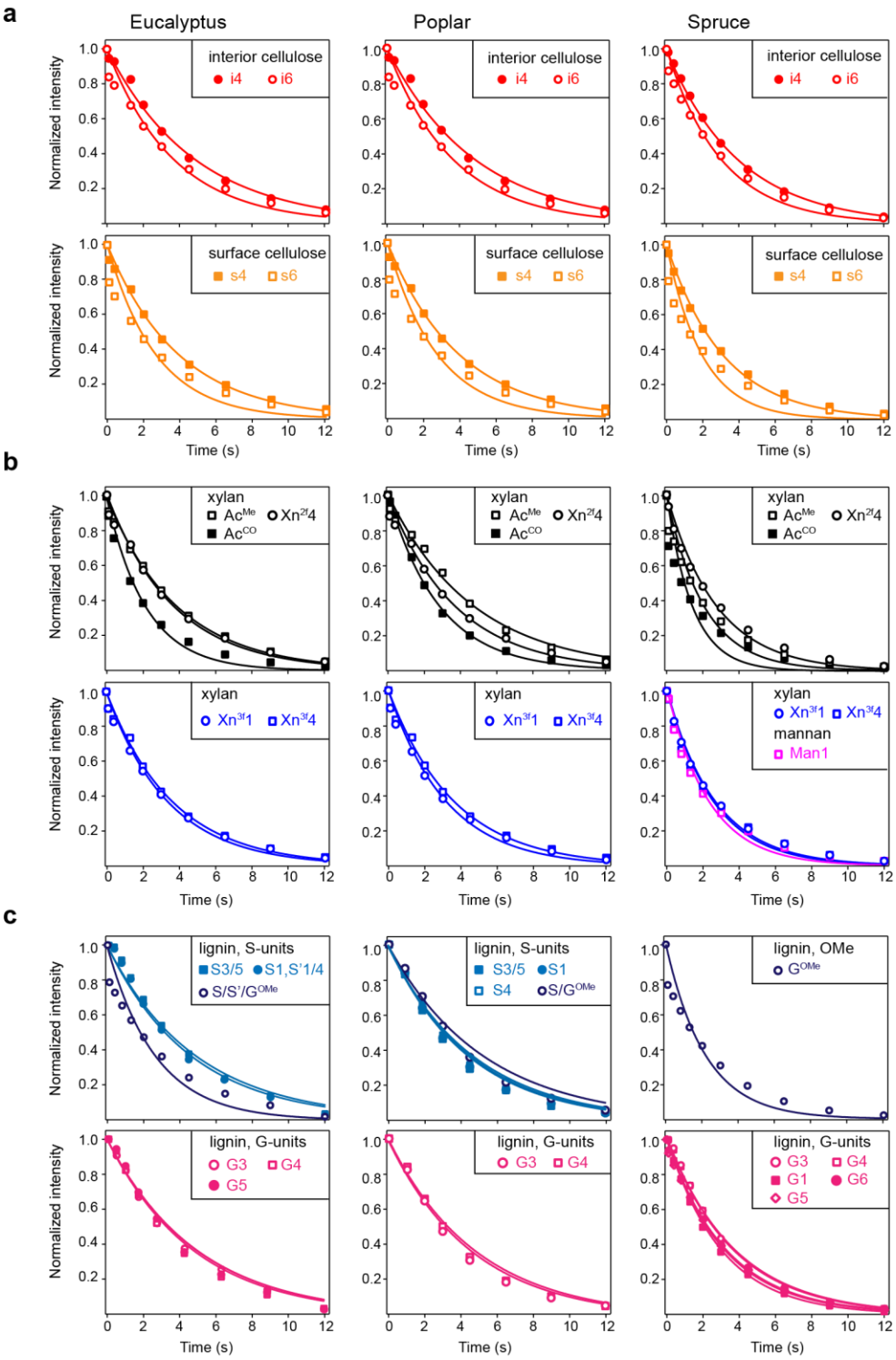

Figure F.14. The ^{13}C-T_1 relaxation curves of polysaccharides and lignin. The ^{13}C-T_1 relaxation curves of a) cellulose (interior and surface glucan chains), b) hemicellulose (2-fold and 3-fold xylan; mannan), and c) lignin (S and G units) are shown. The left, middle, and right columns are for eucalyptus, poplar, and spruce, respectively. The data are fitted using a single exponential equation. The fit parameters are summarized in Supplementary Table 6.14.

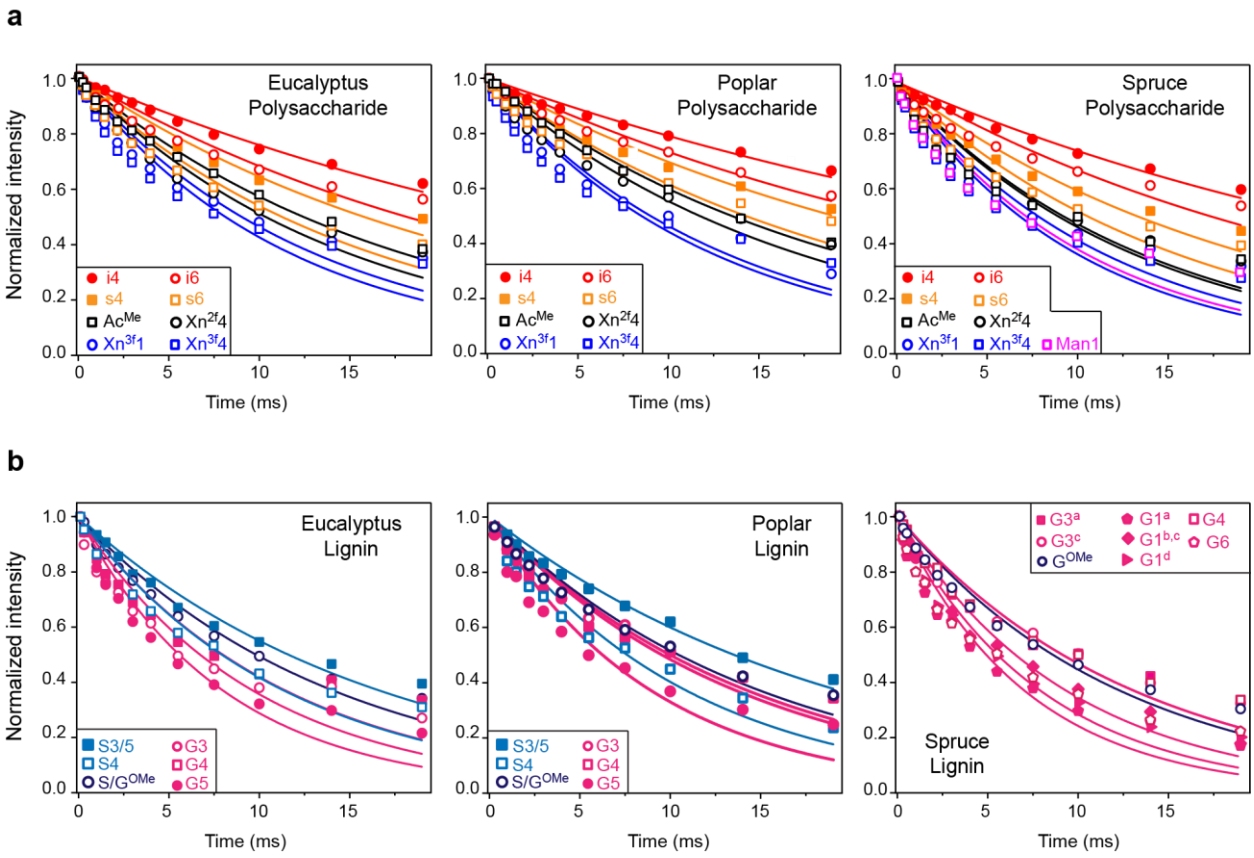

Figure F.15. ^{1}H-T$_{1\rho}$ relaxation curves of polysaccharides and lignin in woody plants. The ^{1}H-T$_{1\rho}$ relaxation curves of a, polysaccharides and b, lignin data are shown for eucalyptus, poplar, and spruce. The data are fitted using a single exponential equation. Xylan shows faster relaxation times compared to cellulose. Within lignin, the G residue has faster ^{1}H-T$_{1\rho}$ relaxation than the S unit. The fit parameters are summarized in Supplementary Table 15.

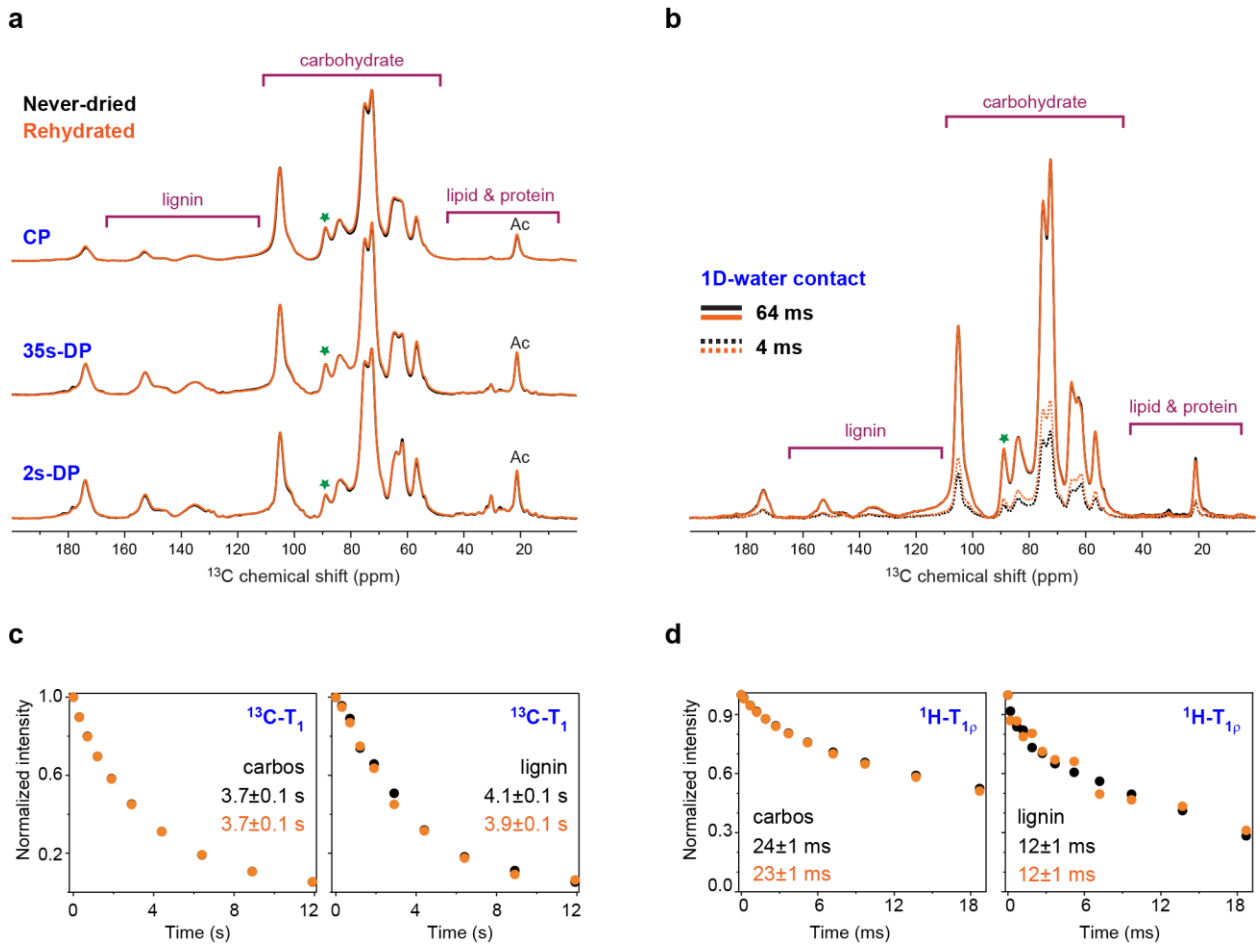

Figure F.16. Effect of freeze-drying and rehydration on hardwood eucalyptus. a) CP (rigid components selection), quantitative DP and DP (mobile components selection) normalized to i4 peak at 89 ppm. Distinct chemical shift intervals for lignin, carbohydrate, and lipid are highlighted. b) T_2-filtered (water-edited) 1D experiments. Signal maxima observed after 64 ms of spin diffusion, in comparison to the previous 36 ms and 26% signal difference in the absence of diffusion upon rehydration are consistent with both a sample less prone to deep hydration and a slight betterment of its surface water access after freeze-drying. c) Average ^{13}C T_1 relaxation curves, using an evolution of integrals of spectral regions established in panel (a). d) Average ^{1}H-$T_{1\rho}$ relaxation using the same two integrated intervals. Error bars are standard deviations of the fitting derived parameters. All these spectra and fitted relaxation parameters are very close for the fresh and rehydrated samples, demonstrating that structure and dynamics are not significantly altered by this sample preparation method. Their overall consistency with the main text eucalyptus sample also validates experimental reproducibility.

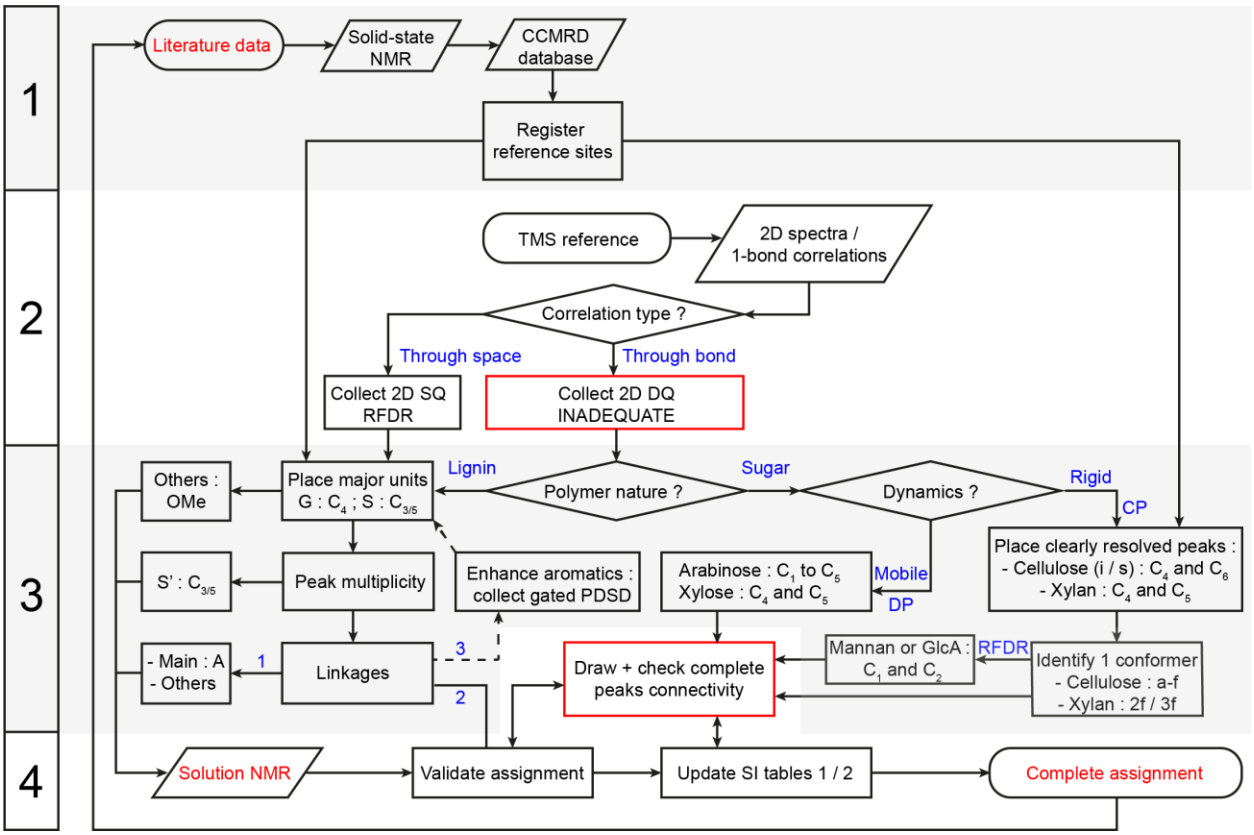

Figure F.17. Representative flow chart for resonance assignment. Shading and numbering on the left highlight the four main steps, while red coloring denotes essential sub-steps of the protocol followed for assigning chemical shifts. 1) Collection of reference chemical shifts for expected resolved peaks from solid-state NMR literature and databases. For each carbon site, we report associated references in Supplementary Table 19. 2) Acquisition of 2D solid-state NMR spectra. Subsequent assignments rely primarily on the resolution provided by the DQ dimension of INADEQUATE spectra. 3) Sequential assignment (boxes from right to left), from well-established cellulose and xylan conformers to mobile primary cell wall polysaccharides, ending with lignin and its linkages. For each polymer, we indicate a well-established site from which assignment can be easily initiated, while less resolved sites are either identified via cross-peaks connections or from literature reported values. 4) Safeguarding steps taken to provide accountability in the final assignments. Particularly for the complex lignin assignment, a good match is demanded with solution NMR spectra, as summarized in Supplementary Tables 5 and 19.

Table F.1. ^{13}C chemical shifts of rigid polysaccharides and lignin in wood secondary cell walls. The rigid components are identified from ^{13}C CP-based INADEQUATE and RFDR spectra. Superscripts are used to denote different allomorphs. Unidentified signals are indicated as (-). Not applicable (/)

	Lignin	C1	C2	C3	C4	C5	C6	OMe	C7 (α)	C8(β)	C9(γ)	Plant
G	guaiacyl	-	111.1	148.9	144.9	115.9	-	57.0	/	/	/	Eucalyptus
G^a		130.7	113.4	152.2	145.3	116.3	-	56.7	/	/	/	Spruce
G^b		133.5	110.5	149.7	146.1	-	120.2	57.0	/	/	/	Spruce
G^c		134.2	113.5	147.6	144.1	-	119.2	57.0	/	/	/	Spruce
G^d		136.0	109.5	151.6	142.2	-	121.1	57.0	/	/	/	Spruce
G^a		-	112.1	148.2	144.9	116.1	-	56.6				Poplar
G^b		-	113.8	148.2	144.9	116.1	-	56.6	/	/	/	Poplar
S^a	syringyl	134.9	102.8	153.3	133.5	153.3	102.8	57.0	/	/	/	Eucalyptus
S^b		-	109.7	153.2	137.2	153.2	109.7	57.0	/	/	/	Eucalyptus
S^a		134.2	104.0	153.1	134.6	153.1	104.0	56.6	/	/	/	Poplar
S^b		137.1	102.5	152.7	135.8	152.7	102.5	56.6	/	/	/	Poplar
S'^a	Cα-oxidized syringyl	134.1	109.2	144.8	136.3	144.8	109.2	56.5	/	/	/	Eucalyptus
S'^b		136.5	112.5	145.5	138.5	145.5	112.5	56.5	/	/	/	Eucalyptus
A(S)	β-O-4’	/	/	/	/	/	/	/	72.3	84.5	59.4	Eucalyptus
A (G)		/	/	/	/	/	/	/	72.4	84.3	59.9	Spruce
A(S)		/	/	/	/	/	/	/	72.0	86.3	60.4	Poplar
B	γ-acylated β-β’	/	/	/	/	/	/	/	84.4	53.5	71.2	Eucalyptus
B’	β-β’	/	/	/	/	/	/	/		53.5	74.4	Eucalyptus
B		/	/	/	/	/	/	/		53.9	70.3	Spruce
B’		/	/	/	/	/	/	/	83.9	52.9	74.1	Spruce
B		/	/	/	/	/	/	/	84.8	52.6	70.5	Poplar
C’	β-5’	/	/	/	/	/	/	/	90.2	49.9		Spruce
C’	γ-acylated β-5’	/	/	/	/	/	/	/	86.7	49.6		Spruce
C		/	/	/	/	/	/	/	88.1	54.2		Spruce
E	β’-1’	/	/	/	/	/	/	/	81.1	59.6		Eucalyptus
		/	/	/	/	/	/	/	81.4	60.0		Spruce
		/	/	/	/	/	/	/	80.3	59.7		Poplar
	Carbohydrate	C1	C2	C3	C4	C5	C6	Ac^{CO}	Ac^{Me}			
Xn^{2f}	2-fold xylan	104.8	72.2	74.0	82.2	64.0	/	174.0	21.0			Eucalyptus
Xn^{3f}	3-fold xylan	102.5	73.4	74.1	77.4	63.3	/	174.0	21.0			

(table cont,d)

	Carbohydrate	C1	C2	C3	C4	C5	C6	Ac^{CO}	Ac^{M}			
Xn^{3f}	3-fold xylan	102.5	73.4	74.1	77.4	63.3	/	174.0	21.0			Eucalyptus
Xn	xylan mix	-	-	74.2	78.5	64.1	/	174.0	21.0			Eucalyptus
Xn^{2f}	2-fold xylan	104.8	72.1	73.2	82.0	63.9	/	174.0	21.0			Poplar
Xn^{3f}	3-fold xylan	102.2	73.6	74.2	77.9	64.1	/	174.0	21.0			
Xn^{2f}	2-fold xylan	104.8	72.2	73.3	82.2	63.9	/	174.0	21.0			Spruce
Xn^{3f}	3-fold xylan	103.5	73.9	74.2	77.8	65.4	/	174.0	21.0			
x	xylose in XyG	-	-	74.1	70.4	62.5	/	/	/			All samples
$GlcA^{a}$	GlcA in GAX	101.5	71.3	79.8	69.9	76.6	-					All samples
$GlcA^{b}$	GlcA in GAX	99.2	69.9	-	-	-	-					All samples
$GlcA^{c}$	GlcA in GAX	98.5	71.6	80.8	-	-	-					All samples
GalA	galacturonic acid	100.2	68.1	-	79.6	-	-					All samples
M	mannan	101.2	71.3	75.1	-	75.1	62.1					Spruce
M^{Ac}	acetylated mannan	101.6	72.1	75.1	80.7	75.1	62.1					Spruce
A (t-Ara)	arabinose	108.1	82.1	-	85.6	62.1	/					Spruce
i^{a}	interior cellulose	104.9	72.1	75.2	88.7	72.3	65.0					Eucalyptus
i^{b}		104.9	72.1	75.2	88.7	72.3	65.0					
i^{c}		104.9	72.1	74.1	87.9	71.1	65.7					
s^{f}	surface cellulose	104.9	72.1	74.6	84.4	74.6	62.3					Eucalyptus
s^{g}		104.9	72.1	73.6	83.5	73.6	61.4					
i^{a}	interior cellulose	104.8	72.1	75.0	88.9	72.4	64.9					Poplar
i^{b}		104.8	72.1	75.0	88.9	72.4	64.9					
i^{c}		104.8	72.1	74.3	87.9	70.1	65.5					
s^{f}	surface cellulose	104.8	72.1	75.7	84.3	75.0	62.3					Poplar
s^{g}		104.8	72.1	75.2	83.4	73.7	61.3					
i^{a}	interior cellulose	104.8	72.2	75.3	89.0	72.4	65.0					Spruce
i^{b}		104.8	72.2	75.3	89.0	72.4	65.0					
i^{c}		104.8	72.2	74.3	88.1	71.0	65.6					
s^{f}	surface cellulose	104.8	72.2	75.1	84.5	75.0	62.1					Spruce
s^{g}		104.8	72.2	74.3	84.3	74.3	61.4					

Table F.2. ^{13}C chemical shifts of mobile molecules in woods. The mobile components are identified from ^{13}C DP-based INADEQUATE spectra measured with short recycle delays of 2 s. Superscripts are used to denote different allomorphs. Not applicable (/). Unidentified (-).

	carbohydrate	C1	C2	C3	C4	C5	C6	Plants
A^a	arabinose	107.8	81.8	77.2	84.6	61.8	/	All samples
A^b		107.8	80.1	-	-	-	/	All samples
A^c		109.7	81.8	77.4	82.9	67.6	/	All samples
A^d		106.9	85.3	-	-	-	/	Eucalyptus
Gal	galactose	104.9	72.3	-	-	-	-	All samples
α-Glc	α-glucose	92.7	-	-	-	-	-	Spruce
β-Glc	β-glucose	96.6		-	-	-	-	Spruce
x	xylose in XyG	100.3	72.3	-	71.9	61.3	/	All samples
$i^{a,b}$	cellulose	-	-	75.5	88.9	72.4	64.9	Eucalyptus
i^c		-	-	75.5	88.9	70.9	65.8	Eucalyptus
$i^{a,b}$		-	-	75.5	88.9	72.4	64.9	Poplar
i^c		-	-	75.5	88.9	70.9	65.8	Poplar
s^f		-	-	-	-	75.0	61.4	All samples
s^g		-	-	-	-	73.7	61.2	Eucalyptus
s^g		-	-	-	-	73.7	61.2	Poplar
	lignin	C1	C2	C3	C4	C5	C6	Plants
G^a	guaiacyl	136.3	-	144.1	144.1	-	-	Eucalyptus
G^b		136.3	-	145.2	145.2	-	-	
S^a	syringyl	136.7	-	152.9	-	152.9	-	
S^b		135.5	-	151.7	-	151.7	-	
G	guaiacyl	130.1	-	147.8	146.4	-	-	Poplar
S^a	syringyl	-	-	152.6	-	152.6	-	
S^b		-	-	151.9	-	151.9	-	
G	guaiacyl	-	-	148.9	144.7	-	-	Spruce
G		-	-	152.3	-	152.3	-	

Table F.3. Molar composition of polysaccharides in wood secondary cell walls. For each plant, the composition of cellulose, xylan, mannan, and the primary cell wall component xyloglucan (XyG) is given. Cellulose contains interior glucan chains ($i^{a,b}$: middle layer; i^{c}: embedded core chains) and surface glucan chains (s^{f}: hydrophilic surface; s^{g}: hydrophobic surface). Xylan contains the backbone (Xn^{2f}: two-fold xylan; Xn^{3f}: three-fold xylan; Xn: mixed conformation) and sidechains (GlcA and/or Ara). For Mannan, only the mannose residues (M: unacetylated; M^{Ac}: acetylated) are resolved, while the actual fraction of mannan should be higher than the value reported here due to the presence of Glc residues in the backbone. The sidechain α-xylose (x) is used to denote xyloglucan.

Eucalyptus

Cellulose 74.0%				Xylan 25.5%					Mannan -		XyG 0.5%
interior chains 38.2%		surface chains 35.8%		backbone 16.8%			sidechains 8.7%		- -		
$i^{a,b}$	i^{c}	s^{f}	s^{g}	Xn^{2f}	Xn	Xn^{3f}	GlcA	Ara	M	M^{Ac}	x
28.3%	9.8%	21.2%	14.6%	10.0%	2.0%	4.9%	8.7%	-	-	-	0.5%

Poplar

Cellulose 81.4%				Xylan 18.0%					Mannan -		XyG 0.6%
interior chains 45.0%		surface chains 36.4%		backbone 13.3%			sidechains 4.8%		-		
$i^{a,b}$	i^{c}	s^{f}	s^{g}	Xn^{2f}	Xn	Xn^{3f}	GlcA	Ara	M	M^{Ac}	x
32.7%	12.3%	21.9%	14.6%	7.9%	1.6%	3.8%	4.8%	-	-	-	0.6%

Spruce

Cellulose 75.8%				Xylan 11.8%					Mannan 10.5%		XyG 1.9%
interior chains 37.1%		surface chains 38.7%		backbone 10.4%			sidechains 1.5%				
$i^{a,b}$	i^{c}	s^{f}	s^{g}	Xn^{2f}	Xn	Xn^{3f}	GlcA	Ara	M	M^{Ac}	x
28.1%	8.9%	23.6%	15.2%	6.9%	-	3.5%	0.5%	1.0%	6.2%	4.3%	1.9%

The area of the following well-resolved peak pairs in CP J-INADEQUATE spectra are used:
$i^{a,b}$: the average of $i5^{a,b}$ - $i6^{a,b}$, $i4^{a,b}$ - $i5^{a,b}$, and $i3^{a,b}$ - $i4^{a,b}$.
i^{c} : the average of $i5^{c}$ - $i6^{c}$, $i4^{c}$ - $i5^{c}$, and $i3^{c}$ - $i4^{c}$.
s^{f} : the average of $s5^{f}$ - $s6^{f}$, $s4^{f}$ - $i5/3^{f}$. The integration of $s4^{f}$ - $i5/3^{f}$ has been doubled because 2 peak pairs are included (carbon 4-carbon 5 and carbon 4-carbon 3).
s^{g} : the average of $s5^{g}$ - $s6^{g}$, $s4^{g}$ - $i5/3^{g}$. The integration of $s4^{g}$ - $i5/3^{g}$ has been doubled because 2 peak pairs are included (carbon 4-carbon 5 and carbon 4-carbon 3).
Xn^{2f}: the average of $Xn4^{2f}$ and $Xn5^{2f}$.
Xn: the average of Xn4 and Xn5.
Xn^{3f}: the average of $Xn4^{3f}$ and $Xn5^{3f}$.
GlcA: the average of GlcA1 and GlcA2. The value reported are the sum of $GlcA^{a}$, $GlcA^{b}$ and $GlcA^{c}$.
Ara: the average of A1 and A2.
M: the average of M1 and M2.
M^{Ac}, the average of $M1^{Ac}$ and $M2^{Ac}$.
x: the average of x4 and x5.

Table F.4. Solution NMR HSQC ^{1}H and ^{13}C chemical shifts of lignin aromatics and linkages. Unidentified or unresolved (-)

		Eucalyptus		Poplar		Spruce	
		^{13}C (ppm)	^{1}H (ppm)	^{13}C (ppm)	^{1}H (ppm)	^{13}C (ppm)	^{1}H (ppm)
G2	guaiacyl	111.9	6.99	111.6	7.00	111.6	7.0
G5	guaiacyl	115.5	6.67	115.7	6.78	114.9	6.77
		& 115.8	& 6.97	& 115.8	& 6.97	& 115.9	& 6.93
G6	guaiacyl	119.9	6.99	119.8	6.83	119.7	6.86
G'2	oxidized guaiacyl	112.2	7.53	112.4	7.53	112.2	7.51
G'6	oxidized guaiacyl	124.2	7.16	123.8	7.60	123.6	7.57
S2/6	syringyl	104.3	6.71	104.6	6.73	-	-
S'2/6	oxidized syringyl	107.3	7.32	107.2	7.24	-	-
			& 7.12		& 7.09		
H2/6		126.9	7.20	128.6	7.22	-	-
Aα (G)	β-O-4'	71.8	4.65	71.8	4.65	71.9	4.77
Aα (S)	β-O-4'	72.6	4.88	72.6	4.88		
Aβ(G)	β-O-4'	84.5	4.31	84.6	4.31	84.6	4.31
Aβ(S)	β-O-4'	86.7	4.14	86.7	4.14		
Aγ	β-O-4'	60.5	3.42	-	-	-	-
			& 3.67				
Bα	β-β' (resinol)	85.8	4.68	84.6	4.76	85.6	4.65
Bβ	β-β' (resinol)	53.8	3.14	54.3	3.10	53.9	3.14
Bγ	β-β' (resinol)	71.7	3.88	70.5	3.73	70.3	3.77
			& 4.20				
Cα	β-5' (phenylcoumaran)	87.7	5.49	87.7	5.49	87.6	5.49
Cβ	β-5' (phenylcoumaran)	53.8	3.14	54.1	3.49	54.2	3.42
Cγ	β-5' (phenylcoumaran)	62.7	3.44	-	-	-	-
			& 3.59				
Dα	5-5' (dibenzodioxocin)	83.8	4.90	-	-	-	-
Dβ	5-5' (dibenzodioxocin)	85.6	3.91	85.6	3.92	84.9	3.88
Eα	β-1' (spirodienone)	81.8	5.07	81.9	5.08	83.7	5.02
Eα'	β-1' (spirodienone)	86.9	4.41	87.0	4.42	-	-
Eβ	β-1' (spirodienone)	60.4	2.79	60.7	2.80	61.8	2.8
Eβ'	β-1' (spirodienone)	-	-	78.7	4.14	-	-

(table cont'd.)

		Eucalyptus		Poplar		Spruce	
		^{13}C (ppm)	^{1}H (ppm)	^{13}C (ppm	^{1}H (ppm)	^{13}C (ppm)	^{1}H (ppm)
E2/2’	β-1’ (spirodienone)	114.9	6.24	114.2	6.23	114.3	6.21
E6/6’	β-1’ (spirodienone)	119.5	6.12	119.2	6.15	119.5	6.11
Iα	cinnamyl alcohol	128.3	6.46	129.0	6.45	129.5	6.48
Iβ	cinnamyl alcohol	129.7	6.25	129.5	6.27	129.1	6.32
Iγ	cinnamyl alcohol	62.4	4.11	62.3	4.12	62.5	4.13
Jα	cinnamaldehyde	154.5	7.65	154.2	7.64	154.4	7.66
Jβ	cinnamaldehyde	126.7	6.81	127.1	6.80	127.4	6.88
J6	cinnamaldehyde	122.4	7.21	123.9	7.22	124.3	7.20
PB2/6	*p*-hydroxybenzoate	-	-	132.1	7.70	-	-
Stα/β	stilbene	-	-	-	-	127.1	6.88

Table F.5. Average solution NMR chemical shifts of lignin from literature. The reference (Ref.) for each chemical shift is provided. Not detected (-).

	Eucalyptus			Poplar			Spruce		
	^{13}C (ppm)	^{1}H (ppm)	Ref.	^{13}C (ppm)	^{1}H (ppm)	Ref.	^{13}C (ppm)	^{1}H (ppm)	Ref.
G2	111.3	6.98	215,217,218,222,223	111.1	6.98	209,219-221,224	110.3	6.94	310,311
G5	115.2	6.72	222 / 215,218,223	115.0	6.80	209,219-221,224	115.2	6.85	310,311
		& 6.94	222 / 215,218	-	-	-	-	-	-
G6	119.3	6.80	215,217,218,222,223	119.1	6.8	209,219-221,224	118.9	6.83	310,311
G'2	112.4	7.50	218	111.4	7.51	224	-	-	218 / 224
G'6	124.0	7.00	218	123.3	7.60	224	-	-	224
S2/6	104.2	6.99	215,217,218,222,223	103.8	6.67	209,219-221,224	-	-	-
S'2/6	106.5	7.31	215,217,218,222,223	106.1	7.22	209,219-221,224	-	-	-
H2/6	-	-	-	127.9	7.19	224	-	-	-
Aα(G)	71.6	4.74	222 / 215,218	71.5	4.75	219	71.1	4.75	210,310
Aα (S)	72.2	4.87	215,217,218,222,223	71.9	4.83	209,219-221	-	-	210,310
Aβ(G)	83.9(1)	4.29	215,217,218,222,223	83.7 [a]	4.29	219,224 / 209	84.0	4.29	210,310
Aβ(S)	86.4	4.09	215,217,218,222,223	85.8	4.13	219,224 / 209,221	-	-	210,310
Aγ	59.8	3.39	217,218,222/ 223	59.9	3.45	219,224 / 221	59.9	3.24	210,310
		& 3.69	217,218,222/ 223			219,224		& 3.61	210,310
Bα	85.2	4.66	215,217,218,222,223	85.0	4.64	209,219-221,224	85.0	4.65	210,310
Bβ	53.7	3.08	217,218,222/ 223	53.6	3.07	219,224 / 221	53.6	3.07	210,310
Bγ	71.4	3.82	217,218,222/ 223	70.6	3.81	219,224	70.9	3.74	210,310
Cα	87.1	5.46	215,217,218,222,223	87.0	5.47	209,219-221,224	87.0	5.47	210,310
Cβ	53.5	3.45	217,218,222/ 223	53.2	3.48	219,220,224	53.1	3.46	210,310
Cγ	62.7	3.67	217,222/ 223	62.5	3.74	219,224	62.8	3.72	210,310

(table cont'd.)

	Eucalyptus			Poplar			Spruce		
	^{13}C (ppm)	^{1}H (ppm)	Ref.	^{13}C (ppm)	^{1}H (ppm)	Ref.	^{13}C (ppm)	^{1}H (ppm)	Ref.
Dα	83.6	4.83	[222]	81.4	4.7	[219]	83.3	4.84	[210,310]
Dβ	85.9	3.88	[222]	-	-	-	85.4	3.88	[210,310]
Eα	81.4	5.09	[217,222]	81.2	5.07	[224]	81.7	5.03	[210]
Eα’	86.6	4.39	[222]	-	-	-	-	-	-
Eβ	60.0	2.74	[217,222]	59.7	2.77	[224]	59.3	2.77	[210]
Eβ’	79.5	4.11	[217,222]	79.5	4.12	[224]	-	-	-
E2/2’	112.4	6.26	[217,222]	113.3	6.22	[224]	-	-	[217,222 / 224]
E6/6’	119.1	6.07	[217,222]	118.9	6.07	[224]	-	-	[217,222 / 224]
Iα	-	-	-	128.4	6.44	[224]	-	-	-
Iβ	-	-	-	128.2	6.25	[224]	-	-	-
Iγ	61.7	4.09	[217,218,222]	61.4	4.10	[224]	61.5	4.08	[210,310]
Jα	-	-	-	153.5	7.60	[224]	153.7	7.61	[310]
Jβ	-	-	-	126.1	6.76	[224]	126.3	6.77	[310]
J6	-	-	-	-	-	-	123.2	7.22	[310]
PB2/6	-	-	-	131.1	7.66	[209,219-221,224]	-	-	[310]
Stα/β	126	7.0	[223]	-	-	-	128.3	7.12	[310]

[a] May also includes Aβ(G/H)

Table F.6. Spectral deconvolution of quantitative ^{13}C spectra for lignin compositional analysis. The attributed chemical shifts are labeled. Unidentified (-).

Eucalyptus

Chemical Shift [ppm]	Amplitude	Width [ppm]	Integral [%]	Attribution
180.6	117	4.2	2.2	-
177.9	170	2.6	1.9	-
173.8	956	3.9	16.2	Ac^{CO}
171.8	211	3.2	3.0	-
169.4	306	1.5	2.0	-
168.4	314	0.4	0.5	-
167.5	385	0.4	0.7	-
157.3	36	0.1	0.02	-
152.2	401	3.5	6.2	S3/5
147.7	171	3.4	2.6	G3
144.8	550	2.6	6.3	G4/S'3
138.4	63	2.6	0.7	$S'^{b}4$
136.4	341	4.4	6.6	$S1/S'^{a}4$
132.2	149	5.5	3.6	-
129.8	79	0.6	0.2	-
128.2	128	1.9	1.1	-
125.0	133	2.0	1.2	-
119.9	70	3.8	1.2	
114.7	195	6.0	5.2	G5
109.4	185	4.9	4.0	S'2/6
107.6	229	0.9	0.9	A1
104.6	2261	2.6	25.5	$i/s/Xn1^{2f}$
102.2	75	0.3	0.1	$Xn1^{3f}$
100.8	444	2.4	4.6	Man1
98.5	281	1.9	2.4	-
96.4	209	0.8	0.7	-
92.6	135	0.8	0.5	-

Poplar

Chemical Shift [ppm]	Amplitude	Width [ppm]	Integral [%]	Attribution
181.0	109	6.7	3.1	
173.6	1037	3.2	14.1	Ac^{CO}
171.7	173	1.1	0.8	
152.6	744	3.8	12.2	S3/5
148.2	217	3.3	3.0	G3
145.2	151	2.3	1.5	G4
136.9	165	2.9	2.0	$S^{b}4$

(table cont'd.)

Poplar

Chemical Shift [ppm]	Amplitude	Width [ppm]	Integral [%]	Attribution
134.2	315	5.1	S^a4	
131.2	193	3.9	3.2	
120.0	42	2.4	0.4	
115.5	188	8.4	6.8	G5
108.9	16	1.9	0.1	
104.7	3650	2.6	40.1	$i/s/Xn1^{2f}$
102.4	60	0.5	0.1	$Xn1^{3f}$
100.6	632	2.7	7.2	
96.5	62	0.3	0.1	

Spruce

Chemical Shift [ppm]	Amplitude	Width [ppm]	Integral [%]	Attribution
183.0	96	3.3	1.2	
181.7	248	1.4	1.3	
178.0	206	2.5	1.9	
174.1	836	3.1	9.5	Ac^{CO}
171.9	224	2.1	1.7	
169.5	36	1.1	0.1	
157.4	375	0.4	0.6	
153.4	323	5.3	6.3	
148.2	466	5.3	9.2	$G^a3/4$
145.5	289	3.6	3.8	$G^b3/4$
137.1	89	2.8	0.9	G^b1
134.6	163	2.6	1.6	$G^{c/d}1$
132.1	322	3.8	4.5	
129.9	389	1.2	1.7	G^a1
128.6	266	1.7	1.7	
125.0	52	7.6	1.4	
120.1	57	2.9	0.6	G6
114.7	389	14.2	20.6	G2/5
107.7	623	0.9	2.1	A1
104.8	2103	2.6	18.4	
101.8	275	1.6	1.6	
100.4	907	1.4	4.6	M1
98.8	492	1.5	2.8	
96.5	477	0.7	1.2	β-Glc1
92.6	308	0.7	0.7	α-Glc1

Table F.7. The Intensities of intermolecular cross peaks of eucalyptus. In summary, 98 intermolecular interactions are identified, including 45 strong, 29 medium, and 24 weak restraints. In gated 1-s PDSD spectra, a peak higher than 4% is categorized as a strong restraint (s, in bold), between 2% - 4% for medium (m) restraint, and below 2% for weak (w) restraint. All the peaks shown in the gated 100-ms PDSD spectrum are categorized as strong restraints.

	Atom1 (ω_1)	Atom2 (ω_2)	Gated 100 ms PDSD (%)	Gated 1s PDSD (%)	Type
cellulose-xylan	Ac^{CO}	i4		0.13	w
	Ac^{Me}	i4		1.40	w
	Ac^{CO}	s4		0.16	w
	Ac^{Me}	s4		0.85	w
cellulose-lignin	G3	i4		1.84	w
	G4,S'3/5	i4		0.49	w
	G5	i4		3.29	m
	$S1/4^a,S'1^a$	i4	**2.11**	**7.81**	**s**
	$S/S'4^b$	i4		1.28	w
	S3/5	i4		1.27	w
	OMe	i4	**0.67**	**0.99**	**s**
	G3	s4		2.39	m
	G3	s6	**0.94**	**4.05**	**s**
	G4,S'3/5	s4		1.24	w
	G4,S'3/5	s6		3.49	m
	G5	s4		0.83	w
	$S1/4^a,S'1^a$	s4		2.35	m
	$S1/4^a,S'1^a$	s6	**1.23**	**5.49**	**s**
	S3/5	s4		1.34	w
	S3/5	s6		4.21	**s**
	$S/S'4^b$	s4		1.24	w
	$S/S'4^b$	s6		**5.25**	**s**
	OMe	s4	**0.98**	**1.77**	**s**
	OMe	s6	**1.34**	**3.39**	**s**
lignin-lignin	G3	$S1/4^a,S'1^a$		3.42	m
	G3	$S2/6^b$		2.41	m
	G3	S3/5		7.00	**s**
	G3	$S/S'4^b$		3.37	m
	G4,S'3/5	$S2/6^a$		1.34	w
	G4,S'3/5	$S2/6^b$		3.45	m
	G4,S'3/5	S3/5		**4.75**	**s**
	G5	$S1/4^a,S'1^a$	**1.36**	**7.34**	**s**
	G5	$S2/6^a$		3.26	m
	G5	S3/5		5.18	**s**
	G5	$S/S'4^b$		3.91	m
	$S1/4^a,S'1^a$	G3		3.87	m
	S3/5	G2		2.40	m
	S3/5	G3		1.88	w
	S3/5	G4,S'3/5		1.88	w
	S3/5	G5		0.48	w

(table cont'd)

	Atom1 (ω_1)	Atom2 (ω_2)	Gated 100 ms PDSD (%)	Gated 1s PDSD (%)	Type
	S3/5	S'1^{b}/4^{a}		3.39	m
	S/S'4^{b}	G3		2.58	m
	S/S'4^{b}	G5		2.20	m
xylan-lignin	Ac^{CO}	G4,S'3/5		2.26	m
	Ac^{CO}	G5		0.47	w
	Ac^{CO}	S1/4^{a},S'1^{a}		1.83	w
	Ac^{CO}	S3/5		2.01	m
	Ac^{CO}	OMe		**4.61**	**s**
	G3	Ac^{CO}		3.85	m
	G4,S'3/5	Ac^{CO}	**3.12**	**8.98**	**s**
	G5	Ac^{CO}		**6.87**	**s**
	S3/5	Ac^{CO}		3.58	m
	S/S'4^{b}	Ac^{CO}	**2.65**	**8.08**	**s**
	OMe	Ac^{CO}		**6.01**	**s**
	Ac^{Me}	G4,S'3/5		1.56	w
	Ac^{Me}	S3/5		2.33	m
	Ac^{Me}	S/S'4^{b}		1.95	w
	Ac^{Me}	OMe		2.85	m
	G3	Ac^{Me}		**5.12**	**s**
	G4,S'3/5	Ac^{Me}	**0.99**	**6.31**	**s**
	G5	Ac^{Me}	**1.19**	**6.94**	**s**
	S1/4^{a},S'1^{a}	Ac^{Me}		**4.26**	**s**
	S3/5	Ac^{Me}		3.60	m
	S/S'4^{b}	Ac^{Me}		**4.27**	**s**
	OMe	Ac^{Me}		**4.34**	**s**
	G3	Xn4^{2f}		3.34	m
	G3	Xn5$^{2f, 3f}$		3.34	m
	G4,S'3/5	Xn4^{2f}		1.59	w
	G4,S'3/5	Xn4^{3f}		1.19	w
	G4,S'3/5	Xn5$^{2f, 3f}$	**1.68**	5.03	**s**
	G5	Xn4^{2f}		2.11	m
	G5	Xn4^{3f}		2.81	m
	G5	Xn5$^{2f, 3f}$		1.33	w
	S1/4^{a},S'1^{a}	Xn4^{2f}		**5.29**	**s**
	S1/4^{a},S'1^{a}	Xn4^{3f}	**0.64**	**2.71**	s
	S1/4^{a},S'1^{a}	Xn5$^{2f, 3f}$		**5.64**	**s**
	S3/5	Xn4^{2f}		3.42	m
	S3/5	Xn5$^{2f, 3f}$		**4.92**	**s**
	S/S'4^{b}	Xn4^{2f}		2.86	m
	S/S'4^{b}	Xn4^{3f}		**4.07**	**s**
	S/S'4^{b}	Xn5$^{2f, 3f}$		**4.15**	**s**
	OMe	Xn4^{2f}	**0.96**	**3.66**	s
	OMe	Xn4^{3f}	**1.34**	**1.55**	**s**
	OMe	Xn5$^{2f, 3f}$	**1.67**	**3.85**	**s**
mixed sugar-lignin	G3	i/s/Xn1^{2f}	**2.61**	**6.08**	**s**
	G3	Xn2/3^{3f},Xn3^{2f},i2/5,s2/3	**4.36**	**23.70**	**s**
	G4,S'3/5	i/s/Xn1^{2f}		1.23	w
	G4,S'3/5	Xn2/3^{3f},Xn3^{2f},i2/5,s2/3	**3.96**	**18.03**	**s**

(table cont'd.)

	Atom1 (ω_1)	Atom2 (ω_2)	Gated 100 ms PDSD (%)	Gated 1s PDSD (%)	Type
	G5	i/s/Xn1^{2f}		**5.84**	**s**
	G5	Xn2/3^{3f},Xn3^{2f},i2/5,s2/3	**7.36**	**22.50**	**s**
	S1/4^{a},S'1^{a}	i/s/Xn1^{2f}	**2.71**	**8.47**	**s**
	S3/5	i/s/Xn1^{2f}	**2.62**	**7.68**	**s**
	S3/5	Xn2/3^{3f},Xn3^{2f},i2/5,s2/3		26.12	**s**
	S/S'4^{b}	i/s/Xn1^{2f}		2.22	m
	S/S'4^{b}	Xn2/3^{3f},Xn3^{2f},i2/5,s2/3		**17.08**	**s**
	OMe	i/s/Xn1^{2f}		**8.71**	**s**
	OMe	Xn2/3^{3f},Xn3^{2f},i2/5,s2/3		**14.56**	**s**

Table F.8. The Intensities of intermolecular cross peaks of poplar wood. In sum, 80 intermolecular interactions are identified, including 22 strong, 33 medium, and 25 weak restraints. In gated 1-s PDSD spectra, a peak higher than 4% is categorized as a strong restraint (s, in bold), between 2% - 4% for medium (m) restraint, and below 2% for weak (w) restraint. All the peaks shown in the gated 100-ms PDSD spectrum are categorized as strong restraints. The intensity is a relative ratio of the peak, which is normalized by the integral of the ^{13}C cross-section.

	Atom1 (ω_1)	Atom2 (ω_2)	Gated 100 ms PDSD (%)	Gated 1s PDSD (%)	Type
cellulose-xylan	Ac^{Me}	i4		2.16	m
	Ac^{CO}	s4		3.37	m
	Ac^{Me}	s4		1.76	w
	Ac^{Me}	s6		2.13	m
cellulose-lignin	G4	i4		1.80	w
	$S1^a$	i4		2.36	m
	$S1^b$	i4		2.51	m
	S3/5	i4		1.11	w
	OMe	i4		0.90	w
	$S1^a$	s4		1.78	w
	$S1^a$	s6		**4.26**	**s**
	$S1^b$	s4		1.55	w
	$S1^b$	s6		**5.32**	**s**
	S3/5	s4		3.21	m
	S3/5	s6		**6.04**	**s**
	G4	s4		2.52	m
	G4	s6		**4.01**	**s**
	OMe	s4		1.89	w
	OMe	s6		3.07	m
lignin-lignin	$S1^a$	$G2^a$		2.15	m
	$S1^a$	G3		2.88	m
	$S1^a$	G4		1.98	w
	$S1^a$	G5		2.62	m
	$S1^b$	$G2^a$		1.86	w
	$S1^b$	$G2^b$		1.27	w
	$S1^b$	G3		1.85	w
	$S1^b$	G4		1.81	w
	$S1^b$	G5		1.31	w
	G4	$S1^a$		**4.36**	**s**
	G4	$S1^b$		1.67	w
	G4	$S2/6^a$		3.67	m
	G4	S3/5	**2.97**	**9.76**	**s**
	S3/5	G3		2.48	m
	S3/5	G4		1.13	w
	S3/5	G5		2.20	m
xylan-lignin	Ac^{CO}	$G2^a$		2.02	m
	Ac^{CO}	G3		1.28	w
	Ac^{CO}	G4		1.12	w
	Ac^{CO}	G5		1.38	w
	Ac^{CO}	$S1^a$		1.37	w
	Ac^{CO}	$S1^b$		0.57	w
	Ac^{CO}	$S2/6^b$		2.44	m

(table cont'd.)

	Atom1 (ω_1)	Atom2 (ω_2)	Gated 100 ms PDSD (%)	Gated 1s PDSD (%)	Type
xylan-lignin	Ac^{CO}	S3/5		2.71	m
	Ac^{CO}	OMe		**5.09**	**s**
	G4	Ac^{CO}		3.91	m
	$S1^{a}$	Ac^{CO}		2.48	m
	$S1^{b}$	Ac^{CO}		**6.49**	**s**
	S3/5	Ac^{CO}		**4.58**	**s**
	Ome	Ac^{CO}		**6.99**	**s**
	Ac^{Me}	$G2^{b}$		0.80	w
	Ac^{Me}	G4		0.65	w
	Ac^{Me}	$S1^{b}$		0.51	w
	Ac^{Me}	$S2/6^{b}$		**4.91**	**s**
	Ac^{Me}	S3/5		3.08	m
	Ac^{Me}	S4		1.39	w
	Ac^{Me}	Ome		3.48	m
	G4	Ac^{Me}		3.48	m
	$S1^{a}$	Ac^{Me}		3.81	m
	$S1^{b}$	Ac^{Me}		**5.00**	**s**
	S3/5	Ac^{Me}	**1.44**	**2.87**	**s**
	Ome	Ac^{Me}	**1.62**	**3.91**	**s**
	G4	$Xn4^{2f}$		2.37	m
	G4	$Xn4^{3f}$		3.93	m
	G4	$Xn5^{2f, 3f}$		2.55	m
	$S1^{a}$	$Xn4^{2f}$		2.43	m
	$S1^{a}$	$Xn4^{3f}$		3.97	m
	$S1^{a}$	$Xn5^{2f, 3f}$	**1.17**	**3.58**	**s**
	$S1^{b}$	$Xn4^{2f}$		1.72	w
	$S1^{b}$	$Xn4^{3f}$		2.28	m
	$S1^{b}$	$Xn5^{2f, 3f}$		**5.16**	**s**
	S3/5	$Xn4^{2f}$		2.15	m
	S3/5	$Xn4^{3f}$		3.36	m
	S3/5	$Xn5^{2f, 3f}$		**4.66**	**s**
	Ome	$Xn4^{2f}$	**1.88**	**3.29**	**s**
	Ome	$Xn4^{3f}$	**1.56**	**2.53**	**s**
	Ome	$Xn5^{2f, 3f}$	**2.09**	**4.13**	**s**
mixed sugar-lignin	G4	$i/s/Xn1^{2f}$		2.33	m
	$S1^{a}$	$i/s/Xn1^{2f}$		2.92	m
	S3/5	$i/s/Xn1^{2f}$	**2.47**	**5.04**	**s**
	Ome	$i/s/Xn1^{2f}$	**1.95**	**11.46**	**s**

Table F.9. The Intensities of intermolecular cross peaks of poplar spruce. In sum, 94 intermolecular interactions are identified, including 51 strong, 9 medium, and 34 weak restraints. In gated 1-s PDSD spectra, a peak higher than 4% is categorized as a strong restraint (s, in bold), between 2% - 4% for medium (m) restraint, and below 2% for weak (w) restraint. All the peaks shown in the gated 100-ms PDSD spectrum are categorized as strong restraints. The intensity is a relative ratio of the peak, which is normalized by the integral of the ^{13}C cross-section.

	Atom1 (ω_1)	Atom2 (ω_2)	Gated 100 ms PDSD (%)	Gated 1s PDSD (%)	Type
cellulose-xylan	Ac^{CO}	i4		0.66	w
	Ac^{CO}	i6		3.06	m
	Ac^{Me}	i4		1.38	w
	Ac^{Me}	i6		2.08	m
	Ac^{CO}	s4	**0.96**	**3.08**	**s**
	Ac^{CO}	s6	**2.06**	**13.45**	**s**
	Ac^{Me}	s4	**1.21**	**3.92**	**s**
	Ac^{Me}	s6	**2.23**	**9.84**	**s**
cellulose-lignin	$G1^{a}$	i4	**1.12**	**2.50**	**s**
	$G1^{a}$	i6	**0.69**	**2.26**	**s**
	$G1^{b,c}$	i4	**0.36**	**1.10**	**s**
	$G1^{d}$	i4	**0.68**	**1.52**	**s**
	$G3^{a}$	i4	**1.03**	**2.93**	**s**
	$G3^{a}$	i6	**0.78**	**1.29**	**s**
	$G3^{c}$	i4		1.47	w
	$G4^{a,b,c}$	i4	**2.66**	**4.48**	**s**
	Ome	i4	**3.98**	**9.61**	**s**
	$G1^{a}$	s4		2.20	m
	$G1^{a}$	s6	**2.36**	**5.98**	**s**
	$G1^{b,c}$	s4	**1.22**	**2.39**	**s**
	$G1^{b,c}$	s6	**2.94**	**8.96**	**s**
	$G1^{d}$	s4		1.82	w
	$G3^{a}$	s4		1.44	w
	$G3^{a}$	s6	**2.36**	**5.05**	**s**
	$G3^{c}$	s4	**1.07**	**2.21**	**s**
	$G3^{c}$	s6	**1.98**	**8.07**	**s**
	$G4^{a,b,c}$	s4	**1.17**	**3.57**	**s**
	$G4^{a,b,c}$	s6	**2.32**	**6.63**	**s**
	Ome	s4	**3.63**	**9.99**	**s**
	Ome	s6	**4.01**	**23.53**	**s**
xylan-lignin	Ac^{CO}	$G1^{a}$		0.73	w
	Ac^{CO}	$G1^{b,c}$		0.67	w
	Ac^{CO}	$G1^{d}$		0.93	w
	Ac^{CO}	$G2^{a,c}$		1.98	w
	Ac^{CO}	$G2^{d}$		1.95	w
	Ac^{CO}	$G3^{a}$	**1.06**	**4.90**	**s**
	Ac^{CO}	$G3^{b}$		0.11	w
	Ac^{CO}	$G3^{c}$		2.61	m
	Ac^{CO}	$G3^{d}$		0.24	w
	Ac^{CO}	$G4^{a,b,c}$		3.22	m
	Ac^{CO}	$G6^{c}$		1.57	w
	Ac^{CO}	OMe	**2.59**	**7.82**	**s**

(table cont'd.)

	Atom1 (ω_1)	Atom2 (ω_2)	Gated 100 ms PDSD (%)	Gated 1s PDSD (%)	Type
	$G1^{a}$	Ac^{CO}	**2.36**	**6.31**	**s**
	$G1^{b,c}$	Ac^{CO}	**1.29**	**3.06**	**s**
	$G1^{d}$	Ac^{CO}		1.92	w
	$G3^{a}$	Ac^{CO}	**2.22**	**5.09**	**s**
	$G3^{c}$	Ac^{CO}	**1.03**	**2.09**	**s**
	$G4^{a,b,c}$	Ac^{CO}	**0.69**	**1.55**	**s**
	OMe	Ac^{CO}	**1.19**	**3.49**	**s**
	Ac^{Me}	$G1^{a}$		1.33	w
	Ac^{Me}	$G1^{b,c}$		0.30	w
	Ac^{Me}	$G2^{a,c}$		1.65	w
	Ac^{Me}	$G3^{a}$		2.26	m
	Ac^{Me}	$G3^{c}$		3.00	m
	Ac^{Me}	$G3^{d}$		0.67	w
	Ac^{Me}	$G4^{a,b,c}$		1.66	w
	Ac^{Me}	$G4^{d}$		1.67	w
	Ac^{Me}	$G6^{c}$		1.64	w
	Ac^{Me}	OMe	**1.49**	**5.37**	**s**
	$G1^{a}$	Ac^{Me}		3.40	m
	$G1^{b,c}$	Ac^{Me}		1.36	w
	$G1^{d}$	Ac^{Me}		1.20	w
	$G3^{a}$	Ac^{Me}		0.41	w
	$G3^{c}$	Ac^{Me}		0.72	w
	$G4^{a,b,c}$	Ac^{Me}		1.59	w
	OMe	Ac^{Me}	**1.20**	**2.29**	**s**
	$G1^{a}$	$Xn4^{2f}$	**0.86**	**3.88**	**s**
	$G1^{a}$	$Xn4^{3f}$		1.13	w
	$G1^{b,c}$	$Xn4^{2f}$	**0.98**	**2.75**	**s**
	$G1^{b,c}$	$Xn4^{3f}$	**1.12**	**2.27**	**s**
	$G1^{d}$	$Xn4^{2f}$	**1.21**	**2.09**	**s**
	$G1^{d}$	$Xn4^{3f}$	**1.51**	**3.06**	**s**
	$G1^{d}$	$Xn5^{2f, 3f}$	**2.67**	**6.47**	**s**
	$G3^{a}$	$Xn4^{2f}$	**1.36**	**2.82**	**s**
	$G3^{a}$	$Xn4^{3f}$	**1.54**	**4.14**	**s**
	$G3^{a}$	$Xn5^{2f, 3f}$	**1.11**	**2.46**	**s**
	$G3^{c}$	$Xn4^{2f}$	**2.01**	**4.43**	**s**
	$G3^{c}$	$Xn4^{3f}$		1.94	w
	$G4^{a,b,c}$	$Xn4^{2f}$	**1.86**	**4.48**	**s**
	$G4^{a,b,c}$	$Xn4^{3f}$	**0.87**	**2.48**	**s**
	$G4^{a,b,c}$	$Xn5^{2f, 3f}$	**0.99**	**2.79**	**s**
	OMe	$Xn4^{2f}$	**4.69**	**13.7**	**s**
	OMe	$Xn4^{3f}$	**3.96**	**9.92**	**s**
mannan-lignin	$G3^{c}$	Man1		1.19	w
	OMe	Man1		2.59	m

(table cont'd.)

	Atom1 (ω_1)	Atom2 (ω_2)	Gated 100 ms PDSD (%)	Gated 1s PDSD (%)	Type
mannan-xylan	Ac^{CO}	Man1	**1.32**	**2.04**	**s**
mixed sugar-lignin	$G1^{a}$	$i/s/Xn1^{2f}$		0.94	w
	$G1^{b,c}$	$i/s/Xn1^{2f}$		0.60	w
	$G1^{d}$	$i/s/Xn1^{2f}$		0.58	w
	$G3^{a}$	$i/s/Xn1^{2f}$		1.53	w
	$G3^{c}$	$i/s/Xn1^{2f}$		1.43	w
	$G4^{a,b,c}$	$i/s/Xn1^{2f}$	**0.66**	**1.53**	**s**
	OMe	$i/s/Xn1^{2f}$	**2.61**	**5.99**	**s**
	OMe	$Xn2/3^{3f}$,$Xn3^{2f}$,i2/5,s2/3	**3.39**	**15.46**	**s**

Table F.10. Intermolecular interactions of polymers in intact plant stems. In the summary of intermolecular cross-peaks between different polymers of the secondary cell wall of woods, a total of 272 cross-peaks have been identified and categorized as 112 strong, 75 medium, and 85 weak interactions.

	Interactions	**s**	**m**	**w**	**Total**
Eucalyptus	cellulose-xylan	0	0	4	**4**
	cellulose-lignin	8	4	8	**20**
	lignin-lignin	4	11	4	**19**
	xylan-lignin	22	13	7	**42**
	mixed sugar-lignin	11	1	1	**13**
Poplar	cellulose-xylan	0	3	1	**4**
	cellulose-lignin	4	5	6	**15**
	lignin-lignin	2	6	8	**16**
	xylan-lignin	14	17	10	**41**
	mixed sugar-lignin	2	2	0	**4**
Spruce	cellulose-xylan	4	2	2	**8**
	cellulose-lignin	18	1	3	**22**
	lignin-lignin	0	0	0	**0**
	xylan-lignin	25	5	23	**53**
	Mannan-lignin	0	1	1	**2**
	Mannan-xylan	1	0	0	**1**
	mixed sugar-lignin	3	0	5	**8**
Total		**112**	**75**	**85**	**272**

Table F.11. Water-edited intensities of polysaccharide and lignin of Eucalyptus. The intensity ratio is obtained by comparing the water-edited and control 2D ^{13}C-^{13}C correlation spectra. Standard deviations of NMR signal-to-noise ratios are used as error bars. The numbers (bold) in parentheses indicate the average intensities under each type of the polysaccharide or lignin.

Type	cross peaks	Intensity
interior cellulose **(0.24)**	i4-1	0.44±0.03
	i4-3[a]	042±0.05
	i4-3[b,c]	0.42±0.03
	i4-2/5	0.42±0.09
	i4-6	0.40±0.07
	i6-1	0.48±0.19
	i6-4	0.4±0.2
	i6-3[a,b]	0.5±0.1
	i6-3[c]	0.5±0.1
	i6-2/5,2	0.5±0.1
surface cellulose **(0.36)**	s4-1	0.55±0.09
	s4-3/5	0.6±0.1
	s4-2	0.6±0.1
	s4-6	0.5±0.1
xylan[2f] **(0.31)**	Xn[2f]4-1	0.52±0.09
	Xn[2f]4-3	0.55±0.08
	Xn[2f]4-5	0.47±0.09
	Xn[2f]4-2	0.7±0.2
xylan[3f] **(0.44)**	Xn[3f]2/3-1	0.7±0.2
	Xn[3f]2/3-4	0.6±0.2
	Xn[3f]2/3-5	0.6±0.2
	Xn[3f]5-1	0.5±0.1
	Xn[3f]5-4	0.5±0.1
lignin **(0.51)**	S3/5-S1[b]	0.50±0.08
	S3/5-S1[a]	0.48±0.03
	S3/5-S2/6[a]	0.61±0.04
	S3/5-S2/6[b]	0.49±0.09
	S3/5-OMe	0.53±0.08
	S'3/5-4	0.61±0.09
	S'3/5-2, G4-2	0.5±0.1
	S'3/5-OMe, G4-OMe	0.5±0.1
	S4-S3/5	0.46±0.09
	S4-S2/6	0.44±0.08
	S4-S1	0.47±0.08
	S4-OMe	0.51±0.09
	S2/6-S3/5	0.6±0.2
	S2/6-S1	0.5±0.2
	S2/6-S4	0.5±0.1
	S2/6-OMe	0.51±0.09
lignin OMe **(0.42)**	OMe-S3/5	0.42±0.06
	OMe-G3	0.43±0.07
	OMe-S1	0.40±0.09
	OMe-S4	0.5±0.1
	OMe-S2/6	0.4±0.1

Table F.12. Water-edited intensities of polymers in poplar. The intensity ratio is obtained by comparing the water-edited and control 2D ^{13}C-^{13}C correlation spectra. Standard deviations of NMR signal-to-noise ratios are used as error bars. The numbers (bold) in parentheses indicate the average intensities under each type of the polysaccharide or lignin.

Type	cross peaks	Absolute Intensity
interior cellulose **(0.11)**	i4-1	0.11±0.04
	i4-3[a]	0.09±0.07
	i4-3[b,c]	0.09±0.07
	i4-2/5	0.10±0.08
	i6-1	0.12±0.05
	i6-4	0.12±0.03
	i6-3[a,b]	0.11±0.03
	i6-3[c]	0.11±0.04
	i6-2/5	0.11±0.02
surface cellulose **(0.11)**	s4-1	0.12±0.06
	s4-3/5	0.10±0.04
	s4-2	0.11±0.04
	s4-6	0.11±0.03
xylan[2f] **(0.30)**	Xn4[2f]-1	0.36±0.06
	Xn4[2f]-3	0.42±0.06
	Xn4[2f]-2	0.20±0.05
	Xn4[2f]-5	0.21±0.06
xylan[3f] **(0.25)**	Xn[3f]2/3-1	0.23±0.05
	Xn[3f]2/3-4	0.39±0.09
	Xn[3f]2/3-5	0.15±0.03
	Xn[3f]5-1	0.31±0.07
	Xn[3f]5-4	0.18±0.09
guaiacyl **(0.19)**	G5-3	0.14±0.04
	G5-1	0.14±0.03
	G5-OMe	0.18±0.02
	G2-3	0.28±0.06
	G2-1	0.16±0.05
	G2-6	0.21±0.04
	G2-OMe	0.21±0.03
syringyl **(0.16)**	S3/5-1[b]	0.16±0.09
	S3/5-1[a]	0.21±0.06
	S3/5-2/6	0.15±0.04
	S3/5-OMe	0.14±0.05
	S1[b]-S3/5	0.14±0.07
	S1[b]-S2/6	0.20±0.06
	S1[b]-OMe	0.15±0.06
	S1[a]-S3/5	0.13±0.03
	S1[a]-OMe	0.11±0.03
	S2/6-S3/5	0.17±0.04
	S2/6-S1[b]	0.20±0.06
	S2/6-OMe	0.11±0.03
syringyl/guaicyl OMe **(0.14)**	OMe-S3/5	0.13±0.04
	OMe-G3	0.14±0.03
	OMe-S1	0.14±0.04
	OMe-G5	0.15±0.05
	OMe-S2/6	0.15±0.03

Table F.13. Water-edited intensities of polysaccharides and lignin of spruce. The intensity ratio is obtained by comparing the water-edited and control 2D ^{13}C-^{13}C correlation spectra. Standard deviations of NMR signal-to-noise ratios are used as error bars. The numbers (bold) in parentheses indicate the average intensities under each type of the polysaccharide or lignin.

Type	cross peaks	Absolute Intensity
interior cellulose **(0.38)**	i4-1	0.44±0.02
	i4-3[a]	0.37±0.04
	i4-3[b,c]	0.37±0.03
	i4-2/5	0.39±0.03
	i6-1	0.42±0.07
	i6-4	0.4±0.1
	i6-3	0.32±0.05
	i6-2/5,2	0.4±0.1
surface cellulose **(0.43)**	s4-1	0.5±0.1
	s4-2/5	0.44±0.03
	s4-3	0.4±0.2
	s4-6	0.46±0.03
xylan[2f] **(0.57)**	Xn[2f]4-1	0.7±0.1
	Xn[2f]4-3	0.43±0.04
	Xn[2f]4-5	0.57±0.04
	Xn[2f]4-1	0.67±0.05
	Xn[2f]4-2	0.56±0.06
xylan [3f] **(0.40)**	Xn[3f]2/3-1	0.4±0.1
	Xn[3f]2/3-4	0.32±0.07
	Xn[3f]2/3-5	0.4±0.1
	Xn[3f]5-4	0.44±0.05
	Xn[3f]5-1	0.48±0.04
mannan **(0.76)**	Man1-4	0.86±0.06
	Man1-5	0.63±0.06
	Man1-6	0.79±0.05
guaiacyl **(0.47)**	G3-1	0.4±0.1
	G3-2	0.47±0.04
	G3-OMe	0.52±0.09
	G1-3	0.5±0.1
	G6-3	0.40±0.06
	G6-OMe	0.35±0.03
	G2-3[b,c]	0.51±0.06
	G2-3[a]	0.65±0.05
	G2-OMe	0.54±0.15
guaiacyl OMe **(0.42)**	OMe-G3	0.45±0.08
	OMe-G1	0.40±0.06
	OMe-G2	0.42±0.07

Table F.14. ^{13}C-T_1 relaxation times of lignin and polysaccharides in the three woods. The data are fit using single exponential equations $I(t) = 1 - 2e^{-t/T}$ for T_1, DP (inversion recovery) and $I(t) = e^{-t/T}$ for T_1, CP (Torchia CP). Standard deviations of the fitting parameters are used as error bars. Unidentified (-).

	Eucalyptus				Poplar				Spruce			
	Atom (ppm)	T_1, CP (s)	Atom (ppm)	T_1, DP (s)	Atom (ppm)	T_1, CP (s)	Atom (ppm)	T_1, DP (s)	Atom (ppm)	T_1, CP (s)	Atom (ppm)	T_1, DP (s)
Ac^{CO}	174	2.1±0.1	174	1.6±0.2	174	2.83±0.05	174	2.4±0.2	174	1.4±0.2	174	1.3±0.1
S3/5	-	-	153	3.1±0.5	-	-	153	1.3±0.1	-	-	-	-
G3	148	4.6±0.2	-	-	148	4.2±0.2	-	-	148	3.7±0.1	148	-
G4/ S'3/5	145	4.7±0.3	145	1.8±0.2	145	4.1±0.1	145	2.4±0.2	145	3.6±0.1	145	2.4±0.2
S1	136	4.5±0.2	136	2.2±0.3	-	-	136	2.7±0.2	-	-	-	-
S4	134.5	4.7±0.3	134.5	1.9±0.3	134.5	4.2±0.1	134.5	2.7±0.2	-		-	
G1	-	-	-	-	-	-	-	-	130.8	2.9±0.1	130.8	0.9±0.1
G6	-	-	-	-	-	-	-	-	120.5	3.3±0.1	120.5	2.6±0.3
OMe	57	4.6±0.3	57	2.5±0.2	57	4.4±0.3	56.5	2.8±0.2	57	3.4±0.3	57	2.1±0.2
i/s/$Xn^{2f}1$	105	4.1±0.1	105	2.3±0.7	105	4.1±0.1	105	3.7±0.2	105	3.45±0.04	105	3.2±0.2
i4	89	4.8±0.2	89	4.4±0.2	89	4.8±0.2	89	4.3±0.2	89	3.97±0.06	89	3.9±0.2
s4	84	3.9±0.1	84	2.3±0.3	84	3.7±0.2	84	3.1±0.2	84	3.12±0.09	84	1.5±0.2
i6	65	3.7±0.3	65	2.9±0.3	65	3.6±0.3	65	3.4±0.3	65	3.0±0.2	65	2.4±0.3
s6	62	2.7±0.3	61	-	62	2.7±0.3	-	-	62	2.0±0.2	-	-
$Xn^{3f}1$	102.5	3.4±0.2	102.5	2.1±0.3	102.5	3.4±0.2	102.5	2.2±0.2	102.5	2.7±0.1	102.5	1.7±0.2
Man	-	-	-	-	-	-	-	-	100.2	2.3±0.1	100	0.8±0.1
$Xn^{2f}4$	82	3.7±0.2	82	1.4±0.2	82	3.7±0.2	82	2.1±0.4	81.8	2.8±0.1	82	1.1±0.2
$Xn^{3f}4$	78	3.6±0.2	78	1.2±0.2	78	3.6±0.2	78	1.4±0.3	78	2.5±0.1	78	0.8±0.1
$Xn^{2f/3f}Ac^{Me}$	21.5	3.9±0.1	21.5	2.2±0.2	21.5	4.7±0.2	21.5	1.5±0.1	21.5	2.1±0.2	21.5	1.1±0.1

Table F.15. ^{1}H-$T_{1\rho}$ relaxation times of lignin and polysaccharides in three samples. The data are fit using a single exponential equation: $I\ (t) = e^{-t/T}$. Standard deviations of the fitting parameters are used as error bars. Unidentified (-).

	Eucalyptus		Spruce		Poplar	
	Atom (ppm)	T_1 (ms)	Atom (ppm)	T_1 (ms)	Atom (ppm)	T_1 (ms)
S3/5	153.9	16.8±0.8	-	-	153.2	19.5±0.6
G1[a]	-	-	131	8.3±0.6	-	-
G1[b/c]	-	-	134	11.6±0.5	-	-
G1[d]	-	-	136	10.1±0.7	-	-
G3[a]	148.1	10±1	152.2	13±1	148.1	14±1
G3[c]	-	-	147.6	12.8±0.9	-	-
S'3/5/G4	145.6	11.4±0.8	-	-	145.0	13.8±0.9
S4	135.9	12±1	-	8.0±0.5	-	-
G1	-	-	134.2	8.9±0.7	-	-
S'[b]4	130.1	11.1±0.7	-	-	-	-
G6	-	-	119.0	8.8±0.6	-	-
G5	115.3	8.0±0.7	116.3	8.2±0.7	116.2	9.1±0.8
G2	-	-	113.5	8.3±0.6	-	-
S'1	110.9	10.1±0.9	-	-	-	-
OMe	57	14.2±0.7	57	12.5±0.7	57	15.1±0.8
i/s/Xn1[2f]	105.0	28.1±0.9	105.0	29±2	105.0	36±2
i4	89.0	35±1	89.0	35±1	89.0	43±2
s4	84.2	22 ±1	84.1	20±1	84.5	28±2
i6	65.0	26±2	65.0	26±2	64.8	32±2
s6	61.5	16±1	61.5	15±1	61.5	19±1
Xn1[3f]	102.5	12.8±0.9	102.3	12±1	102.4	13.0±0.8
Man1	-	-	101	10.4±0.9	-	-
Xn4[2f]	82.0	14.6±0.9	82.0	13.7±0.9	81.8	17±1
Xn4[3f]	78.1	11.5±0.9	78.0	10.2±0.9	78.0	12±1
Xn[2f,3f]Ac[Me]	21.0	17.6±0.6	21.0	13±1	21.5	19.5±0.5

Table F.16. Parameters of 1D solid-state NMR experiments measured on the three wood samples. Recycle delay (d1); number of scans (NS); number of points of time domain for the direct (td2) and indirect (td1) dimensions; the acquisition time of the direct dimension (aq2); the evolution time of indirect dimension (aq1); excitation frequency for proton ($\nu^{1}H$) and carbon ($\nu^{13}C$) channels.

	CP	DP	Quantitative DP	^{13}C-T_1 Torchia	^{13}C-T_1 Inversion-recovery	^{1}H-$T_{1\rho}$	1D Water-edited
Field (T)	14.1	14.1	14.1	9.4	9.4	9.4	9.4
Temp. (K)	294	294	294	300	300	300	278
MAS (kHz)	14	14	14	10	10	10	10
d1(s)	1.7	2	35/40[a]	2	30	2	1.8
NS	128	128	64	256	128	256/128/64[b]	512
td2	2048	2800	2800	1600	1600	1400	1400
aq2 (ms)	14	19.6	19.6	16	16	14	14
$\nu^{1}H$ (kHz)	83.3	-	-	62.5	-	62.5	83.3
$\nu^{13}C$ (kHz)	62.5	62.5	62.5	62.5	62.5	-	62.5
CP ($^{1}H/^{13}C$) (kHz)	62.5	-	-	62.5	-	51[c]	62.5
CP contact time (ms)	1	-	-	1	-	1.0	1.0
^{1}H decoupling (kHz)	83.3	83.3	83.3	62.5	83.3	62.5	83.3
Processing	GM (-7, 0.07)	GM (-7, 0.07)	GM (-7, 0.07)	GM (-7, 0.07)	GM (-7, 0.07)	GM (-5, 0.1)	GM (-5, 0.1)

[a]Recycle delays are 40s (for eucalyptus) and 35s (for the other two). [b]To protect the probe during longer LG-SL time (14 ms and 19 ms), smaller NSs are used (128/64). [c]For ^{1}H-$T_{1\rho}$, 51 kHz for CP matching means $w1_{eff}$ is 62.5 kHz during LG-SL and LG-CP.

Table F.17. Parameters of 2D NMR experiments measured on the three wood samples. Recycle delay (d1); number of scans (NS); number of points of time domain for the direct (td2) and indirect (td1) dimensions; the acquisition time of the direct dimension (aq2); the evolution time of indirect dimension (aq1); excitation frequency for proton ($\nu^{1}H$) and carbon ($\nu^{13}C$) channels.

	CP-INADQ	DP-INADQ	RFDR	Dipolar-gated PDSD	2D Water-edited	DARR	DIPSHIFT	DP-PDSD	HSQC
Field (T)	14.1	14.1	9.4	14.1	9.4	9.4	9.4	9.4	11.8
Temp. (K)	294	294	298	294	278	278	298	298	-
MAS (kHz)	14	14	10	14	10	10	7.5	12	-
d1(s)	1.6	1.6	2.0	1.48	1.65	1.65	2.0	1.7	1
NS	32	16	128	160	128/256 [a]	128	128	192	224
td2	1400	1800	1600	1400	1400	1400	1600	1600	2048
td1	340	112	280	180	152	152	13	200	256
aq2 (ms)	14	18	16	14	14	14	16	16	12.78
aq1 (ms)	4.5	4.5	7.00	3.42	4.94	4.94	0.14	4.20	3.91
$\nu^{1}H$ (kHz)	83.3	-	71.4	83.3	83.3	83.3	83.3	-	31.3
$\nu^{13}C$ (kHz)	62.5	62.5	62.5	62.5	62.5	62.5	62.5	62.5	20.8
CP ($^{1}H/^{13}C$) (kHz)	62.5	-	62.5	62.5	62.5	62.5	62.5	-	-
CP contact time (ms)	1	-	1	1	1	1	1	-	-
^{1}H decoupling (kHz)	83.3	83.3	71.4	83.3	83.3	83.3	83.3	83.3	31.3
Mixing time (ms)	-	-	1.6	20/100/1000 [b]	50	50	-	100	0.86[c]
Processing	QSINE (ssb:2.8)	QSINE (ssb:3)	GM (-10, 0.05) QSINE (ssb:4)[e]	GM (-15, 0.04) QSINE (ssb:3)[e]	GM (-15, 0.04) QSINE (ssb:4.5)[e]	GM (-30, 0.03) QSINE (ssb:4.5)[e]	GM (-5, 0.1)	GM (-30, 0.03) QSINE (ssb:4)[e]	QSINC (ssb:3.5) QSINE (ssb:3.5)[d]

[a] 128 NS for control one and 256 NS for 4ms-SD water edited one. [b] 1000ms/100ms for long and short mixing time and spruce also has 20-ms mixing time spectrum. [c] $1/(8J_{CH})$. [d] Along direct and indirect dimensions respectively. For the later forward linear prediction is applied with 32 coefficients. [e] GM for lignin region and QSINE for carbohydrate region.

Table F.18. Parameters of ssNMR experiments measured for never-dried spruce and eucalyptus samples. The same experiments with same parameters were measured again for both two wood samples after lyophilization and rehydration. Never-dried spruce was involved in all 1D and 2D experiments, and never-dried eucalyptus was only involved in 1D experiments. Recycle delay (d1); number of scans (NS); number of points of time domain for the direct (td2) and indirect (td1) dimensions; the acquisition time of the direct dimension (aq2); the evolution time of indirect dimension (aq1); excitation frequency for proton ($\nu^{1}H$) and carbon ($\nu^{13}C$) channels.

	CP	DP	Quantitative DP	^{13}C-T_1 Torchia	^{1}H-$T_{1\rho}$	1D Water-edited	2D Water-edited	CP-INADQ	DP-INADQ	53-ms CORD
Field (T)	9.4	9.4	9.4	9.4	9.4	9.4	9.4	9.4	9.4	9.4
Temp. (K)	298	298	298	298	298	280	280	298	298	298
MAS (kHz)	10	10	10	10	10	10	10	10	10	10
d1(s)	2	2	35	2	2	2	1.7	1.8	2	2
NS	1k	1k	512	512	512/256/128[a]	1k/512	96	192	192	128
td2	1600	1600	1600	1600	1600	1400	1600	1400	1600	1600
td1	1	1	1	1	1	1	166	90	90	166
aq2 (ms)	16	16	16	16	16	14	16	14	16	16
aq1 (ms)	-	-	-	-	-	-	4.15	5.31	5.31	4.15
$\nu^{1}H$ (kHz)	83.3	-	-	83.3	62.5	83.3	83.3	83.3	-	83.3
$\nu^{13}C$ (kHz)	62.5	62.5	62.5	62.5	-	62.5	62.5	62.5	62.5	62.5
CP match (^{1}H/^{13}C) (kHz)	62.5	-	-	62.5	51[b]	62.5	62.5	62.5	-	62.5
CP contact time (ms)	1.0	-	-	1.0	1.0	1.0	1.0	1.0	-	1.0
^{1}H decoupling (kHz)	83.3	83.3	83.3	83.3	62.5	83.3	83.3	83.3	83.3	83.3
Processing	GM (-5, 0.1)	GM (-10, 0.05)	GM (-10, 0.05)	GM (-5, 0.1)	GM (-5, 0.1)	GM (-5, 0.1)	GM (-20, 0.04) QSINE (ssb:4)[c]	QSINE (ssb:4)	QSINE (ssb:4)	GM (-30, 0.03)

[a] To protect the probe during longer LG-SL time (14 ms and 19 ms), smaller NSs are used (256/128). [b] For ^{1}H-$T_{1\rho}$, 51 kHz for CP matching means $w1_{eff}$ is 62.5 kHz during LG-SL and LG-CP. [c] GM for lignin region and QSINE for carbohydrate region.

Table F.19. Comparison of ^{13}C chemical shifts with literature-reported values. The comparison results are shown for carbohydrates, lignin aromatic carbons as well as covalent linkers. The references are indicated for each comparison.

Carbohydrate		Eucalyptus	Poplar	Spruce	reference 1	reference 2	reference 3
					Wang et al. 2014[312]	*Kang et al. 2019*[8]	*Gao et al. 2020*[162]
	C1	104.9	104.8	104.8	105.0	105.8	105.2
	C2	72.1	72.1	72.2	72.9	71.5	72.8
i[a]	C3	75.2	75.0	75.3	75.8	75.8	75.1
	C4	88.7	88.9	89.0	89.2	89.1	88.1
	C5	72.3	72.4	72.4	72.9	72.5	72.8
	C6	65.0	64.9	65.0	65.2	64.9	64.8
					Wang et al. 2014	*Kang et al. 2019*	*Gao et al. 2020*
	C1	104.9	104.8	104.8	105.0	105.1	105.2
	C2	72.1	72.1	72.2	72.5	72.9	72.8
i[b]	C3	75.2	75.0	75.3	75.6	74.1	75.8
	C4	88.7	88.9	89.0	88.8	89.1	89.0
	C5	72.3	72.4	72.4	72.5	72.5	72.6
	C6	65.0	64.9	65.0	65.1	65.0	65.4
					Wang et al. 2014	*Kang et al. 2019*	*Gao et al. 2020*
	C1	104.9	104.8	104.8	105.0	104.2	105.2
	C2	72.1	72.1	72.2	72.5	71.1	72.8
i[c]	C3	74.1	74.3	74.3	75.4	-	75.8
	C4	87.9	87.9	88.1	88.8	87.9	89.5
	C5	71.1	70.1	71.0	72.5	-	73.0
	C6	65.7	65.5	65.6	65.1	65.8	65.3
					Wang et al. 2014	*Kang et al. 2019*	*Gao et al. 2020*
	C1	104.9	104.8	104.8	105.0	105.2	105.2
	C2	72.1	72.1	72.2	72.5	72.7	72.8
s[f]	C3	74.6	75.7	75.1	75.6	75.8	75.1
	C4	84.4	84.3	84.5	84.7	84.3	83.8
	C5	74.6	75.0	75.0	75.7	75.4	75.1
	C6	62.3	62.3	62.1	62.9	62.5	61.8
					Wang et al. 2014	*Kang et al. 2019*	*Gao et al. 2020*
	C1	104.9	104.8	104.8	105.0	106.1	105.2
	C2	72.1	72.1	72.2	72.5	73.0	72.8
s[g]	C3	73.6	75.2	74.3	75.6	73.1	75.4
	C4	83.5	83.4	84.3	84.7	83.5	84.1
	C5	73.6	73.7	74.3	75.9	74.6	75.4
	C6	61.4	61.3	61.4	62.0	61.5	62.2

(table cont'd.)

Carbohydrate		Eucalyptus	Poplar	Spruce	reference 1	reference 2	reference 3
					Simmons et al. 2016[10]	*Kang et al. 2019*	*Gao et al. 2020*
Xn^{2f}	C1	104.8	104.8	104.8	105.2	105.1	105.1
	C2	7.2	72.1	72.2	72.3	72.5	72.3
	C3	74.0	73.2	73.3	75.2	73.5	75.3
	C4	82.2	82.0	82.2	82.2	82.3	82.1
	C5	64.0	63.9	63.9	64.3	64.6	64.1
	AC^{CO}	174.0	174.0	174.0	173.6	174.0	174.0
	AC^{Me}	21.0	21.0	21.0	21.6	21.0	21.4
					Simmons et al. 2016	*Kang et al. 2019*	*Gao et al. 2020*
Xn^{3f}	C1	102.5	102.2	103.5	102.6	102.5	102.5
	C2	73.4	73.6	73.9	73.7	73.5	73.7
	C3	74.1	74.2	74.2	74.7	74.5	74.7
	C4	77.4	77.9	77.8	77.4	78.0	77.3
	C5	63.3	64.1	65.4	63.9	62.5	63.8
	AC^{CO}	174.0	174.0	174.0	173.6	174.0	174.0
	AC^{Me}	21.0	21.0	21.0	21.6	21.0	21.4
					Kang et al. 2019		
Xn	C1	-	/		102.5		
	C2	-	/		73.5		
	C3	74.2	/		74.5		
	C4	78.5	/		78.0		
	C5	64.1	/		62.5		
	AC^{CO}				174.0		
	AC^{Me}						
					Duan et al. 2021 [313]		
$GlcA^{a}$	C1	101.5	101.5	101.5	99		
	C2	71.3	71.3	71.3	72		
	C3	79.8	79.8	79.8			
	C4	69.9	69.9	69.9			
	C5	76.6	76.6	76.6			
					Simmons et al. 2016		
$GlcA^{b}$	C1	99.2	99.2	99.2	98.6		
	C2	69.9	69.9	69.9	72.4		
	C3	-	-	-			
	C4	-	-	-			
	C5	-	-	-			

(table cont'd.)

Carbohydrate		Eucalyptus	Poplar	Spruce	reference 1	reference 2	reference 3
					Wang et al. 2014	*Simmons et al. 2016*	
GlcA[c]	C1	98.5	98.5	98.5	98.6	98.6	
	C2	71.6	71.6	71.6	72.4	72.4	
	C3	80.8	80.8	80.8	78.3		
	C4	-	-	-	-		
	C5	-	-	-	72.6		
	C6	-	-	-	177.5		
					Wang et al. 2014	*Terrett et al. 2019*[161]	*Phyo et al. 2017*[314]
GalA	C1	100.2	100.2	100.2	100.2	101.1	99.9
	C2	68.1	68.1	68.1	69.3	69.8	69.0
	C3	-	-	-	-	-	69.8
	C4	79.6	79.6	79.6	-	-	78.8
	C5	-	-	-	-	-	71.3
	C6	-	-	-			171.6
					Wang et al. 2014	*Terrett et al. 2019*	
M	C1	/	/	101.2	100.2	101.9	
	C2	/	/	71.3	69.3	72.0	
	C3	/	/	75.1	-	-	
	C4	/	/	-	-	80.4	
	C5	/	/	75.1	-	75.8	
	C6	/	/	62.1	-	61.6	
					Terrett et al. 2019		
M^{Ac}	C1	/	/	101.6	100.9		
	C2	/	/	72.1	71.9		
	C3	/	/	75.1	75.9		
	C4	/	/	80.7	80.4		
	C5	/	/	75.1	75.8		
	C6	/	/	62.1	61.6		
					Wang et al. 2014	*Terrett et al. 2019*	*Duan et al. 2021*
A(t-Ara)	C1	/	/	108.1	110.0	108.6	109
	C2	/	/	82.1	82.2	82.1	82
	C3	/	/	-	77.7	78.3	
	C4	/	/	85.6	84.9	86.1	
	C5	/	/	62.1	62.3	62.8	

(table cont'd.)

Carbohydrate		Eucalyptus	Poplar	Spruce	reference 1	reference 2	reference 3
					Wang et al. 2014	*Phyo et al. 2017*	
	C1	107.8	107.8	107.8	107.1	107.2	
A[a]	C2	81.8	81.8	81.8	89.8	87.8	
	C3	77.2	77.2	77.2	76.8	76.2	
	C4	84.6	84.6	84.6	78.6	82.4	
	C5	61.8	61.8	61.8	70.7	67.3	
					Wang et al. 2014	*Phyo et al. 2017*	
	C1	107.8	107.8	107.8	107.3	108.4	
A[b]	C2	80.1	80.1	80.1	87.8	85.8	
	C3	-	-	-	72.6	81.1	
	C4	-	-	-	-	81.9	
	C5	-	-	-	-	67.0	
					Wang et al. 2014	*Phyo et al. 2017*	
	C1	109.7	109.7	109.7	110.0	108.4	
A[c]	C2	81.8	81.8	81.8	82.2	81.8	
	C3	77.4	77.4	77.4	77.7	77.8	
	C4	82.9	82.9	82.9	84.9	83.1	
	C5	67.6	67.6	67.6	62.3	67.8	
					Wang et al. 2014	*Phyo et al. 2017*	
	C1	106.9	/	/	109.2	107.7	
A[d]	C2	85.3	/	/	82.1	82.2	
	C3	-	/	/	78.2	77.5	
	C4	-	/	/	85.7	84.9	
	C5	-	/	/	62.4	62.1	

Lignin		Eucalyptus	Poplar	Spruce	reference 1	reference 2	Other solution NMR studies
G					*Kang et al. 2019*	*Ralph et al. 2009*	
	C1	-	/	/	131.6	130.5	

(table cont'd.)

Carbohydrate		Eucalyptus	Poplar	Spruce	reference 1	reference 2	reference 3
	C2	111.1	/	/	-	112.2	111.5 [222] 110.8 [217] 111.7 [315] 111.6 [215] 110.9 [223] 110.9 [224] 110.9 [219] 111.4 [220] 111.4 [221] 110.9 [209] 111.0 [311] 110.3 [310]
	C3	148.9	/	/	148.2	150.3	
	C4	144.9	/	/	148.2	150.1	
	C5	115.9	/	/	115.5	112.2	115.2 [222] 115.4 [315] 115.4 [215] 114.7 [223] 114.9 [224] 115.1 [219] 115.0 [220] 115.4 [221] 114.6 [209] 114.9 [311] 115.2 [310]
	C6	-	/	/	119.6	120.8	119.5 [222] 118.8 [217] 119.6 [315] 119.5 [215] 119.0 [223] 119.0 [224] 118.8 [219] 119.5 [220] 119.3 [221] 119.1 [209] 118.6 [311] 118.9 [310]
	OMe	57.0	/	/	56.9	56.1	

(table cont'd.)

Carbohydrate		Eucalyptus	Poplar	Spruce	reference 1	reference 2	reference 3
					Kang et al. 2019		
	C1	/	-	130.7	132.1		
	C2	/	112.1	113.4	114.5		
	C3	/	48.2	152.2	146.2		
G^a	C4	/	144.9	145.3	146.2		
	C5	/	116.1	116.3	114.5		
	C6	/	-	-	-		
	OMe	/	56.6	56.7	56.7		
					Kang et al. 2019		
	C1	/	-	133.5	134.8		
	C2	/	113.8	110.5	111.5		
	C3	/	148.2	149.7	147.4		
G^b	C4	/	144.9	146.1	147.4		
	C5	/	116.1	-	115.8		
	C6	/	-	120.2	120.4		
	OMe	/	56.6	57.0	57.0		
					Kang et al. 2019		
	C1	/	/	134.2	134.8		
	C2	/	/	113.5	111.5		
	C3	/	/	147.6	147.4		
G^c	C4	/	/	144.1	147.4		
	C5	/	/	-	115.8		
	C6	/	/	119.2	120.4		
	OMe	/	/	57.0	57.0		
					Kang et al. 2019		
	C1	/	/	136.0	134.8		
	C2	/	/	109.5	111.5		
	C3	/	/	151.6	147.4		
G^d	C4	/	/	142.2	147.4		
	C5	/	/	-	115.8		
	C6	/	/	121.1	120.4		
	OMe	/	/	57.0	57.0		
					Kang et al. 2019		
	C1	134.9	134.2	/	136.2		
	C2	102.8	104.0	/	105.5		
	C3	153.3	153.1	/	152.7		
S^a	C4	133.5	134.6	/	134.5		
	C5	153.3	153.1	/	152.7		
	C6	102.8	104.0	/	105.5		
	OMe	57.0	56.6	/	56.7		

(table cont'd.)

Carbohydrate		Eucalyptus	Poplar	Spruce	reference 1	reference 2	reference 3
					Kang et al. 2019		
	C1	-	137.1	/	136.2		
	C2	109.7	102.5	/	105.5		
	C3	153.2	152.7	/	152.7		
S[b]	C4	137.2	135.8	/	134.5		
	C5	153.2	152.7	/	152.7		
	C6	109.7	102.5	/	105.5		
	OMe	57.0	56.6	/	56.7		
					Rencoret et al. 2011	*Yuan et al. 2011*	
	C1	134.1	/	/			
	C2	109.2	/	/	106.6	106.2	
	C3	144.8	/	/	-	-	
S'[a]	C4	136.3	/	/	-	-	
	C5	144.8	/	/	-	-	
	C6	109.2	/	/	106.6	106.2	
	OMe	56.5	/	/	-	-	
					Rencoret et al. 2011	*Yuan et al. 2011*	
	C1	136.5	/	/			
	C2	112.5	/	/	106.6	106.2	
	C3	145.5	/	/	-	-	
S'[b]	C4	138.5	/	/	-	-	
	C5	145.5	/	/	-	-	
	C6	112.5	/	/	106.6	106.2	
	OMe	56.5	/	/	-	-	

					Chemical shifts from solution NMR spectra		
Lignin Linkages		**Eucalyptus**	**Poplar**	**Spruce**	**Eucalyptus**	**Poplar**	**Spruce**
A(G) / A(S)	C7(α)	72.3	72.0	72.4	71.6 / 72.5 [222] - / 71.8 [217] 71.4 / 72.6 [315] 71.7 / 72.4 [215] - / 71.8 [223]	71.5 / 71.9 [219] - / 72.0 [220] - / 71.8 [221] - / 71.8 [209]	71.1 [310] 71.0 [210]
	C8(β)	84.5	86.3	84.3	84.1 / 86.5 [222] 83.6 / 85.7 [217] 84.1 / 86.4;87.3 [315] 84.1 / 86.4 [215] 83.6 / 85.8 [223]	83.9 / 85.9 [224] 83.4 / 85.8 [219] - / 85.8 [221] 83.8 / 85.8 [209]	84.0 [310] 83.9 [210]
	C9(γ)	59.4	60.4	59.9	60.0 [222] 59.4 [217] 60.1 [315] 59.6 [223]	59.6 [224] 59.8 [219] 60.2 [221]	59.9 [310] 59.8 [210]

(table cont'd.)

Carbohydrate		Eucalyptus	Poplar	Spruce	reference 1	reference 2	reference 3
B	C7(α)	84.4	84.8	-	85.4 [222] 84.7 [217] 85.4 [315] 85.5 [215] 84.8 [223]	84.8 [224] 85.2 [219] 85.7 [220] 84.7 [221] 84.8 [209]	84.9 [310] 85.0 [210]
	C8(β)	53.5	52.6	53.9	53.7 [222] 53.3 [217] 54.1 [315] 53.5 [223]	53.5 [224] 53.6 [219] 53.6 [221]	53.5 [310] 53.6 [210]
	C9(γ)	71.2	70.5	70.3	71.7 [222] 71.0 [217] 71.7 [315] 71.3 [223]	71.0 [224] 70.1 [219]	70.8 [310] 70.9 [210]
B’	C7(α)	-	83.9	/			
	C8(β)	53.5	52.9	/			
	C9(γ)	74.4	74.1	/			
E	C7(α)	81.1	80.3	81.4	81.7 [222] 81.0 [217]	81.2 [224]	81.7 [210]
	C8(β)	59.6	59.7	60.0	60.3 [222] 59.7 [217]	59.7 [224]	59.3 [210]
	C9(γ)	/	/	/			
V	C7(α)	75.8	77.2	76.2			75.8 [316]
	C8(β)	78.4	79.0	78.9			78.0 [316]
	C9(γ)	59.8	60.7	60.1			
C	C7(α)	/	/	88.1	87.7 [222] 86.4 [217] 87.5 [315] 87.4 [215] 86.7 [223]	86.8 [224] 87.0 [219] 87.4 [220] 87.1 [221] 86.8 [209]	87.0 [310] 87.0 [210]
	C8(β)	/	/	54.2	53.7 [222] 53.1 [217] 53.7 [315] 53.5[5]	53.3[224] 53.2 [219] 53.2 [220]	53.1 [310] 53.0 [210]
	C9(γ)	/	/	/	63.3 [222] 62.3 [217] 62.5 [223]	62.5[224] 62.5 [219]	62.8 [310] 62.7 [210]
C’	C7(α)	/	/	90.2			
	C8(β)	/	/	49.9			
	C9(γ)	/	/	/			

APPENDIX G. SUPPORTING INFORMATION FOR CHAPTER 7

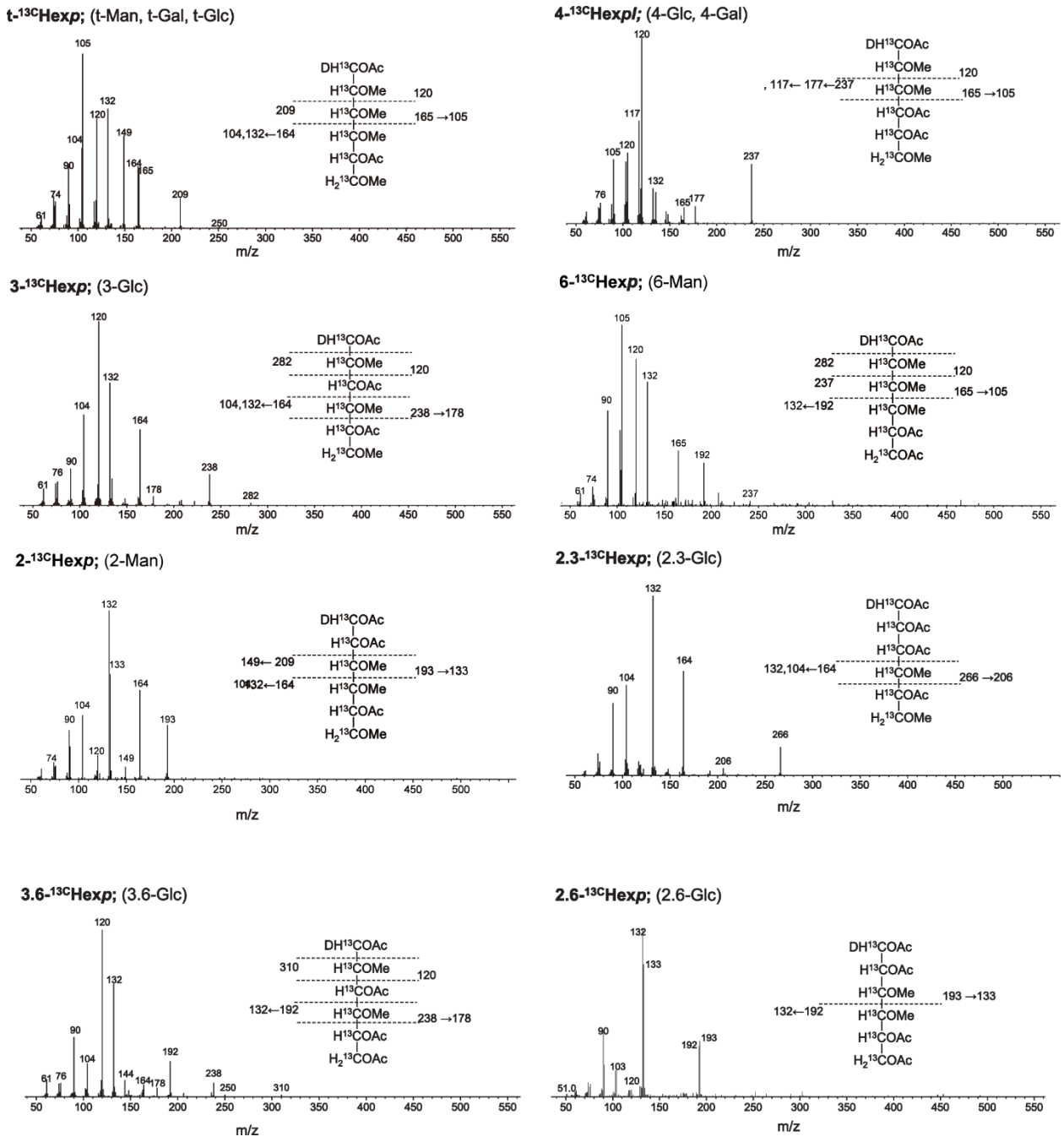

Figure G.1. EI-MS ion fragmentation of partially methylated alditol acetates of ^{13}C neutral hexoses in fungal cell walls. The proposed glycosyl linkage interpretation of the ^{13}C substituted (~100%) carbohydrates is detailed. The given values were calculated based on relative the peak areas originating from GC-MS EI detector response.

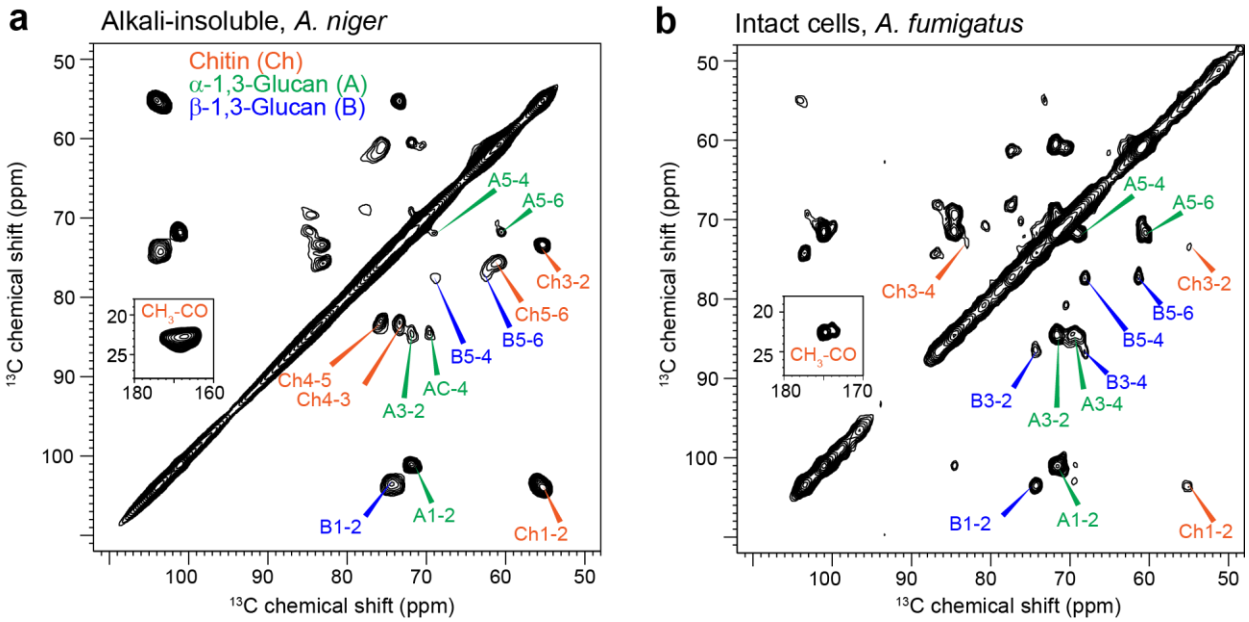

Figure G.2. Comparison of ^{13}C, ^{15}N-labeled *A. niger* and *A. fumigatus*. 2D RFDR spectra of (a) the alkali-insoluble portion of *A. niger* cell walls and (b) intact cells of *A. fumigatus*.

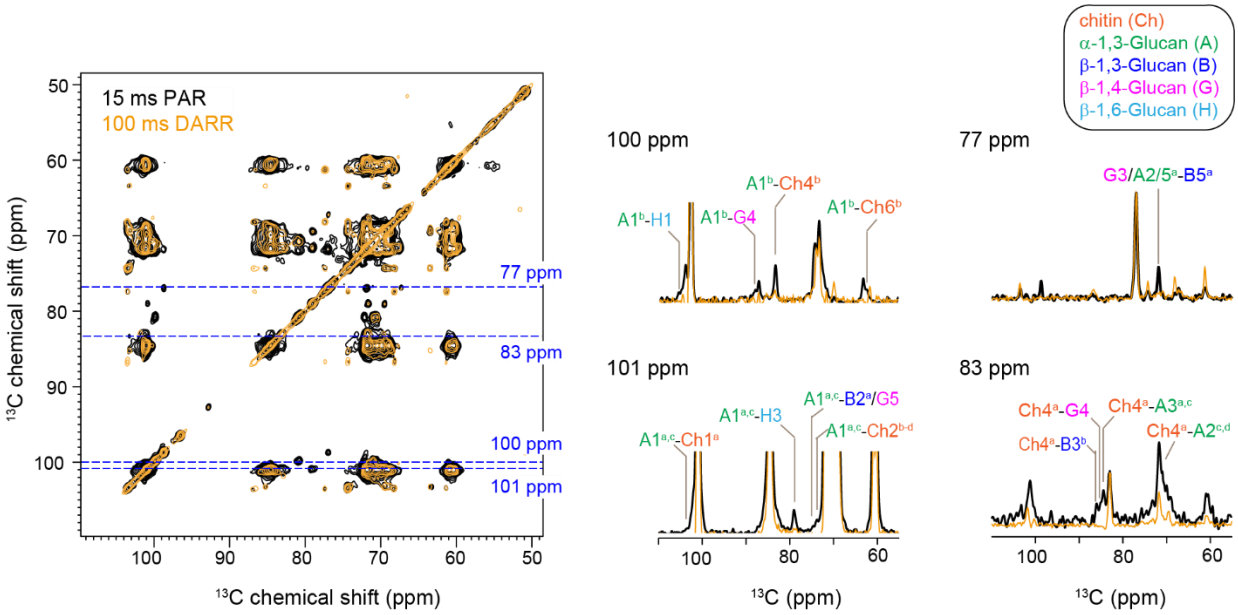

Figure G.3. ^{13}C cross sections of 2D PAR. The ^{13}C cross sections of 2D PAR (black) and 100 ms DARR (yellow) are overlaid for comparison. Dashlines indicate the positions where ^{13}C cross sections are extracted.

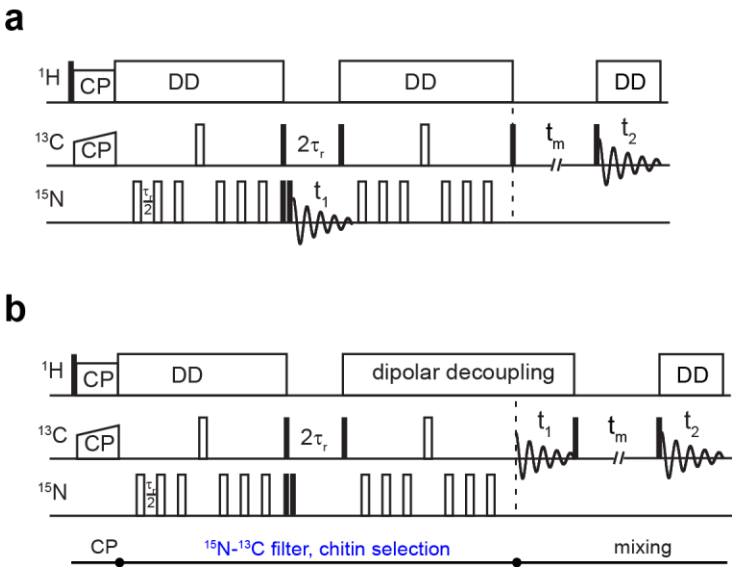

Figure G.4. DNP Experiments for detecting chitin-glucan interactions. (a) ^{15}N-^{13}C correlation experiment. (b) ^{15}N-^{13}C filtered ^{13}C-^{13}C correlation experiment.

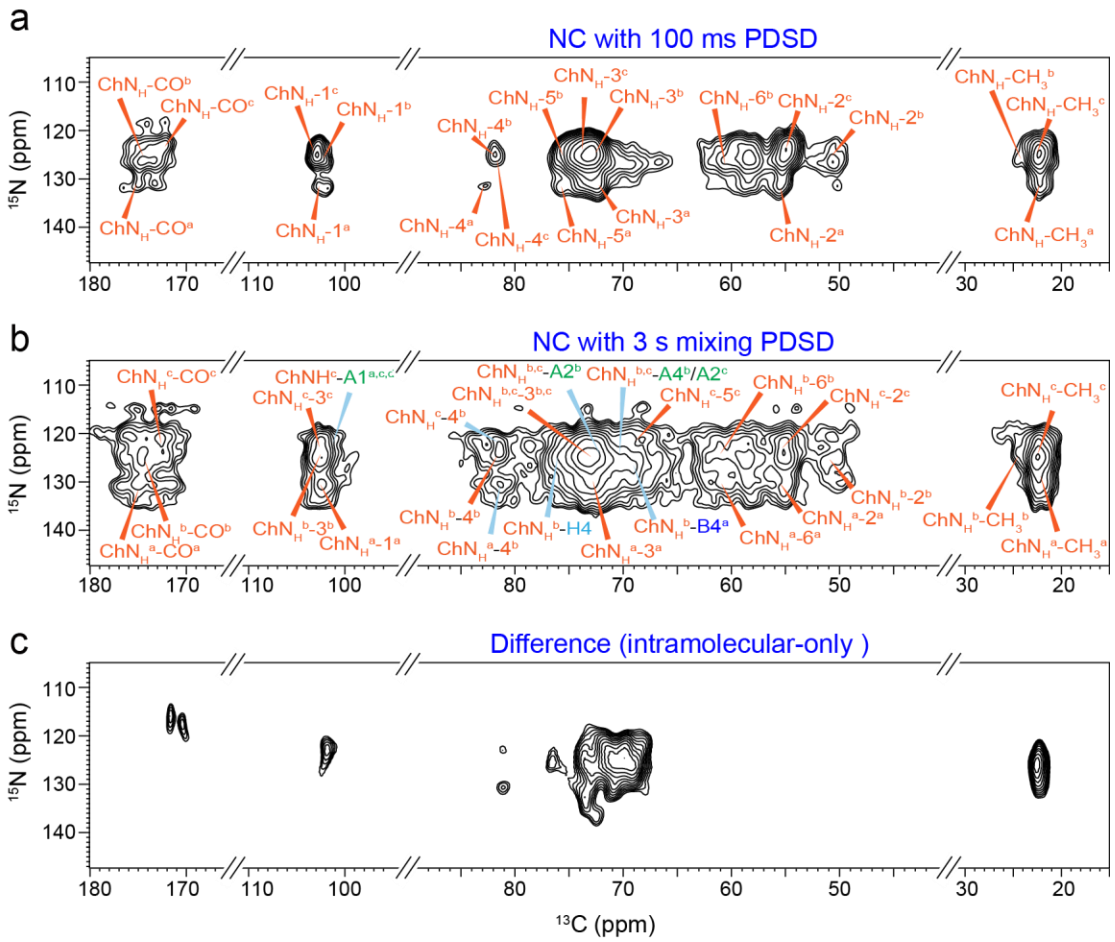

Figure G.5. Parent spectra for generating intermolecular-only ^{15}N-^{13}C correlation spectrum with improved resolution. (a) ^{15}N-^{13}C correlation spectrum with 100 ms mixing times for intramolecular cross peaks. (b) ^{15}N-^{13}C correlation spectrum with 3-s mixing times for both intermolecular and intramolecular cross peaks. (c) Spectral subtraction of b-a results in a difference spectrum with only long-range intermolecular signals. A Topspin gamma value of -0.65 is used for the subtraction.

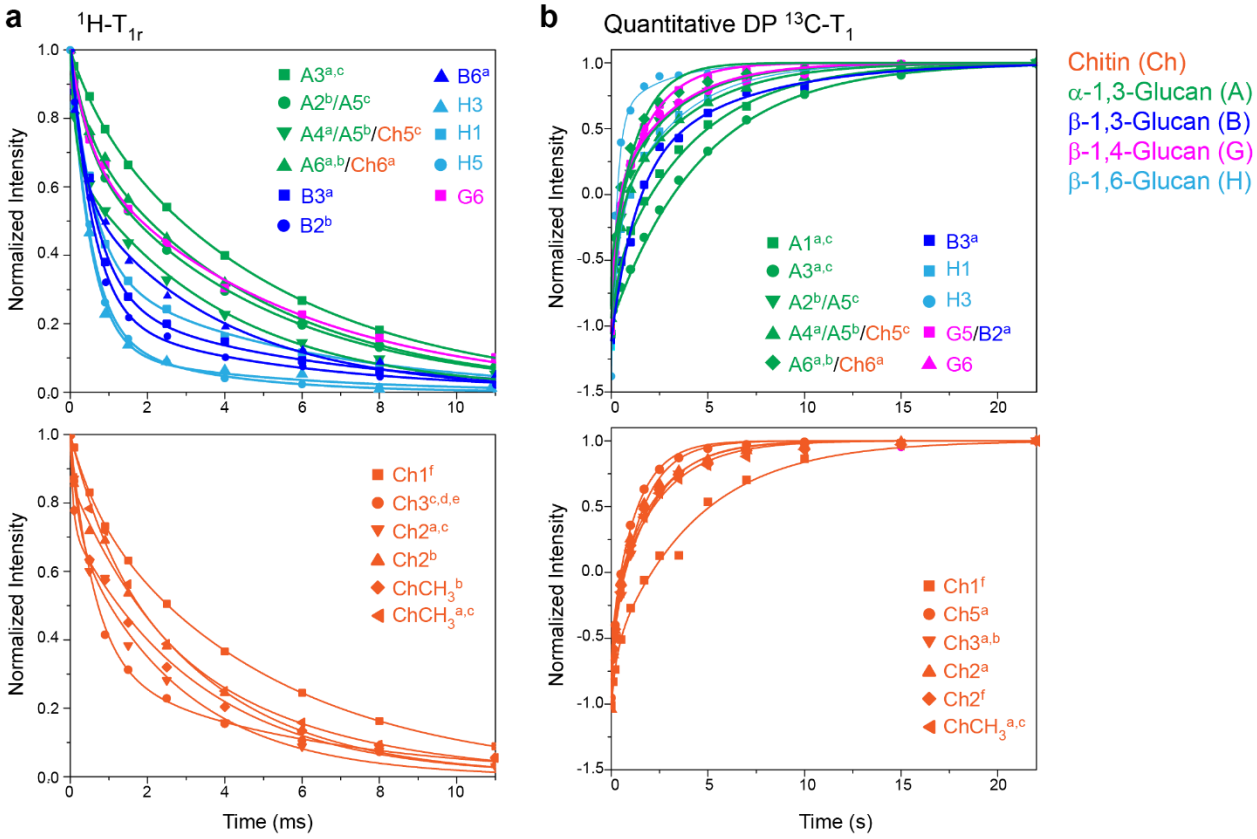

Figure G.6. NMR relaxation curves of polysaccharides. (a) ^{1}H-T$_{1\rho}$ and (b) ^{13}C-T$_1$ relaxation curves of polysaccharides in intact *A. fumigatus* cell walls. The data are collected on a 400 MHz (9.4 Tesla) spectrometer and best-fits are achieved using single or double exponential equations.

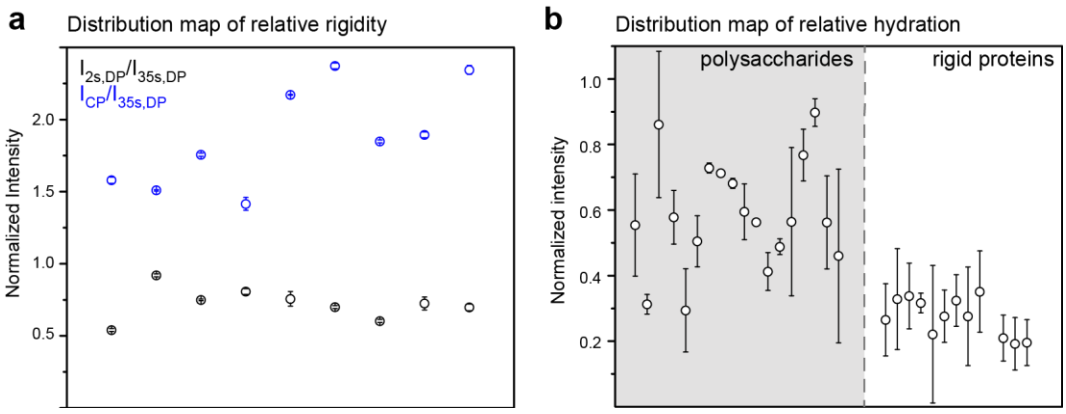

Figure G.7. NMR analysis of the rigid portion of proteins. (a) Comparison of the protein intensities in 1D ^{13}C CP, DP with 2-s recycle delays and DP with 35-s recycle delays. (b) Comparison of polysaccharide and protein hydration. The normalized intensities are obtained using the intensity ratio between two water-edited spectra with 4-ms and 49-ms 1H mixing time. The 4-ms spectrum contains signals from the well hydrated molecules and the 49-ms spectrum reflects the equilibrium condition. The rigid proteins detected in this CP-based experiment are generally more hydrophobic than polysaccharides.

Table G.1. Glycosyl composition analysis of neutral sugars in fungal cell walls. The intact cell walls of *A. fumigatus* and the alkali-insoluble portion of *A. niger* cell walls are reported.

Glycosyl residue of neutral sugars (mole %)						
Sample	Ara[a]	Man[a]	Gal[a]	Glc[a]		
A. fumigatus	0.3	6.9	14.5	78.3		
A. niger	nd.	2.9	15.2	81.9		
Composition of all sugars (mole %)						
Sample	Ara[b]	Man[b]	Gal[b]	Glc[b]	Chitin[c]	Chitosan[c]
A. fumigatus	0.3	6.2	13.1	70.6	9.0	0.9

[a] Data on neutral sugars are obtained directly from glycosyl composition analysis.

[b] Neutral sugar content rescaled by the NMR data of chitin/glucan and chitin-chitosan ratios.

[c] The amount of nitrogenated sugar in *A. fumigatus* is calculated using the chitin-to-glucan ratio (1 : 7.8) obtained by the area of C1-C2 cross peaks in 2D ^{13}C-^{13}C RFDR spectrum (Supplementary Figure 7.1) and the chitin-to-chitosan ratio (9 : 1) obtained using 1D ^{15}N spectra (**Figure 7.2a**).

Table G.2. ^{13}C and ^{15}N chemical shifts of polysaccharides in *A. fumigatus* cell walls. Superscripts are used to denote different allomorphs. Underline denotes the ^{13}C connectivity with ambiguity. Weak signals or minor species are indicated using "w." Not applicable (/). Unidentified (-). Unk: unknown.

	C1	C2	C3	C4	C5	C6	CO	CH_3	N	Experimental methods	References
β-1,3-glucan[a]	103.6	74.4	86.4	68.7	77.1	61.3	/	/	/	^{13}C-^{13}C PDSD, ^{13}C CP J-INADEQUATE	Shim et al. 2007 Fairweather et al. 2004 Hazime Saitô et al. 1979[317-319]
β-1,3-glucan[b] (w)	104.6	75.2	85.9	69.6	78.6	63.0	/	/	/	DNP ^{13}C-^{13}C dipolar-INADEQUATE-PDSD	
β-1,3-glucan[c] (w)	102.6	72.8	84.4	69.7	72.2	60.5	/	/	/	DNP ^{13}C CP J-INADEQUATE	
α-1,3-glucan[a]	101.0	71.9	84.6	69.5	71.7	60.5	/	/	/	^{13}C-^{13}C PDSD, ^{13}C CP J-INADEQUATE	Bhanja et al. 2014 [320] Puanglek et al. 2016 [321]
α-1,3-glucan[b]	99.9	71	80	70.4	69.7	60.9	/	/	/		
α-1,3-glucan[c]	101.2	70.1	84.5	67.7	71.5	60.5	/	/	/		
α-1,3-glucan[d] (w)	101.5	70.2	86.8	69.3	71.2	62.4	/	/	/	^{13}C CP J-INADEQUATE	
β-1,4-glucan	103.3	69.4	71.7	85.3	74.3	63.4	/	/	/		
β-1,6-glucan	102.6	69.4	79.0	71.6	76.9	67.3					Lowman et al. 2011 [322]
β-1,4-mannan	101.0	69.4	76.2	83.4	77.1	61.6	/	/	/	^{13}C DP J-INADEQUATE	Petkowicz et al. 2001 [323] Marchessault et al. 1990 [324]
arabinan[a]	107.6	81.9	77.1	83.3	69.9	/	/	/	/		Renard et al. 1999[325]
arabinan[b]	108.2	81.7	-	-	-	/	/	/	/		
chitin[a]	103.6	55.5	72.9	83.0	75.7	60.9	174.8	22.6	127.9	^{13}C-^{13}C PDSD, ^{13}C CP J-INADEQUATE, ^{15}N-^{13}C N(CA)CX-DARR	Kono et al. 2004 [119] Heux et al. 2000 [326] Kameda et al. 2004 [327] King et al. 2017 [328] Tanner 1990 [329]
	103.4	56.0	73.9	-	-	-	-	22.2	127.7	RT ^{13}C CP J-INADEQUATE, ^{15}N-^{13}C N(CA)CX-DARR (800M)	
	-	55.9	-	-	-	-	-		130.8		

Table G.3. Intensities of 64 long-range intermolecular cross peaks. The intensities are relative ratios of the peak area normalized by the integral of a ^{13}C cross section. For non-DNP experiments, a peak higher than 2% is categorized as strong restraints (in bold) and 0.8% for intermediate restraints (underline). For DNP enhanced experiments, given the relatively large values for all cross peaks and the distribution of peak intensities, the thresholds have been increased to 15% and 8% for strong and intermediate restraints, respectively.

	atom 1	atom 2	15 ms CC-PAR (%)	3s PDSD (%)	DNP NC-edited CC PDSD (%)	DNP NC with 3s PDSD (%)	DNP 15 ms NN-PAR (%)
β-1,3-glucan-α-1,3-glucan	B5[a]	A3[a,c]	1.05		9.2		
	A1[a,c]	B1[a]/Ch1[a]	**8.11**				
	B5[a]	A4[c]	**7.72**				
	B5[a]	A2[a,b]	**18.54**				
	B5[a]	A6[a,b,c]	**5.57**				
	A6[b]/Ch6[a]	B6[a]	0.35				
	B5[a]	A1[a,c]		**3.91**			
	A1[a,c]	B5[a]		0.88			
	A1[a,c]	B6[a]		0.97			
	A1[a,c]	B5[a]		0.39			
	B1[a]	A2[c]			**15.29**		
Chitin-α-1,3-glucan	A5[a,c]	Ch3[a,c]	**2.22**				
	A6[b]Ch6[a]	Ch6[c]	1.33				
	Ch3[d,e]	A2[c,d]	0.15				
	Ch4[a]	A3[a,c]	**4.63**				
	Ch4[a]	A2[c,d]	**4.62**				
	A1[b]	Ch4[b]	**8.10**				
	A1[b]	Ch6[b]	**3.16**				
	A1[a,c]	Ch4[c]	0.19				
	A1[a,c]	Ch2[b,c,d]	0.36				
	A3[a,c]	Ch2[a,c]		0.48			
	A3[a,c]	Ch1[a,c]		**2.04**			
	A3[a,c]	Ch5[a]		**2.06**			
	Ch2[e]	A3[a,c]			6.35		
	A2[b]	$ChCH_3$[a,c]			4.67		
	ChN_H[c]	A1[a,c,d]				10.25	
	ChN_H[b,c]	A2[b]				**15.68**	
	ChN_H[b,c]	A4[b]/A2[c]				9.87	
Chitin-β-1,3-glucan	Ch4[a]	B3[b]	**3.49**				
	Ch3[d,e]	B5[c]	0.13				
	Ch2[f]	B6[a]			0.49		
	Ch2[d,e]	B6[a]			11.93		
	B2[a]	Ch2[d]			11.54		
	B2[b]	$ChCH_3$[a,c]			3.51		
	B5[a]	$ChCH_3$[a,c]			2.86		
	B5[a]	Ch4[a]			8.92		
	B5[a]	Ch2[d]			7.83		
	Ch4[a]	B6[b]			7.95		
	B1[b]	Ch2[b]			9.53		
	B1[b]	Ch2[d]			13.94		
	ChN_H[b]	B4[a]				10.04	
Chitin-Chitin	Ch2[d]	Ch4[a]			6.5		

Table G.4. Water-edited intensities of polysaccharide cross peaks. Error bars are standard deviations propagated from NMR signal-to-noise ratios.

Type	Cross peaks	Intensities	Type	Cross peaks	Intensities
Chitin	Ch1-3[a]	0.3 ± 0.1	β-1,4-glucan	G1-4	0.6 ± 0.2
	Ch1-2[a]	0.08 ± 0.07		G1-2	0.60 ± 0.08
	Ch4-2[a]	0.3 ± 0.3		G1-6	0.6 ± 0.2
	Ch5-2[a]	0.1 ± 0.3		G5-4	0.6 ± 0.1
	Ch3-2[a]	0.3 ± 0.3		G5-2	0.7 ± 0.1
	Ch6-2[a]	0.02 ± 0.03		G5-6	0.59 ± 0.07
	Ch2-1[a]	0.02 ± 0.03		G2-1	0.58 ± 0.06
	Ch2-5[a]	0.4 ± 0.4		G2-4	0.61 ± 0.08
	Ch2-4[a]	0.1 ± 0.1		G2-5	0.63 ± 0.08
	Ch2-3[a]	0.20 ± 0.1		G1-1/B1-1[a]	0.57 ± 0.02
	Ch2-6[a]	0.4 ± 0.4		G1-5/B1-2[a]	0.66 ± 0.03
	Ch2-2[a]	0.37 ± 0.05		G5-1/B2-1[a]	0.63 ± 0.03
	Ch5-3[e]	0.04 ± 0.01		G5-5 /B2-2[a]	0.58 ± 0.02
	Ch4-3[f]	0.4 ± 0.1		G2-2/A4-4[a]/H4-4	0.70 ± 0.01
β-1,3-glucan	B1-3[a]	0.7 ± 0.1		G2-6	0.7 ± 0.1
	B1-5[a]	0.6 ± 0.1	α-1,3-glucan	A4-1[a]	0.33 ± 0.02
	B1-4[a]	0.6 ± 0.1		A4-3[a]	0.26 ± 0.04
	B1-6[a]	0.6 ± 0.1		A4-2[a]	0.31 ± 0.02
	B2-3[a]	0.7 ± 0.1		A4-6[b]	0.39 ± 0.06
	B2-5[a]	0.6 ± 0.1		A4-6[a]	0.24 ± 0.03
	B2-4[a]	0.6 ± 0.1		A6-1[a,c]	0.23 ± 0.03
	B2-6[a]	0.6 ± 0.1		A6-3[a,c]	0.20 ± 0.04
	B6-1[a]	0.7 ± 0.2		A6-2[b]/A6-5[c]	0.38 ± 0.01
	B6-3[a]	0.8 ± 0.3		A4-6[a]	0.28 ± 0.02
	B6-5[a]	0.7 ± 0.1		A6-4[b]	0.25 ± 0.01
	B6-2[a]	0.7 ± 0.1		A6-2/5[a]	0.39 ± 0.08
	B6-4[a]	0.7 ± 0.1		A5-2[b]	0.41 ± 0.02
	B6-6[a]/A6-6[a]	0.6 ± 0.0	β-1,6-glucan	H2-3	1.0 ± 0.3
	B4-3[a]	0.8 ± 0.2		H2-6	0.7 ± 0.3

Table G.5. Relative intensities of polysaccharide signals in 1D ^{13}C CP and DP spectra. Error bars are standard deviations propagated from NMR signal-to-noise ratios.

Assignments	^{13}C (ppm)	$I_{2s,dp}/I_{35s,dp}$	$I_{cp}/I_{35s,dp}$
A1[a,c]	101.1	0.34 ± 0.01	2.06 ± 0.01
A3[a,c]	84.6	0.25 ± 0.01	2.12 ± 0.02
A4[a]	69.9	0.38 ± 0.01	1.80 ± 0.01
A6[a,c]	60.4	0.53 ± 0.01	2.02 ± 0.01
Ch1[b]	102.4	0.79 ± 0.02	1.48 ± 0.03
Ch4[a]	83.1	0.57 ± 0.03	1.74 ± 0.07
Ch4[b]	81.3	0.96 ± 0.05	1.7 ± 0.1
B5[a]	77.3	0.84 ± 0.02	1.42 ± 0.03
B6[a]	61.1	0.86 ± 0.03	1.49 ± 0.01
G6	63.7	0.88 ± 0.02	0.46 ± 0.02
G5	74.8	0.93 ± 0.01	1.45 ± 0.05
H3	78.9	0.94 ± 0.04	1.45 ± 0.05
H6	67.5	0.79 ± 0.01	1.00 ± 0.02
Ch4[c]	82.2	0.85 ± 0.05	1.09 ± 0.06
Ch3[c,d,e]	73.5	0.88 ± 0.01	0.71 ± 0.01
Ch2[e]	57.4	0.85 ± 0.04	0.80 ± 0.04
Ch2[d]	56.9	0.70 ± 0.03	0.95 ± 0.04
Ch2[c]	54.5	0.95 ± 0.02	0.71 ± 0.02
Ch2[f]	52.9	0.76 ± 0.03	0.92 ± 0.04
Ch-CH_3[a,c]	22.8	0.85 ± 0.01	1.16 ± 0.02

Table G.6. ^{1}H-$T_{1\rho}$ relaxation times of polysaccharides in intact *A. fumigatus* cell walls. Single and double exponential equations are used to fit the data $I(t) = e^{-t/T_{1\rho,b}}$ and $I(t) = ae^{-t/T_{1\rho,a}} + be^{-t/T_{1\rho,b}}$, where b=1-a.

Assignment	^{13}C (ppm)	A	B	$T_{1\rho, A}$(ms)	$T_{1\rho, B}$(ms)
H1	102.8	-	1	-	1.3±0.2
Ch1[f]	100.6	0.17±0.01	0.83±0.01	0.65±0.04	4.90±0.05
B3[a]	86.5	-	1	-	1.2±0.1
A3[a,c]	84.8	0.12±0.02	0.88±0.02	0.7±0.2	5.1±0.1
H3	78.6	-	1	-	0.68±0.04
H5	76.5	-	1	-	0.72±0.04
B2[b]	75.2	-	1	-	0.92±0.08
Ch3[c,d,e]	73.7	-	1	-	1.3±0.2
A2[b]/A5[c]	71.3	0.29±0.03	0.71±0.02	0.46±0.07	4.7±0.2
A4[a]/A5[b]/Ch5[c]	69.8	0.22±0.03	0.78±0.02	0.42±0.08	4.6±0.2
B6[a]	61.3	-	1	-	1.6±0.2
A6[a,b,c]/Ch6[a,b]	60.7	0.33±0.02	0.67±0.02	0.14±0.02	3.8±0.2
Ch2[a,c]	54.7	0.14±0.03	0.86±0.02	0.05±0.03	3.2±0.2
Ch2[b]	51.1	-	1	-	1.7±0.2
Ch-CH3[b]	24.0	-	1	-	1.9±0.3
Ch-CH3[a,c]	22.3	-	1	-	2.8±0.2

Table G.7. ^{13}C-T_1 relaxation times of polysaccharides. The data are fit using single and double exponential equations: $I(t) = 1 - e^{-t/T_{1b}}$ and $I(t) = a(1 - e^{-t/T_{1a}}) + b(1 - e^{-t/T_{1b}})$, where a=1-b.

Assignment	^{13}C (ppm)	a	b	T_{1a} (s)	T_{1b} (s)
H1	102.8	-	1	-	1.54±0.15
A1[a,c]	101.2	-	1	-	2.8±0.9
Ch1[f]	100.6	-	1	-	3.0±0.9
B3[a]	86.5	-	1	-	2.5±0.4
A3[a,c]	84.8	-	1	-	4.3±0.1
H3	78.7	-	1	-	0.4±0.1
Ch5[a]	76.0	0.26±0.05	0.74±0.05	0.17±0.05	1.3±0.1
B2[a]/G5	74.3	-	1	-	1.02±0.07
Ch3[a,b]	72.8	-	1	-	0.95±0.08
A2[b]/A5[c]	71.3	-	1	-	1.6±0.1
A4[a]/A5[b]/Ch5[c]	69.8	-	1	-	1.18±0.09
G6	63.2	-	1	-	1.00±0.09
A6[a,b,c]/Ch6[a]	60.7	0.38±0.07	0.62±0.07	0.17±0.05	1.6±0.2
Ch2[a]	55.4	-	1	-	1.14±0.09
Ch2[f]	52.5	-	1	-	1.0±0.1
Ch-CH_3[a,c]	22.6	-	1	-	1.11±0.09

Table G.8. Relative intensities of proteins signals in 1D ^{13}C CP and DP spectra. Error bars are standard deviations propagated from NMR signal-to-noise ratios.

Atom (ppm)	$I_{2s,dp}/I_{35s,dp}$	$I_{cp}/I_{35s,dp}$
33.7	0.54±0.01	1.58±0.02
31.2	0.92±0.01	1.51±0.01
28.3	0.75±0.01	1.76±0.01
21.6	0.81±0.02	1.42±0.05
20.4	0.76±0.05	2.17±0.01
19.3	0.70±0.01	2.37±0.02
17.6	0.60±0.01	1.85±0.01
16.2	0.72±0.05	1.89±0.02
15.6	0.70±0.02	2.34±0.03

Table G.9. Water-edited intensities of polysaccharide and proteins signals. The ratios are obtained by comparing the intensity of each ^{13}C peak in 1D water-edited spectra measured with 4-ms and 49-ms ^{1}H mixing times. Error bars are standard deviations propagated from NMR signal-to-noise ratios.

Type	Atom (ppm)	intensities	Type	Atom (ppm)	intensities
Polysaccharides	104.0	0.55±0.16	Proteins	32.0	0.27±0.11
	101.7	0.31±0.03		31.4	0.33±0.15
	99.6	0.86±0.22		30.7	0.34±0.10
	87.0	0.58±0.08		30.2	0.32±0.03
	85.2	0.29±0.13		29.3	0.22±0.21
	83.6	0.50±0.08		28.0	0.28±0.08
	81.3	0.73±0.02		26.2	0.32±0.08
	79.8	0.71±0.01		25.9	0.28±0.15
	78.0	0.68±0.02		23.6	0.35±0.12
	74.9	0.59±0.09		20.7	0.21±0.07
	74.2	0.56±0.01		19.5	0.19±0.08
	72.3	0.41±0.06		19.1	0.20±0.07
	70.1	0.49±0.02			
	68.9	0.56±0.23			
	68.0	0.77±0.08			
	67.3	0.90±0.04			
	63.8	0.56±0.14			
	61.6	0.46±0.27			

APPENDIX H. LETTER OF PERMISSION FOR CHAPTER 7

12/7/21, 8:12 PM RightsLink® by Copyright Clearance Center

RightsLink

Help Email Support

SPRINGER NATURE

Molecular architecture of fungal cell walls revealed by solid-state NMR

Author: Xue Kang et al
Publication: Nature Communications
Publisher: Springer Nature
Date: Jul 16, 2018

Copyright © 2018, The Author(s)

Creative Commons

This is an open access article distributed under the terms of the Creative Commons CC BY license, which permits unrestricted use, distribution, and reproduction in any medium, provided the original work is properly cited.

You are not required to obtain permission to reuse this article.
To request permission for a type of use not listed, please contact Springer Nature

© 2021 Copyright - All Rights Reserved | Copyright Clearance Center, Inc. | Privacy statement | Terms and Conditions
Comments? We would like to hear from you. E-mail us at customercare@copyright.com

https://s100.copyright.com/AppDispatchServlet?title=Molecular architecture of fungal cell walls revealed by solid-state NMR&author=Xue Kang et al&c... 1/1

REFERENCES

1. Jarvis, M. Chemistry: cellulose stacks up. *Nature* **426**, 611-612, doi:Doi 10.1038/426611a (2003).

2. Latge, J. P. The cell wall: a carbohydrate armour for the fungal cell. *Mol. Microbiol.* **66**, 279-290, doi:10.1111/j.1365-2958.2007.05872.x (2007).

3. Cosgrove, D. J. & Jarvis, M. C. Comparative structure and biomechanics of plant primary and secondary cell walls. *Front. Plant. Sci.* **3**, doi:10.3389/Fpls.2012.00204 (2012).

4. Albersheim, P., Darvill, A., Roberts, K., Sederoff, R. & Staehelin, A. *Plant Cell Walls*. (Garland Science, Taylor & Francis Group, LLC, 2011).

5. Wang, T., Zabotina, O. & Hong, M. Pectin-cellulose interactions in the *Arabidopsis* primary cell wall from two-dimensional magic-angle-spinning solid-state nuclear magnetic resonance. *Biochemistry* **51**, 9846-9856, doi:Doi 10.1021/Bi3015532 (2012).

6. Buchanan, B. B., Gruissem, W. & Jones, R. L. *Biochemistry and Molecular Biology of Plants*. (American Society of Plant Physiologists, 2000).

7. Caffall, K. H. & Mohnen, D. The structure, function, and biosynthesis of plant cell wall pectic polysaccharides. *Carbohydr. Res.* **344**, 1879-1900, doi:DOI 10.1016/j.carres.2009.05.021 (2009).

8. Kang, X. *et al.* Lignin-polysaccharide interactions in plant secondary cell walls revealed by solid-state NMR. *Nat. Commun.* **10**, 347, doi:10.1038/s41467-018-08252-0 (2019).

9. Mortimer, J. C. *et al.* Absence of branches from xylan in Arabidopsis gux mutants reveals potential for simplification of lignocellulosic biomass. *Proc. Natl. Acad. Sci. USA* **107**, 17409-17414, doi:10.1073/pnas.1005456107 (2010).

10. Simmons, T. J. *et al.* Folding of xylan onto cellulose fibrils in plant cell walls revealed by solid-state NMR. *Nat. Commun.* **7**, 13902, doi:10.1038/ncomms13902 (2016).

11. Lawoko, M. & van Heiningen, A. R. P. Fractionation and Characterization of Completely Dissolved Ball Milled Hardwood. *J. Wood. Chem. Technol.* **31**, 183-203, doi:10.1080/02773813.2010.515048 (2011).

12. Cheng, K., Sorek, H., Zimmermann, H., Wemmer, D. E. & Pauly, M. Solution-State 2D NMR Spectroscopy of Plant Cell Walls Enabled by a Dimethylsulfoxide-d(6)/1-Ethyl-3-methylimidazolium Acetate Solvent. *Anal. Chem.* **85**, 3213-3221, doi:10.1021/ac303529v (2013).

13. Terashima, N. *et al.* 2D-NMR (HSQC) difference spectra between specifically C-13-enriched and unenriched protolignin of Ginkgo biloba obtained in the solution state of whole cell wall material. *Holzforschung* **63**, 379-384, doi:10.1515/Hf.2009.074 (2009).

14. Kang, X. *et al.* Molecular architecture of fungal cell walls revealed by solid-state NMR. *Nat. Commun.* **9**, 2747, doi:10.1038/S41467-018-05199-0 (2018).

15. Adair, W. S. & Snell, W. Organization and in vitro assembly of the Chlamydomonas reinhardtii cell wall. *Self-assembling architecture*, 25-41 (1988).

16. Cegelski, L. *et al.* Plant Cell-Wall Cross-Links by REDOR NMR Spectroscopy. *J. Am. Chem. Soc.* **132**, 16052-16057, doi:10.1021/ja104827k (2010).

17. Keller, B. Structural cell wall proteins. *Plant physiology* **101**, 1127 (1993).

18. Dupree, R. *et al.* Probing the Molecular Architecture of Arabidopsis thaliana Secondary Cell Walls Using Two- and Three-Dimensional ^{13}C Solid State Nuclear Magnetic Resonance Spectroscopy. *Biochemistry* **54**, 2335-2345, doi:10.1021/bi501552k (2015).

19. Dick-Perez, M. *et al.* Structure and interactions of plant cell wall polysaccharides by two- and three-dimensional magic-angle-spinning solid-state NMR. *Biochemistry* **50**, 989-1000, doi:Doi 10.1021/Bi101795q (2011).

20. Dick-Perez, M., Wang, T., Salazar, A., Zabotina, O. A. & Hong, M. Multidimensional solid-state NMR studies of the structure and dynamics of pectic polysaccharides in uniformly ^{13}C-labeled Arabidopsis primary cell walls. *Magn. Reson. Chem.* **50**, 539-550, doi:Doi 10.1002/Mrc.3836 (2012).

21. Wang, T. *et al.* Sensitivity-enhanced solid-state NMR detection of expansin's target in plant cell walls. *Proc. Natl. Acad. Sci. USA* **110**, 16444-16449, doi:DOI 10.1073/pnas.1316290110 (2013).

22. Wang, T., Yang, H., Kubicki, J. D. & Hong, M. Cellulose Structural Polymorphism in Plant Primary Cell Walls Investigated by High-Field 2D Solid-State NMR Spectroscopy and Density Functional Theory Calculations. *Biomacromolecules* **17**, 2210-2222, doi:10.1021/acs.biomac.6b00441 (2016).

23. Rossini, A. J. *et al.* Dynamic Nuclear Polarization Surface Enhanced NMR Spectroscopy. *Acc. Chem. Res.* **46**, 1942-1951, doi:10.1021/ar300322x (2013).

24. Ni, Q. Z. *et al.* High Frequency Dynamic Nuclear Polarization. *Acc. Chem. Res.* **46**, 1933-1941 (2013).

25. Perras, F. A. *et al.* Atomic-Level Structure Characterization of Biomass Pre- and Post-Lignin Treatment by Dynamic Nuclear Polarization-Enhanced Solid-State NMR. *J. Phys. Chem. A* **121**, 623-630, doi:10.1021/acs.jpca.6b11121 (2017).

26. Schmidt-Rohr, K. & Spiess, H. W. (Multidimensional Solid-State NMR and Polymer, Academic Press, San Diego, CA, 1994).

27. Polenova, T., Gupta, R. & Goldbourt, A. (ACS Publications, 2015).

28. Elena, B., Lesage, A., Steuernagel, S., Bockmann, A. & Emsley, L. Proton to carbon-13 INEPT in solid-state NMR spectroscopy. *J. Am. Chem. Soc.* **127**, 17296-17302, doi:10.1021/ja054411x (2005).

29. Dumez, J. N. & Emsley, L. A master-equation approach to the description of proton-driven spin diffusion from crystal geometry using simulated zero-quantum lineshapes. *Phys. Chem. Chem. Phys.* **13**, 7363-7370, doi:10.1039/c1cp00004g (2011).

30. Meier, B. H. (Adv. Magn. Opt. Reson. , 1994).

31. Takegoshi, K., Nakamura, S. & Terao, T. ^{13}C-^{1}H dipolar-assisted rotational resonance in magic-angle spinning NMR. *Chem. Phys. Lett.* **344**, 631-637, doi:Doi 10.1016/S0009-2614(01)00791-6 (2001).

32. De Paepe, G. Dipolar recoupling in magic angle spinning solid-state nuclear magnetic resonance. *Annu. Rev. Phys. Chem.* **63**, 661-684, doi:10.1146/annurev-physchem-032511-143726 (2012).

33. Takegoshi, K., Nakamura, S. & Terao, T. 13 C–1 H dipolar-driven 13 C–13 C recoupling without 13 C rf irradiation in nuclear magnetic resonance of rotating solids. *The Journal of chemical physics* **118**, 2325-2341 (2003).

34. Lange, A., Luca, S. & Baldus, M. Structural constraints from proton-mediated rare-spin correlation spectroscopy in rotating solids. *Journal of the American Chemical Society* **124**, 9704-9705 (2002).

35. Aluas, M. *et al.* CHHC and ^{1}H-^{1}H magnetization exchange: Analysis by experimental solid-state NMR and 11-spin density-matrix simulations. *J. Magn. Reson.* **199**, 173-187, doi:10.1016/j.jmr.2009.04.013 (2009).

36. Cadars, S. *et al.* The refocused INADEQUATE MAS NMR experiment in multiple spin-systems: Interpreting observed correlation peaks and optimising lineshapes. *J. Magn. Reson.* **188**, 24-34, doi:10.1016/j.jmr.2007.05.016 (2007).

37. Lesage, A., Auger, C., Caldarelli, S. & Emsley, L. Determination of through-bond carbon-carbon connectivities in solid-state NMR using the INADEQUATE experiment. *J. Am. Chem. Soc.* **119**, 7867-7868, doi:Doi 10.1021/Ja971089k (1997).

38. Huster, D., Yao, X. L. & Hong, M. Membrane Protein Topology Probed by 1H Spin Diffusion from Lipids Using Solid-State NMR Spectroscopy. *J. Am. Chem. Soc.* **124**, 874-883 (2002).

39. Hong, M. *et al.* Coupling amplification in 2D MAS NMR and its application to torsion angle determination in peptides. *J. Magn. Reson.* **129**, 85-92, doi:DOI 10.1006/jmre.1997.1242 (1997).

40. Mansfield, P. J. Orchard, DC Stalker and KHB Richards. *Phys. Rev. B* **7**, 90 (1973).

41. Bielecki, A., Kolbert, A. C. & Levitt, M. H. Frequency-Switched Pulse Sequences - Homonuclear Decoupling and Dilute Spin NMR in Solids. *Chem. Phys. Lett.* **155**, 341-346, doi:Doi 10.1016/0009-2614(89)87166-0 (1989).

42. Kirui, A. *et al.* Atomic Resolution of Cotton Cellulose Structure Enabled by Dynamic Nuclear Polarization Solid-State NMR. *Cellulose* **26**, 329-339 (2019).

43. Murrey, H. E. & Hsieh-Wilson, L. C. The chemical neurobiology of carbohydrates. *Chemical reviews* **108**, 1708-1731 (2008).

44. Cosgrove, D. J. Growth of the plant cell wall. *Nat. Rev. Mol. Cell Biol.* **6**, 850-861, doi:Doi 10.1038/Nrm1746 (2005).

45. Furtado, A. *et al.* Modifying plants for biofuel and biomaterial production. *Plant biotechnology journal* **12**, 1246-1258 (2014).

46. Loqué, D., Scheller, H. V. & Pauly, M. Engineering of plant cell walls for enhanced biofuel production. *Current opinion in plant biology* **25**, 151-161 (2015).

47. Latge, J. P. Aspergillus fumigatus and aspergillosis. *Clin. Microbiol. Rev.* **12**, 310-350 (1999).

48. Ragauskas, A. J. *et al.* The path forward for biofuels and biomaterials. *Science* **311**, 484-489, doi:10.1126/science.1114736 (2006).

49. Service, R. F. Cellulosic ethanol - Biofuel researchers prepare to reap a new harvest. *Science* **315**, 1488-1491, doi:DOI 10.1126/science.315.5818.1488 (2007).

50. Somerville, C., Youngs, H., Taylor, C., Davis, S. C. & Long, S. P. Feedstocks for Lignocellulosic Biofuels. *Science* **329**, 790-792, doi:10.1126/science.1189268 (2010).

51. Schiavone, M. *et al.* A combined chemical and enzymatic method to determine quantitatively the polysaccharide components in the cell wall of yeasts. *FEMS yeast Research* **14**, 933-947 (2014).

52. Mansfield, S. D., Kim, H., Lu, F. C. & Ralph, J. Whole plant cell wall characterization using solution-state 2D NMR. *Nat. Protoc.* **7**, 1579-1589, doi:10.1038/nprot.2012.064 (2012).

53. Tan, L. *et al.* An Arabidopsis Cell Wall Proteoglycan Consists of Pectin and Arabinoxylan Covalently Linked to an Arabinogalactan Protein. *Plant Cell* **25**, 270-287, doi:10.1105/tpc.112.107334 (2013).

54. Kollar, R., Petrakova, E., Ashwell, G., Robbins, P. W. & Cabib, E. Architecture of the Yeast-Cell Wall - the Linkage between Chitin and Beta(1-3)-Glucan. *J. Biol. Chem.* **270**, 1170-1178, doi:DOI 10.1074/jbc.270.3.1170 (1995).

55. Kollar, R. *et al.* Architecture of the yeast cell wall - beta(1->6)-glucan interconnects mannoprotein, beta(1-3)-glucan, and chitin. *J. Biol. Chem.* **272**, 17762-17775, doi:DOI 10.1074/jbc.272.28.17762 (1997).

56. Mccann, M. C. *et al.* Old and new ways to probe plant cell wall architecture. *Can. J. Bot.* **73**, S103-S113 (1995).

57. Whitney, S. E. C., Brigham, J. E., Darke, A. H., Reid, J. S. G. & Gidley, M. J. In-Vitro Assembly of Cellulose/Xyloglucan Networks - Ultrastructural and Molecular Aspects. *Plant J* **8**, 491-504, doi:DOI 10.1046/j.1365-313X.1995.8040491.x (1995).

58. Zykwinska, A. W., Ralet, M. C. J., Garnier, C. D. & Thibault, J. F. J. Evidence for *in vitro* binding of pectin side chains to cellulose. *Plant Physiol.* **139**, 397-407, doi:DOI 10.1104/pp.105.065912 (2005).

59. Kiemle, S. N. *et al.* Role of (1,3)(1,4)-beta-Glucan in Cell Walls: Interaction with Cellulose. *Biomacromolecules* **15**, 1727-1736, doi:10.1021/bm5001247 (2014).

60. Pogorelko, G., Lionetti, V., Bellincampi, D. & Zabotina, O. Cell wall integrity: targeted post-synthetic modifications to reveal its role in plant growth and defense against pathogens. *Plant signaling & behavior* **8**, e25435 (2013).

61. Wang, T., Park, Y. B., Cosgrove, D. J. & Hong, M. Cellulose-Pectin Spatial Contacts Are Inherent to Never-Dried Arabidopsis thaliana Primary Cell Walls: Evidence from Solid-State NMR. *Plant Physiol.* **168**, 871-884 (2015).

62. Wang, T., Salazar, A., Zabotina, O. A. & Hong, M. Structure and dynamics of *Brachypodium* primary cell wall polysaccharides from two-dimensional ^{13}C solid-state nuclear magnetic resonance spectroscopy. *Biochemistry* **53**, 2840-2854, doi:Doi 10.1021/Bi500231b (2014).

63. Grantham, N. J. *et al.* An even pattern of xylan substitution is critical for interaction with cellulose in plant cell walls. *Nat. Plants* **3**, 859-865, doi:10.1038/s41477-017-0030-8 (2017).

64. Komatsu, T. & Kikuchi, J. Selective Signal Detection in Solid-State NMR Using Rotor-Synchronized Dipolar Dephasing for the Analysis of Hemicellulose in Lignocellulosic Biomass. *J. Phys. Chem. Lett.* **4**, 2279-2283, doi:10.1021/jz400978g (2013).

65. Chatterjee, S., Prados-Rosales, R., Itin, B., Casadevall, A. & Stark, R. E. Solid-state NMR Reveals the Carbon-based Molecular Architecture of Cryptococcus neoformans Fungal Eumelanins in the Cell Wall. *J. Biol. Chem.* **290**, 13779-13790, doi:10.1074/jbc.M114.618389 (2015).

66. Zhong, J., Frases, S., Wang, H., Casadevall, A. & Stark, R. E. Following fungal melanin biosynthesis with solid-state NMR: biopolymer molecular structures and possible connections to cell-wall polysaccharides. *Biochemistry* **47**, 4701-4710, doi:10.1021/bi702093r (2008).

67. Kang, X. *et al.* Molecular architecture of fungal cell walls revealed by solid-state NMR. *Nature communications* **9**, 2747 (2018).

68. Takahashi, H. *et al.* Solid-state NMR on bacterial cells: selective cell wall signal enhancement and resolution improvement using dynamic nuclear polarization. *J. Am. Chem. Soc.* **135**, 5105-5110, doi:10.1021/ja312501d (2013).

69. Wang, T. & Hong, M. Solid-state NMR investigations of cellulose structure and interactions with matrix polysaccharides in plant primary cell walls. *J. Exp. Bot.* **67**, 503-514, doi:10.1093/jxb/erv416 (2016).

70. Mentink-Vigier, F., Akbey, Ü., Oschkinat, H., Vega, S. & Feintuch, A. Theoretical aspects of magic angle spinning-dynamic nuclear polarization. *Journal of Magnetic Resonance* **258**, 102-120 (2015).

71. Gupta, R. *et al.* Dynamic nuclear polarization enhanced MAS NMR spectroscopy for structural analysis of HIV-1 protein assemblies. *The Journal of Physical Chemistry B* **120**, 329-339 (2016).

72. Takahashi, H., Hediger, S. & De Paëpe, G. Matrix-free dynamic nuclear polarization enables solid-state NMR 13 C–13 C correlation spectroscopy of proteins at natural isotopic abundance. *Chemical Communications* **49**, 9479-9481 (2013).

73. Ni, Q. Z. *et al.* High frequency dynamic nuclear polarization. *Accounts of chemical research* **46**, 1933-1941 (2013).

74. Koers, E. J. *et al.* NMR-based structural biology enhanced by dynamic nuclear polarization at high magnetic field. *J. Biomol. NMR* **60**, 157-168, doi:10.1007/s10858-014-9865-8 (2014).

75. Saliba, E. P. *et al.* Electron Decoupling with Dynamic Nuclear Polarization in Rotating Solids. *J Am Chem Soc* **139**, 6310-6313, doi:10.1021/jacs.7b02714 (2017).

76. Mentink-Vigier, F. *et al.* Efficient cross-effect dynamic nuclear polarization without depolarization in high-resolution MAS NMR. *Chem Sci* **8**, 8150-8163, doi:10.1039/c7sc02199b (2017).

77. Smith, A. N., Twahir, U. T., Dubroca, T., Fanucci, G. E. & Long, J. R. Molecular Rationale for Improved Dynamic Nuclear Polarization of Biomembranes. *The Journal of Physical Chemistry B* **120**, 7880-7888 (2016).

78. Hill, T. W. & Kafer, E. Improved protocols for Aspergillus minimal medium: trace element and minimal medium salt stock solutions. *Fungal Genetics Reports* **48**, 20-21 (2001).

79. Rossini, A. J. *et al.* Dynamic nuclear polarization surface enhanced NMR spectroscopy. *Accounts of chemical research* **46**, 1942-1951 (2013).

80. Sauvée, C. *et al.* Highly efficient, water-soluble polarizing agents for dynamic nuclear polarization at high frequency. *Angewandte Chemie* **125**, 11058-11061 (2013).

81. Phyo, P. *et al.* Gradients in Wall Mechanics and Polysaccharides along Growing Inflorescence Stems. *Plant Physiol.* **175**, 1593-1607, doi:10.1104/pp.17.01270 (2017).

82. White, P. B., Wang, T., Park, Y. B., Cosgrove, D. J. & Hong, M. Water-polysaccharide interactions in the primary cell wall of *Arabidopsis thaliana* from polarization transfer solid-state NMR. *J. Am. Chem. Soc.* **136**, 10399-10409, doi:Doi 10.1021/Ja504108h (2014).

83. Jippo, T., Kamo, O. & Nagayama, K. Determination of long-range proton-carbon 13 coupling constants with selective two-dimensional INEPT. *Journal of Magnetic Resonance (1969)* **66**, 344-348 (1986).

84. Morris, G. A. Sensitivity enhancement in nitrogen-15 NMR: polarization transfer using the INEPT pulse sequence. *Journal of the American Chemical Society* **102**, 428-429 (1980).

85. Cadars, S. *et al.* The refocused INADEQUATE MAS NMR experiment in multiple spin-systems: interpreting observed correlation peaks and optimising lineshapes. *Journal of Magnetic Resonance* **188**, 24-34 (2007).

86. Lesage, A., Bardet, M. & Emsley, L. Through-bond carbon− carbon connectivities in disordered solids by NMR. *Journal of the American Chemical Society* **121**, 10987-10993 (1999).

87. Bennett, A. E. *et al.* Homonuclear radio frequency-driven recoupling in rotating solids. *The Journal of chemical physics* **108**, 9463-9479 (1998).

88. Lu, X., Guo, C., Hou, G. & Polenova, T. Combined zero-quantum and spin-diffusion mixing for efficient homonuclear correlation spectroscopy under fast MAS: broadband recoupling and detection of long-range correlations. *Journal of biomolecular NMR* **61**, 7-20 (2015).

89. Wang, T., Zabotina, O. & Hong, M. Pectin–cellulose interactions in the Arabidopsis primary cell wall from two-dimensional magic-angle-spinning solid-state nuclear magnetic resonance. *Biochemistry* **51**, 9846-9856 (2012).

90. Wang, T. *et al.* Sensitivity-enhanced solid-state NMR detection of expansin's target in plant cell walls. *P Natl Acad Sci USA* **110**, 16444-16449, doi:DOI 10.1073/pnas.1316290110 (2013).

91. Liao, S. Y., Lee, M., Wang, T., Sergeyev, I. V. & Hong, M. Efficient DNP NMR of membrane proteins: sample preparation protocols, sensitivity, and radical location. *J. Biomol. NMR* **64**, 223-237, doi:10.1007/s10858-016-0023-3 (2016).

92. Takahashi, H. *et al.* Rapid Natural-Abundance 2D 13C-13C Correlation Spectroscopy Using Dynamic Nuclear Polarization Enhanced Solid-State NMR and Matrix-Free Sample

Preparation. *Angew. Chem. Int. Edit.* **51**, 11766-11769, doi:10.1002/anie.201206102 (2012).

93. Atalla, R. H. & Vanderhart, D. L. Native cellulose: a composite of two distinct crystalline forms. *Science* **223**, 283-285, doi:DOI 10.1126/science.223.4633.283 (1984).

94. Atalla, R. H. & Agarwal, U. P. Raman Microprobe Evidence for Lignin Orientation in the Cell-Walls of Native Woody Tissue. *Science* **227**, 636-638, doi:DOI 10.1126/science.227.4687.636 (1985).

95. Atalla, R. H. & Vanderhart, D. L. The role of solid state ^{13}C NMR spectroscopy in studies of the nature of native celluloses. *Solid State Nucl. Magn. Reson.* **15**, 1-19 (1999).

96. Larsson, P. T., Hult, E. L., Wickholm, K., Pettersson, E. & Iversen, T. CP/MAS ^{13}C NMR spectroscopy applied to structure and interaction studies on cellulose I. *Solid State Nucl. Magn. Reson.* **15**, 31-40, doi:Doi 10.1016/S0926-2040(99)00044-2 (1999).

97. Wang, T., Phyo, P. & Hong, M. Multidimensional solid-state NMR spectroscopy of plant cell walls. *Solid State Nucl. Magn. Reson.* **78**, 56-63, doi:10.1016/j.ssnmr.2016.08.001 (2016).

98. Phyo, P., Wang, T., Yang, Y., O'Neill, H. & Hong, M. Direct Determination of Hydroxymethyl Conformations of Plant Cell Wall Cellulose Using ^{1}H Polarization Transfer Solid-State NMR. *Biomacromolecules* **19**, 1485-1497, doi:10.1021/acs.biomac.8b00039 (2018).

99. Kono, H. & Numata, Y. Structural investigation of cellulose I_a and I_b by 2D RFDR NMR spectroscopy: determination of sequence of magnetically inequivalent D-glucose units along cellulose chain. *Cellulose* **13**, 317-326 (2006).

100. Nishiyama, Y., Langan, P. & Chanzy, H. Crystal structure and hydrogen-bonding system in cellulose I_b from synchrotron X-ray and neutron fiber diffraction. *J. Am. Chem. Soc.* **124**, 9074-9082, doi: 10.1021/Ja0257319 (2002).

101. Nishiyama, Y. *et al.* Periodic disorder along ramie cellulose microfibrils. *Biomacromolecules* **4**, 1013-1017, doi:Doi 10.1021/Bm025772x (2003).

102.. Lee, D., Hediger, S. & De Paepe, G. Is solid-state NMR enhanced by dynamic nuclear polarization? *Solid State Nucl. Magn. Reson.* **66-67**, 6-20, doi:10.1016/j.ssnmr.2015.01.003 (2015).

103. Mentink-Vigier, F., Vega, S. & De Paepe, G. Fast and accurate MAS-DNP simulations of large spin ensembles. *Phys. Chem. Chem. Phys.* **19**, 3506-3522, doi:10.1039/c6cp07881h (2017).

104. Rossini, A. J. *et al.* Dynamic Nuclear Polarization NMR Spectroscopy of Microcrystalline Solids. *J. Am. Chem. Soc.* **134**, 16899-16908 (2012).

105. Takahashi, H., Hediger, S. & De Paepe, G. Matrix-free dynamic nuclear polarization enables solid-state NMR ^{13}C-^{13}C correlation spectroscopy of proteins at natural isotopic abundance. *Chem. Commun.* **49**, 9479-9481, doi:10.1039/c3cc45195j (2013).

106. Dubroca, T. *et al.* A quasi-optical and corrugated waveguide microwave transmission system for simultaneous dynamic nuclear polarization NMR on two separate 14.1 T spectrometers. *J. Magn. Reson.* **289**, 35-44, doi:10.1016/j.jmr.2018.01.015 (2018).

107. Hohwy, M., Rienstra, C. M., Jaroniec, C. P. & Griffin, R. G. Fivefold symmetric homonuclear dipolar recoupling in rotating solids: Application to double quantum spectroscopy. *J. Chem. Phys.* **110**, 7983-7992, doi:Doi 10.1063/1.478702 (1999).

108. Ling, Z. *et al.* Effects of ball milling on the structure of cotton cellulose. *Cellulose* **26**, 305-328, doi:10.1007/s10570-018-02230-x (2019).

109. Fernandes, A. N. *et al.* Nanostructure of cellulose microfibrils in spruce wood. *Proc. Natl. Acad. Sci. USA* **108**, E1195-E1203, doi:DOI 10.1073/pnas.1108942108 (2011).

110. Cosgrove, D. J. Re-constructing our models of cellulose and primary cell wall assembly. *Curr. Opin. Plant Biol.* **22C**, 122-131, doi:10.1016/j.pbi.2014.11.001 (2014).

111. Hill, J. L., Hammudi, M. B. & Tien, M. The Arabidopsis Cellulose Synthase Complex: A Proposed Hexamer of CESA Trimers in an Equimolar Stoichiometry. *Plant Cell* **26**, 4834-4842, doi:10.1105/tpc.114.131193 (2014).

112. Newman, R. H., Hill, S. J. & Harris, P. J. Wide-angle x-ray scattering and solid-state nuclear magnetic resonance data combined to test models for cellulose microfibrils in mung bean cell walls. *Plant Physiol.* **163**, 1558-1567, doi:10.1104/pp.113.228262 (2013).

113. Sethaphong, L. *et al.* Tertiary model of a plant cellulose synthase. *Proc. Natl. Acad. Sci. USA* **110**, 7512-7517, doi:10.1073/pnas.1301027110 (2013).

114. Vandavasi, V. G. *et al.* A Structural Study of CESA1 Catalytic Domain of Arabidopsis Cellulose Synthesis Complex: Evidence for CESA Trimers. *Plant Physiol.* **170**, 123-135 (2016).

115. Larsson, P. T. & Westlund, P. O. Line shapes in CP/MAS ^{13}C NMR spectra of cellulose I. *Spectrochim. Acta A* **62**, 539-546, doi:DOI 10.1016/j.saa.2005.01.021 (2005).

116. Newman, R. H. & Hemmingson, J. A. ^{13}C NMR distinction between categories of molecular order and disorder in cellulose. *Cellulose* **2**, 95-110, doi:Doi 10.1007/Bf00816383 (1995).

117. Kono, H., Erata, T. & Takai, M. Determination of the through-bond carbon-carbon and carbon-proton connectivities of the native celluloses in the solid state. *Macromolecules* **36**, 5131-5138, doi:Doi 10.1021/Ma021769u (2003).

118. Kono, H., Erata, T. & Takai, M. Complete assignment of the CP/MAS ^{13}C NMR spectrum of cellulose III$_I$. *Macromolecules* **36**, 3589-3592, doi:Doi 10.1021/Ma021015f (2003).

119. Kono, H. Two-dimensional magic angle spinning NMR investigation of naturally occurring chitins: Precise H-1 and C-13 resonance assignment of alpha- and beta-chitin. *Biopolymers* **75**, 255-263, doi:10.1002/bip.20124 (2004).

120. Nishiyama, Y., Sugiyama, J., Chanzy, H. & Langan, P. Crystal structure and hydrogen bonding system in cellulose Ia, from synchrotron X-ray and neutron fiber diffraction. *J. Am. Chem. Soc.* **125**, 14300-14306, doi:Doi 10.1021/Ja037055w (2003).

121. Kubicki, J. D., Mohamed, M. N. A. & Watts, H. D. Quantum mechanical modeling of the structures, energetics and spectral properties of I alpha and I beta cellulose. *Cellulose* **20**, 9-23, doi:10.1007/s10570-012-9838-6 (2013).

122. Kubicki, J. D., Watts, H. D., Zhao, Z. & Zhong, L. H. Quantum mechanical calculations on cellulose-water interactions: structures, energetics, vibrational frequencies and NMR chemical shifts for surfaces of I alpha and I beta cellulose. *Cellulose* **21**, 909-926, doi:10.1007/s10570-013-0029-x (2014).

123. Yang, H. *et al.* Structural factors affecting ^{13}C NMR chemical shifts of cellulose: a computational study. *Cellulose* **25**, 23-36, doi:10.1007/s10570-017-1549-6 (2018).

124. Kang, X. *et al.* CCMRD: a solid-state NMR database for complex carbohydrates. *J. Biomol. NMR* **74**, 239-245, doi:10.1007/s10858-020-00304-2 (2020).

125. Scheller, H. V. & Ulvskov, P. Hemicelluloses. *Annu. Rev. Plant Biol.* **61**, 263-289 (2010).

126. Vaahtera, L., Schulz, J. & Hamann, T. Cell wall integrity maintenance during plant development and interaction with the environment. *Nat. Plants* **5**, 924-932, doi:10.1038/s41477-019-0502-0 (2019).

127. Ridley, B. L., O'Neill, M. A. & Mohnen, D. Pectins: Structure, biosynthesis, and oligogalacturonide-related signaling. *Phytochemistry* **57**, 929-967 (2001).

128. Mohnen, D. Pectin structure and biosynthesis. *Curr. Opin. Plant Biol.* **11**, 266-277, doi:10.1016/j.pbi.2008.03.006 (2008).

129. Pelloux, J., Rusterucci, C. & Mellerowicz, E. J. New insights into pectin methylesterase structure and function. *Trends Plant Sci.* **12**, 267-277 (2007).

130. O'Neill, M., Albersheim, P. & Darvill, A. The pectic polysaccharides of primary cell walls. *Methods in Plant Biochemistry* **2**, 415-441 (1990).

131. Wachsman, G., Zhang, J., Moreno-Risueno, M. A., Anderson, C. & Benfey, P. N. Cell Wall Remodeling and Vesicle Trafficking Mediate the Root Clock in Arabidopsis. *Science* **370**, 819-823 (2020).

132. Du, J. *et al.* Mutations in the Pectin Methyltransferase QUASIMODO2 Influence Cellulose Biosynthesis and Wall Integrity in Arabidopsis thaliana. *Plant Cell*, doi:10.1105/tpc.20.00252 (2020).

133. Goubet, F. & Mohnen, D. Solubilization and partial characterization of homogalacturonan-methyltransferase from microsomal membranes of suspension-cultured tobacco cells. *Plant Physiol.* **121**, 281-290, doi:10.1104/pp.121.1.281 (1999).

134. Li, Y. Q. *et al.* Detection and localization of pectin methylesterase isoforms in pollen tubes of Nicotiana tabacum L. *Planta* **214**, 734-740, doi:10.1007/s004250100664 (2002).

135. Atmodjo, M. A., Hao, Z. & Mohnen, D. Evolving Views of Pectin Biosynthesis. *Annu. Rev. Plant Biol.* **64**, 747-779 (2013).

136. Tan, L. *et al.* An Arabidopsis Cell Wall Proteoglycan Consists of Pectin and Arabinoxylan Covalently Linked to an Arabinogalactan Protein. *Plant Cell* **25**, 270-287 (2013).

137. Duan, J., Wang, X., Dong, Q., Fang, J.-N. & Li, X. Structural features of a pectic arabinogalactan with immunological activity from the leaves of Diospyros kaki. *Carbohydr. Res.* **338**, 1291-1297 (2003).

138. Duan, J., Zheng, Y., Dong, Q. & Fang, J. Structural analysis of a pectic polysaccharide from the leaves of Diospy. *Biopolymers* **93**, 649-656 (2004).

139. Keegstra, K., Talmadge, K. W., Bauer, W. D. & Albersheim, P. The structure of plant cell walls. III. A model of the walls of suspension cultured sycamore cells based on the interconnections of the macromolecular components. *Plant Physiol.* **51**, 188-196 (1973).

140. Zykwinska, A., Thibault, J. F. & Ralet, M. C. Competitive binding of pectin and xyloglucan with primary cell wall cellulose. *Carbohydr. Polym.* **74**, 957-961 (2008).

141. Zhao, W., Fernando, L. D., Kirui, A., Deligey, F. & Wang, T. Solid-state NMR of plant and fungal cell walls: A critical review. *Solid State Nucl. Magn. Reson.* **107**, 101660, doi:10.1016/j.ssnmr.2020.101660 (2020).

142. Reif, B., Ashbrook, S. E., Emsley, L. & Hong, M. Solid-State NMR Spectroscopy. *Nat. Rev. Methos Primers* **1**, 2 (2021).

143. Kelly, J. E., Chrissian, C. & Stark, R. E. Tailoring NMR experiments for structural characterization of amorphous biological solids: A practical guide. *Solid State Nucl. Magn. Reson.* **109**, 101686, doi:10.1016/j.ssnmr.2020.101686 (2020).

144. Gao, Y. & Mortimer, J. C. Unlocking the architecture of native plant cell walls via solid-state nuclear magnetic resonance. *Methods Cell Biol.* **160**, 121-143, doi:10.1016/bs.mcb.2020.05.001 (2020).

145. Martinez-Sanz, M., Gidley, M. J. & Gilbert, E. P. Application of X-ray and neutron small angle scattering techniques to study the hierarchical structure of plant cell walls: A review. *Carbohydr. Polym.* **125**, 120-134, doi:10.1016/j.carbpol.2015.02.010 (2015).

146. Park, Y. B. & Cosgrove, D. J. A revised architecture of primary cell walls based on biomechanical changes induced by substrate-specific endoglucanases. *Plant Physiol.* **158**, 1933-1943, doi:10.1104/pp.111.192880 (2012).

147. Xiao, C., Somerville, C. & Anderson, C. T. POLYGALACTURONASE INVOLVED IN EXPANSION1 functions in cell elongation and flower development in Arabidopsis. *Plant Cell* **26**, 1018-1035, doi:10.1105/tpc.114.123968 (2014).

148. Phyo, P., Wang, T., Xiao, C. W., Anderson, C. T. & Hong, M. Effects of Pectin Molecular Weight Changes on the Structure, Dynamics, and Polysaccharide Interactions of Primary Cell Walls of Arabidopsis thaliana: Insights from Solid-State NMR. *Biomacromolecules* **18**, 2937-2950, doi:10.1021/acs.biomac.7b00888 (2017).

149. Biswal, A. K. *et al.* Sugar release and growth of biofuel crops are improved by downregulation of pectin biosynthesis. *Nat. Biotechnol.* **36**, 249-257 (2018).

150. Chiniquy, D. *et al.* PMR5, an acetylation protein at the intersection of pectin biosynthesis and defense against fungal pathogens. *The Plant journal : for cell and molecular biology* **100**, 1022-1035 (2019).

151. Held, M. A. *et al.* CGR3: a Golgi-localized protein influencing homogalacturonan methylesterification. *Mol. Plant* **4**, 832-844, doi:10.1093/mp/ssr012 (2011).

152. Miao, Y., Li, H. Y., Shen, J., Wang, J. & Jiang, L. QUASIMODO 3 (QUA3) is a putative homogalacturonan methyltransferase regulating cell wall biosynthesis in Arabidopsis suspension-cultured cells. *J. Exp. Bot.* **62**, 5063-5078, doi:10.1093/jxb/err211 (2011).

153. Mouille, G. *et al.* Homogalacturonan synthesis in Arabidopsis thaliana requires a Golgi-localized protein with a putative methyltransferase domain. *The Plant journal : for cell and molecular biology* **50**, 605-614, doi:10.1111/j.1365-313X.2007.03086.x (2007).

154. Krupkova, E., Immerzeel, P., Pauly, M. & Schmulling, T. The TUMOROUS SHOOT DEVELOPMENT2 gene of Arabidopsis encoding a putative methyltransferase is required for cell adhesion and co-ordinated plant development. *The Plant journal : for cell and molecular biology* **50**, 735-750, doi:10.1111/j.1365-313X.2007.03123.x (2007).

155. Frank, M. *et al.* Tumorous shoot development (TSD) genes are required for co-ordinated plant shoot development. *The Plant journal : for cell and molecular biology* **29**, 73-85, doi:10.1046/j.1365-313x.2002.01197.x (2002).

156. El Hariri El Nokab, M. & van der Wel, P. C. A. Use of solid-state NMR spectroscopy for investigating polysaccharide-based hydrogels: A review. *Carbohydr. Polym.* **240**, 116276, doi:10.1016/j.carbpol.2020.116276 (2020).

157. Hou, G., Yan, S., Trebosc, J., Amoureux, J. P. & Polenova, T. Broadband homonuclear correlation spectroscopy driven by combined R2(n)(v) sequences under fast magic angle spinning for NMR structural analysis of organic and biological solids. *J. Magn. Reson.* **232**, 18-30, doi:10.1016/j.jmr.2013.04.009 (2013).

158. Munowitz, M. G., Griffin, R. G., Bodenhausen, G. & Huang, T. H. Two-Dimensional Rotational Spin-Echo Nuclear Magnetic-Resonance in Solids - Correlation of Chemical-Shift and Dipolar Interactions. *J. Am. Chem. Soc.* **103**, 2529-2533, doi:Doi 10.1021/Ja00400a007 (1981).

159. Tan, L. *et al.* Arabinogalactan-proteins and the research challenges for these enigmatic plant cell surface proteoglycans. *Front. Plant Sci.* **27** (2012).

160. Wang, T., Williams, J. K., Schmidt-Rohr, K. & Hong, M. Relaxation-compensated difference spin diffusion NMR for detecting 13C-13C long-range correlations in proteins and polysaccharides. *J. Biomol. NMR* **61**, 97-107, doi:10.1007/s10858-014-9889-0 (2015).

161. Terrett, O. M. *et al.* Molecular architecture of softwood revealed by solid-state NMR. *Nat. Commun.* **10**, 4978, doi:10.1038/s41467-019-12979-9 (2019).

162. Gao, Y., Lipton, A. S., Wittmer, Y., Murray, D. T. & Mortimer, J. C. A grass-specific cellulose-xylan interaction dominates in sorghum secondary cell walls. *Nature communications* **11**, 6081, doi:10.1038/s41467-020-19837-z (2020).

163. Hass, K. T., Wightwan, R., Meyerowitz, E. M. & Peaucelle, A. Pectin homogalacturonan nanofilament expansion drives morphogenesis in plant epidermal cells. *Science* **367**, 1003-1007 (2020).

164. Phyo, P., Gu, Y. & Hong, M. Impact of acidic pH on plant cell wall polysaccharide structure and dynamics: insights into the mechanism of acid growth in plants from solid-state NMR. *Cellulose* **26**, 291-304, doi:10.1007/s10570-018-2094-7 (2019).

165. Poovaiah, C. R., Nageswara-Rao, M., Soneji, J. R., Baxter, H. L. & Stewart, C. N. Altered lignin biosynthesis using biotechnology to improve lignocellulosic biofuel feedstocks. *Plant Biotechnol. J.* **12**, 1163-1173, doi:10.1111/pbi.12225 (2014).

166. Vanholme, R., Morreel, K., Ralph, J. & Boerjan, W. Lignin engineering. *Curr. Opin. Plant Biol.* **11**, 278-285, doi:10.1016/j.pbi.2008.03.005 (2008).

167. Loque, D., Scheller, H. V. & Pauly, M. Engineering of plant cell walls for enhanced biofuel production. *Curr. Opin. Plant Biol.* **25**, 151-161, doi:10.1016/j.pbi.2015.05.018 (2015).

168. Salmen, L. Micromechanical understanding of the cell-wall structure. *C. R. Biologies* **327**, 873-880 (2004).

169. Terashima, N., Yoshida, M., Hafren, J., Fukushima, K. & Westermark, U. Proposed supramolecular structure of lignin in softwood tracheid compound middle lamella regions. *Holzforschung* **66**, 907-915, doi:10.1515/hf-2012-0021 (2012).

170. Langan, P. *et al.* Common processes drive the thermochemical pretreatment of lignocellulosic biomass. *Green Chem.* **16**, 63-68, doi:10.1039/c3gc41962b (2014).

171. Haigler, C. H. *et al.* Molecular Modeling and Imaging of Initial Stages of Cellulose Fibril Assembly: Evidence for a Disordered Intermediate Stage. *PLOS One* **9**, doi:10.1371/journal.pone.0093981 (2014).

172. Li, S. D. *et al.* Cellulose synthase complexes act in a concerted fashion to synthesize highly aggregated cellulose in secondary cell walls of plants. *Proc. Natl. Acad. Sci. USA* **113**, 11348-11353, doi:10.1073/pnas.1613273113 (2016).

173. Komatsu, T. & Kikuchi, J. Comprehensive Signal Assignment of C-13-Labeled Lignocellulose Using Multidimensional Solution NMR and C-13 Chemical Shift Comparison with Solid-State NMR. *Anal. Chem.* **85**, 8857-8865, doi:10.1021/ac402197h (2013).

174. Houtman, C. J. & Atalla, R. H. Cellulose-Lignin Interactions (A Computational Study). *Plant Physiol.* **107**, 977-984 (1995).

175. Musel, G. *et al.* Structure and distribution of lignin in primary and secondary cell walls of maize coleoptiles analyzed by chemical and immunological probes. *Planta* **201**, 146-159, doi:Doi 10.1007/Bf01007699 (1997).

176. Bonawitz, N. D. *et al.* Disruption of Mediator rescues the stunted growth of a lignin-deficient Arabidopsis mutant. *Nature* **509**, 376-380, doi:10.1038/nature13084 (2014).

177. Can, T. V., Ni, Q. Z. & Griffin, R. G. Mechanisms of dynamic nuclear polarization in insulating solids. *J. Magn. Reson.* **253**, 23-35 (2015).

178. Charlier, L. & Mazeau, K. Molecular Modeling of the Structural and Dynamical Properties of Secondary Plant Cell Walls: Influence of Lignin Chemistry. *J. Phys. Chem. B* **116**, 4163-4174, doi:10.1021/jp300395k (2012).

179. Busse-Wicher, M. *et al.* The pattern of xylan acetylation suggests xylan may interact with cellulose microfibrils as a twofold helical screw in the secondary plant cell wall of Arabidopsis thaliana. *Plant J.* **79**, 492-506, doi:10.1111/tpj.12575 (2014).

180. Gall, C. M., Cross, T. A., Diverdi, J. A. & Opella, S. J. Protein Dynamics by Solid-State NMR- Aromatic Rings of the Coat Protein in Fd Bacteriophage. *Proc. Natl. Acad. Sci. USA* **79**, 101-105, doi:DOI 10.1073/pnas.79.1.101 (1982).

181. Olsson, A. M., Bjurhager, I., Gerber, L., Sundberg, B. & Salmen, L. Ultra-structural organisation of cell wall polymers in normal and tension wood of aspen revealed by polarisation FTIR microspectroscopy. *Planta* **233**, 1277-1286, doi:10.1007/s00425-011-1384-1 (2011).

182. Grabber, J. H., Ralph, J. & Hatfield, R. D. Model studies of ferulate-coniferyl alcohol cross-product formation in primary maize walls: Implications for lignification in grasses. *J. Agr. Food Chem.* **50**, 6008-6016, doi:10.1021/jf0205312 (2002).

183. Grabber, J. H., Ralph, J. & Hatfield, R. D. Cross-linking of maize walls by ferulate dimerization and incorporation into lignin. *J. Agr. Food Chem.* **48**, 6106-6113, doi:10.1021/jf0006978 (2000).

184. Jeffries, T. W. Biodegradation of lignin-carbohydrate complexes. *Biodegradation* **1**, 163-176, doi:Doi 10.1007/Bf00058834 (1990).

185. Donaldson, L. A. Lignification and lignin topochemistry - an ultrastructural view. *Phytochemistry* **57**, 859-873 (2001).

186. Hao, Z. Y. & Mohnen, D. A review of xylan and lignin biosynthesis: Foundation for studying Arabidopsis irregular xylem mutants with pleiotropic phenotypes. *Crit. Rev. Biochem. Mol.* **49**, 212-241, doi:10.3109/10409238.2014.889651 (2014).

187. Lairez, D. *et al.* Aggregation during coniferyl alcohol polymerization in pectin solution: A biomimetic approach of the first steps of lignification. *Biomacromolecules* **6**, 763-774, doi:10.1021/bm049390y (2005).

188. Hill, S. J., Franich, R. A., Callaghan, P. T. & Newman, R. H. Nature's Nanocomposites: A New Look at Molecular Architecture in Wood Cell Walls. *N. Z. J. For. Sci.* **39**, 251-257 (2009).

189. Smakman, G. & Hofstra, R. J. J. Energy-Metabolism of Plantago-Lanceolata, as Affected by Change in Root Temperature. *Physiol. Plant.* **56**, 33-37, doi:DOI 10.1111/j.1399-3054.1982.tb04896.x (1982).

190. deVisser, R., Vianden, H. & Schnyder, H. Kinetics and relative significance of remobilized and current C and N incorporation in leaf and root growth zones of Lolium perenne after defoliation: Assessment by C-13 and N-15 steady-state labelling. *Plant Cell Environ.* **20**, 37-46, doi:DOI 10.1046/j.1365-3040.1997.d01-9.x (1997).

191. Massiot, D. *et al.* Modelling one- and two-dimensional solid-state NMR spectra. *Magn. Reson. Chem.* **40**, 70-76, doi:10.1002/mrc.984 (2002).

192. Schmidt-Rohr, K., Fritzsching, K. J., Liao, S. Y. & Hong, M. Spectral editing of two-dimensional magic-angle-spinning solid-state NMR spectra for protein resonance assignment and structure determination. *J. Biomol. NMR* **54**, 343-353, doi:10.1007/s10858-012-9676-8 (2012).

193. Williams, J. K., Schmidt-Rohr, K. & Hong, M. Aromatic spectral editing techniques for magic-angle-spinning solid-state NMR spectroscopy of uniformly (13)C-labeled proteins. *Solid State Nucl. Magn. Reson.* **72**, 118-126, doi:10.1016/j.ssnmr.2015.09.006 (2015).

194. Etzkorn, M. *et al.* Secondary structure, dynamics, and topology of a seven-helix receptor in native membranes, studied by solid-state NMR spectroscopy. *Angew. Chem. Int. Ed. Engl.* **46**, 459-462, doi:10.1002/anie.200602139 (2007).

195. Torchia, D. A. Measurement of Proton-Enhanced ^{13}C-T_1 Values by a Method Which Suppresses Artifacts. *J. Magn. Reson.* **30**, 613-616, doi:Doi 10.1016/0022-2364(78)90288-3 (1978).

196. Akbey, U., van Rossum, B. J. & Oschkinat, H. Practical aspects of high-sensitivity multidimensional C-13 MAS NMR spectroscopy of perdeuterated proteins. *J. Magn. Reson.* **217**, 77-85, doi:10.1016/j.jmr.2012.02.015 (2012).

197. Kirui, A. *et al.* Atomic resolution of cotton cellulose structure enabled by dynamic nuclear polarization solid-state NMR. *Cellulose*, doi:10.1007/s10570-018-2095-6 (2018).

198. Sauvee, C. *et al.* Highly Efficient, Water-Soluble Polarizing Agents for Dynamic Nuclear Polarization at High Frequency. *Angew. Chem. Int. Edit.* **52**, 10858-10861, doi:10.1002/anie.201304657 (2013).

199. Bar-On, Y. M., Phillips, R. & Milo, R. The biomass distribution on Earth. *Proc. Natl. Acad. Sci. USA* **115**, 6506-6511, doi:10.1073/pnas.1711842115 (2018).

200. Moon, R. J., Martini, A., Nairn, J., Simonsen, J. & Youngblood, J. Cellulose nanomaterials review: structure, properties and nanocomposites. *Chem. Soc. Rev.* **40**, 3941-3994, doi:10.1039/c0cs00108b (2011).

201. Himmel, M. E. *et al.* Biomass Recalcitrance: Engineering Plants and Enzymes for Biofuels Production. *Science* **315**, 804-805 (2007).

202. McCann, M. C. & Carpita, N. C. Biomass recalcitrance: a multi-scale, multi-factor, and conversion-specific property. *J. Exp. Bot.* **66**, 4109-4118 (2015).

203. Ragauskas, A. J. *et al.* Lignin Valorization: Improving Lignin Processing in the Biorefinery. *Science* **344**, 709-+, doi:10.1126/Science.1246843 (2014).

204. Cai, Y. *et al.* Enhancing digestibility and ethanol yield of Populus wood via expression of an engineered monolignol 4-O-methyltransferase. *Nat. Commun.* **7**, 11989, doi:10.1038/ncomms11989 (2016).

205. Purushotham, P., Ho, R. & Zimmer, J. Architecture of a catalytically active homotrimeric plant cellulose synthase complex. *Science* **369**, 1089-1094, doi:10.1126/science.abb2978 (2020).

206. Yang, H. & Kubicki, J. A density functional theory study on the shape of the primary cellulose microfibril in plants: effects of C6 exocyclic group conformation and H-bonding. *Cellulose* **27**, 2389-2402 (2020).

207. Thomas, L. H. *et al.* Nanostructural deformation of high-stiffness spruce wood under tension. *Scientific reports* **11**, 453, doi:10.1038/s41598-020-79676-2 (2021).

208. Vanholme, R., Demedts, B., Morreel, K., Ralph, J. & Boerjan, W. Lignin biosynthesis and structure. *Plant Physiol.* **153**, 895-905, doi:10.1104/pp.110.155119 (2010).

209. Wang, H. M. *et al.* Structural Variations of Lignin Macromolecules from Early Growth Stages of Poplar Cell Walls. *ACS Sustainable Chem. Eng.* **8**, 1813-1822 (2020).

210. Du, X. *et al.* Analysis of lignin-carbohydrate and lignin-lignin linkages after hydrolase treatment of xylan-lignin, glucomannan-lignin and glucan-lignin complexes from spruce wood. *Planta* **239**, 1079-1090 (2014).

211. Giummarella, N., Pu, Y., Ragauskas, A. J. & Lawoko, M. A critical review on the analysis of lignin carbohydrate bonds. *Green Chem.* **21**, 1573-1595 (2019).

212. Zhang, T., Vavylonis, D., Durachko, D. M. & Cosgrove, D. J. Nanoscale movements of cellulose microfibrils in primary cell walls. *Nat. Plants* **3**, doi:10.1038/Nplants.2017.56 (2017).

213. Reif, B., Ashbrook, S. E., Emsley, L. & Hong, M. Solid-State NMR Spectroscopy. *Nat. Rev. Methods Primers* **1**, 2 (2021).

214. Simmons, B. A., Loque, D. & Blanch, H. W. Next-generation biomass feedstocks for biofuel production. *Genome Biol.* **9**, 242, doi:10.1186/gb-2008-9-12-242 (2008).

215. Rencoret, J. *et al.* Lignin Composition and Structure in Young versus Adult Eucalyptus globulus Plants. *Plant Physiol.* **155**, 667-682 (2011).

216. Rinaldi, R. *et al.* Paving the Way for Lignin Valorisation: Recent Advances in Bioengineering, Biorefining and Catalysis. *Angew Chem Int Edit* **55**, 8164-8215 (2016).

217. Rico, A., Rencoret, J., del Rio, J. C., Martinez, A. T. & Gutierrez, A. In-Depth 2D NMR Study of Lignin Modification During Pretreatment of Eucalyptus Wood with Laccase and Mediators. *Bioenergy Res.* **8**, 211-230 (2015).

218. Ibarra, D. *et al.* Structural modification of eucalypt pulp lignin in a totally chlorine-free bleaching sequence including a laccase-mediator stage. *Holzforschung* **61**, 634-646 (2007).

219. Li, M. *et al.* The effect of liquid hot water pretreatment on the chemical–structural alteration and the reduced recalcitrance in poplar. . *Biotechnology for biofuels* **10**, 237 (2017).

220. Samuel, R. *et al.* HSQC (heteronuclear single quantum coherence) 13C–1H correlation spectra of whole biomass in perdeuterated pyridinium chloride–DMSO system: An effective tool for evaluating *Fuel* **90**, 2836-2842 (2011).

221. Samuel, R. *et al.* Investigation of the fate of poplar lignin during autohydrolysis pretreatment to understand the biomass recalcitrance. *RSC Adv.* **3**, 5305-5309 (2013).

222. Rencoret, J. *et al.* HSQC-NMR analysis of lignin in woody (Eucalyptus globulus and Picea abies) and non-woody (Agave sisalana) ball-milled plant materials at the gel state 10th EWLP, Stockholm, Sweden, August 25–28, 2008. *Holzforschung* **63**, 691-698 (2009).

223. Wen, J. L., Sun, S. L., Yuan, T. Q., Xu, F. & Sun, R. C. Structural elucidation of lignin polymers of Eucalyptus chips during organosolv pretreatment and extended delignification. *Journal of agricultural and food chemistry* **61**, 11067-11075 (2013).

224. Yuan, T.-Q., Sun, S.-N., Xu, F. & Sun, R.-C. Characterization of Lignin Structures and Lignin–Carbohydrate Complex (LCC) Linkages by Quantitative ^{13}C and 2D HSQC NMR Spectroscopy. *J. Agric. Food Chem.* **59**, 10604-10614 (2011).

225. Su, Y., Andreas, L. & Griffin, R. G. Magic angle spinning NMR of proteins: high-frequency dynamic nuclear polarization and ^{1}H detection. *Annu. Rev. Biochem.* **84**, 465-497, doi:10.1146/annurev-biochem-060614-034206 (2015).

226. Mentink-Vigier, F., Akbey, U., Oschkinat, H., Vega, S. & Feintuch, A. Theoretical aspects of Magic Angle Spinning - Dynamic Nuclear Polarization. *J. Magn. Reson.* **258**, 102-120, doi:10.1016/j.jmr.2015.07.001 (2015).

227. Yang, H. *et al.* Quantum Calculations on Plant Cell Wall Component Interactions. *Interdisciplinary sciences, computational life sciences* **11**, 485-495, doi:10.1007/s12539-018-0293-4 (2019).

228. Cresswell, R. *et al.* Importance of Water in Maintaining Softwood Secondary Cell Wall Nanostructure. *Biomacromolecules* **in press** (2021).

229. Wang, T., Park, Y. B., Cosgrove, D. J. & Hong, M. Cellulose-Pectin Spatial Contacts Are Inherent to Never-Dried Arabidopsis thaliana Primary Cell Walls: Evidence from Solid-State NMR. *Plant Physiol.* **168**, 871-884 (2015).

230. Vermaas, J. V., Crowley, M. F. & Beckham, G. T. A Quantitative Molecular Atlas for Interactions Between Lignin and Cellulose. *ACS Sustainable Chem. Eng.* **7**, 19570-19583 (2019).

231. Berglund, J. *et al.* Wood hemicelluloses exert distinct biomechanical contributions to cellulose fibrillar networks. *Nature communications* **11**, 4692, doi:10.1038/s41467-020-18390-z (2020).

232. Ramage, M. H. *et al.* The wood from the trees: The use of timber in construction. *Renew. Sust. Energ. Rev.* **68**, 333-359, doi:10.1016/j.rser.2016.09.107 (2017).

233. Ehren, H. L. *et al.* Characterization of the cell wall of a mushroom forming fungus at atomic resolution using solid-state NMR spectroscopy. *Cell surface* **6**, 100046, doi:10.1016/j.tcsw.2020.100046 (2020).

234. Chrissian, C. *et al.* Solid-state NMR spectroscopy identifies three classes of lipids in Cryptococcus neoformans melanized cell walls and whole fungal cells. *The Journal of biological chemistry* **295**, 15083-15096, doi:10.1074/jbc.RA120.015201 (2020).

235. Martin, R. W., Kelly, J. E. & Kelz, J. I. Advances in instrumentation and methodology for solid-state NMR of biological assemblies. *J. Struct. Biol.* **206**, 73-89 (2019).

236. Bougault, C., Ayala, I., Vollmer, W., Simorre, J. P. & Schanda, P. Studying intact bacterial peptidoglycan by proton-detected NMR spectroscopy at 100 kHz MAS frequency. *J. Struct. Biol.* **206**, 66-72, doi:10.1016/j.jsb.2018.07.009 (2019).

237. Mao, H. *et al.* Designing hierarchical nanoporous membranes for highly efficient gas adsorption and storage. *Sci. Adv.* **6**, eabb0694 (2020).

238. Thongsomboon, W. *et al.* Phosphoethanolamine cellulose: A naturally produced chemically modified cellulose. *Science* **359**, 334-338, doi:10.1126/science.aao4096 (2018).

239. Chakraborty, A. *et al.* A molecular vision of fungal cell wall organization by functional genomics and solid-state NMR. *Nature communications* **12**, 6346 (2021).

240. Poulhazan, A. *et al.* Identification and Quantification of Glycans in Whole Cells: Architecture of Microalgal Polysaccharides Described by Solid-State Nuclear Magnetic Resonance. *J Am Chem Soc*, in press, doi:10.1021/jacs.1c07429 (2021).

241. Bennett, A. E. *et al.* Homonuclear radio frequency-driven recoupling in rotating solids. *J. Chem. Phys.* **108**, 9463-9479, doi:Doi 10.1063/1.476420 (1998).

242. Kang, X. *et al.* CCMRD: A Solid-State NMR Database for Complex Carbohydrates. *J. Biomol. NMR* **74**, 239-250 (2019).

243. Ader, C. *et al.* Structural Rearrangements of Membrane Proteins Probed by Water-Edited Solid-State NMR Spectroscopy. *J. Am. Chem. Soc.* **131**, 170-176, doi:10.1021/ja806306e (2009).

244. Munowitz, M. G., Griffin, R. G., Bodenhausen, G. & Huang, T. H. Two-dimensional rotational spin-echo nuclear magnetic-resonance in solids: correlation of chemical-shift and dipolar interactions. *J Am Chem Soc* **103**, 2529-2533 (1981).

245. Yelle, D. J., Ralph, J. & Frihart, C. Characterization of nonderivatized plant cell walls using high-resolution solution-state NMR spectroscopy. *Magn. Reson. Chem.* **46**, 508-517 (2008).

246. Grabber, J. H., Ralph, J. & Hatfield, R. D. Model studies of ferulate-coniferyl alcohol cross-product formation in primary maize walls: implications for lignification in grasses. *J. Agric. Food Chem.* **50**, 6008-6016 (2002).

247. Grabber, J. H., Ralph, J. & Hatfield, R. D. Cross-linking of maize walls by ferulate dimerization and incorporation into lignin. *J. Agric. Food Chem.* **48**, 6106-6113 (2000).

248. Viger-Gravel, J. *et al.* Topology of Pretreated Wood Fibers Using Dynamic Nuclear Polarization. *J. Phys. Chem. C.* **123**, 30407-30415, doi:10.1021/acs.jpcc.9b09272 (2019).

249. Zhao, W. *et al.* Solid-state NMR of unlabeled plant cell walls: high-resolution structural analysis without isotopic enrichment. *Biotechnology for biofuels* **14**, 14, doi:10.1186/s13068-020-01858-x (2021).

250. Szabo, L. *et al.* Structure of a family 15 carbohydrate-binding module in complex with xylopentaose. Evidence that xylan binds in an approximate 3-fold helical conformation. *The Journal of biological chemistry* **276**, 49061-49065, doi:10.1074/jbc.M109558200 (2001).

251. Rassolov, V. A., Ratner, M. A., Pople, J. A., Redfern, P. C. & Curtiss, L. A. 6-31G* basis set for third-row atoms. *J. Comput. Chem.* **22**, 976-984 (20001).

252. Cances, E., Mennucci, B. & Tomasi, J. A new integral equation formalism for the polarizable continuum model: Theoretical background and applications to isotropic and anisotropic dielectrics. . *J Chem Phys* **107**, 3032-3041 (1997).

253. Frisch, M. e. a. (Gaussian, Inc., Wallingford CT, 2009).

254. Raju, R. K., Ramraj, A., Hillier, I. H., Vicent, M. A. & Burton, N. A. Carbohydrate–aromatic π interactions: a test of density functionals and the DFT-D method. *Phys. Chem. Chem. Phys.* **11**, 3411-3416 (2009).

255. Yang, H., Zimmer, J., Yingling, Y. G. & Kubicki, J. D. How Cellulose Elongates-A QM/MM Study of the Molecular Mechanism of Cellulose Polymerization in Bacterial CESA. *J. Phys. Chem. B* **119**, 6525-6535 (2015).

256. Brown, G. D. *et al.* Hidden Killers: Human Fungal Infections. *Sci. Transl. Med.* **4**, doi:10.1126/scitranslmed.3004404 (2012).

257. Denning, D. W. Invasive aspergillosis. *Clin. Infect. Dis.* **26**, 781-803 (1998).

258. Denning, D. W. Therapeutic outcome in invasive aspergillosis. *Clin. Infect. Dis.* **23**, 608-615 (1996).

259. Andriole, V. T. Infections with Aspergillus Species. *Clin. Infect. Dis.* **17**, S481-S486 (1993).

260. Becksague, C. M. & Jarvis, W. R. Secular Trends in the Epidemiology of Nosocomial Fungal-Infections in the United-States, 1980-1990. *J. Infect. Dis.* **167**, 1247-1251 (1993).

261. Le, T. *et al.* A Trial of Itraconazole or Amphotericin B for HIV-Associated Talaromycosis. *New. Engl. J. Med.* **376**, 2329-2340, doi:10.1056/Nejmoa1613306 (2017).

262. Ghannoum, M. A. & Rice, L. B. Antifungal agents: Mode of action, mechanisms of resistance, and correlation of these mechanisms with bacterial resistance. *Clin. Microbiol. Rev.* **12**, 501-517 (1999).

263. Lin, S. J., Schranz, J. & Teutsch, S. M. Aspergillosis case - Fatality rate: Systematic review of the literature. *Clin. Infect. Dis.* **32**, 358-366, doi:Doi 10.1086/318483 (2001).

264. Lipke, P. N. & Ovalle, R. Cell wall architecture in yeast: new structure and new challenges. *J. Bacteriol.* **180**, 3735-3740 (1998).

265. Barreto-Bergter, E. & Figueiredo, R. T. Fungal glycans and the innate immune recognition. *Front. Cell. Infect. Microbiol.* **4**, 145, doi:10.3389/fcimb.2014.00145 (2014).

266. Marco, F., Pfaller, M. A., Messer, S. A. & Jones, R. N. Antifungal activity of a new triazole, voriconazole (UK-109,496), compared with three other antifungal agents tested against clinical isolates of filamentous fungi. *Med. Mycol.* **36**, 433-436 (1998).

267. Odds, F. C., Brown, A. J. P. & Gow, N. A. R. Antifungal agents: mechanisms of action. *Trends Microbiol.* **11**, 272-279, doi:10.1016/S0966-842x(03)00117-3 (2003).

268. Perlin, D. S. Current perspectives on echinocandin class drugs. *Future Microbiol.* **6**, 441-457, doi:10.2217/Fmb.11.19 (2011).

269. Bowman, S. M. & Free, S. J. The structure and synthesis of the fungal cell wall. *Bioessays* **28**, 799-808, doi:10.1002/bies.20441 (2006).

270. Fesel, P. H. & Zuccaro, A. beta-glucan: Crucial component of the fungal cell wall and elusive MAMP in plants. *Fungal. Genet. Biol.* **90**, 53-60, doi:10.1016/j.fgb.2015.12.004 (2016).

271. Wang, T., Chen, Y. N., Tabuchi, A., Cosgrove, D. J. & Hong, M. The Target of beta-Expansin EXPB1 in Maize Cell Walls from Binding and Solid-State NMR Studies. *Plant Physiol.* **172**, 2107-2119, doi:10.1104/pp.16.01311 (2016).

272. Linden, A. H. *et al.* Neurotoxin II Bound to Acetylcholine Receptors in Native Membranes Studied by Dynamic Nuclear Polarization NMR. *J. Am. Chem. Soc.* **133**, 19266-19269, doi:10.1021/ja206999c (2011).

273. Sergeyev, I. V., Itin, B., Rogawski, R., Day, L. A. & McDermott, A. E. Efficient assignment and NMR analysis of an intact virus using sequential side-chain correlations and DNP sensitization. *Proc. Natl. Acad. Sci. USA* **114**, 5171-5176, doi:10.1073/pnas.1701484114 (2017).

274. Gupta, R. *et al.* Dynamic Nuclear Polarization Enhanced MAS NMR Spectroscopy for Structural Analysis of HIV-1 Protein Assemblies. *J. Phys. Chem. B.* **120**, 329-339, doi:10.1021/acs.jpcb.5b12134 (2016).

275. Thurber, K. R. & Tycko, R. Theory for cross effect dynamic nuclear polarization under magic-angle spinning in solid state nuclear magnetic resonance: The importance of level crossings. *J. Chem. Phys.* **137**, doi:10.1063/1.4747449 (2012).

276. Lu, X., Guo, C., Hou, G. & Polenova, T. Combined zero-quantum and spin-diffusion mixing for efficient homonuclear correlation spectroscopy under fast MAS: broadband recoupling and detection of long-range correlations. *J. Biomol. NMR* **61**, 7-20, doi:10.1007/s10858-014-9875-6 (2015).

277. Kasaai, M. R. Determination of the degree of N-acetylation for chitin and chitosan by various NMR spectroscopy techniques: A review. *Carbohydr. Polym.* **79**, 801-810, doi:10.1016/j.carbpol.2009.10.051 (2010).

278. Sikorski, P., Hori, R. & Wada, M. Revisit of alpha-Chitin Crystal Structure Using High Resolution X-ray Diffraction Data. *Biomacromolecules* **10**, 1100-1105, doi:10.1021/bm801251e (2009).

279. Yui, T., Taki, N., Sugiyama, J. & Hayashi, S. Exhaustive crystal structure search and crystal modeling of beta-chitin. *Int. J. Biol. Macromol.* **40**, 336-344, doi:10.1016/j.ijbiomac.2006.08.017 (2007).

280. Donovan, K. J., Jain, S. K., Silvers, R., Linse, S. & Griffin, R. G. Proton-Assisted Recoupling (PAR) in Peptides and Proteins. *J. Phys. Chem. B* **121**, 10804-10817, doi:10.1021/acs.jpcb.7b08934 (2017).

281. Lewandowski, J. R., De Paepe, G., Eddy, M. T. & Griffin, R. G. ^{15}N-^{15}N proton assisted recoupling in magic angle spinning NMR. *J. Am. Chem. Soc.* **131**, 5769-5776, doi:10.1021/ja806578y (2009).

282. Hall, D. A. *et al.* Polarization-enhanced NMR spectroscopy of biomolecules in frozen solution. *Science* **276**, 930-932, doi:DOI 10.1126/science.276.5314.930 (1997).

283. Gullion, T. & Schaefer, J. Rotational-Echo Double-Resonance NMR. *J. Magn. Reson.* **81**, 196-200, doi:Doi 10.1016/0022-2364(89)90280-1 (1989).

284. Jaroniec, C. P., Filip, C. & Griffin, R. G. 3D TEDOR NMR experiments for the simultaneous measurement of multiple carbon-nitrogen distances in uniformly (13)C,(15)N-labeled solids. *J. Am. Chem. Soc.* **124**, 10728-10742 (2002).

285. Wang, T., Jo, H., DeGrado, W. F. & Hong, M. Water Distribution, Dynamics, and Interactions with Alzheimer's beta-Amyloid Fibrils Investigated by Solid-State NMR. *J. Am. Chem. Soc.* **139**, 6242-6252, doi:10.1021/jacs.7b02089 (2017).

286. Rappleye, C. A., Eissenberg, L. G. & Goldman, W. E. Histoplasma capsulatum alpha-(1,3)-glucan blocks innate immune recognition by the beta-glucan receptor. *Proc. Natl. Acad. Sci. USA* **104**, 1366-1370, doi:10.1073/pnas.0609848104 (2007).

287. Fontaine, T., Mouyna, I., Hartland, R. P., Paris, S. & Latge, J. P. From the surface to the inner layer of the fungal cell wall. *Biochem. Soc. Trans.* **25**, 194-199, doi:Doi 10.1042/Bst0250194 (1997).

288. Aimanianda, V. *et al.* Surface hydrophobin prevents immune recognition of airborne fungal spores. *Nature* **460**, 1117-U1179, doi:10.1038/nature08264 (2009).

289. Fontaine, T. *et al.* Molecular organization of the alkali-insoluble fraction of Aspergillus fumigatus cell wall. . *J Biol Chem* **275**, 41528-41529 (2000).

290. Ruiz-Herrera, J. *Fungal Cell Wall: Structure, Synthesis, and Assembly*. (CRC Press, 1991).

291. Perez, P. & Ribas, J. C. Cell wall analysis. *Methods* **33**, 245-251, doi:10.1016/j.ymeth.2003.11.020 (2004).

292. Francois, J. M. A simple method for quantitative determination of polysaccharides in fungal cell walls. *Nat. Protoc.* **1**, 2995-3000, doi:10.1038/nprot.2006.457 (2006).

293. Lesage, G. & Bussey, H. Cell wall assembly in Saccharomyces cerevisiae. *Microbiol. Mol. Biol. Rev.* **70**, 317-343, doi:10.1128/Mmbr.00038-05 (2006).

294. Haido, R. M. *et al.* Analysis of peptidogalactomannans from the mycelial surface of Aspergillus fumigatus. *Med. Mycol.* **36**, 313-321 (1998).

295. Masuoka, J. Surface glycans of Candida albicans and other pathogenic fungi: physiological roles, clinical uses, and experimental challenges. *Clin. Microbiol. Rev.* **17**, 281-310 (2004).

296. Cheung, R. C. F., Ng, T. B., Wong, J. H. & Chan, W. Y. Chitosan: An Update on Potential Biomedical and Pharmaceutical Applications. *Mar. Drugs* **13**, 5156-5186, doi:10.3390/md13085156 (2015).

297. Baker, L. G., Specht, C. A. & Lodge, J. K. Cell Wall Chitosan Is Necessary for Virulence in the Opportunistic Pathogen Cryptococcus neoformans. *Eukaryotic Cell* **10**, 1264-1268, doi:10.1128/Ec.05138-11 (2011).

298. Eisenman, H. C. *et al.* Microstructure of cell wall-associated melanin in the human pathogenic fungus cryptococcus neoformans. *Biochemistry* **44**, 3683-3693, doi:10.1021/bi047731m (2005).

299. Eisenman, H. C. & Casadevall, A. Synthesis and assembly of fungal melanin. *Appl. Microbiol. Biot.* **93**, 931-940, doi:10.1007/s00253-011-3777-2 (2012).

300. Heinekamp, T. *et al.* Aspergillus fumigatus melanins: interference with the host endocytosis pathway and impact on virulence. *Front. Microbiol.* **3**, doi:10.3389/Fmicb.2012.00440 (2013).

301. Pihet, M. *et al.* Melanin is an essential component for the integrity of the cell wall of Aspergillus fumigatus conidia. *BMC Microbiol.* **9**, doi:10.1186/1471-2180-9-177 (2009).

302. Cosgrove, D. J. & Jarvis, M. C. Comparative structure and biomechanics of plant primary and secondary cell walls. *Front. Plant Sci.* **3**, doi:10.3389/Fpls.2012.00204 (2012).

303. Ciucanu, I. & Kerek, F. A simple and rapid method for the permethylation of carbohydrates. . *Carbohydr. Res.* **131**, 209-217 (1984).

304. Rienstra, C. M. *et al.* De novo determination of peptide structure with solid-state magic-angle spinning NMR spectroscopy. *Proc. Natl. Acad. Sci. USA* **99**, 10260-10265, doi:10.1073/pnas.152346599 (2002).

305. Baldus, M., Petkova, A. T., Herzfeld, J. & Griffin, R. G. Cross polarization in the tilted frame: assignment and spectral simplification in heteronuclear spin systems. *Molecular Physics* **95**, 1197-1207, doi:10.1080/00268979809483251 (1998).

306. De Paepe, G., Lewandowski, J. R., Loquet, A., Bockmann, A. & Griffin, R. G. Proton assisted recoupling and protein structure determination. *J. Chem. Phys.* **129**, doi:10.1063/1.3036928 (2008).

307. Jarvis, M. C. Structure of native cellulose microfibrils, the starting point for nanocellulose manufacture. *Philos. Trans. Royal Soc. A* **376**, doi:10.1098/Rsta.2017.0045 (2018).

308. Smakman, G. & Rinie, H. Energy metabolism of Plantago lanceolata, as affected by change in root temperature *Physiol. Plant.* **56**, 33-37 (1982).

309. De Visser, R., Vianden, H. & Schnyder, H. Kinetics and relative significance of remobilized and current C and N incorporation in leaf and root growth zones of Lolium perenne after defoliation: assessment by 13C and 15N steady-state labelling. . *Plant Cell Environ.* **20**, 37-46 (1997).

310. Lagerquist, L. *et al.* Structural and thermal analysis of softwood lignins from a pressurized hot water extraction biorefinery process and modified derivatives. . *Molecules* **24**, 335 (2019).

311. Michalak, L., Knutsen, S. H., Aarum, I. & Westereng, B. Effects of pH on steam explosion extraction of acetylated galactoglucomannan from Norway spruce. *Biotechnology for biofuels* **11**, 1-12 (2018).

312. Wang, T., Salazar, A., Zabotina, O. & Hong, M. Structure and Dynamics of Brachypodium Primary Cell Walls Polysaccharides from 2D 13C Solid-State NMR Spectroscopy. *Biochemistry-Us*, 2840-2854 (2014).

313. Duan, P. *et al.* Xylan Structure and Dynamics in Native Brachypodium Grass Cell Walls Investigated by Solid-State NMR Spectroscopy. *ACS Omega* **6**, 15460-15471 (2021).

314. Phyo, P., Wang, T., Xiao, C., Anderson, C. & Hong, M. Effects of Pectin Molecular-Weight Changes on the Structure, Dynamics and Polysaccharide Interactions of Primary Cell Walls of Arabidopsis thaliana: Insights from Solid-State NMR. *Biomacromolecules* **18**, 2937-2950 (2017).

315. Ibarra, D. *et al.* Lignin Modification during Eucalyptus globulus Kraft pulping followed by totally chlorine-free bleaching: A two-dimensional nuclear magnetic resonance, fourier transform infrared, and pyrolysis− gas chromatography/mass spectrometry study. *Journal of agricultural and food chemistry* **55**, 3477-3490 (2007).

316. Rencoret, J. *et al.* Hydroxystilbene glucosides are incorporated into Norway spruce bark lignin. . *Plant Physiol.* **180**, 1310-1321 (2019).

317. Shim, J. H. *et al.* Antitumor effect of soluble beta-1,3-glucan from Agrobacterium sp. R259 KCTC 1019. *J. Microbiol. Biotechnol.* **17**, 1513-1520 (2007).

318. Fairweather, J. K., Him, J. L. K., Heux, L., Driguez, H. & Bulone, V. Structural characterization by 13C-NMR spectroscopy of products synthesized in vitro by polysaccharide synthases using 13C-enriched glycosyl donors: application to a UDP-glucose:(1→3)-β-d-glucan synthase from blackberry (Rubus fruticosus) *Glycobiology* **14**, 775-781 (2009).

319. Saitô, H., Ohki, T. & Sasaki, T. A 13C-nuclear magnetic resonance study of polysaccharide gels. Molecular architecture in the gels consisting of fungal, branched (1 → 3)-β-d-glucans (lentinan and schizophyllan) as manifested by conformational changes induced by sodium hydroxide. *Carbohydr. Res.* **74**, 227-240 (1979).

320. Bhanja, S. K. *et al.* Water-insoluble glucans from the edible fungus Ramaria botrytis. *Bioactive Carbohydrates and Dietary Fibre* **3**, 52-58 (2014).

321 Puanglek, S. *et al.* In vitro synthesis of linear alpha-1,3-glucan and chemical modification .to ester derivatives exhibiting outstanding thermal properties. *Sci. Rep.* **6**, doi:10.1038/Srep30479 (2016).

322. Lowman, D. W. *et al.* New Insights into the Structure of (1 -> 3,1 -> 6)-beta-D-Glucan Side Chains in the Candida glabrata Cell Wall. *PLOS One* **6**, doi:10.1371/journal.pone.0027614 (2011).

323. Petkowicz, C. L. D., Reicher, F., Chanzy, H., Taravel, F. R. & Vuong, R. Linear mannan in the endosperm of Schizolobium amazonicum. *Carbohydr. Polym.* **44**, 107-112 (2001).

324. Marchessault, R. H. & Taylor, M. G. 13C CP/MAS NMR spectra of poly-β-D(1 → 4) mannose: mannan. *Can. J. Chem.* **68**, 1992-1995 (1990).

325. Renard, C. M. G. C. & Jarvis, M. C. A cross-polarization, magic-angle-spinning, C-13-nuclear-magnetic-resonance study of polysaccharides in sugar beet cell walls. *Plant Physiol.* **119**, 1315-1322, doi:DOI 10.1104/pp.119.4.1315 (1999).

326. Heux, L., Brugnerotto, J., Desbrieres, J., Versali, M. F. & Rinaudo, M. Solid state NMR for determination of degree of acetylation of chitin and chitosan. *Biomacromolecules* **1**, 746-751, doi:Doi 10.1021/Bm000070y (2000).

327. Kameda, T., Miyazawa, M., Ono, H. & Yoshida, M. Hydrogen bonding structure and stability of alpha-chitin studied by C-13 solid-state NMR. *Macromol. Biosci.* **5**, 103-106, doi:10.1002/mabi.200400142 (2004).

328. King, C., Stein, R. S., Shamshina, J. L. & Rogers, R. D. Measuring the Purity of Chitin with a Clean, Quantitative Solid-State NMR Method. *ACS Sustain. Chem. Eng.* **5**, 8011-8016, doi:10.1021/acssuschemeng.7b01589 (2017).

329. Tanner, S. F., Chanzy, H., Vincendon, M., Roux, J. C. & Gaill, F. High-Resolution Solid-State C-13 Nuclear-Magnetic-Resonance Study of Chitin. *Macromolecules* **23**, 3576-3583, doi:Doi 10.1021/Ma00217a008 (1990).

VITA

Alex Kipchirchir Kirui was born in Nakuru County, Kenya, to Joseph Kerich and Gladys Kerich. He graduated from Loreto Nakuru High School in 2009. He received his Bachelor of Technology in Applied Chemistry (December 2015) from The Technical University of Kenya. After working in the coating industry in Kenya for one and half years, his desire for research saw him apply for graduate school in Louisiana State University.

In fall 2017, he joined the Wang Research group as the first graduate student in the group where he performed research under the tutelage of Professor Tuo Wang. His research is focused on developing solid-state NMR methods to determine the structure and interactions of carbohydrate polymers in intact and native fungal and plant cells, which are either biomedically important human pathogens or energy-rich renewable biomass. He has been developing methods to enable whole-cell characterization using the cutting-edge DNP method. During his PhD career, his productive research has resulted in 11 publications in peer reviewed journals. He anticipates to graduate in May 2022 with a doctorate in Physical Chemistry.